

SERI/STR-217-2559

UC Category: 60

DE85002948

Post-Stall Wind Tunnel Data for NACA 44XX Series Airfoil Sections

A Subcontract Report

**C. Ostowari
D. Naik**

January 1985

**Prepared under Subcontract No. ASC-78348PB
of Rockwell International Corp.**

**Final Report prepared under SERI Task No. 4807.20
FTP No. 495**

SERI Technical Monitor: James Tangler

Solar Energy Research Institute

A Division of Midwest Research Institute

1617 Cole Boulevard
Golden, Colorado 80401

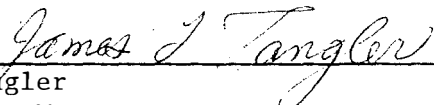
Prepared for the

U.S. Department of Energy

Contract No. DE-AC02-83CH10093

PREFACE

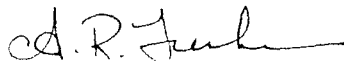
This report was prepared by C. Ostowari and D. Naik under Subcontract No. ASC-78348PB for Rockwell International Corporation's Wind Energy Research Center under their contract No. DE-AC04-76DP03533. As of October 1, 1984, the Wind Energy Research Center is under the operation of the Solar Energy Research Institute, which coordinated the publication of this report under Task No. 4807.20.



J. Tangler
Project Manager

Approved for

SOLAR ENERGY RESEARCH INSTITUTE



A. Trenka, Manager
Wind Systems Program Management



D. Ritchie, Director
Solar Electric Research Division

ACKNOWLEDGEMENT

The authors wish to express their appreciation for the support of this project by Rockwell International, especially J. Tangler of the Wind Energy Research Staff.

Our sincere thanks to P. K. Imbrie of the Texas A&M Low Speed Wind Tunnel Facility for his help during the tests.

SUMMARY

Objective

To characterize the performance of a nonrotating blade in stall as a function of its aspect ratio, airfoil thickness, and Reynolds number.

Discussion

Wind-turbine blades operate over a wide angle of attack range. Unlike aircraft, a wind turbine's angle of attack range extends deep into stall where the three-dimensional performance characteristics of airfoils are not generally known. Peak power predictions upon which wind turbine components are sized depend on a good understanding of a blade's post-stall characteristics.

This report documents results of the wind tunnel investigation of constant chord nonrotating blades having four aspect ratios, with NACA 44XX series airfoil sections, at angles of attack ranging from -10° to 110° . Tests were conducted at Reynolds numbers ranging from 0.25×10^6 to 1.0×10^6 . The thickness ratios studied were 0.18, 0.15, 0.12, and 0.09. The aspect ratios were 6, 9, 12, and infinity.

Results of force and pitching moment measurements over the angle of attack range, for all combinations of Reynolds number, thickness, and aspect ratios, and the effects of boundary layer tripping are presented.

Conclusions

The lift and post-stall drag coefficients decrease with decreasing aspect ratio. The lift coefficient decreases with decreasing thickness ratio while the drag coefficient increases. In the post-stall region both lift and drag coefficient are relatively insensitive to Reynolds number effects and the range tested. The boundary layer tripping decreases the lift curve slope and stalling angle of attack. The drag coefficient (with tripping) is significantly affected only at low aspect ratio.

TABLE OF CONTENTS

	<u>Page</u>
1.0 Introduction.....	1
2.0 Experimental Set-Up.....	2
2.1 Wind Tunnel Description.....	2
2.2 Model Description.....	2
3.0 Test Procedure.....	12
3.1 Test Conditions.....	12
3.2 Procedure.....	12
4.0 Results and Discussion.....	15
4.1 NACA 4418 Section.....	15
4.2 NACA 4415 Section.....	16
4.3 NACA 4412 Section.....	16
4.4 NACA 4409 Section.....	16
4.5 NACA 4415 Section with Boundary Layer Tripping.....	16
4.6 Effect of Aspect Ratio.....	17
4.7 Effect of Airfoil Thickness.....	17
5.0 Conclusions.....	18
6.0 References.....	19
Appendix A Force and Moment Data.....	20
Appendix B Wake Rake Drag Estimation.....	167

LIST OF TABLES

	<u>Page</u>
2-1 Instrument Resolution.....	2
3-1 Test Conditions.....	12
3-2 Summary of Figures.....	13

LIST OF FIGURES

2-1 Schematic of the Texas A&M 2.31-m by 3.05-m Low Speed Wind Tunnel.....	3
2-2 Blade Model Mounted in the Wind Tunnel Test Section.....	4
2-3 Airfoil Coordinates	
(a) NACA 4418 Section.....	5
(b) NACA 4415 Section.....	6
(c) NACA 4412 Section.....	7
(d) NACA 4409 Section.....	8
2-4 NACA 4415 Section Model with Boundary Layer Trip Strips.....	10
2-5 Cross-Sectional View Showing the Model Construction.....	11
A.1 through A.63.....	21 to 165
B.1 through B.4.....	168 to 171

NOMENCLATURE

The force and moment data have been referred to the quarter-chord location on the airfoil. Dimensional quantities are given in SI units. Measurements were made in U.S. Customary Units. Conversion factors between the various units may be found in Ref. 2.

AR	aspect ratio
b	span
c	airfoil reference chord
C_D	drag coefficient = drag/(dynamic pressure x area)
C_L	lift coefficient = lift/(dynamic pressure x area)
C_M	pitching moment coefficient with respect to the 0.25 c location = moment/(dynamic pressure x area x c)
M	Mach number
q	dynamic pressure
RN	Reynolds number
S	wing area
t	airfoil maximum thickness
U	free stream velocity
α	angle of attack

SECTION 1.0

INTRODUCTION

Current research efforts are directed toward the design of cost-effective wind energy conversion devices. The accomplishment of this goal requires good rotor-to-load matching. Proper matching depends on an accurate knowledge of the post-stall airfoil characteristics, upon which peak power prediction is strongly dependent.

Contemporary wind turbine blades are typically of high aspect ratio for cost-effective, high RPM operation. The blade sections are subjected to a large range of angles of attack for which, particularly at post-stall conditions, aerodynamic data are lacking. This report attempts to fill part of this airfoil data void and presents the post-stall aerodynamic characteristics as a function of aspect ratio, airfoil thickness, and Reynolds number. Aspect ratios of 6, 9, 12, and infinity were tested using constant chord blades over the angle of attack range of -18° to 110° . One airfoil series (NACA 44XX) having four different thicknesses (18%, 15%, 12%, and 9%) was investigated. The tests were conducted for Reynolds numbers (with respect to blade chord) of 0.25×10^6 , 0.50×10^6 , 0.75×10^6 , and 1.0×10^6 .

Also presented is the effect of boundary layer tripping on the aerodynamic characteristics of the NACA 4415. Tripping was achieved by applying chart tape at selected chord locations on the blade's upper and lower surfaces. This roughly simulates an unclean blade that has been struck by insects, grit, and bird droppings [1].

The tests were conducted at the Texas A&M University Low Speed Wind Tunnel Facility in July 1983. The blade performance characteristics presented in this report are lift coefficient, drag coefficient, and pitching moment coefficient versus angle of attack.

SECTION 2.0

EXPERIMENTAL SET-UP

2.1 WIND TUNNEL DESCRIPTION

A schematic of the Texas A&M 2.13-m x 3.05-m Low Speed Wind Tunnel is given in Figure 2-1. It is a closed circuit, single return type tunnel. The main balance of the tunnel is a six-component, pyramidal, virtual center external balance. The resolution of the various instrumentation systems is given in Table 2-1.

Table 2-1. Instrument Resolution

Measurement	Resolution		
	Dimensional form	Coefficient form*	
		probable	maximum
Lift (balance)	± 1.78 N	± 0.0002	± 0.0034
Drag (balance)	± 0.89 N	± 0.0001	± 0.0017
Pitch moment (balance)	± 0.27 Nm	± 0.00003	± 0.0005
Angle of attack	$\pm 0.1^\circ$	--	--
Dynamic pressure	$\pm 0.4\%$	--	--

*For infinite aspect ratio blades.

A Perkin-Elmer 8/16 E minicomputer is used for data acquisition and for reduction of final data and plots. More details of the facility may be found in Ref. 3.

2.2 MODEL DESCRIPTION

The models used were of the reflection plane type. This provides an effective aspect ratio that is twice the model aspect ratio. Each model extended into the tunnel section from an external-balance mount that was flush with the tunnel floor (Figure 2-2). All models were of the NACA 44XX family of airfoils. The thickness ratios studied were 0.18, 0.15, 0.12, and 0.09. The four airfoil section geometries are given in Figures 2-3a-d.

For tests in the Texas A&M facility, the models were sized with a 2.13-m span and a 0.305-m chord. This corresponds to a blade with infinite aspect ratio when placed in the 2.13-m x 3.05-m tunnel section. Effective aspect ratios of

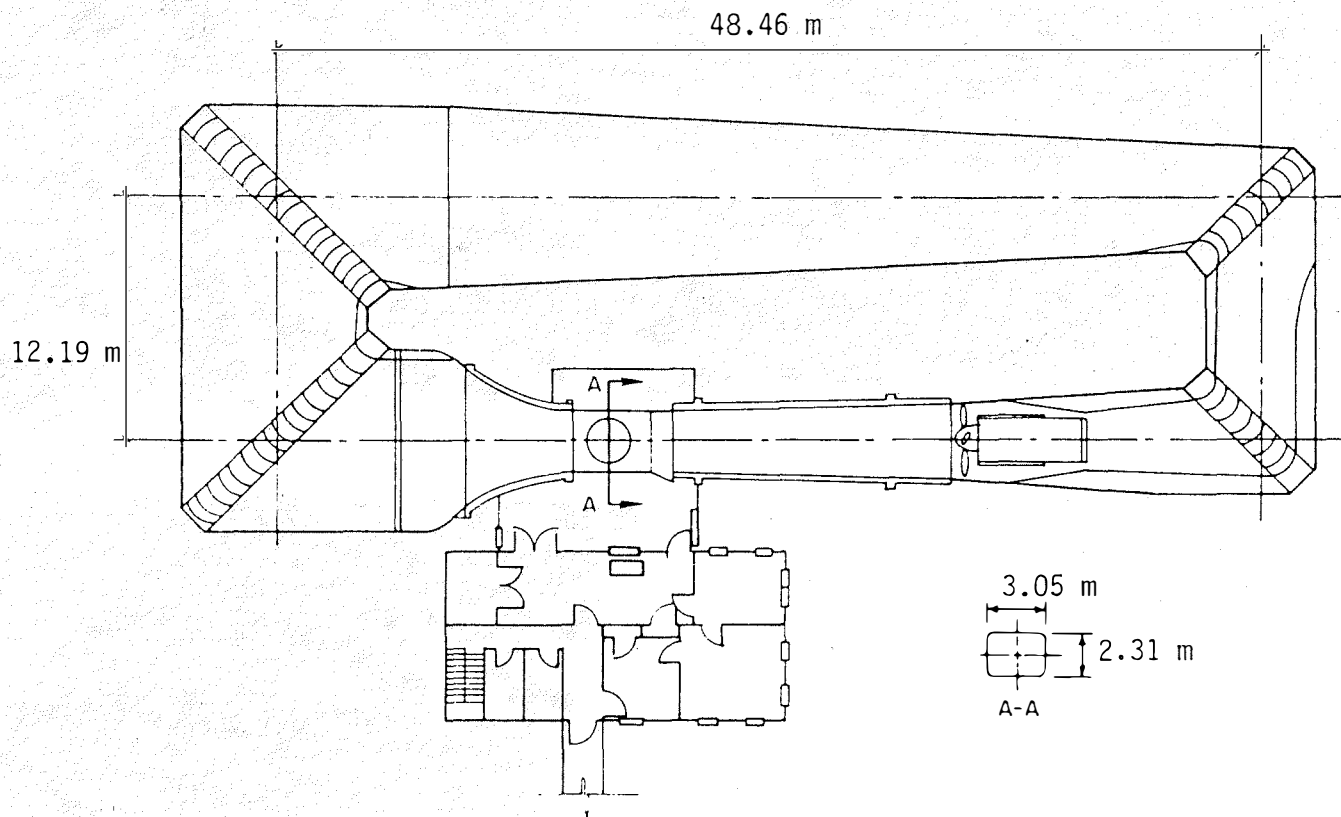
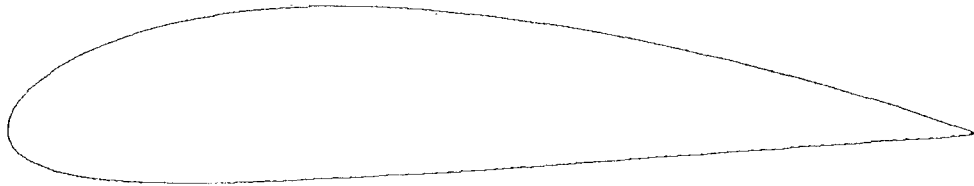


Figure 2-1. Schematic of the Texas A&M 2.31-m by 30.5-m Low Speed Wind Tunnel (adapted from Ref. 3)

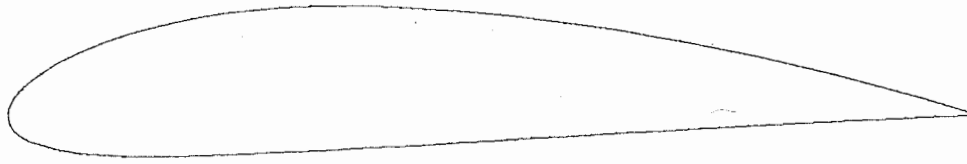


Figure 2-2. Blade Model Mounted in the Wind Tunnel Test Section



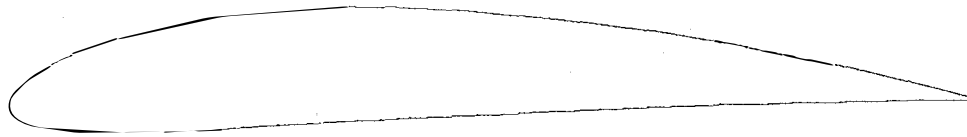
x/c	y_u/c	y_l/c
0.001000	0.008536	-0.008136
0.002000	0.012121	-0.011323
0.003000	0.014890	-0.013695
0.004000	0.017237	-0.015645
0.005000	0.019313	-0.017326
0.006000	0.021197	-0.018815
0.007000	0.022935	-0.020159
0.008000	0.024557	-0.021389
0.009000	0.026083	-0.022524
0.010000	0.027531	-0.023581
0.011000	0.028910	-0.024570
0.012000	0.030229	-0.025501
0.013000	0.031497	-0.026382
0.014000	0.032719	-0.027217
0.015000	0.033899	-0.028011
0.016000	0.035041	-0.028769
0.017000	0.036150	-0.029494
0.018000	0.037227	-0.030189
0.019000	0.038275	-0.030855
0.020000	0.039297	-0.031497
0.021000	0.040294	-0.032114
0.022000	0.041267	-0.032709
0.023000	0.042220	-0.033284
0.024000	0.043152	-0.033840
0.025000	0.044065	-0.034377
0.050000	0.062695	-0.043945
0.075000	0.076592	-0.049405
0.100000	0.087741	-0.052741
0.125000	0.096925	-0.054737
0.150000	0.104552	-0.055802
0.175000	0.110875	-0.056188
0.200000	0.116063	-0.056063
0.225000	0.120238	-0.055550
0.250000	0.123493	-0.054743
0.275000	0.125903	-0.053715
0.300000	0.127526	-0.052526
0.325000	0.128412	-0.051225
0.350000	0.128604	-0.049854
0.375000	0.128138	-0.048450
0.400000	0.127045	-0.047045
0.425000	0.125440	-0.045579
0.450000	0.123433	-0.043989
0.475000	0.121047	-0.042297
0.500000	0.118299	-0.040521
0.525000	0.115208	-0.038680
0.550000	0.111786	-0.036786
0.575000	0.108049	-0.034854
0.600000	0.104006	-0.032895
0.625000	0.099668	-0.030918
0.650000	0.095043	-0.028932
0.675000	0.090138	-0.026943
0.700000	0.084959	-0.024959
0.725000	0.079509	-0.022982
0.750000	0.073794	-0.021016
0.775000	0.067813	-0.019063
0.800000	0.061569	-0.017125
0.825000	0.055061	-0.015200
0.850000	0.048288	-0.013288
0.875000	0.041248	-0.011387
0.900000	0.033938	-0.009494
0.925000	0.026353	-0.007603
0.950000	0.018487	-0.005710
0.975000	0.010336	-0.003808
1.000000	0.001890	-0.001890

Figure 2-3a. NACA 4418 Airfoil Coordinates



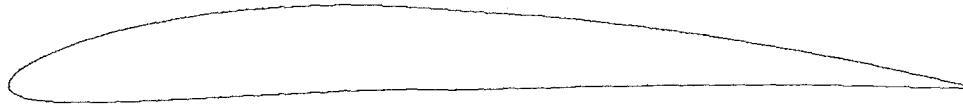
x/c	y_u/c	y_l/c
0.001000	0.007147	-0.006747
0.002000	0.010167	-0.009369
0.003000	0.012508	-0.011313
0.004000	0.014497	-0.012905
0.005000	0.016260	-0.014273
0.006000	0.017863	-0.015481
0.007000	0.019344	-0.016568
0.008000	0.020728	-0.017560
0.009000	0.022033	-0.018473
0.010000	0.023271	-0.019321
0.011000	0.024453	-0.020113
0.012000	0.025585	-0.020857
0.013000	0.026674	-0.021558
0.014000	0.027724	-0.022222
0.015000	0.028740	-0.022852
0.016000	0.029724	-0.023452
0.017000	0.030679	-0.024024
0.018000	0.031609	-0.024571
0.019000	0.032514	-0.025095
0.020000	0.033397	-0.025597
0.021000	0.034260	-0.026080
0.022000	0.035103	-0.026545
0.023000	0.035928	-0.026992
0.024000	0.036736	-0.027424
0.025000	0.037528	-0.027840
0.050000	0.053808	-0.035059
0.075000	0.066092	-0.038905
0.100000	0.076034	-0.041035
0.125000	0.084286	-0.042099
0.150000	0.091189	-0.042439
0.175000	0.096953	-0.042266
0.200000	0.101719	-0.041719
0.225000	0.105589	-0.040901
0.250000	0.108640	-0.039890
0.275000	0.110935	-0.038747
0.300000	0.112521	-0.037521
0.325000	0.113442	-0.036255
0.350000	0.113733	-0.034983
0.375000	0.113422	-0.033735
0.400000	0.112537	-0.032538
0.425000	0.111188	-0.031327
0.450000	0.109481	-0.030037
0.475000	0.107435	-0.028685
0.500000	0.105064	-0.027286
0.525000	0.102384	-0.025856
0.550000	0.099405	-0.024405
0.575000	0.096140	-0.022946
0.600000	0.092598	-0.021487
0.625000	0.088786	-0.020036
0.650000	0.084712	-0.018601
0.675000	0.080381	-0.017187
0.700000	0.075799	-0.015799
0.725000	0.070968	-0.014441
0.750000	0.065893	-0.013115
0.775000	0.060573	-0.011823
0.800000	0.055011	-0.010567
0.825000	0.049206	-0.009345
0.850000	0.043157	-0.008157
0.875000	0.036862	-0.007001
0.900000	0.030319	-0.005874
0.925000	0.023523	-0.004773
0.950000	0.016471	-0.003693
0.975000	0.009157	-0.002629
1.000000	0.001575	-0.001575

Figure 2-3b. NACA 4415 Airfoil Coordinates



x/c	y_u/c	y_l/c
0.00	0.0	0.0
0.005000	0.013207	-0.011219
0.006000	0.014528	-0.012146
0.007000	0.015753	-0.012977
0.008000	0.016899	-0.013731
0.009000	0.017982	-0.014423
0.010000	0.019012	-0.015062
0.011000	0.019996	-0.015657
0.012000	0.020941	-0.016213
0.013000	0.021851	-0.016735
0.014000	0.022729	-0.017228
0.015000	0.023580	-0.017693
0.016000	0.024406	-0.018134
0.017000	0.025209	-0.018554
0.018000	0.025991	-0.018953
0.019000	0.026753	-0.019334
0.020000	0.027498	-0.019698
0.021000	0.028226	-0.020046
0.022000	0.028938	-0.020380
0.023000	0.029636	-0.020700
0.024000	0.030320	-0.021008
0.025000	0.030991	-0.021303
0.050000	0.044922	-0.026172
0.075000	0.055593	-0.028405
0.100000	0.064328	-0.029328
0.125000	0.071648	-0.029460
0.150000	0.077826	-0.029076
0.175000	0.083031	-0.028344
0.200000	0.087375	-0.027375
0.225000	0.090940	-0.026252
0.250000	0.093787	-0.025037
0.275000	0.095966	-0.023779
0.300000	0.097517	-0.022517
0.325000	0.098473	-0.021285
0.350000	0.098861	-0.020111
0.375000	0.098706	-0.019019
0.400000	0.098030	-0.018030
0.425000	0.096937	-0.017076
0.450000	0.095529	-0.016085
0.475000	0.093823	-0.015073
0.500000	0.091829	-0.014051
0.525000	0.089560	-0.013032
0.550000	0.087024	-0.012024
0.575000	0.084232	-0.011037
0.600000	0.081189	-0.010078
0.625000	0.077904	-0.009154
0.650000	0.074380	-0.008269
0.675000	0.070624	-0.007430
0.700000	0.066639	-0.006639
0.725000	0.062428	-0.005900
0.750000	0.057992	-0.005214
0.775000	0.053334	-0.004584
0.800000	0.048453	-0.004009
0.825000	0.043351	-0.003490
0.850000	0.038026	-0.003026
0.875000	0.032476	-0.002615
0.900000	0.026699	-0.002255
0.925000	0.020693	-0.001943
0.950000	0.014455	-0.001677
0.975000	0.007978	-0.001451
1.000000	0.001260	-0.001260

Figure 2-3c. NACA 4412 Airfoil Coordinates



x/c	y_u/c	y_l/c
0.00	0.00	0.00
0.005000	0.010154	-0.006
0.006000	0.011194	-0.008812
0.007000	0.012161	-0.009386
0.008000	0.013070	-0.009902
0.009000	0.013932	-0.010372
0.010000	0.014753	-0.010803
0.011000	0.015540	-0.011200
0.012000	0.016297	-0.011569
0.013000	0.017027	-0.011912
0.014000	0.017735	-0.012233
0.015000	0.018421	-0.012534
0.016000	0.019089	-0.012817
0.017000	0.019739	-0.013083
0.018000	0.020373	-0.013335
0.019000	0.020992	-0.013573
0.020000	0.021598	-0.013798
0.021000	0.022192	-0.014012
0.022000	0.022773	-0.014215
0.023000	0.023344	-0.014408
0.024000	0.023904	-0.014592
0.025000	0.024454	-0.014767
0.050000	0.036035	-0.017285
0.075000	0.045093	-0.017905
0.100000	0.052621	-0.017621
0.125000	0.059009	-0.016822
0.150000	0.064464	-0.015714
0.175000	0.069109	-0.014422
0.200000	0.073031	-0.013032
0.225000	0.076291	-0.011603
0.250000	0.078934	-0.010184
0.275000	0.080998	-0.008811
0.300000	0.082513	-0.007513
0.325000	0.083503	-0.006315
0.350000	0.083990	-0.005240
0.375000	0.083991	-0.004303
0.400000	0.083522	-0.003523
0.425000	0.082685	-0.002824
0.450000	0.081578	-0.002133
0.475000	0.080211	-0.001461
0.500000	0.078594	-0.000816
0.525000	0.076736	-0.000208
0.550000	0.074643	0.000357
0.575000	0.072323	0.000871
0.600000	0.069781	0.001330
0.625000	0.067021	0.001728
0.650000	0.064049	0.002062
0.675000	0.060868	0.002327
0.700000	0.057479	0.002521
0.725000	0.053887	0.002641
0.750000	0.050091	0.002687
0.775000	0.046094	0.002656
0.800000	0.041896	0.002549
0.825000	0.037496	0.002365
0.850000	0.032894	0.002106
0.875000	0.028090	0.001772
0.900000	0.023080	0.001364
0.925000	0.017864	0.000886
0.950000	0.012438	0.000340
0.975000	0.006800	-0.000272
1.000000	0.000945	-0.000945

Figure 2-3d. NACA 4409 Airfoil Coordinates

12, 9, and 6 were obtained by cutting the models at appropriate span locations. Angle of attack variation was achieved through rotation of the turntable built into the tunnel floor. This turntable rotates with the external balance but is isolated from it. For boundary layer trip studies, the NACA 4415 model was fitted with transition strips located at 5% chord on the upper surface and at 10% chord at the lower surface. The transition strips were two layers of 0.127-mm-thick and 2.36-mm-wide chart tape. This is shown in Figure 2-4.

The airfoils were fabricated from 12.7-mm Douglas fir vertical laminates bonded with wood glue. Figure 2-5 shows the bonding for the four airfoil sections. The blade lower ends were shaped to facilitate attachment to the balance mount. Care was taken to ensure that this bulge did not protrude into the tunnel section. Further, the 0.25 chord location was used as a reference point for model mounting to minimize the error in moment transfer.

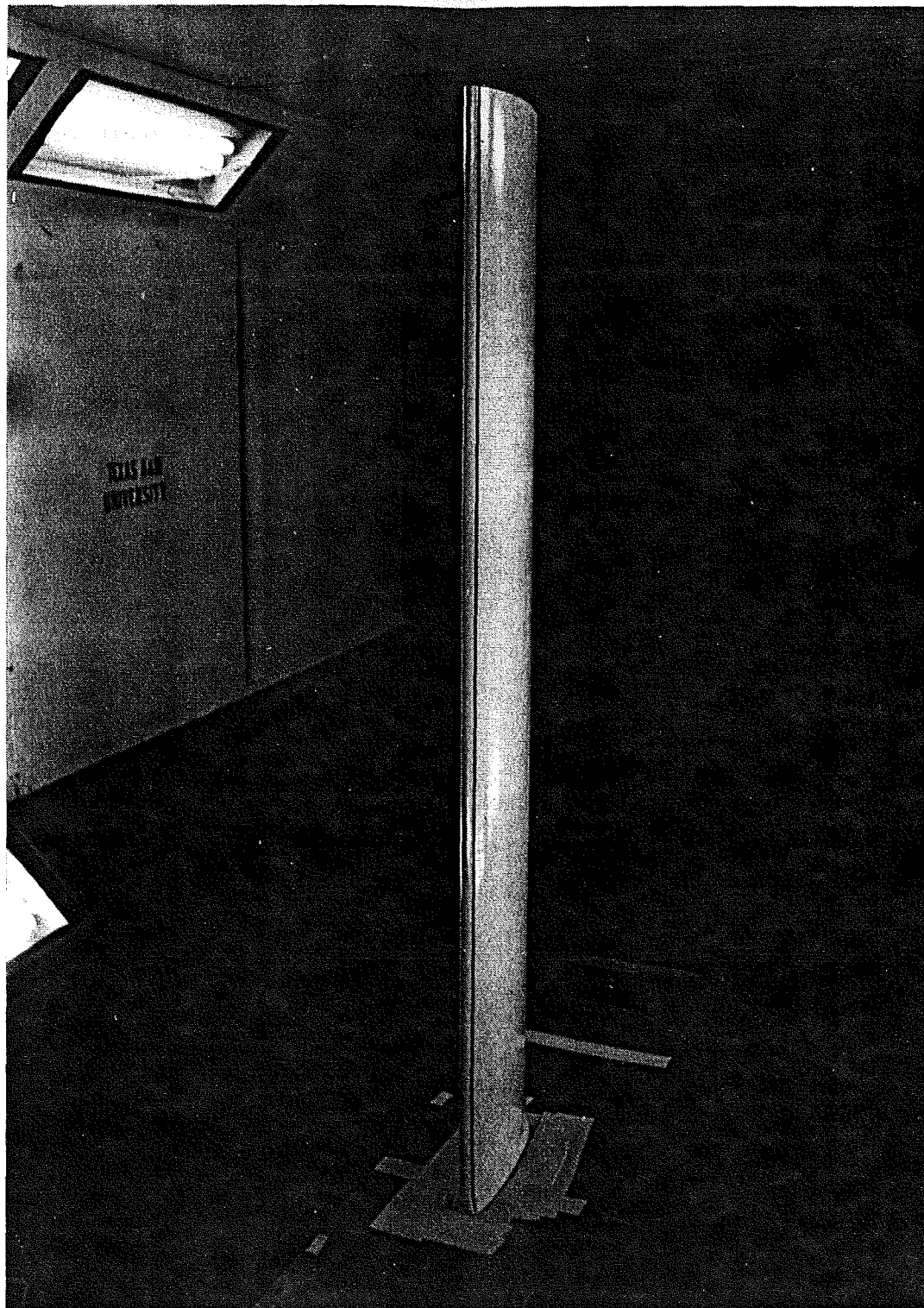


Figure 2-4. NACA 4415 Section Model with Boundary Layer Trip Strips

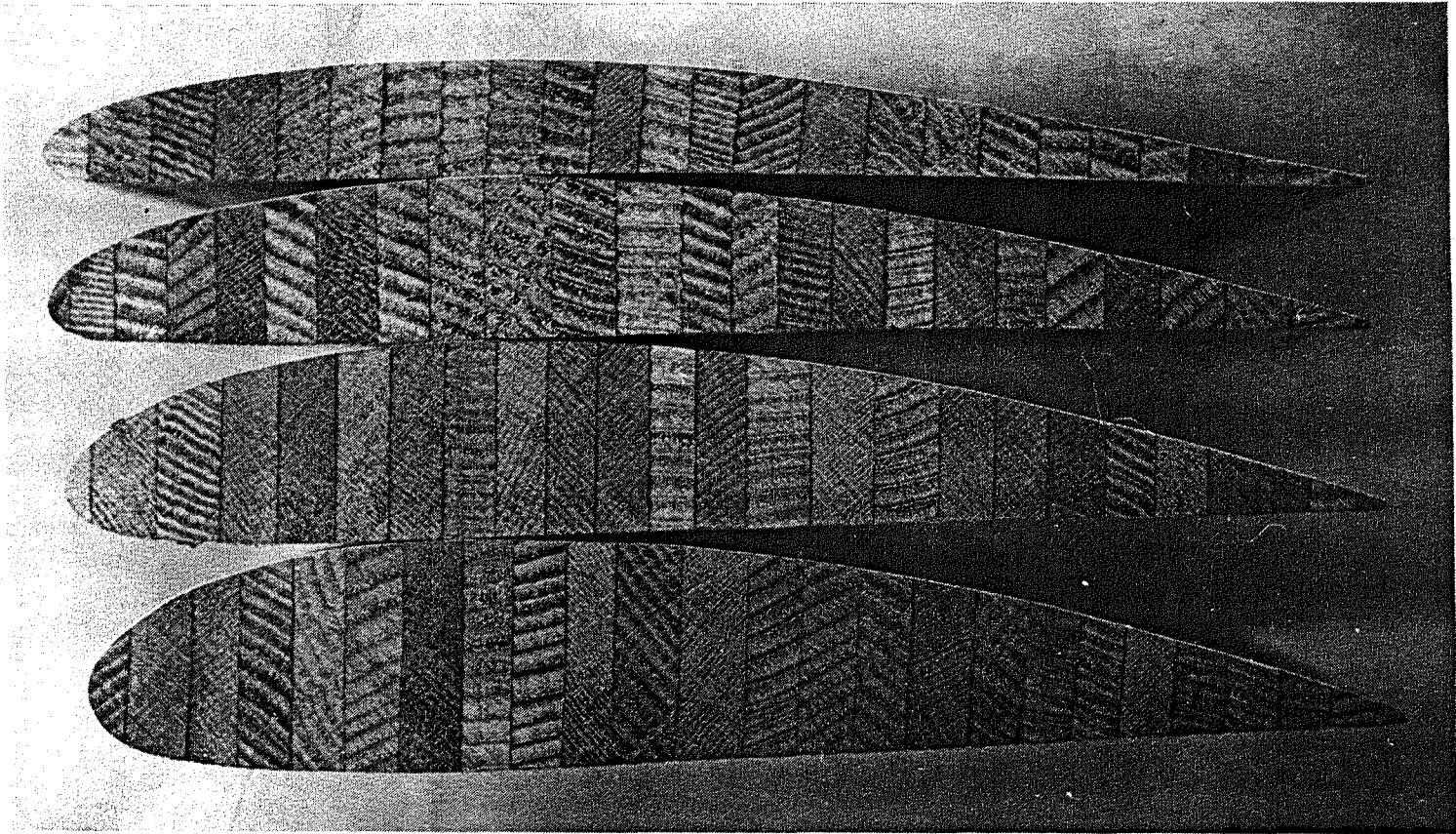


Figure 2-5. Cross-Sectional View Showing the Model Construction

SECTION 3.0

TEST PROCEDURE

3.1 TEST CONDITIONS

The models were tested at the conditions given in Table 3-1.

Table 3-1. Test Conditions

Dynamic Pressure (N/m ²)	Reynolds Number* (x 10 ⁻⁶)	Mach Number
71.82	0.25	0.05
277.7	0.50	0.09
627.23	0.75	0.14
1110.82	1.00	0.19

*The Reynolds number is with respect to airfoil chord.

3.2 PROCEDURE

Section drag measurements were made with the wake rake apparatus for all four infinite aspect ratio blades. Wake rake surveys were made at four different Reynolds numbers with the angle of attack ranging from -10° to 12° in 2° increments. The wake rake was located one chord length behind the model trailing edge.

Force measurements were made for 19 blade configurations (4 aspect ratios, each with 4 airfoil thickness; 3 with trip strips on NACA 4415) at the 4 different Reynolds numbers given above and for angles of attack ranging from -10° to 110° . Table 3-2 summarizes the various measurements and cross plots presented in this report. The three component force measurements were made using the wind tunnel main balance system.

The difference between the force balance drag measurement and wake rake drag estimate is the end-plate and interference drag with the tunnel floor and ceiling, which depends on both the lift coefficient and the section geometry. The wake survey method cannot be used when flow separation is present, so it was not applied to high angles of attack. Under high drag conditions, however, the end-plate tare and interference tare are a relatively small portion of the total drag. Therefore, the tare curve is extrapolated for high lift coefficient conditions and is generally assumed constant past a lift coefficient of roughly 1.3.

All data were corrected for tunnel-wall effects (wake blockage, solid blockage, buoyance drag, etc.) using the standard procedure given in Ref. 1.

Table 3-2. Summary of Figures

Configuration	Type Data	Figure
Tunnel	Schematic	2-1
Model	Model mount	2-2
Airfoils	Model geometry	2-3
NACA 4415	Transition strips	2-4
Airfoils	Model construction	2-5
NACA 4418, AR = ∞	C_L , C_D , C_M	A.1
NACA 4418, AR = 12	C_L , C_D , C_M	A.2
NACA 4418, AR = 9	C_L , C_D , C_M	A.3
NACA 4418, AR = 6	C_L , C_D , C_M	A.4
NACA 4415, AR = ∞	C_L , C_D , C_M	A.5
NACA 4415, AR = 12	C_L , C_D , C_M	A.6
NACA 4415, AR = 9	C_L , C_D , C_M	A.7
NACA 4415, AR = 6	C_L , C_D , C_M	A.8
NACA 4412, AR = ∞	C_L , C_D , C_M	A.9
NACA 4412, AR = 12	C_L , C_D , C_M	A.10
NACA 4412, AR = 9	C_L , C_D , C_M	A.11
NACA 4412, AR = 6	C_L , C_D , C_M	A.12
NACA 4409, AR = ∞	C_L , C_D , C_M	A.13
NACA 4409, AR = 12	C_L , C_D , C_M	A.14
NACA 4409, AR = 9	C_L , C_D , C_M	A.15
NACA 4409, AR = 6	C_L , C_D , C_M	A.16
NACA 4415, AR = ∞ , Trip strips	C_L , C_D , C_M	A.17
NACA 4415, AR = 12, Trip strips	C_L , C_D , C_M	A.18
NACA 4415, AR = 6, Trip strips	C_L , C_D , C_M	A.19
NACA 4415, AR = ∞ , RN = 0.25 mil.	C_L , C_D ; clean/trip	A.20
NACA 4415, AR = ∞ , RN = 0.50 mil.	C_L , C_D ; clean/trip	A.21
NACA 4415, AR = ∞ , RN = 0.75 mil.	C_L , C_D ; clean/trip	A.22
NACA 4415, AR = ∞ , RN = 1.00 mil.	C_L , C_D ; clean/trip	A.23
NACA 4415, AR = 12, RN = 0.25 mil.	C_L , C_D ; clean/trip	A.24
NACA 4415, AR = 12, RN = 0.50 mil.	C_L , C_D ; clean/trip	A.25
NACA 4415, AR = 12, RN = 0.75 mil.	C_L , C_D ; clean/trip	A.26
NACA 4415, AR = 12, RN = 1.00 mil.	C_L , C_D ; clean/trip	A.27
NACA 4415, AR = 6, RN = 0.25 mil.	C_L , C_D ; clean/trip	A.28
NACA 4415, AR = 6, RN = 0.50 mil.	C_L , C_D ; clean/trip	A.29
NACA 4415, AR = 6, RN = 0.75 mil.	C_L , C_D ; clean/trip	A.30
NACA 4415, AR = 6, RN = 1.00 mil.	C_L , C_D ; clean/trip	A.31
NACA 4418, RN = 0.25 mil.	C_L , C_D ; AR effect	A.32
NACA 4418, RN = 0.50 mil.	C_L , C_D ; AR effect	A.33
NACA 4418, RN = 0.75 mil.	C_L , C_D ; AR effect	A.34
NACA 4418, RN = 1.00 mil.	C_L , C_D ; AR effect	A.35
NACA 4415, RN = 0.25 mil.	C_L , C_D ; AR effect	A.36
NACA 4415, RN = 0.50 mil.	C_L , C_D ; AR effect	A.37
NACA 4415, RN = 0.75 mil.	C_L , C_D ; AR effect	A.38
NACA 4415, RN = 1.00 mil.	C_L , C_D ; AR effect	A.39
NACA 4412, RN = 0.25 mil.	C_L , C_D ; AR effect	A.40
NACA 4412, RN = 0.50 mil.	C_L , C_D ; AR effect	A.41

Table 3-2. Summary of Figures (Concluded)

Configuration	Type Data	Figure
NACA 4412, RN = 0.75 mil.	C_L, C_D ; AR effect	A.42
NACA 4412, RN = 1.00 mil.	C_L, C_D ; AR effect	A.43
NACA 4409, RN = 0.25 mil.	C_L, C_D ; AR effect	A.44
NACA 4409, RN = 0.50 mil.	C_L, C_D ; AR effect	A.45
NACA 4409, RN = 0.75 mil.	C_L, C_D ; AR effect	A.46
NACA 4409, RN = 1.00 mil.	C_L, C_D ; AR effect	A.47
AR = ∞ , RN = 0.25 mil.	C_L, C_D ; t/c effect	A.48
AR = ∞ , RN = 0.50 mil.	C_L, C_D ; t/c effect	A.49
AR = ∞ , RN = 0.75 mil.	C_L, C_D ; t/c effect	A.50
AR = ∞ , RN = 1.00 mil.	C_L, C_D ; t/c effect	A.51
AR = 12, RN = 0.25 mil.	C_L, C_D ; t/c effect	A.52
AR = 12, RN = 0.50 mil.	C_L, C_D ; t/c effect	A.53
AR = 12, RN = 0.75 mil.	C_L, C_D ; t/c effect	A.54
AR = 12, RN = 1.00 mil.	C_L, C_D ; t/c effect	A.55
AR = 9, RN = 0.25 mil.	C_L, C_D ; t/c effect	A.56
AR = 9, RN = 0.50 mil.	C_L, C_D ; t/c effect	A.57
AR = 9, RN = 0.75 mil.	C_L, C_D ; t/c effect	A.58
AR = 9, RN = 1.00 mil.	C_L, C_D ; t/c effect	A.59
AR = 6, RN = 0.25 mil.	C_L, C_D ; t/c effect	A.60
AR = 6, RN = 0.50 mil.	C_L, C_D ; t/c effect	A.61
AR = 6, RN = 0.75 mil.	C_L, C_D ; t/c effect	A.62
AR = 6, RN = 1.00 mil.	C_L, C_D ; t/c effect	A.63
NACA 4418, AR = ∞	C_D ; wake rake	B.1
NACA 4415, AR = ∞	C_D ; wake rake	B.2
NACA 4412, AR = ∞	C_D ; wake rake	B.3
NACA 4409, AR = ∞	C_D ; wake rake	B.4

SECTION 4.0

RESULTS AND DISCUSSION

The reduced data presented in Appendix A in Figures A.1 through A.63 are plots of lift coefficient, drag coefficient, and pitching moment coefficient versus angle of attack. In some of these figures, the full angle of attack range (-10° to 110°) is not presented. The angle of attack range was restricted to prevent the thinner blades from breaking, especially at combinations of high AR and high RN. The wake rake drag coefficients are given in Appendix B. Some of the important features of the force balance data are discussed below.

4.1 NACA 4418 SECTION (Figures A.1 through A.4)

Results of lift, drag, and pitching moment measurements are shown for blade aspect ratios ranging from ∞ to 6. For each AR, results are shown for a Reynolds number range of 0.25×10^6 to 1.0×10^6 .

For the two-dimensional case ($AR = \infty$), initial stall occurs at $\alpha = 18^\circ$. Since the blade was only supported at one end (Figure 2-2), a certain amount of bending and twisting occurred at high RN and high C_L conditions. Blade bending and twisting produce a somewhat finite wing, which affects the circulation around the wing and causes some loss of lift while increasing the drag. There has been no attempt to correct either C_{Lmax} or the lift curve slope for this effect. Thus, as can be seen in Figure A.1 (a), C_{Lmax} decreases with increasing RN. For a true 2-D section the trend would have been reversed. The stalling angle of attack, however, is constant over the RN range. The (pre-stall) lift curve slope is more or less constant at 0.09 per degree over the RN range studied. This differs from the slope of 0.1 for RN of 3 to 9×10^6 given in Ref. 4. Beyond 18° the lift coefficient drops to a local minimum of 0.9 at 31° and then rises to a local maximum of 1.2 (secondary stall) at 42° before dropping off sharply with angle of attack beyond 46° . This 'double-humped' lift curve occurs in all later plots. For RNs of 0.75×10^6 and 1.0×10^6 , the local minimum is 1.08 and occurs at 36° .

There is rapid rise in drag past C_{Lmax} [Figure A.1 (b)]. Maximum C_D is reached at $\alpha = 90^\circ$. This maximum value (2.06) is close to the theoretical limit of 2.0 for a two-dimensional flat plate at 90° . The moment curves in Figure A.1 (c) show a somewhat stable characteristic up to $\alpha = 18^\circ$, but a highly unstable characteristic at the higher angles of attack. A considerable amount of erratic change in pitching moment is noticed at low α ($<10^\circ$) for an $RN = 0.25 \times 10^6$. This is primarily due to the lack of sensitivity of the moment balance at such a low dynamic pressure.

Similar trends are observed in Figures A.2, A.3, and A.4 for the finite blade with aspect ratios 12, 9, and 6, respectively. An interesting trend is the decrease in lift curve slope and C_{Lmax} with decreasing AR. There is minimal change in the drag coefficient versus C_L curve, in going from an infinite AR to an AR of 12. However, for $AR = 9$ and $AR = 6$, the C_D curve shows dramatic decreases at high lift coefficients. The effect of AR is discussed in detail later.

4.2 NACA 4415 SECTION (Figures A.5 through A.8)

Lift, drag, and pitching moment curves for this section are shown for the RN and blade AR range mentioned for the previous section. For the infinite AR blade, C_{Lmax} of roughly 1.4 occurs at $\alpha = 18^\circ$. A local minimum of 0.9 occurs at 31° . Secondary stall ($C_L = 1.2$) occurs at roughly 42° . As before, the C_{Lmax} decreases with ascending RN in apparent contradiction to Ref. 4. The $RN = 1.00 \times 10^6$ curve in Figure A.5 (a) shows premature stall. This apparent anomaly is yet to be explained. As for NACA 4418, the drag coefficient reaches a maximum at $\alpha = 90^\circ$. At high α , the airfoil behaves like a flat plate. The lift curve slope is 0.09 per degree compared with 0.1 in Ref. 4. The pitching moment is stable up to 10° angle of attack. At high α , the pitching moment characteristic is highly unstable. As in the NACA 4418 case, erratic variation of C_M at $RN = 0.25 \times 10^6$ [Figure 1.5 (c)] is observed.

Figures A.6, A.7, and A.8 show C_L , C_D , and C_M for aspect ratios of 12, 9, and 6. The same trends (secondary stall, sharp increase in C_D beyond α_{stall} , erratic C_M variation with α at low RN, post-stall unstable characteristics of C_M , etc.) mentioned for the two-dimensional airfoil are followed in these plots. The effect of aspect ratio on the aerodynamic coefficients is discussed later.

4.3 NACA 4412 SECTION (Figures A.9 through A.12)

A C_{Lmax} of about 1.35 occurs at an angle of attack of 17° . The pre-stall lift curve slope is 0.09 compared with the value 0.1 given in Ref. 4. The local minimum (0.9) is the same as that for NACA 4418 and NACA 4415. However, it occurs at a lower (26°) angle of attack. Secondary stall ($C_L = 1.2$) is at roughly 44° . C_{Dmax} (2.06) is at 90° and the low RN C_M is somewhat erratic.

4.4 NACA 4409 SECTION (Figures A.13 through A.16)

Initial stall occurs at 15° and the local minimum (0.92) is at 25° . The lift curve slope is 0.1 per degree. The drag and pitching moment curves follow the same previously mentioned patterns.

4.5 NACA 4415 SECTION WITH BOUNDARY LAYER TRIPPING (Figures A.17 through A.31)

The aerodynamic characteristics of the NACA 4415 airfoil with boundary layer tripping are presented (Figures A.17, A.18, and A.19) along with a comparison with the clean airfoil (Figures A.20 through A.31). The trip strips are described in Section 2.0. Three aspect ratios (∞ , 12, and 6) were investigated at the four Reynolds numbers.

The lift curve slope for the airfoil is roughly 0.086 per degree. The C_{Lmax} is found to decrease (and occur at progressively lower angles of attack) with increase in Reynolds number. However, in all cases the post-stall local

minimum (0.92) occurs at $\alpha = 31^\circ$. Secondary stall occurs between 40° and 45° . C_D reaches a maximum (2.12) at $\alpha = 90^\circ$. The pitching moment shows a stable condition at pre-stall angles and shows highly unstable characteristics at high angles of attack.

For the two-dimensional blade at low RN (Figure A.20), the boundary layer trip decreases the lift curve slope, lowers C_{Lmax} , and generally lowers the lift curve for angles of attack up to the local minima. These minima (0.9 at 31°) and the lift curve beyond this point are the same as that for the clean airfoil. The decrease in the lift curve slope is more pronounced at higher RN (Figures A.21 through A.31). The same trends are observed for the blades with aspect ratios of 12 and 6.

As can be seen in the figures, the drag coefficient is not much affected by the trip strips except at low aspect ratios. The effect on pitching moment is not presented but may be inferred from Figures A.5 through A.9 and A.17 through A.19.

4.6 EFFECT OF ASPECT RATIO (Figures A.32 through A.47)

In these figures the effect of aspect ratio variation on the aerodynamic characteristics (specifically lift and drag coefficients) is presented for the 16 different airfoil section-RN combinations. For example, Figure A.32 shows C_L and C_D for NACA 4418 with AR of ∞ , 12, 9, and 6 at $RN = 0.25 \times 10^6$. A general lowering of the lift coefficient curve over the angle of attack range -10° to 90° is observed to occur with decrease in aspect ratio. An interesting consequence of the AR effect is that in some cases [for example, in Figure A.32 (a) for ARs of 9 and 6] the second local maximum (secondary stall) completely disappears, and the lift falls off continuously from a maximum at initial stall.

The drag coefficient is significantly reduced with a decrease in aspect ratio at post-stall angles of attack. Figure A.32 (b) is a typical representative of this effect. In this figure, C_{Dmax} has a value of 2.06 for an AR of ∞ , but is 1.32 for an AR of 6. Both maxima occur at 90° . These trends may be compared with those given in Ref. 5 for low aspect ratio wings with Clark Y airfoil sections at RN of 0.153×10^6 . The lift and drag coefficient curves in Ref. 5 are qualitatively similar to those in this report. In particular, the C_{Dmax} in both cases occurs at 90° and its value falls in the 1.2 to 1.6 range.

4.7 EFFECT OF AIRFOIL THICKNESS (Figures A.48 through A.63)

The airfoil thickness affects C_{Lmax} and α_{stall} . This is true for the entire RN range studied. C_{Lmax} and α_{stall} both decrease with decrease in thickness. Although the local minimum lift coefficient is the same for all four thicknesses, the angle of attack at which this occurs decreases with decreasing thickness. In general the post-stall drag coefficient increases with decreasing airfoil thickness. This again is true over the entire RN range studied.

SECTION 5.0

CONCLUSIONS

Force and moment data are presented for nonrotating NACA 4418, 4415, 4412, and 4409 wind turbine blades with aspect ratios of infinity, 12, 9, and 6 for Reynolds numbers of 0.25×10^6 , 0.50×10^6 , 0.75×10^6 , and 1.00×10^6 . From these data the following conclusions are observed:

- In general, the lift coefficient data showed both initial and secondary stall over the angle of attack range of -10° to 110° . The maximum drag coefficient occurs at 90° , with the highest value at 2.1 for an infinite aspect ratio blade. The pitching moment is unstable beyond stall.
- The lift coefficient decreases with decreasing aspect ratio. For aspect ratios of 9 and 6, secondary stall is eliminated. The post-stall drag coefficient decreases significantly with a decrease in aspect ratio.
- The lift coefficient and stall angle of attack both decrease with decreasing airfoil thickness ratio. The post-stall drag coefficient increases with a decrease in thickness.
- In the post-stall region, the lift and drag coefficient were relatively insensitive to Reynolds number effects over the range tested. The unexpected increase in maximum lift coefficient with decreasing Reynolds number is attributed to blade bending as a result of the higher dynamic pressure.
- Boundary layer tripping is observed to decrease the lift curve slope, the maximum lift coefficient, and the stall angle of attack. The drag coefficient is significantly affected only at low aspect ratio.

SECTION 6.0

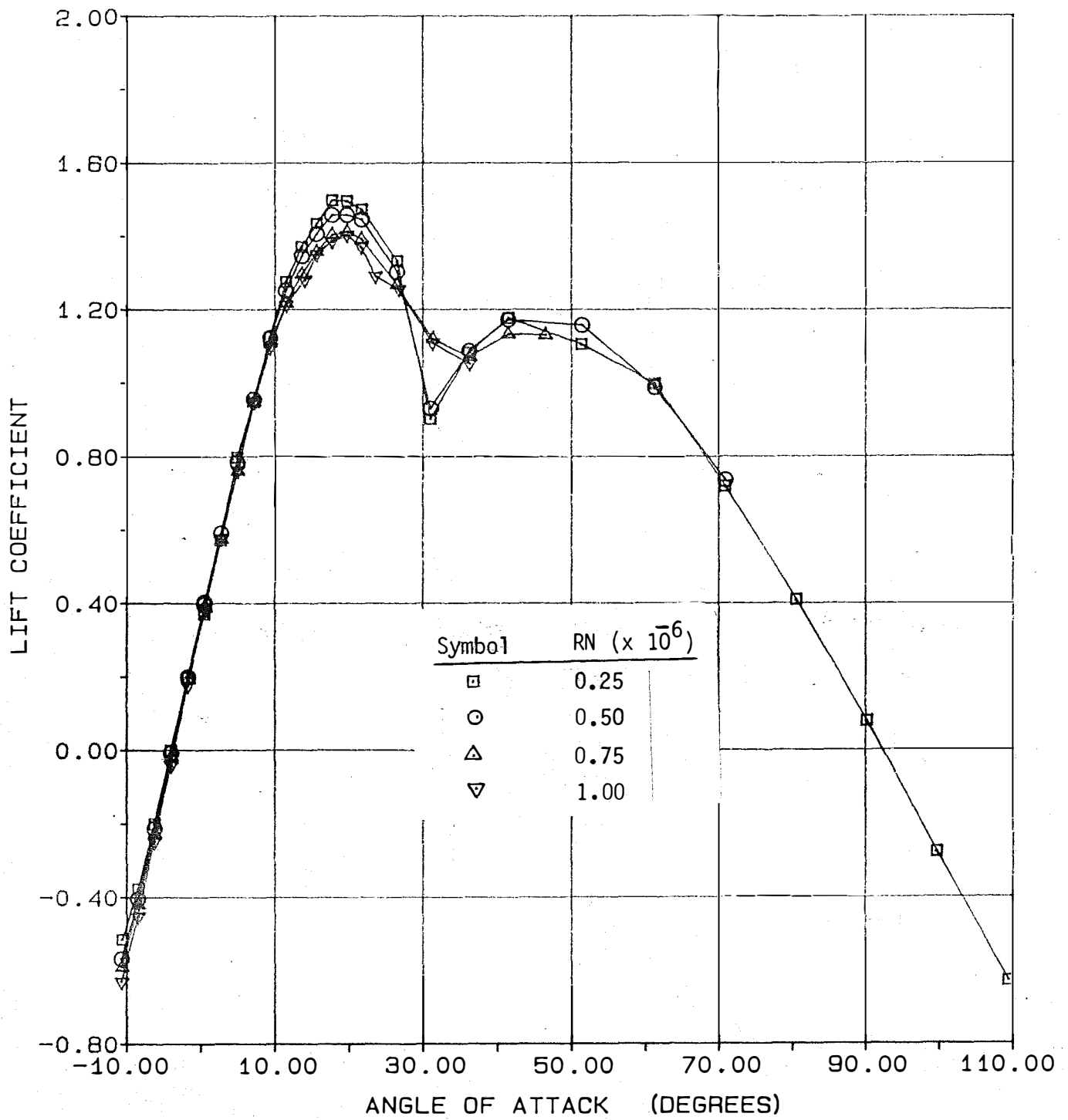
REFERENCES

1. Pope, A. and Harper, J. J., Low-Speed Wind Tunnel Testing, John Wiley & Sons, New York, 1966.
2. Mechtley, E. A., International System of Units - Physical Constants and Conversion Factors (Revised), NASA SP-7012, 1969.
3. Low Speed Wind Tunnel Facility Handbook, Aerospace Engineering Division, Texas Engineering Experiment Station, The Texas A&M University System, College Station, Texas, January, 1982.
4. Abbott, I. H. and Von Doenhoff, A. E., Theory of Wing Sections, Dover Publications, Inc., New York, 1959, pp. 488-493.
5. Knight, M. and Wenzinger, C. J., Wind Tunnel Tests on a Series of Wing Models through a Large Angle of Attack Range, Part I - Force Tests, NACA TR 317, 1929.

APPENDIX A

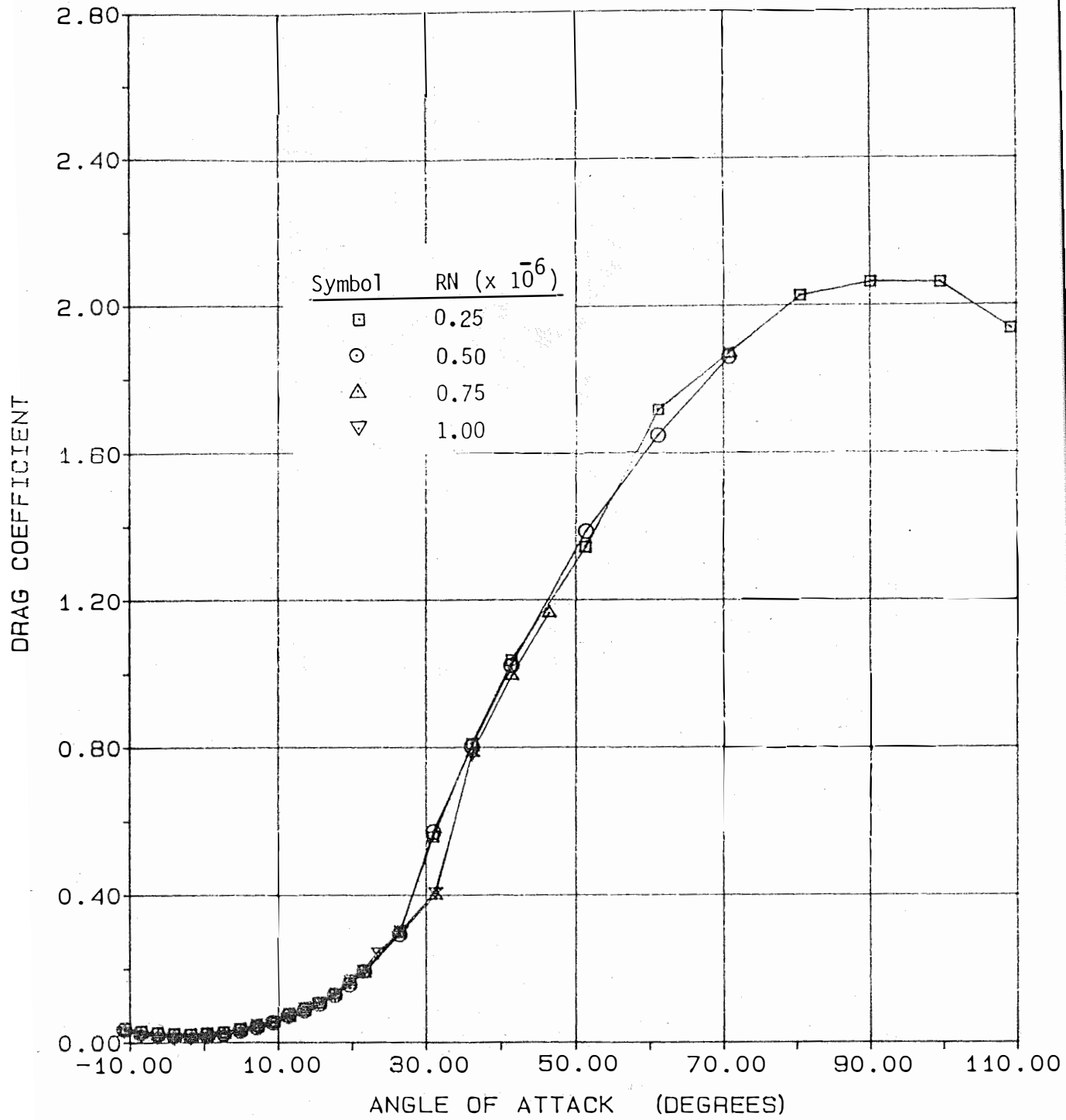
FORCE AND MOMENT DATA

This Appendix contains Figures A.1 through A.63. The figures are summarized in Table 3-2.



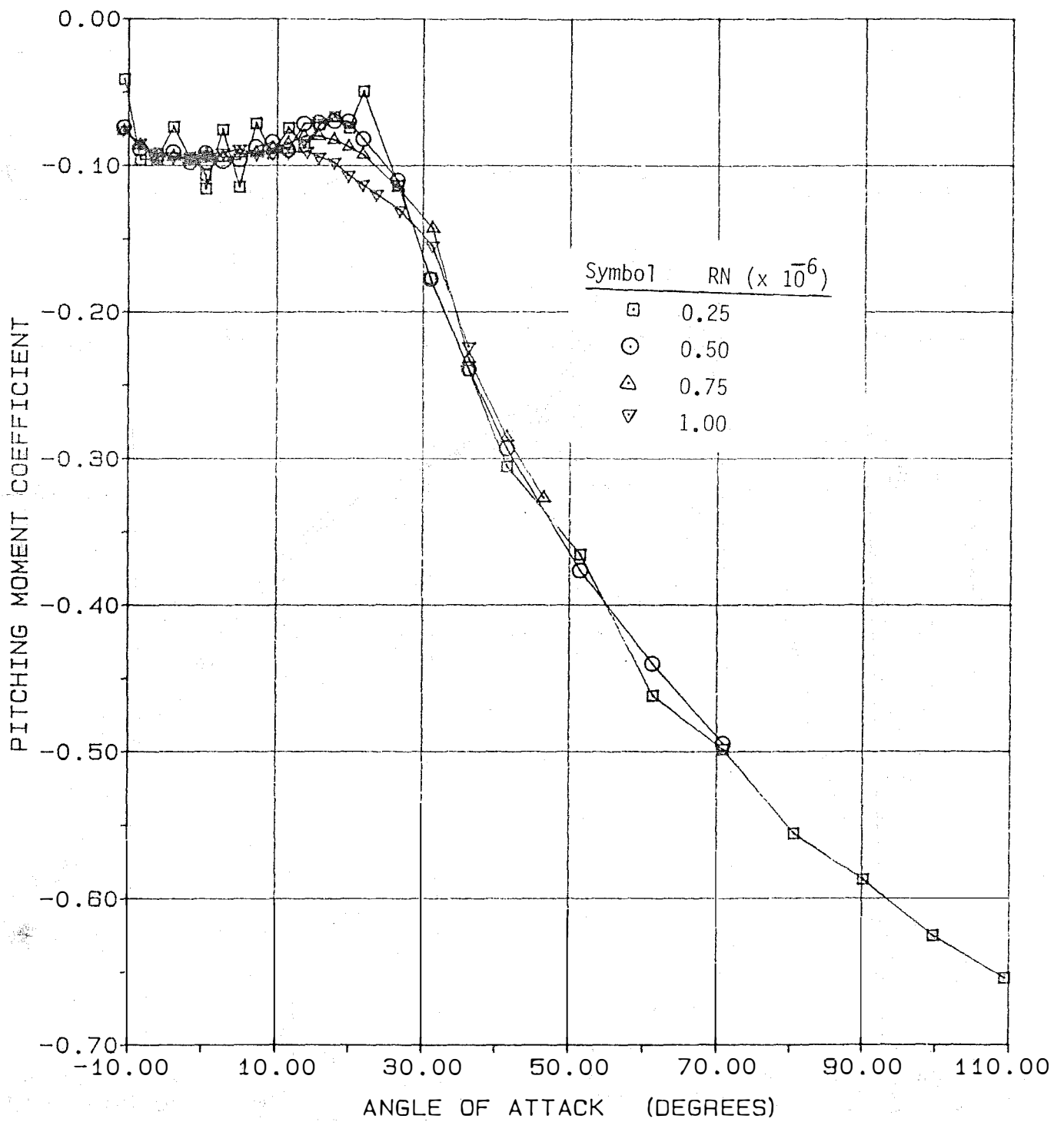
(a) Lift

Figure A.1 - Aerodynamic Coefficients of the NACA 4418 Airfoil, $AR = \infty$.



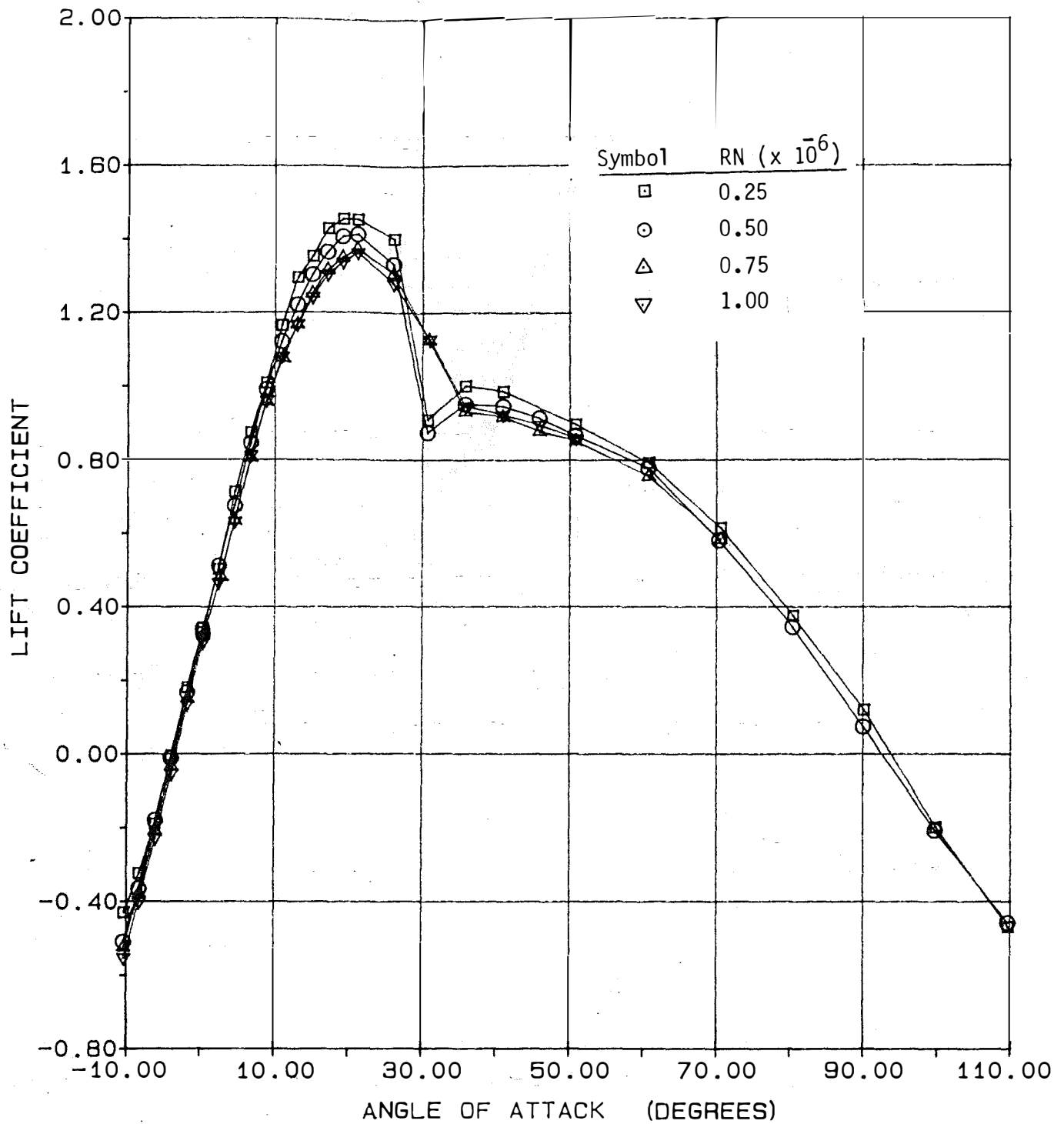
(b) Drag

Figure A.1- Continued.



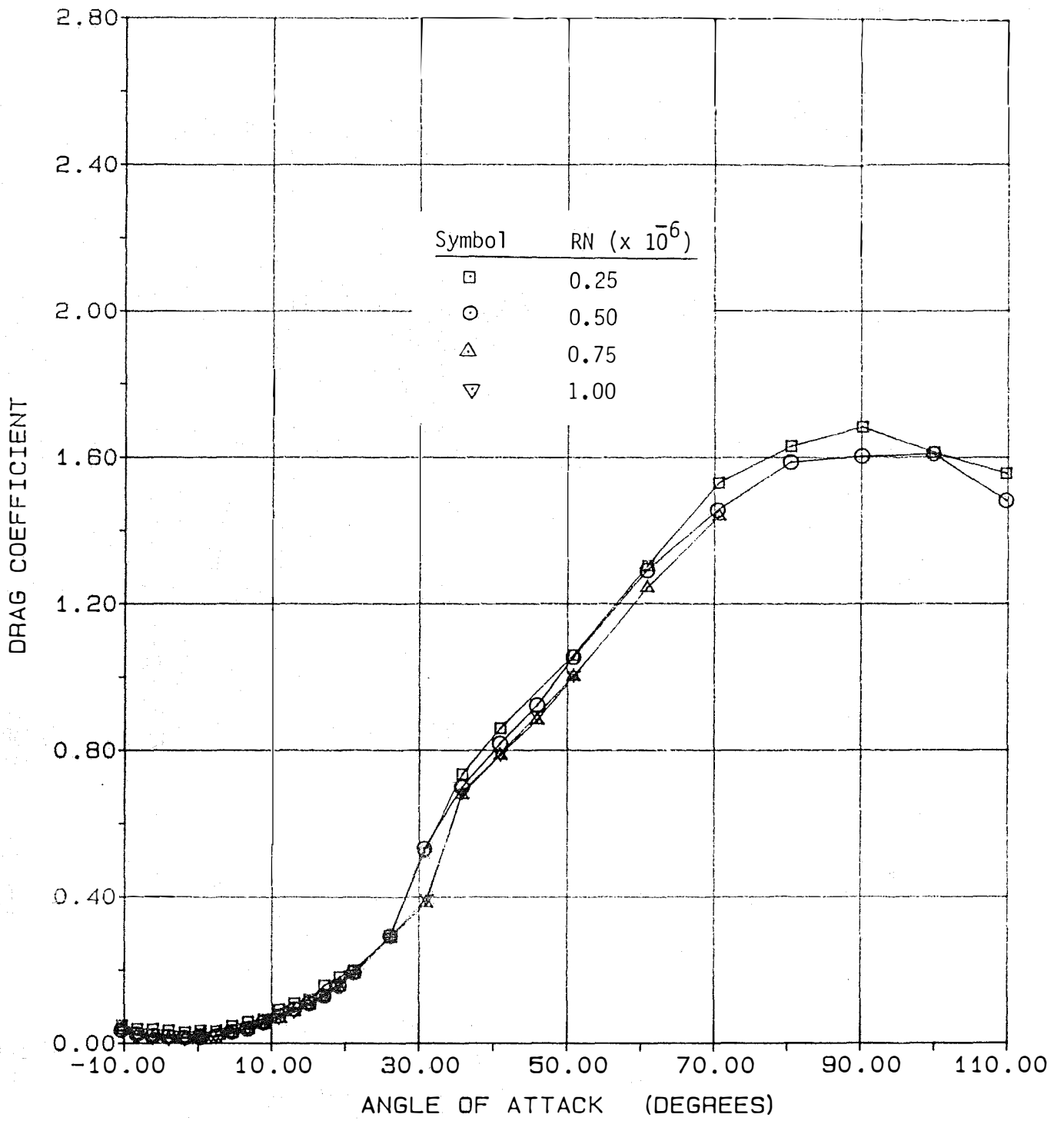
(c) Pitching Moment

Figure A.1 - Concluded.



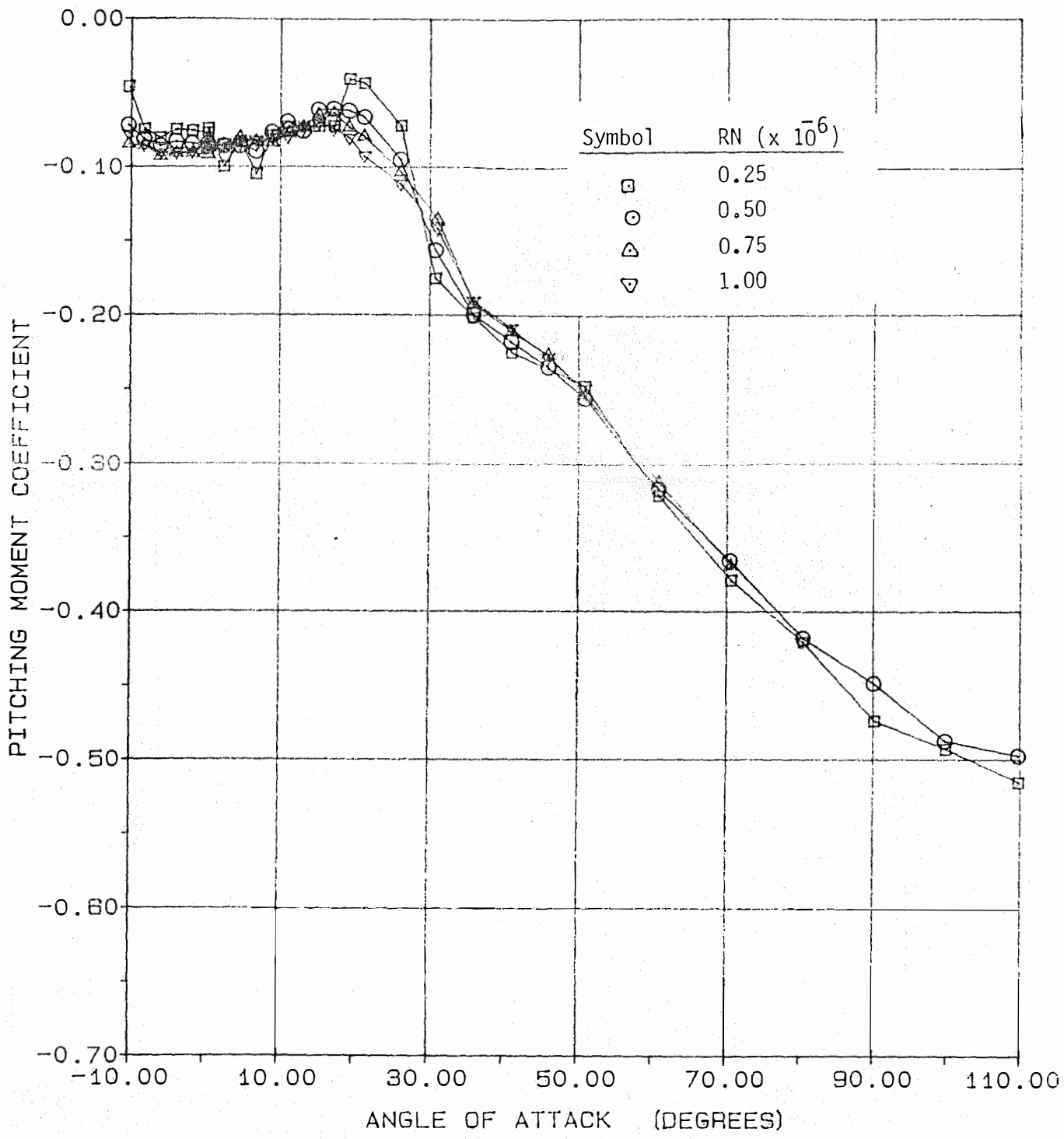
(a) Lift

Figure A.2- Aerodynamic Coefficients of the NACA 4418 Airfoil, AR = 12.



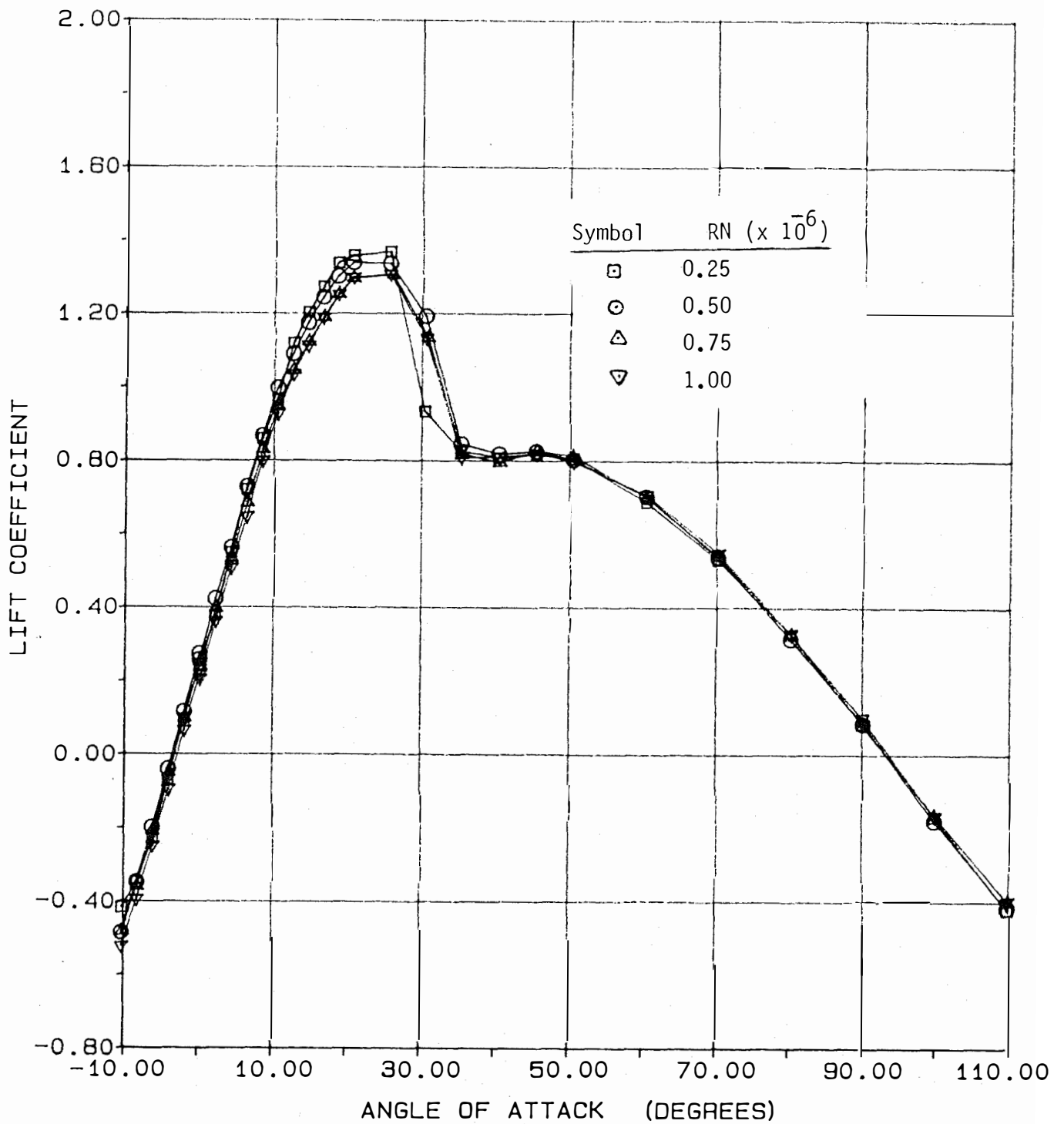
(b) Drag

Figure A.2 - Continued.



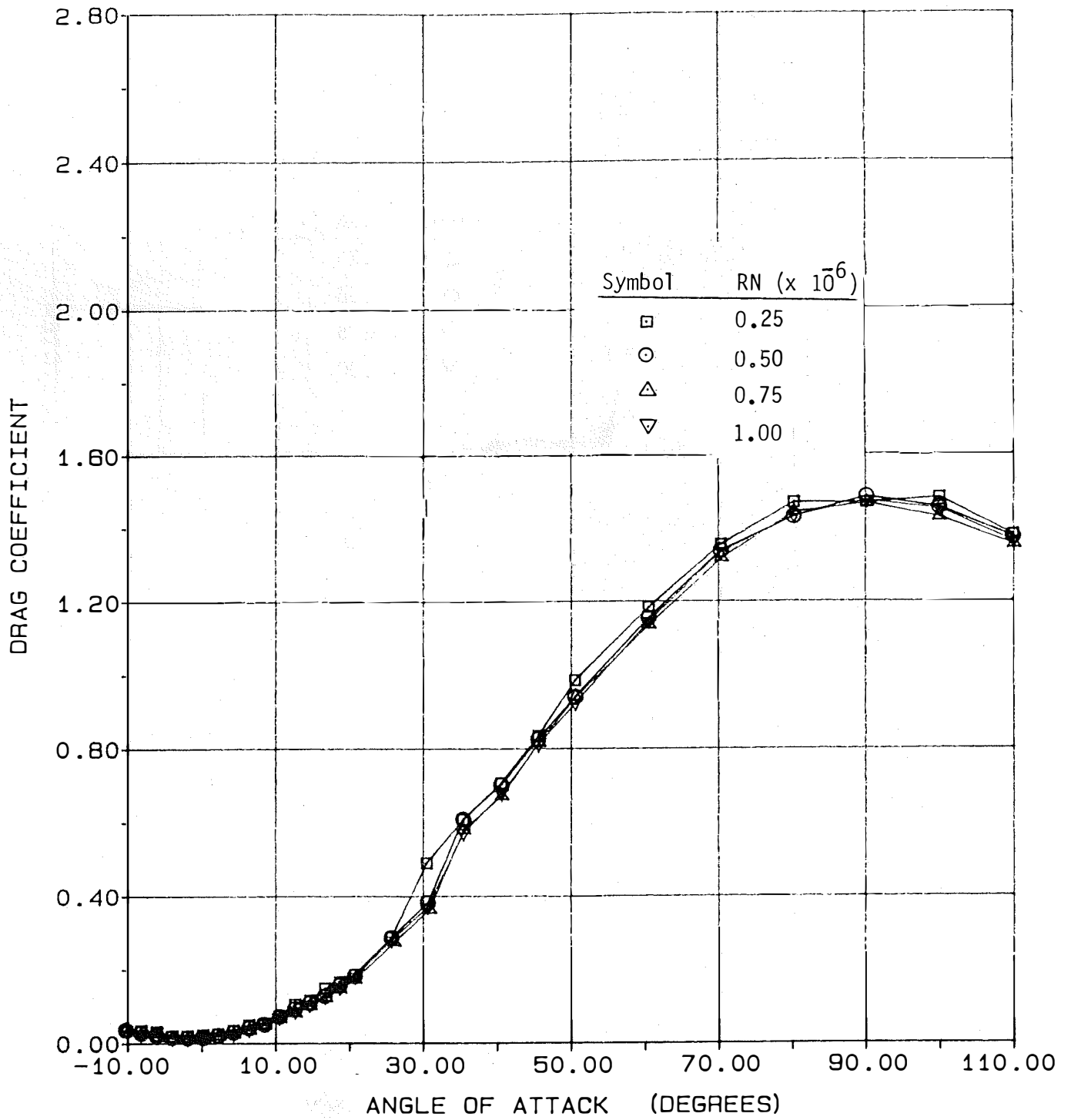
(c) Pitching Moment

Figure A.2 - Concluded.



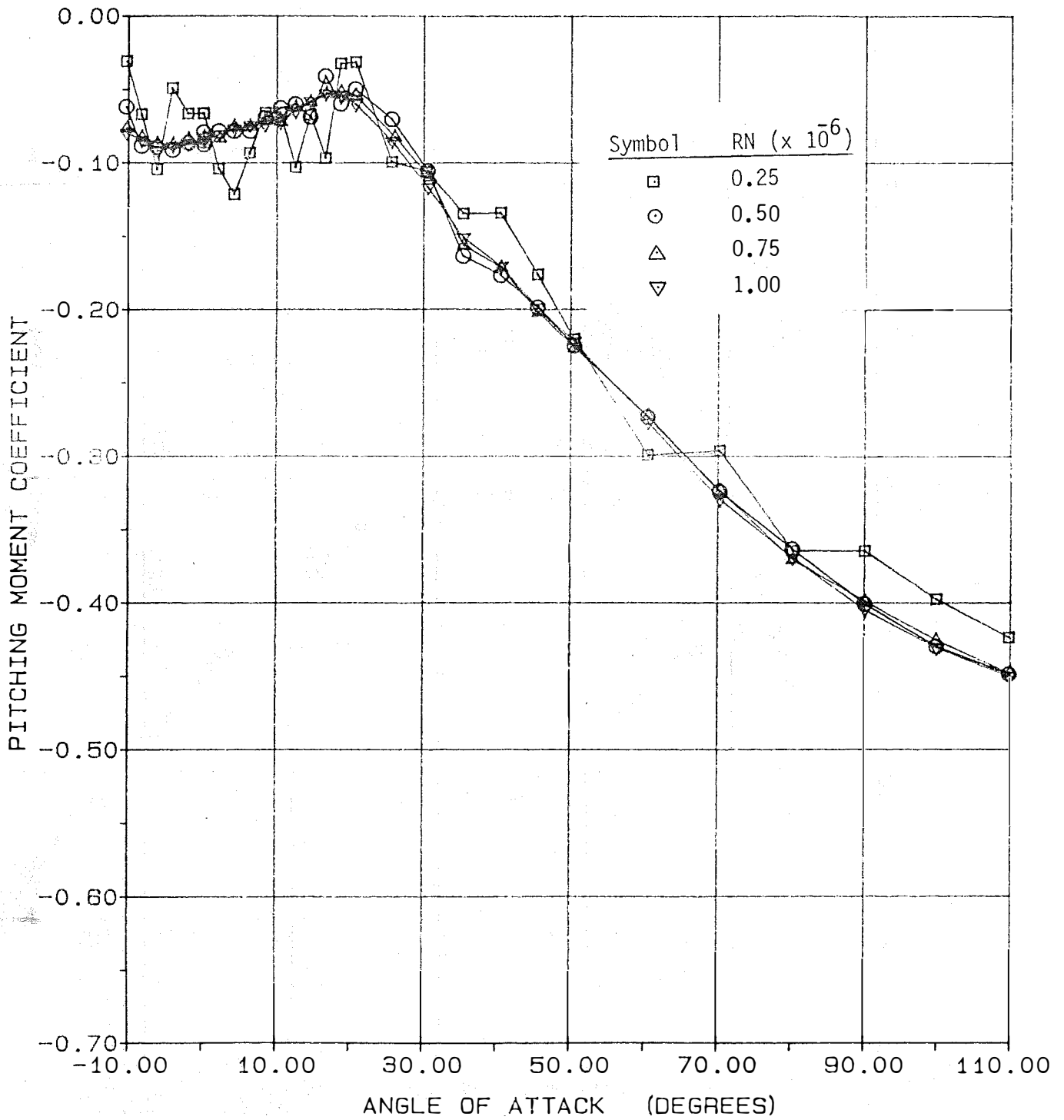
(a) Lift

Figure A.3- Aerodynamic Coefficients of the NACA 4418 Airfoil, AR = 9.



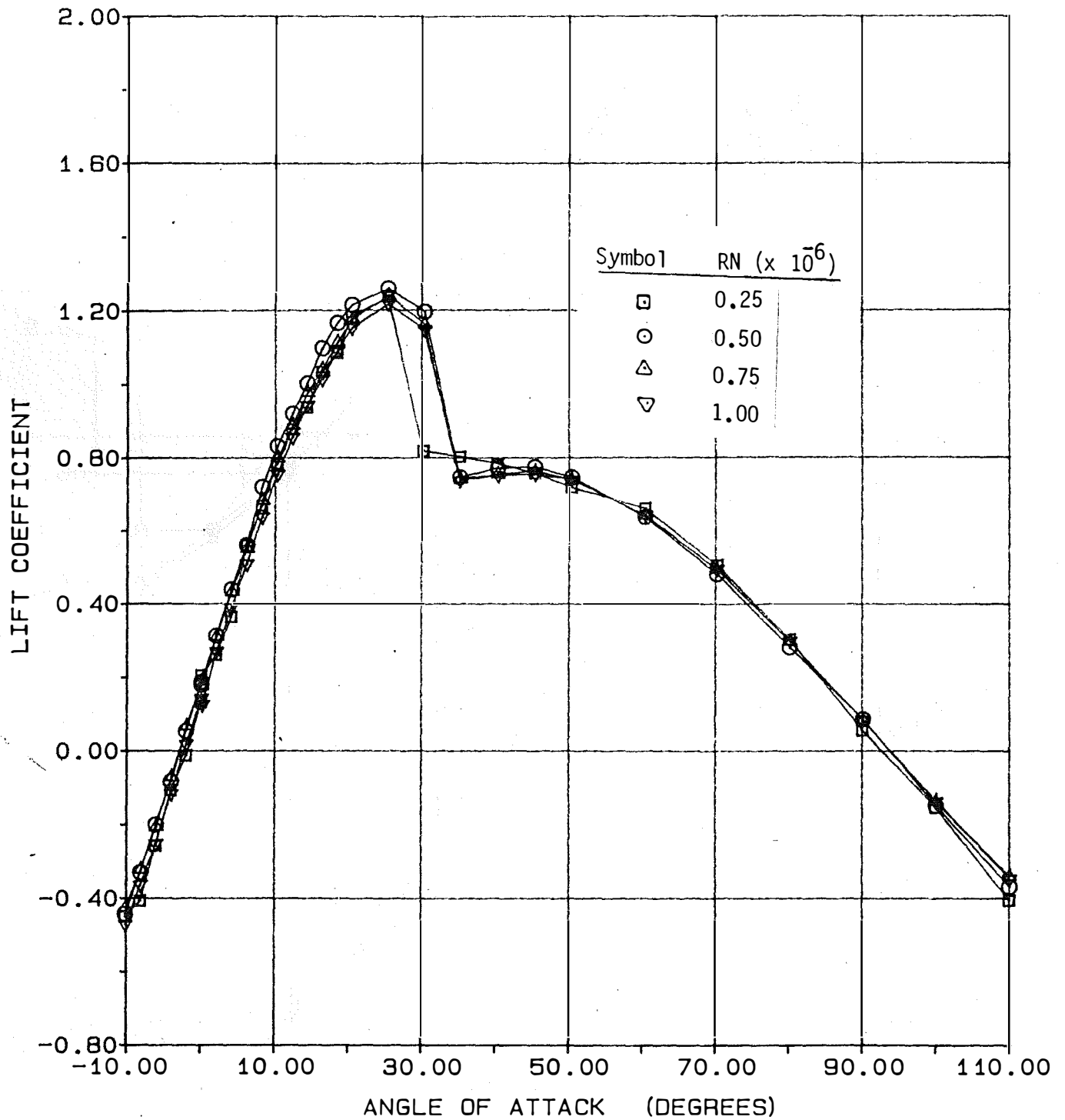
(b) Drag

Figure A.3 - Continued.



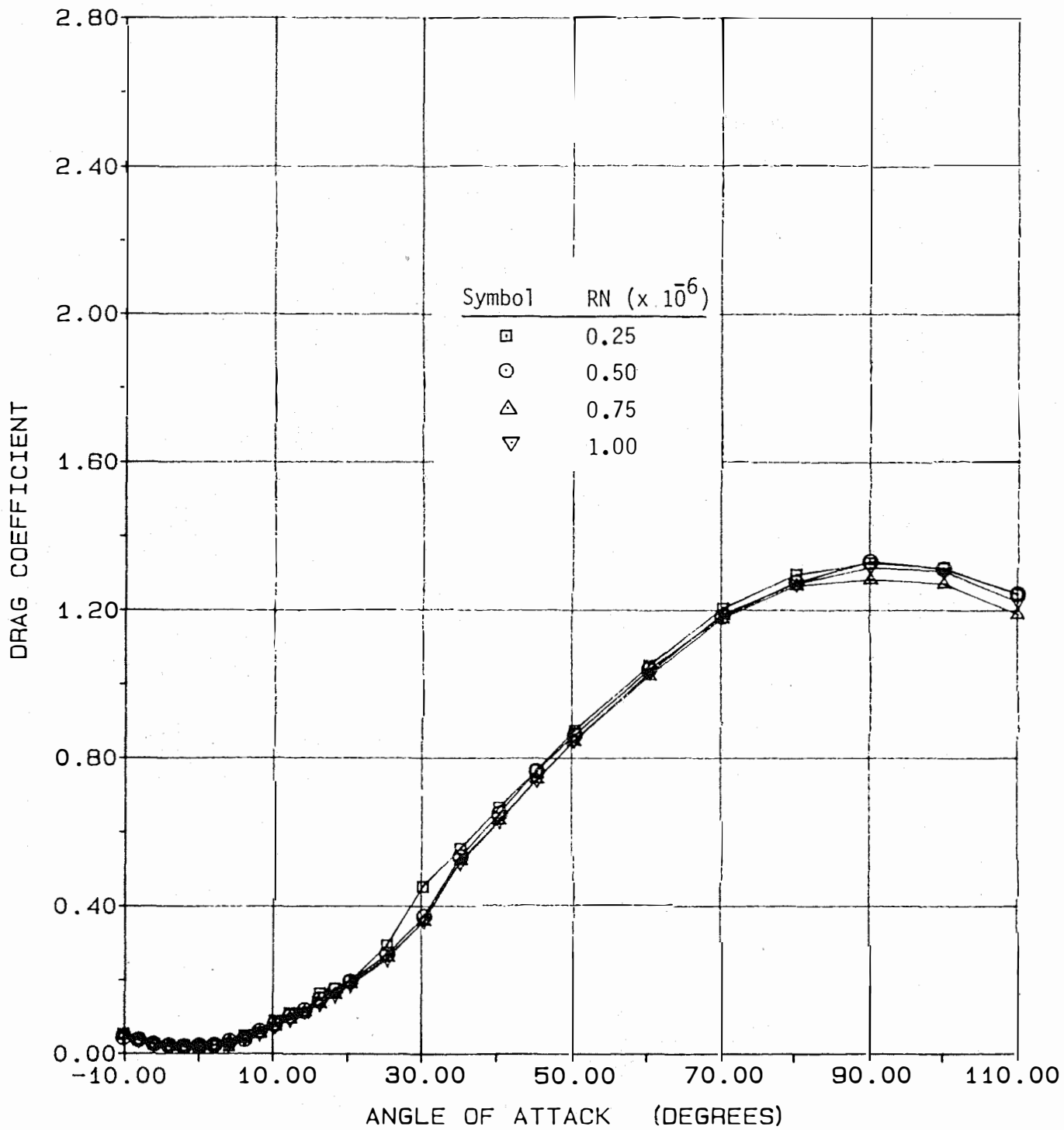
(c) Pitching Moment

Figure A.3- Concluded.



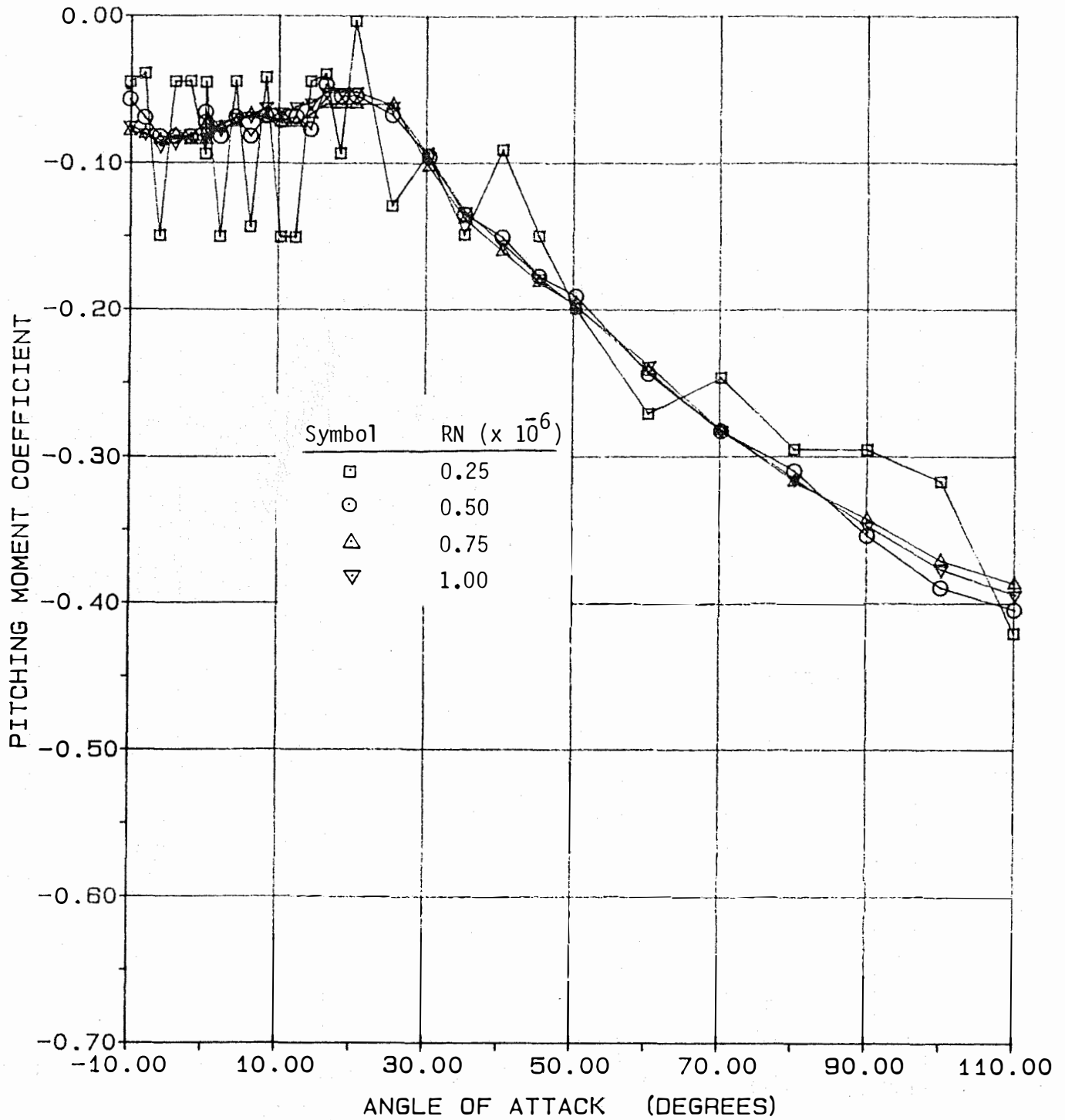
(a) Lift

Figure A.4- Aerodynamic Coefficients of the NACA 4418 Airfoil, AR = 6.



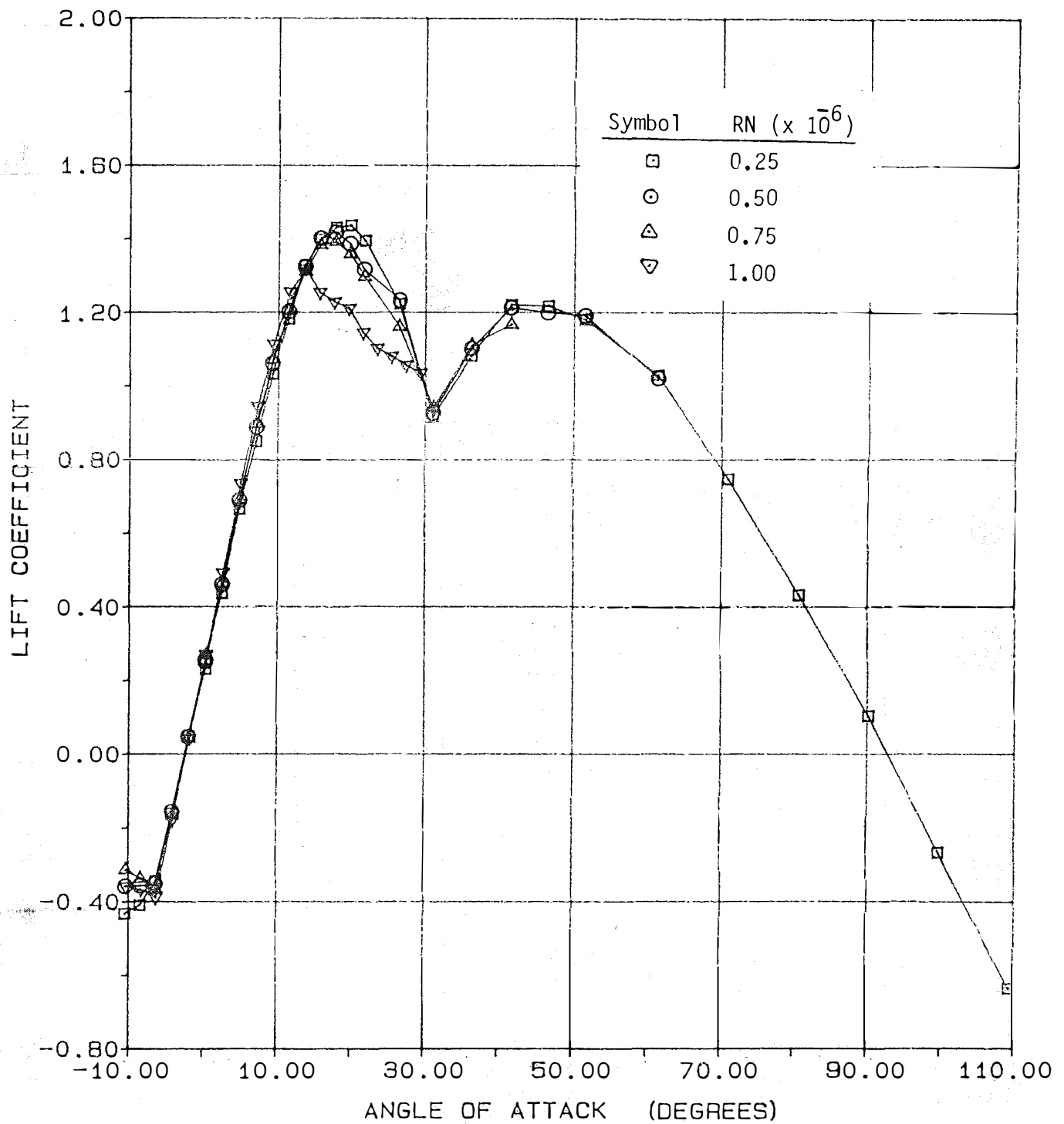
(b) Drag

Figure A.4 - Continued.



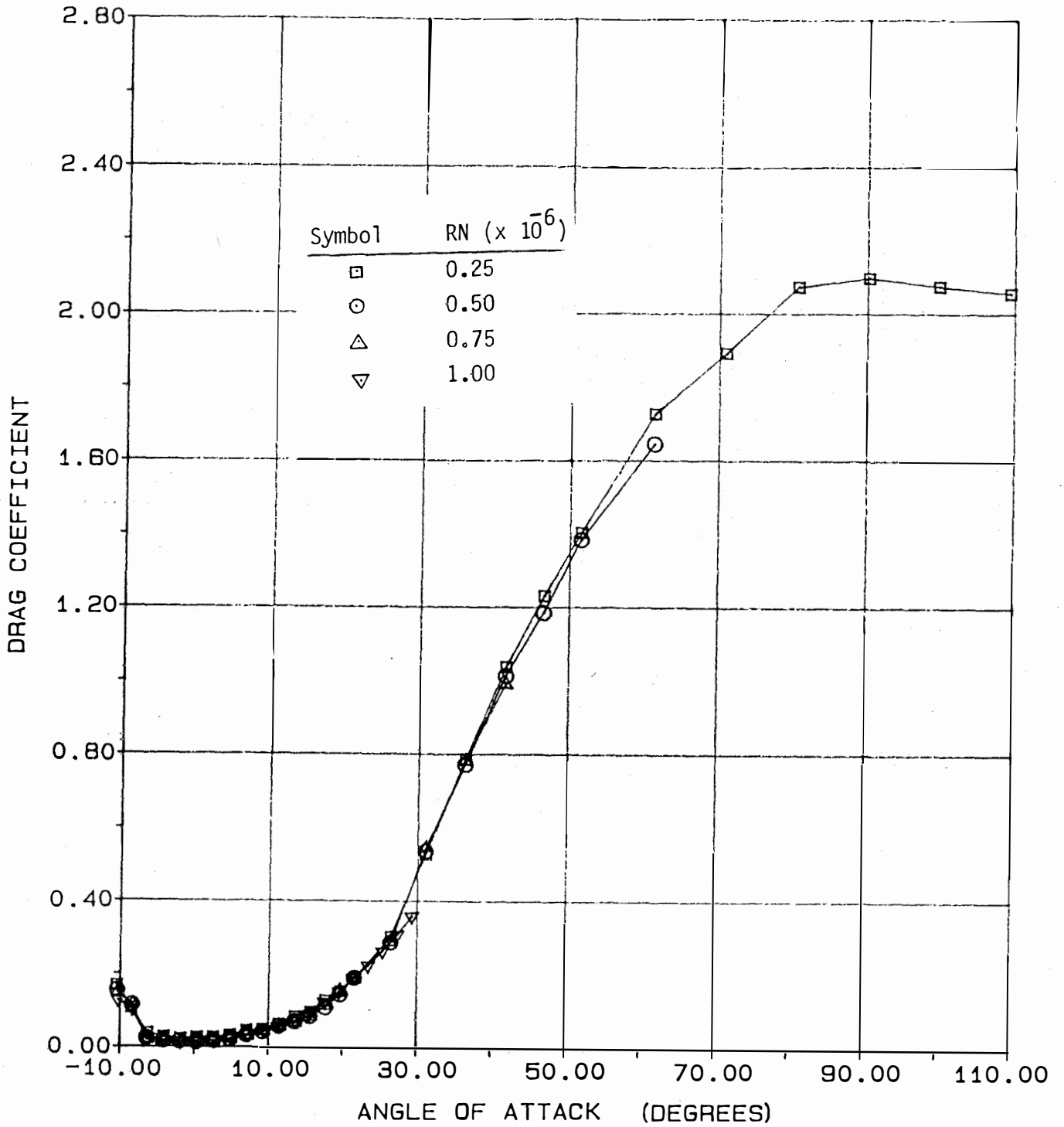
(c) Pitching Moment

Figure A.4 - Concluded.



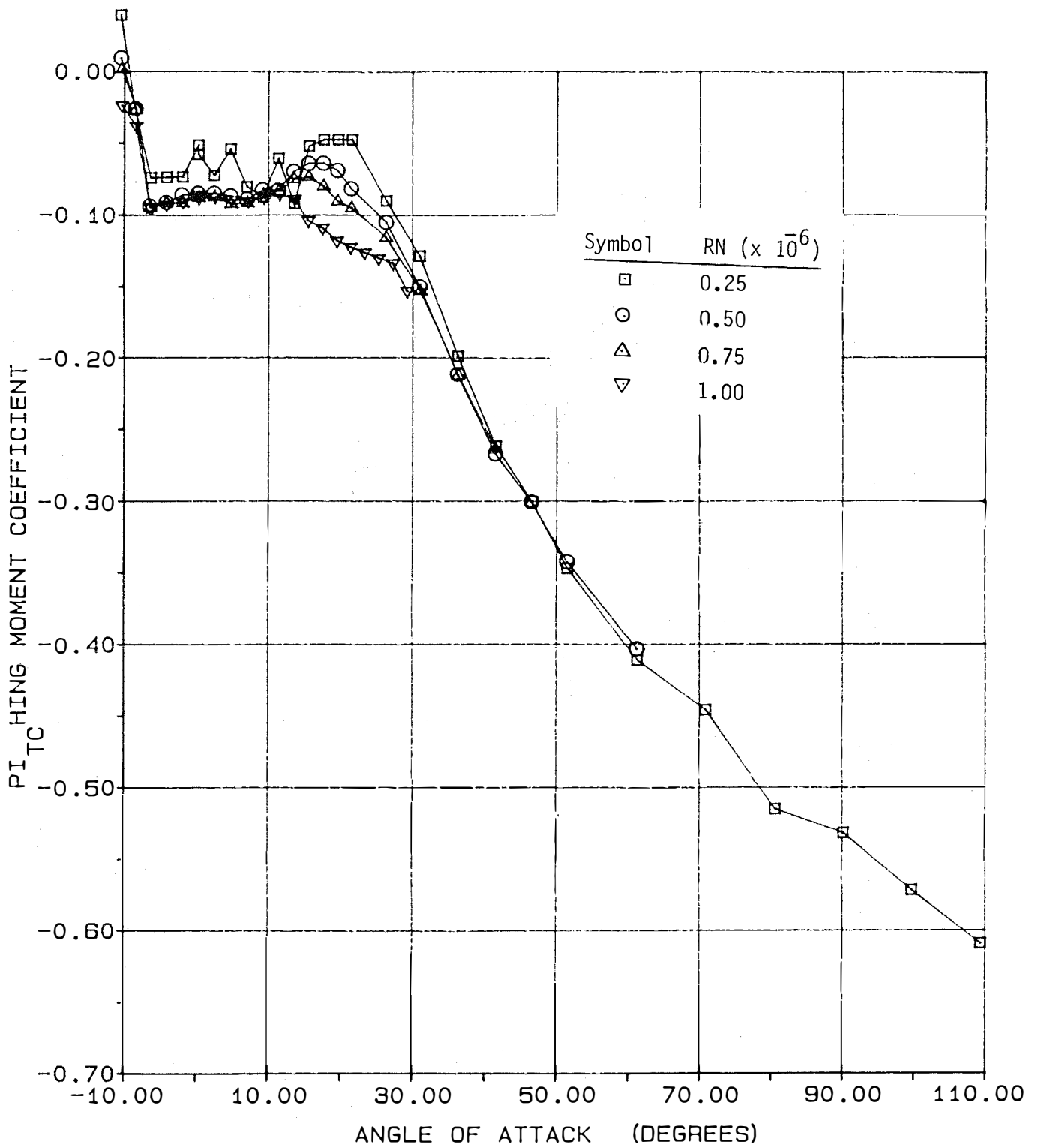
(a) Lift

Figure A.5 - Aerodynamic Coefficients of the NACA 4415 Airfoil, $AR = \infty$.



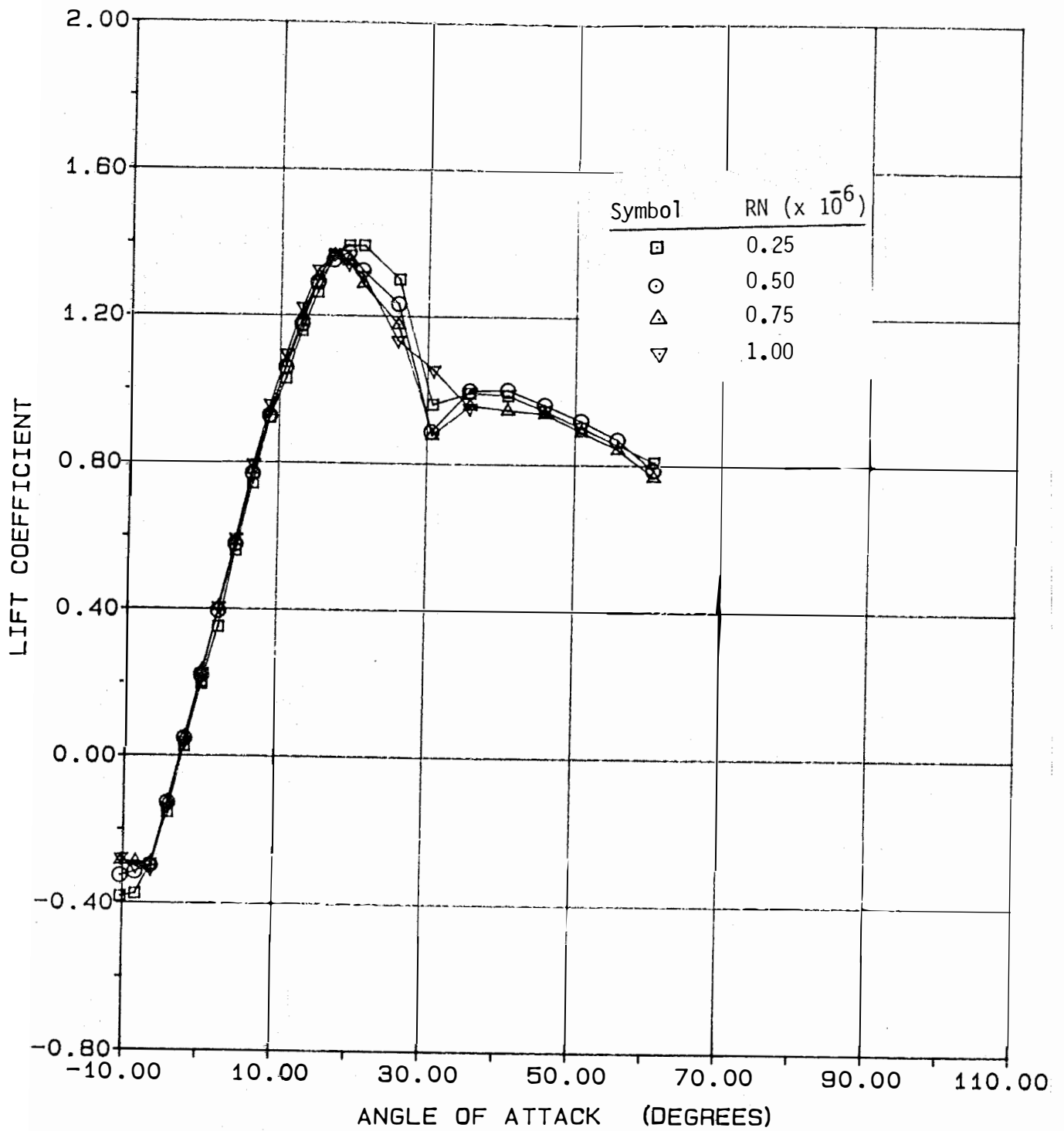
(b) Drag

Figure A.5 - Continued.



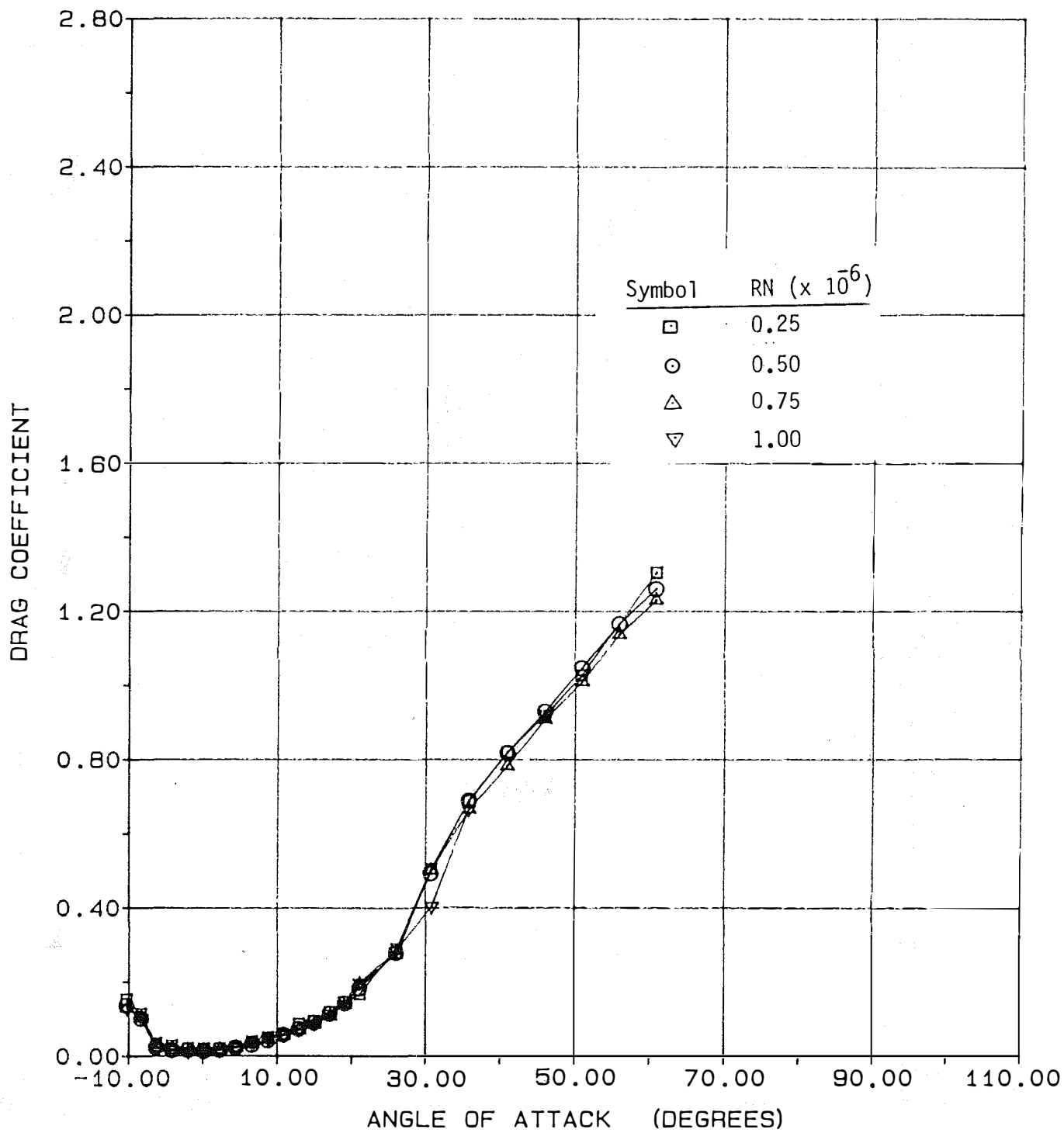
(c) Pitching Moment

Figure A.5 - Concluded.



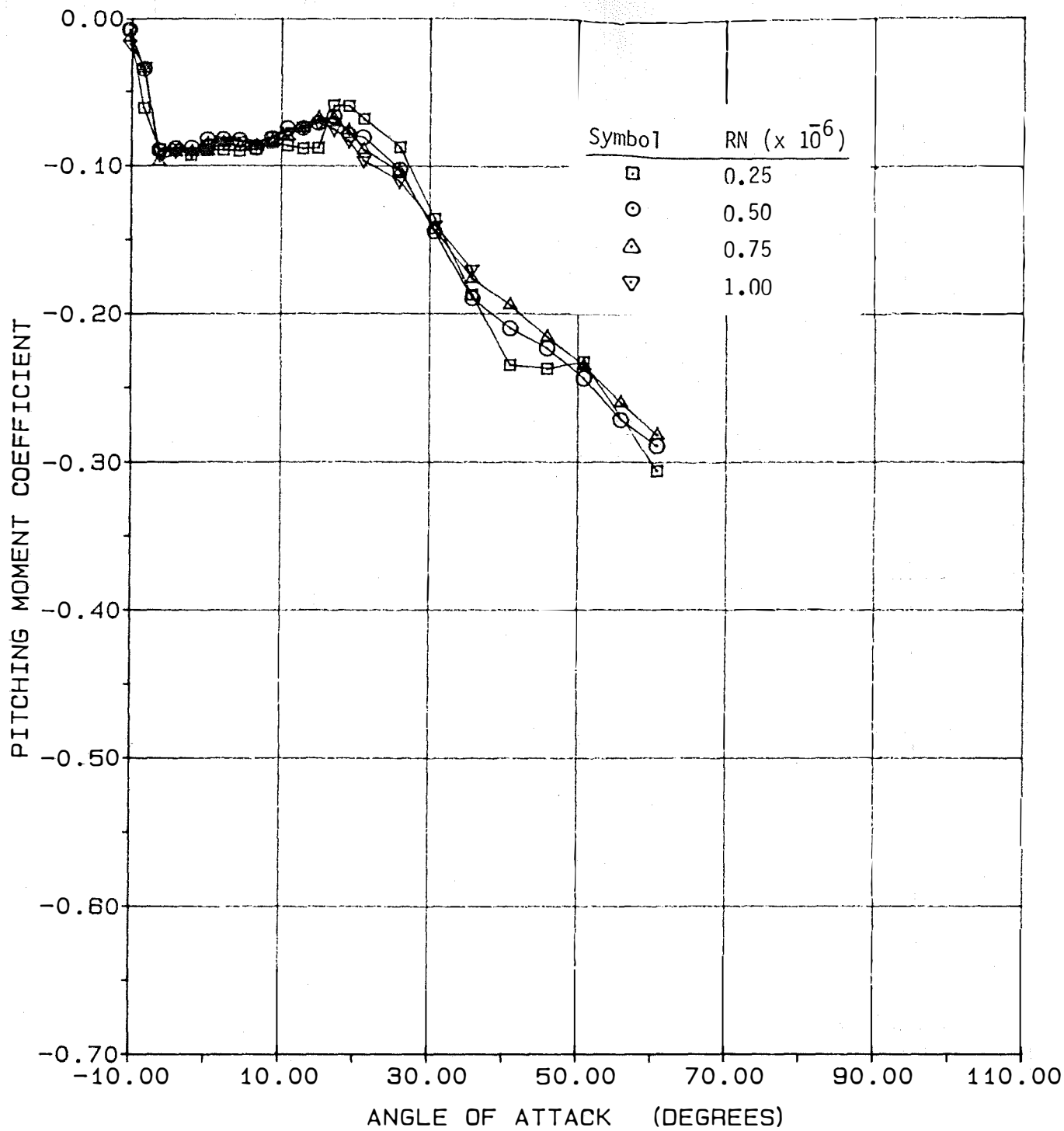
(a) Lift

Figure A.6 - Aerodynamic Coefficients of the NACA 4415 Airfoil, AR = 12.



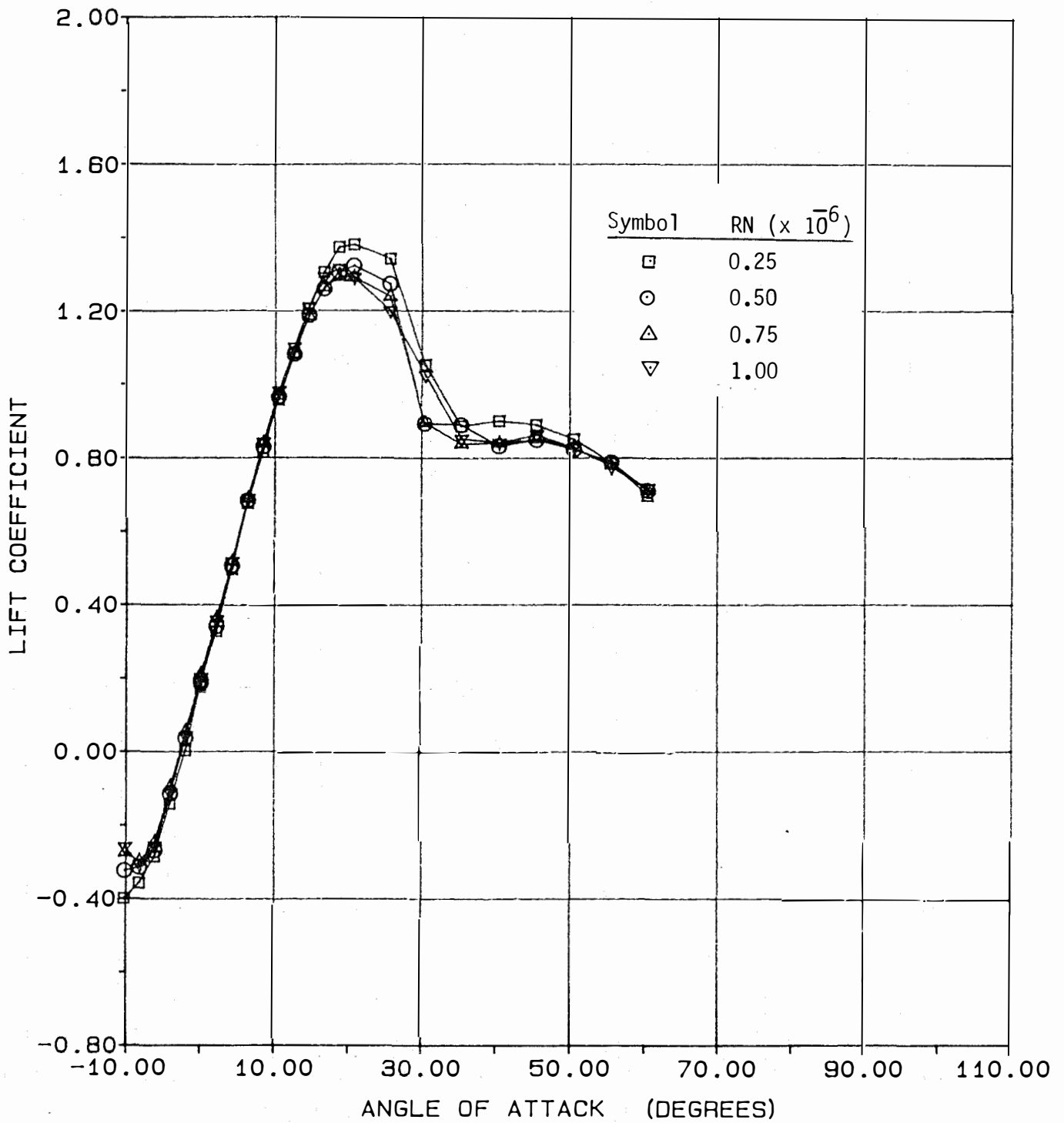
(b) Drag

Figure A.6 - Continued.



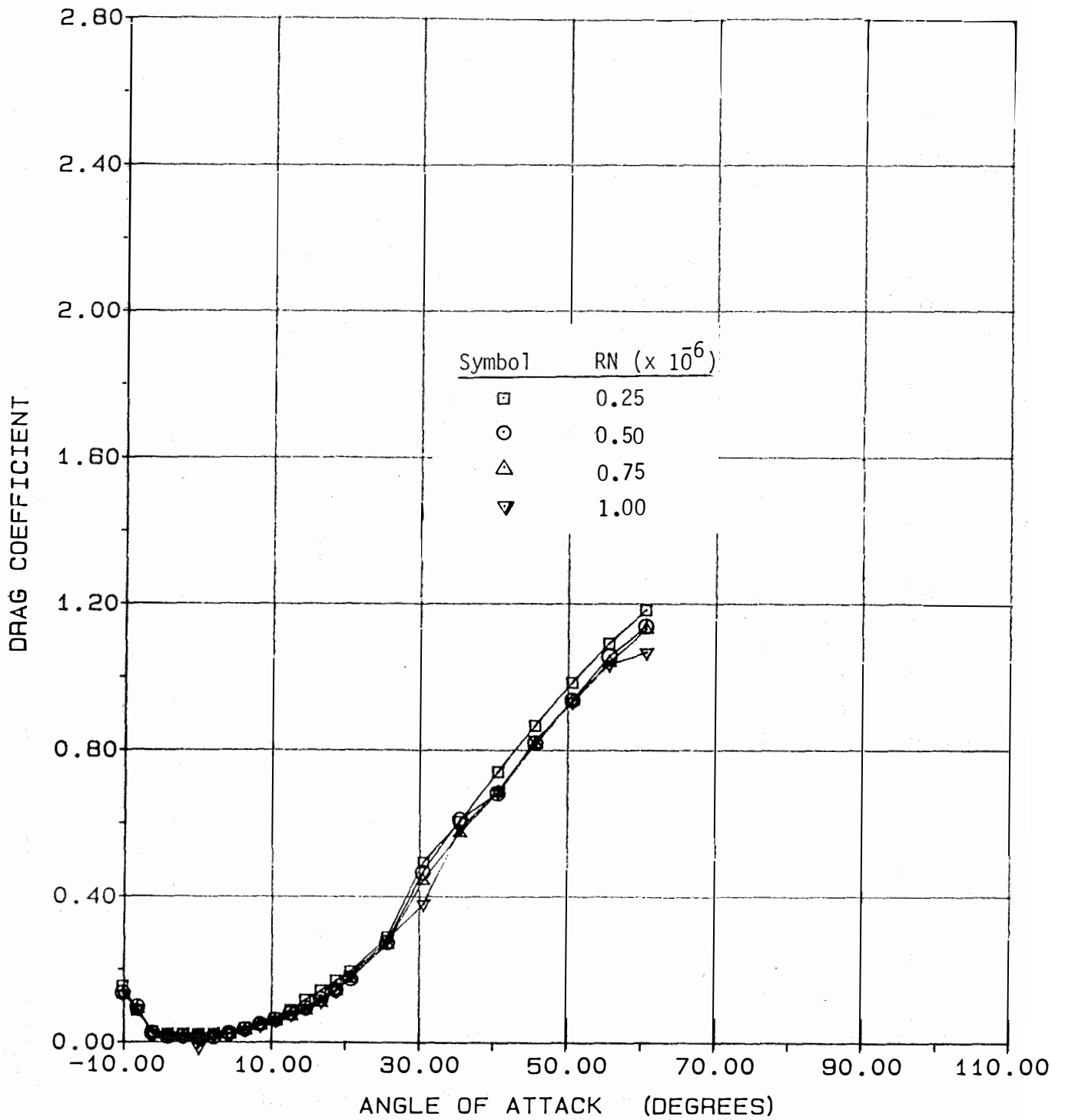
(c) Pitching Moment

Figure A.6 - Concluded.



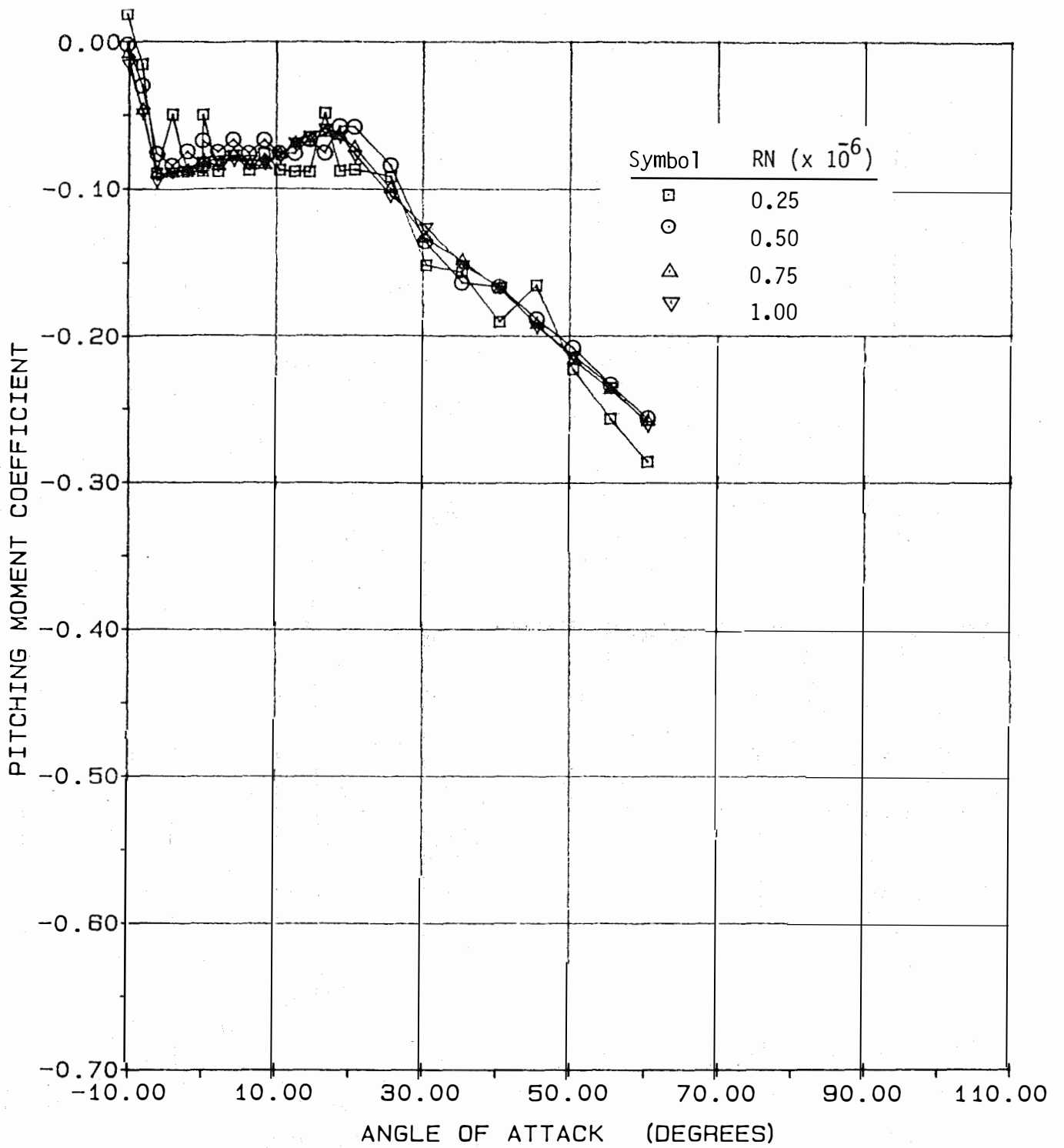
(a) Lift

Figure A.7- Aerodynamic Coefficients of the NACA 4415 Airfoil, AR = 9.



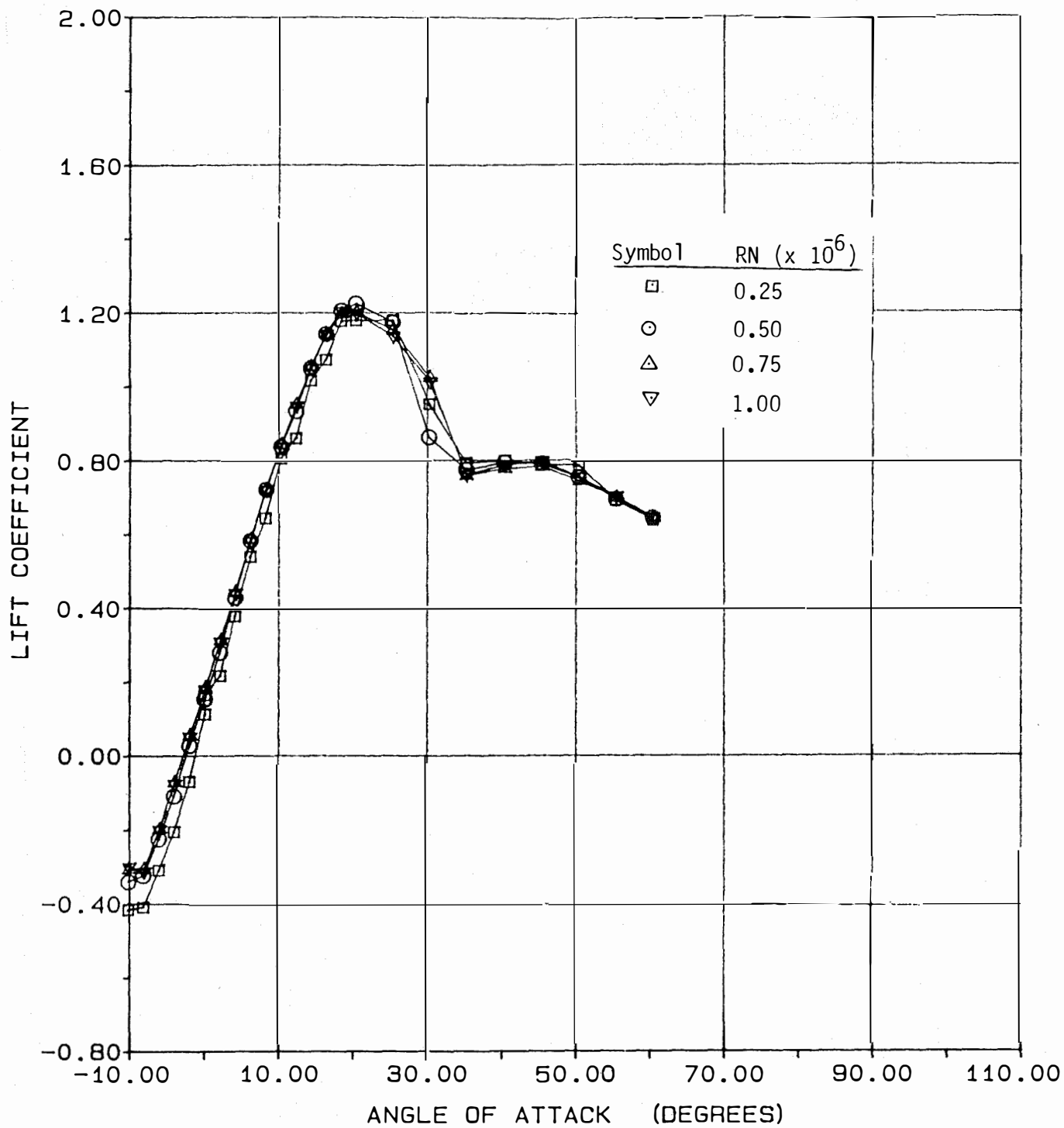
(b) Drag

Figure A.7 - Continued.



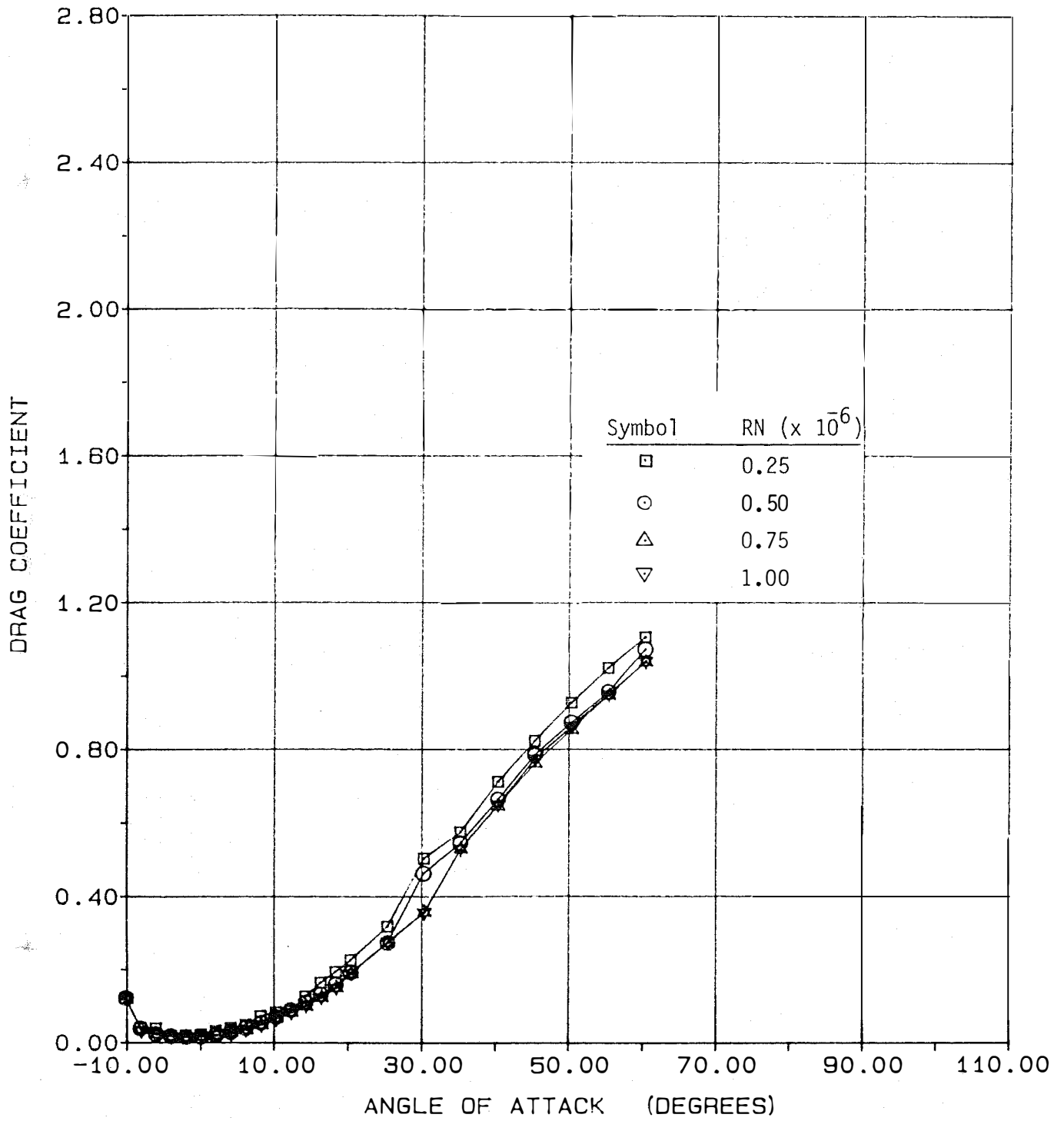
(c) Pitching Moment

Figure A.7 - Concluded.



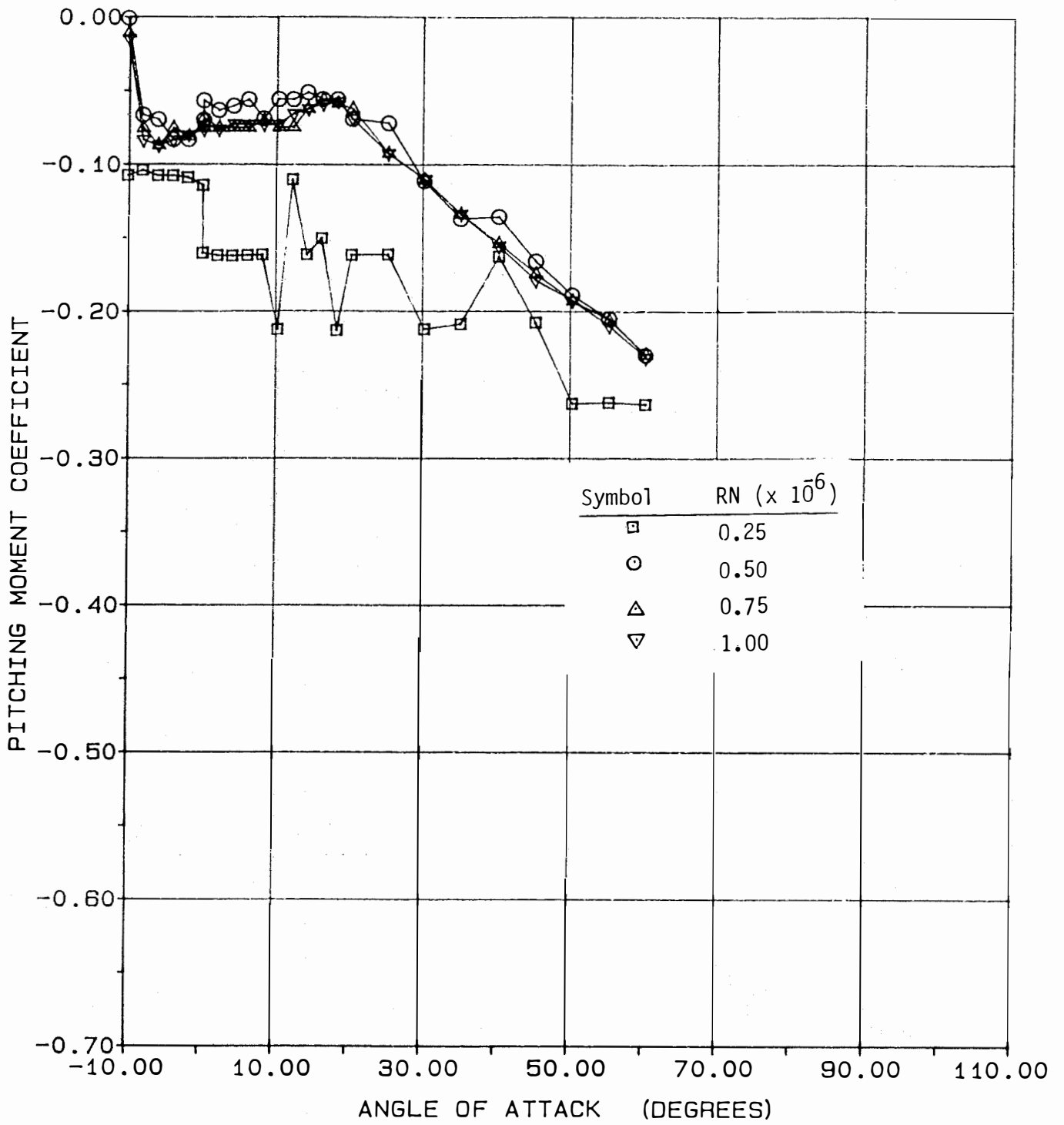
(a) Lift

Figure A.8- Aerodynamic Coefficients of the NACA 4415 Airfoil, AR = 6.



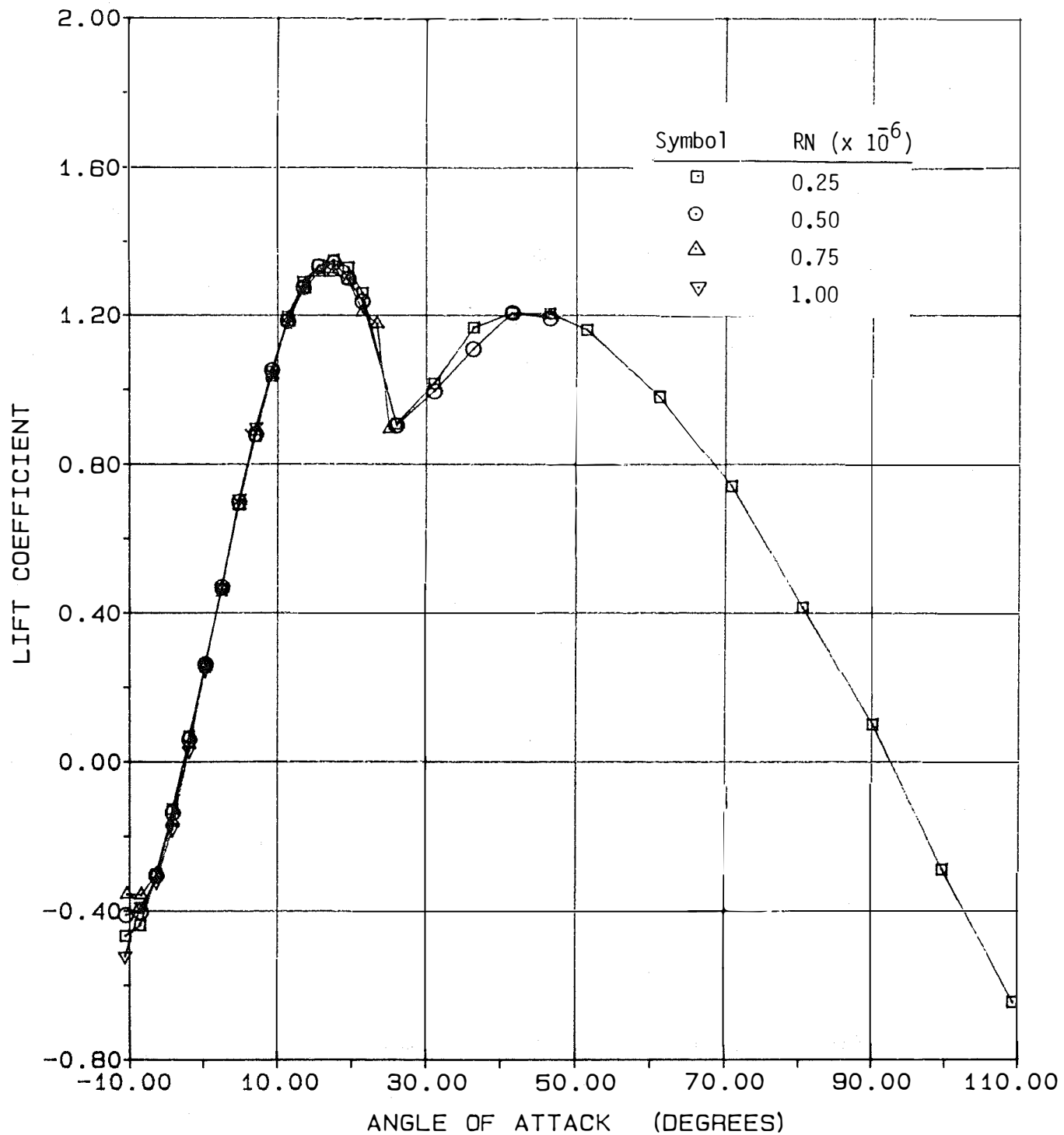
(b) Drag

Figure A.8 - Continued.



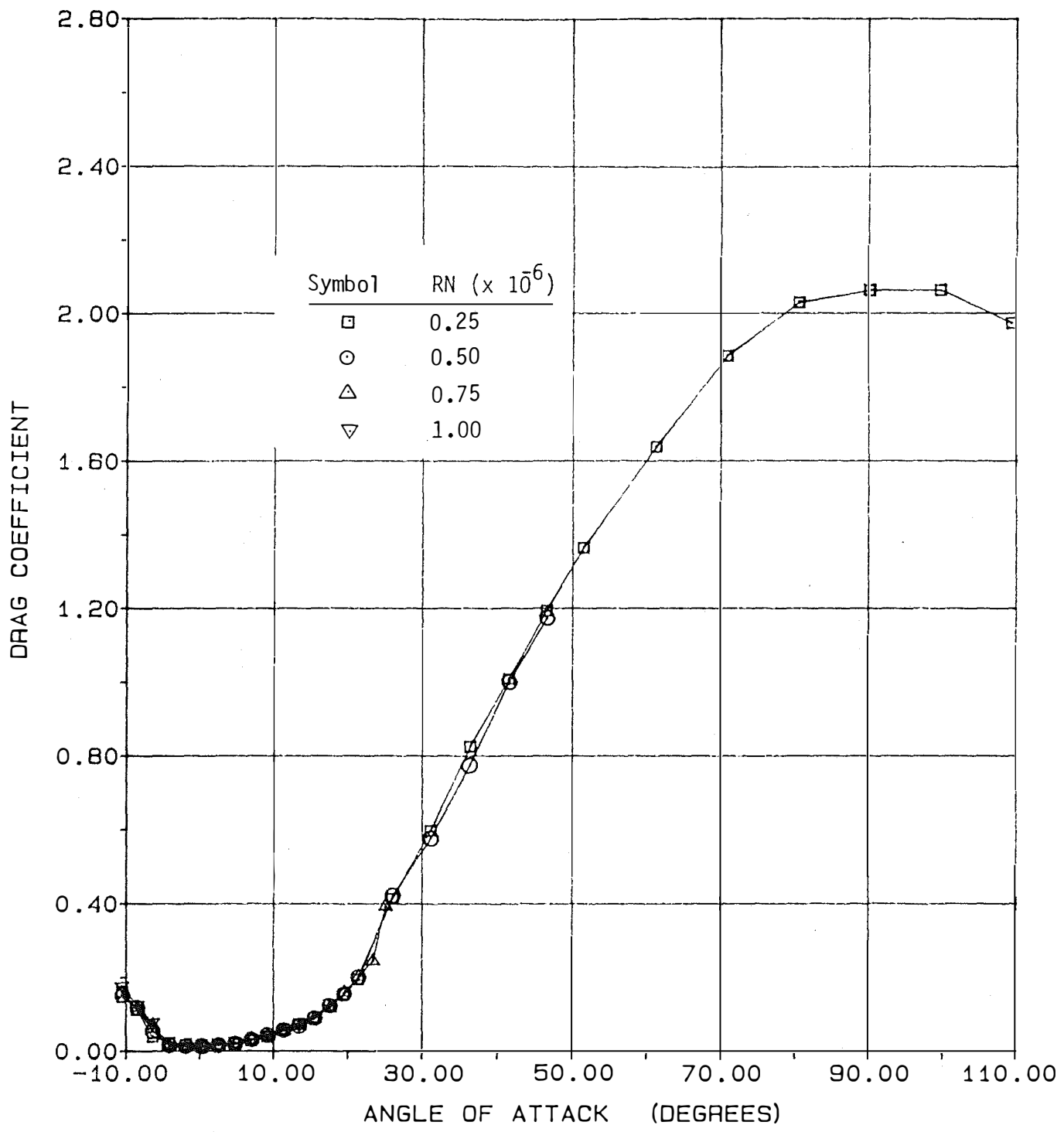
(c) Pitching Moment

Figure A.8- Concluded.



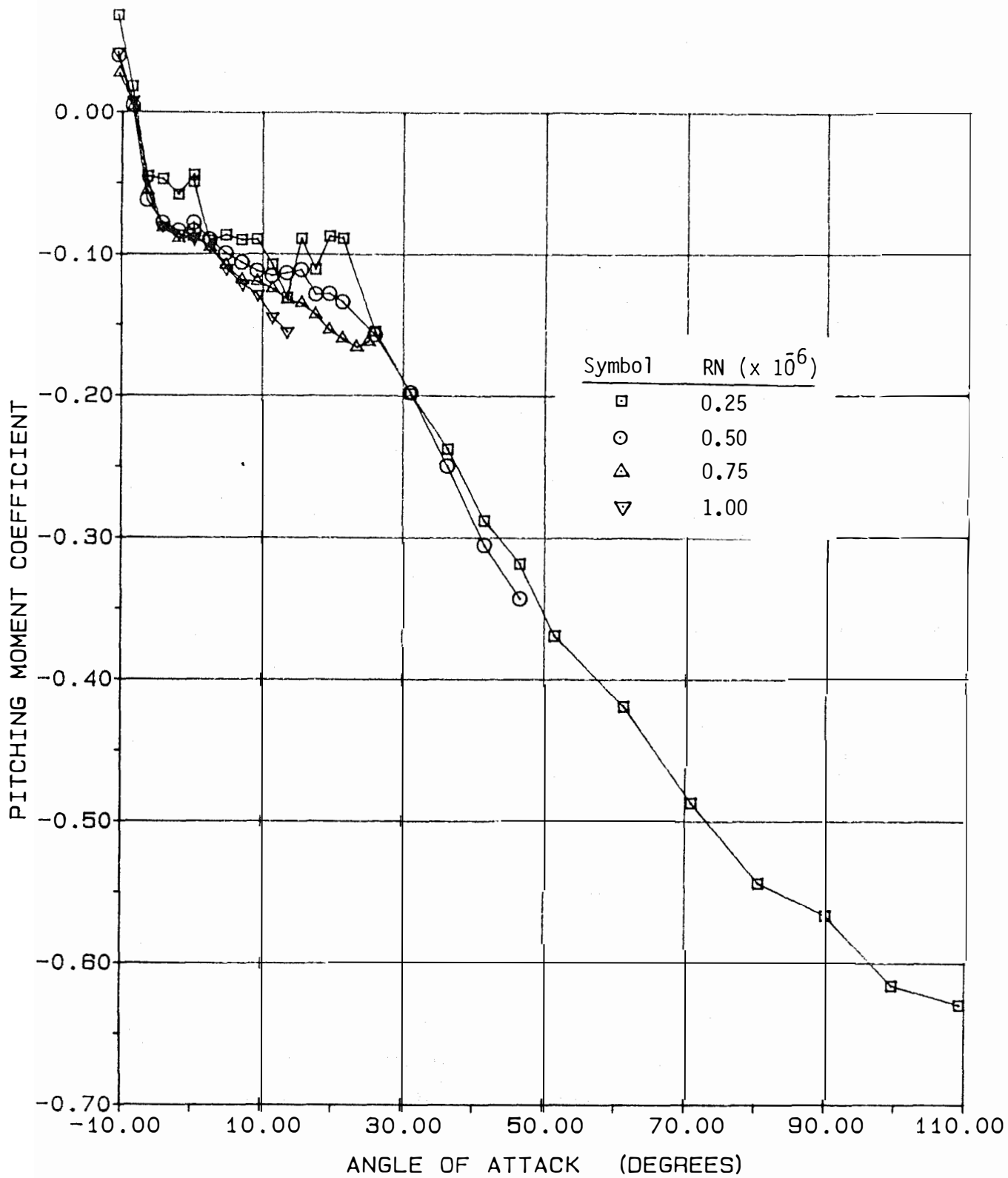
(a) Lift

Figure A.9.- Aerodynamic Coefficients of the NACA 4412 Airfoil, AR = ∞ .



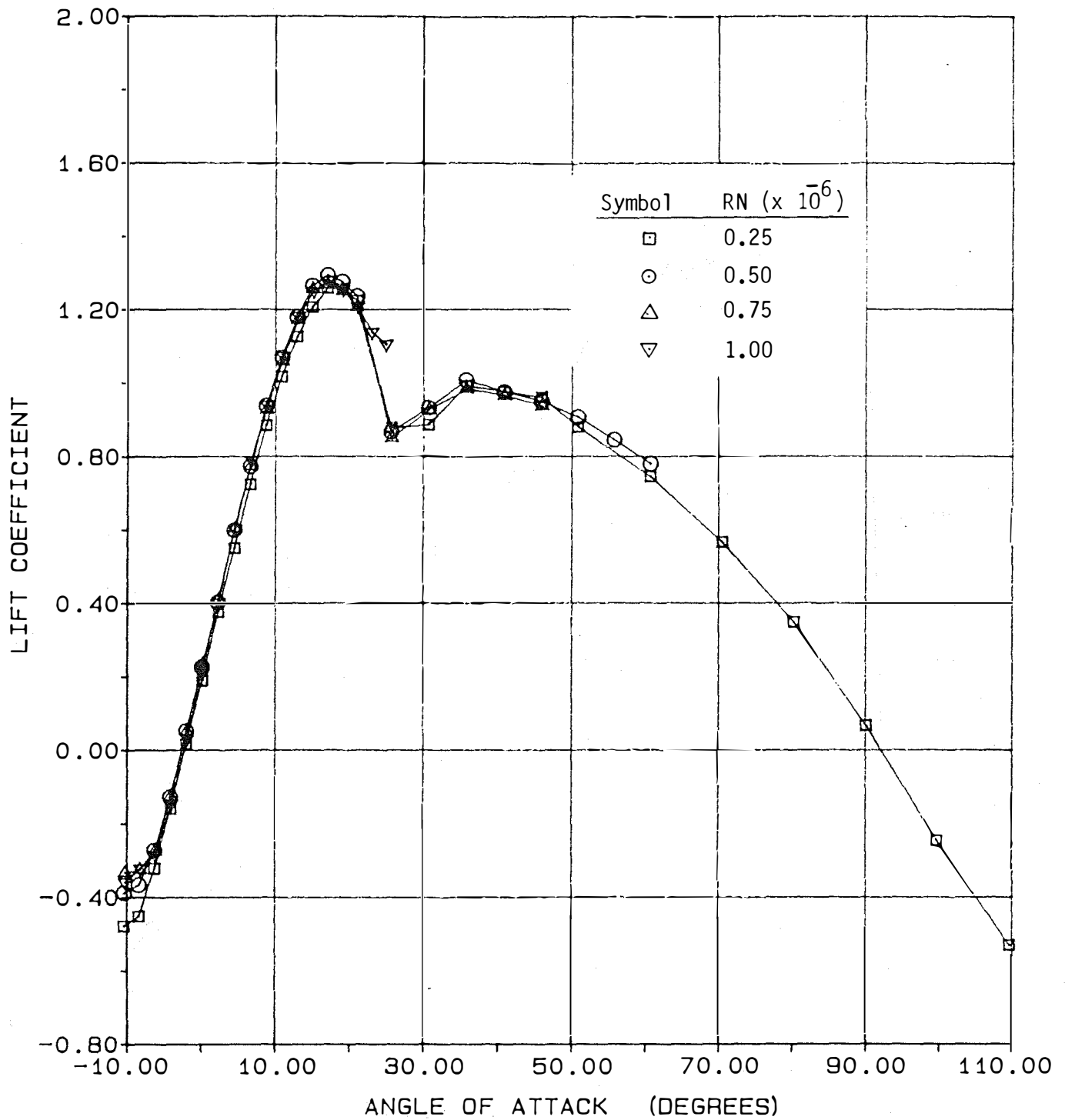
(b) Drag

Figure A.9- Continued.



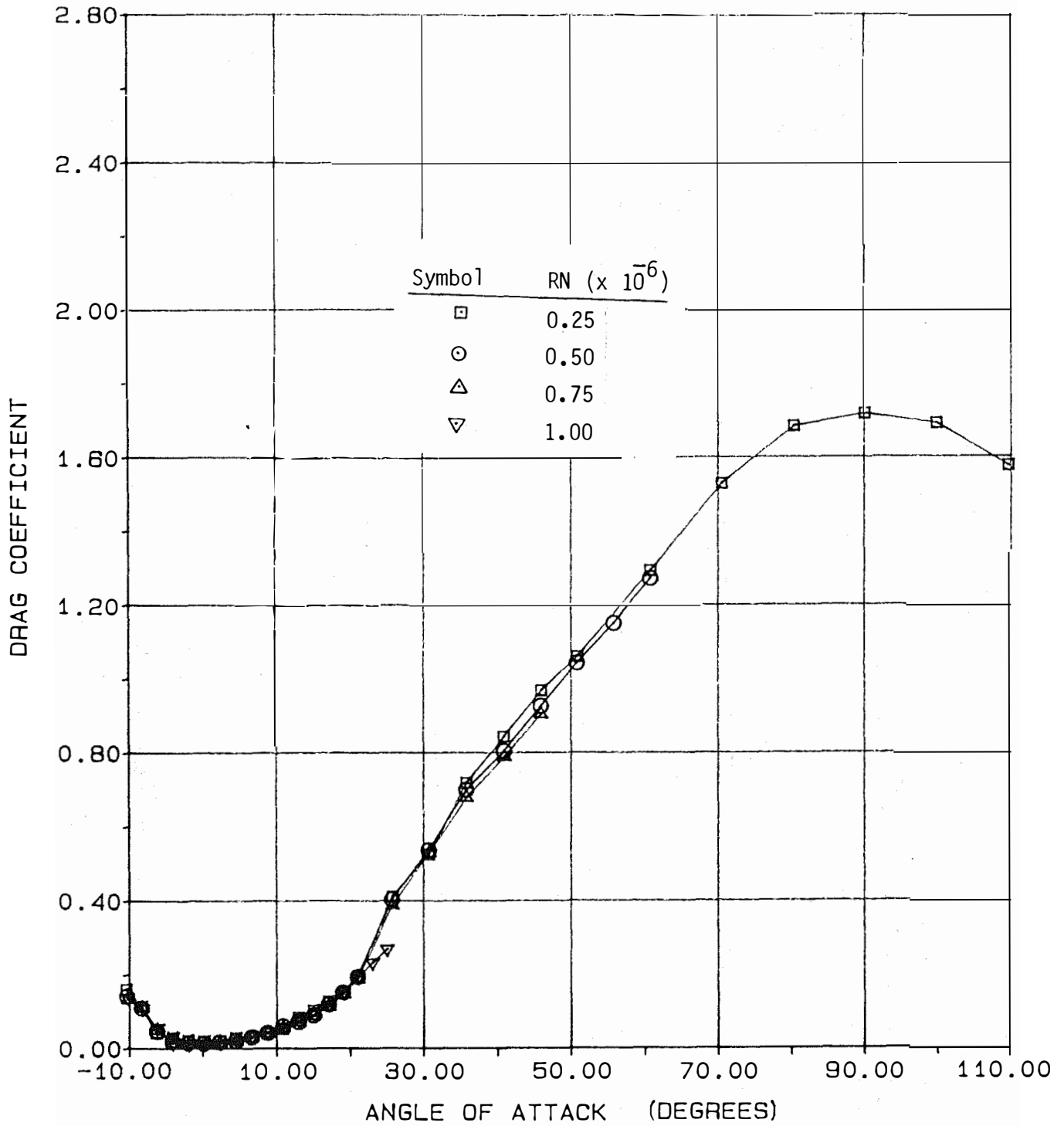
(c) Pitching Moment

Figure A.9- Concluded.



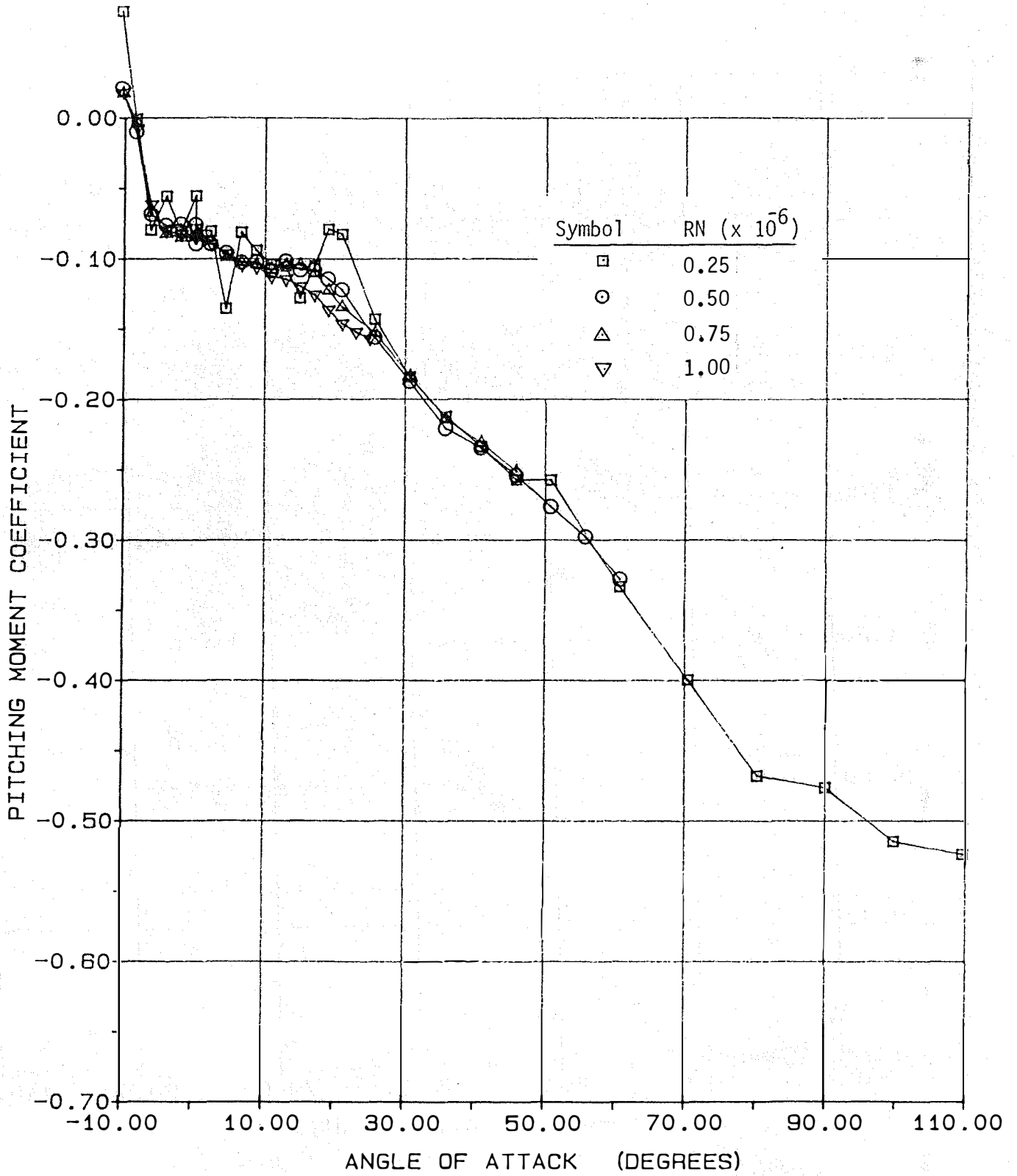
(a) Lift

Figure A.10- Aerodynamic Coefficients of the NACA 4412 Airfoil, AR = 12.

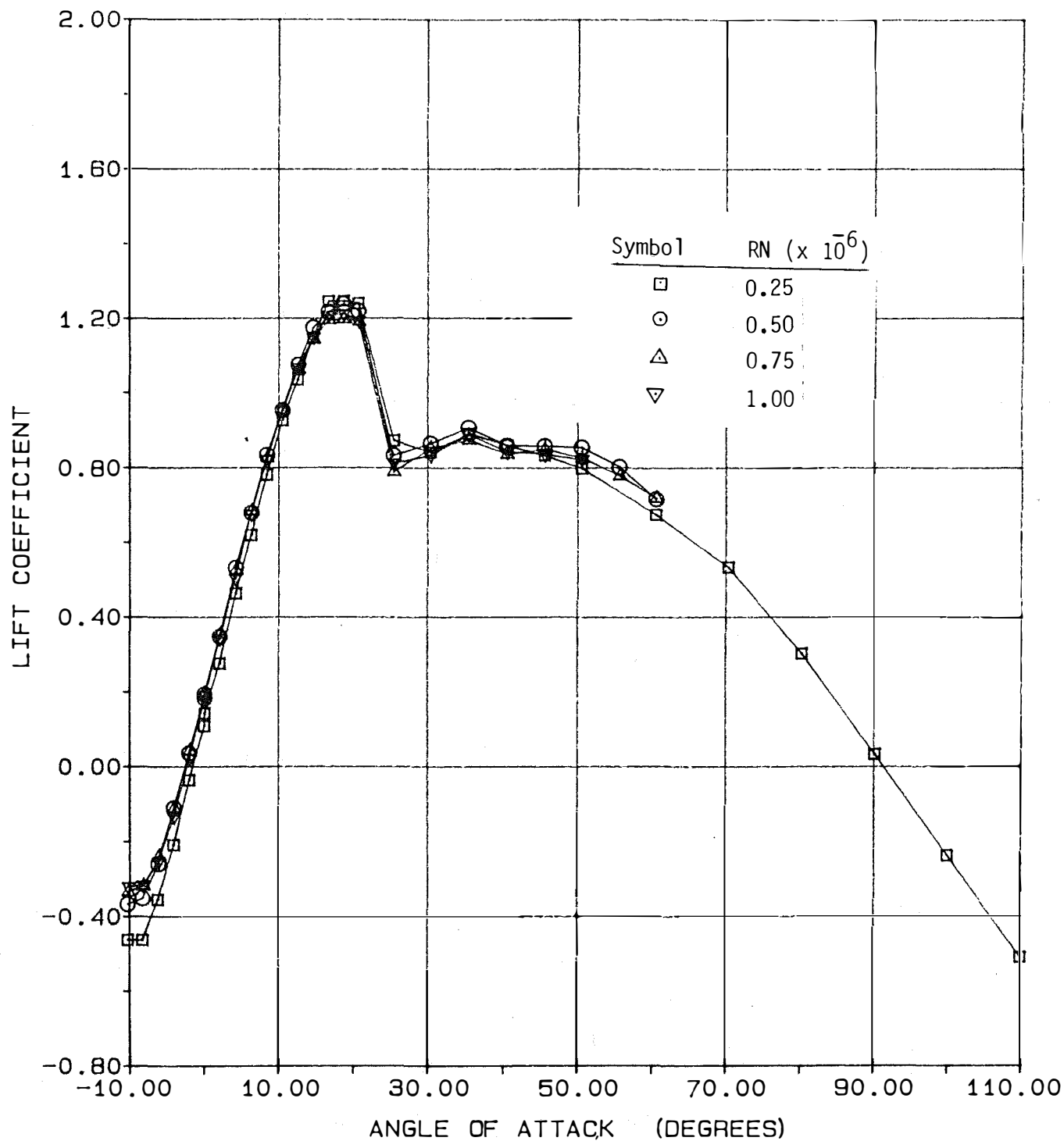


(b) Drag

Figure A.10- Continued.

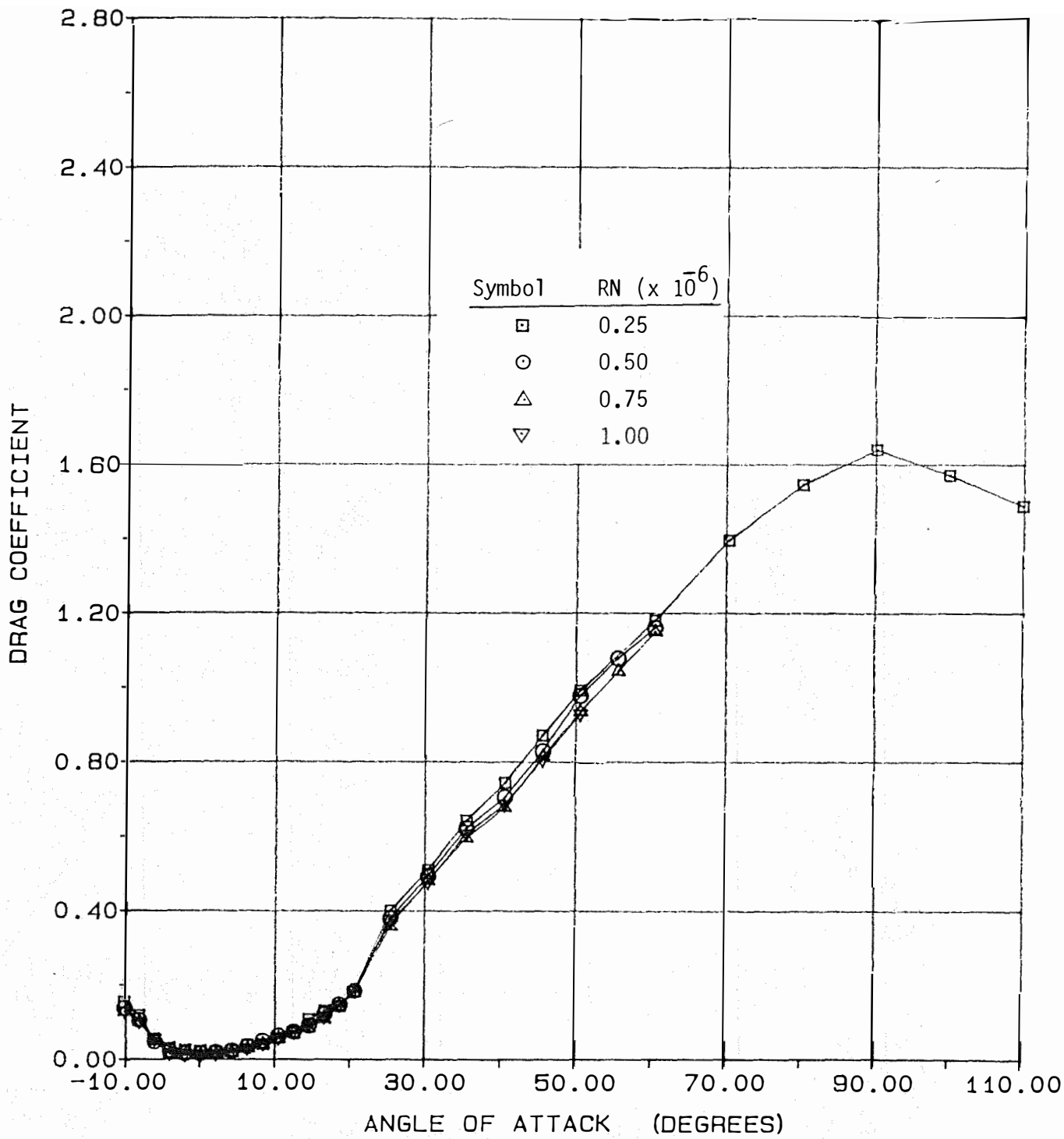


(c) Pitching Moment
 Figure A.10- Concluded.



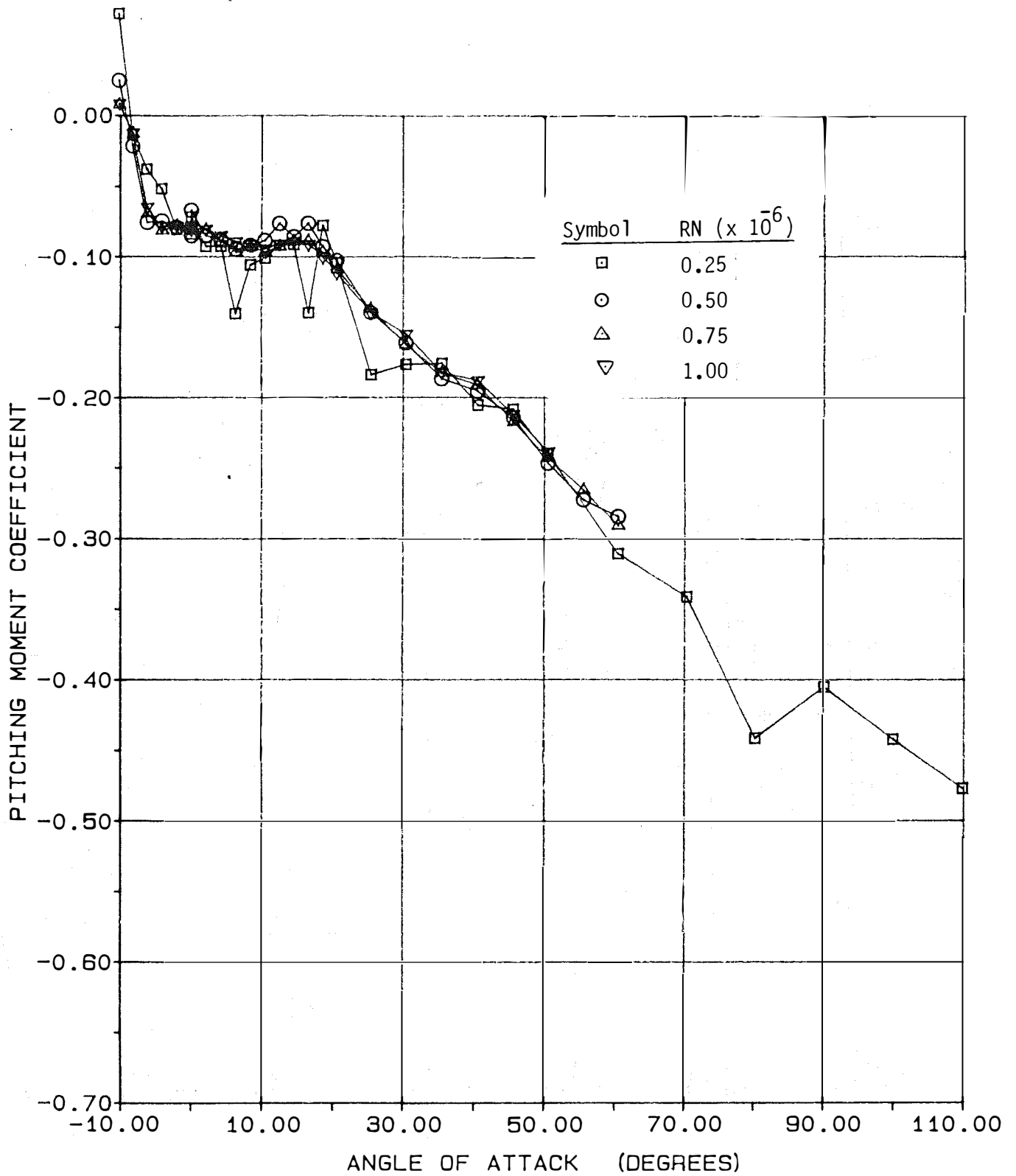
(a) Lift

Figure A.11- Aerodynamic Coefficients of the NACA 4412 Airfoil, AR = 9.



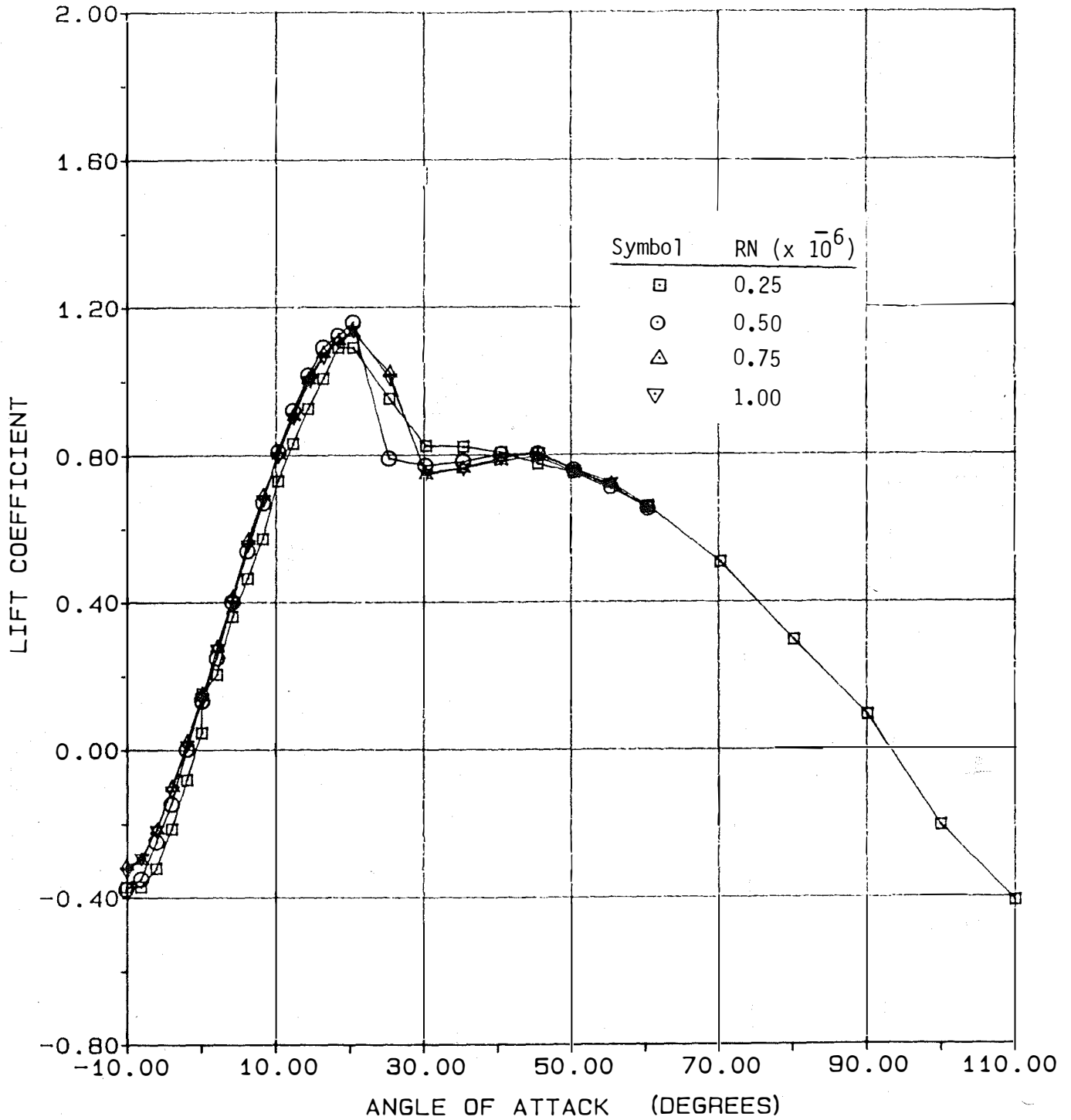
(b) Drag

Figure A.11- Continued.



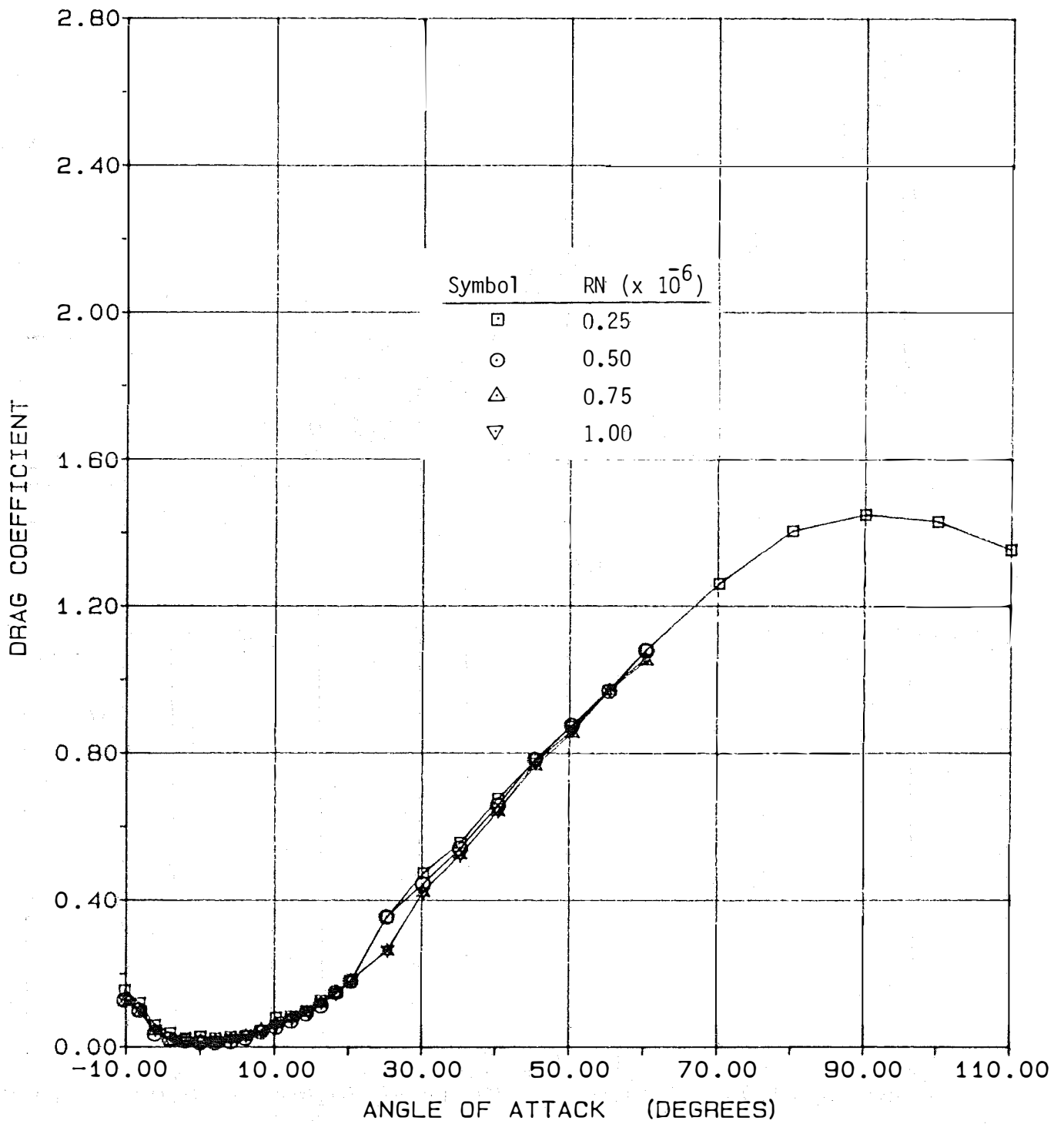
(c) Pitching Moment

Figure A.11- Concluded.



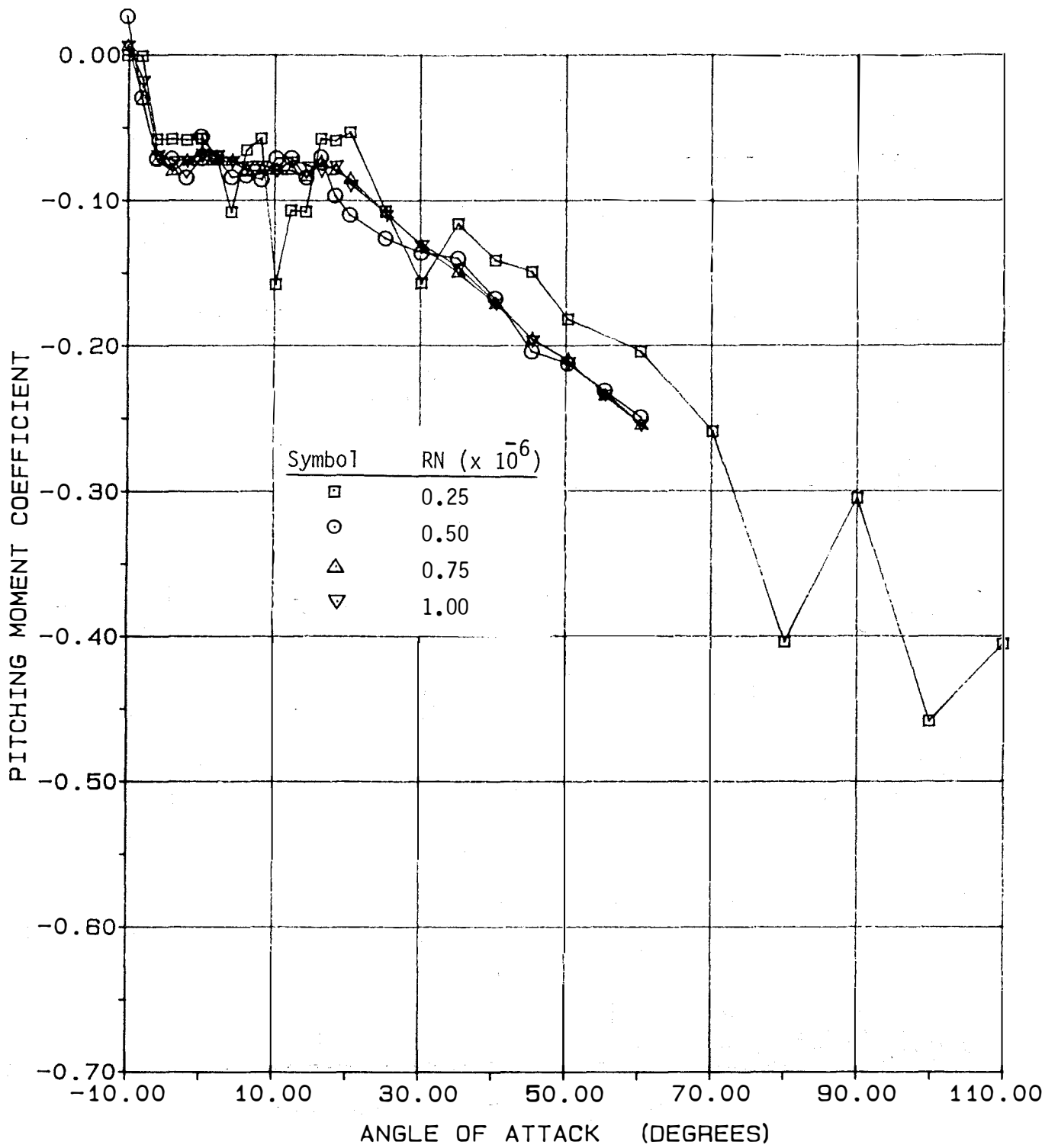
(a) Lift

Figure A.12- Aerodynamic Coefficients of the NACA 4412 Airfoil, AR = 6.



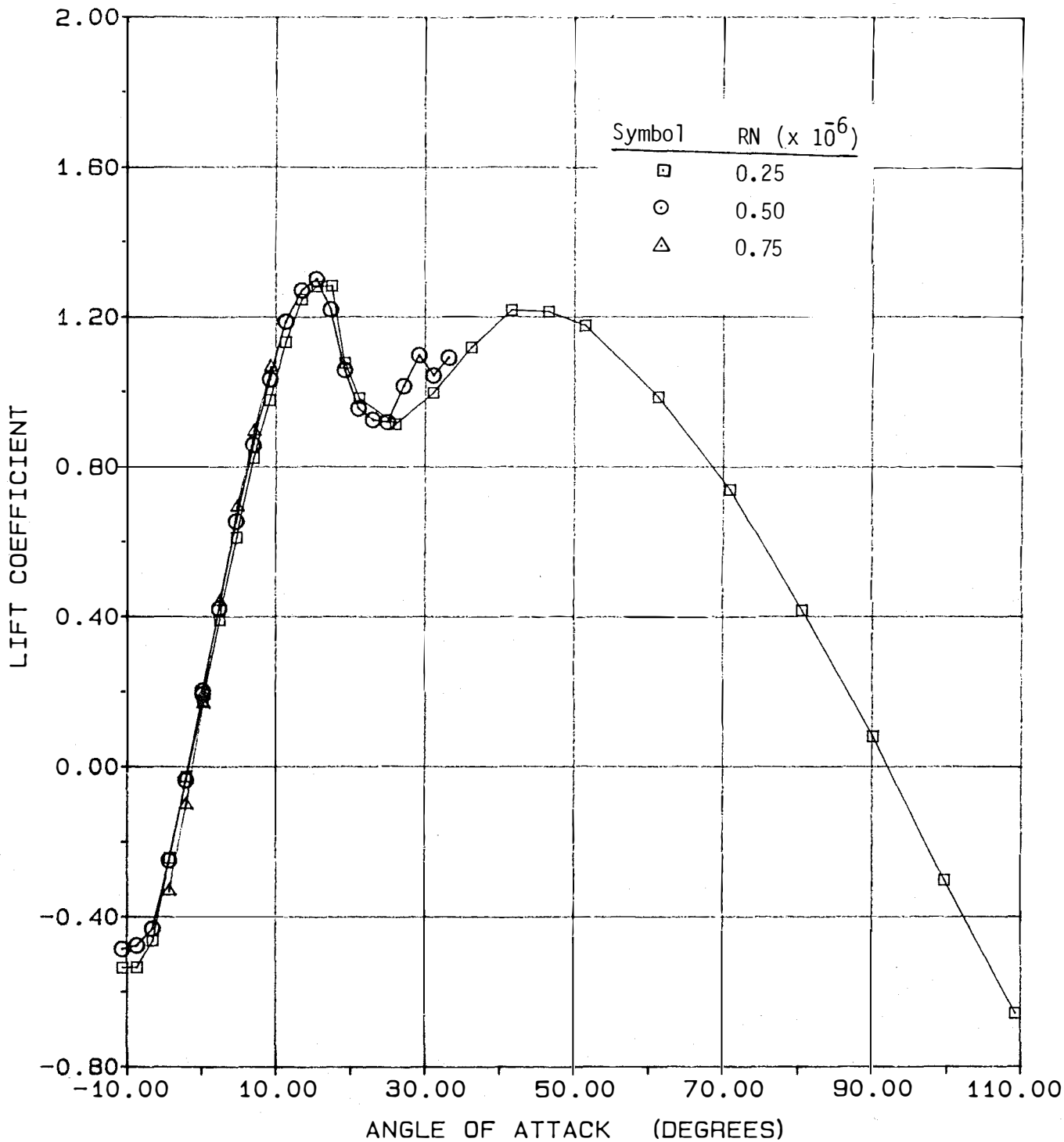
(b) Drag

Figure A.12- Continued.



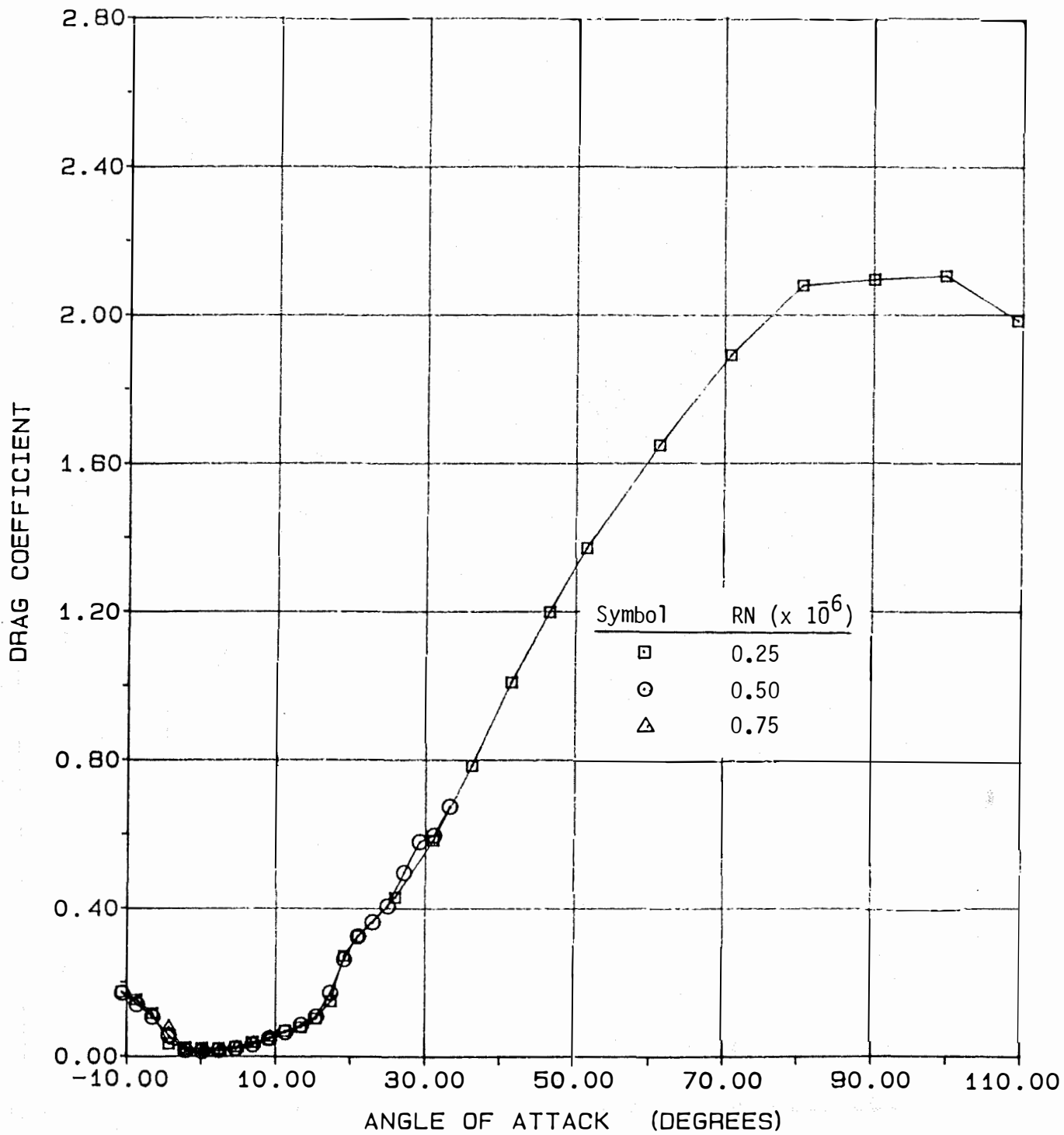
(c) Pitching Moment

FigureA.12- Concluded.



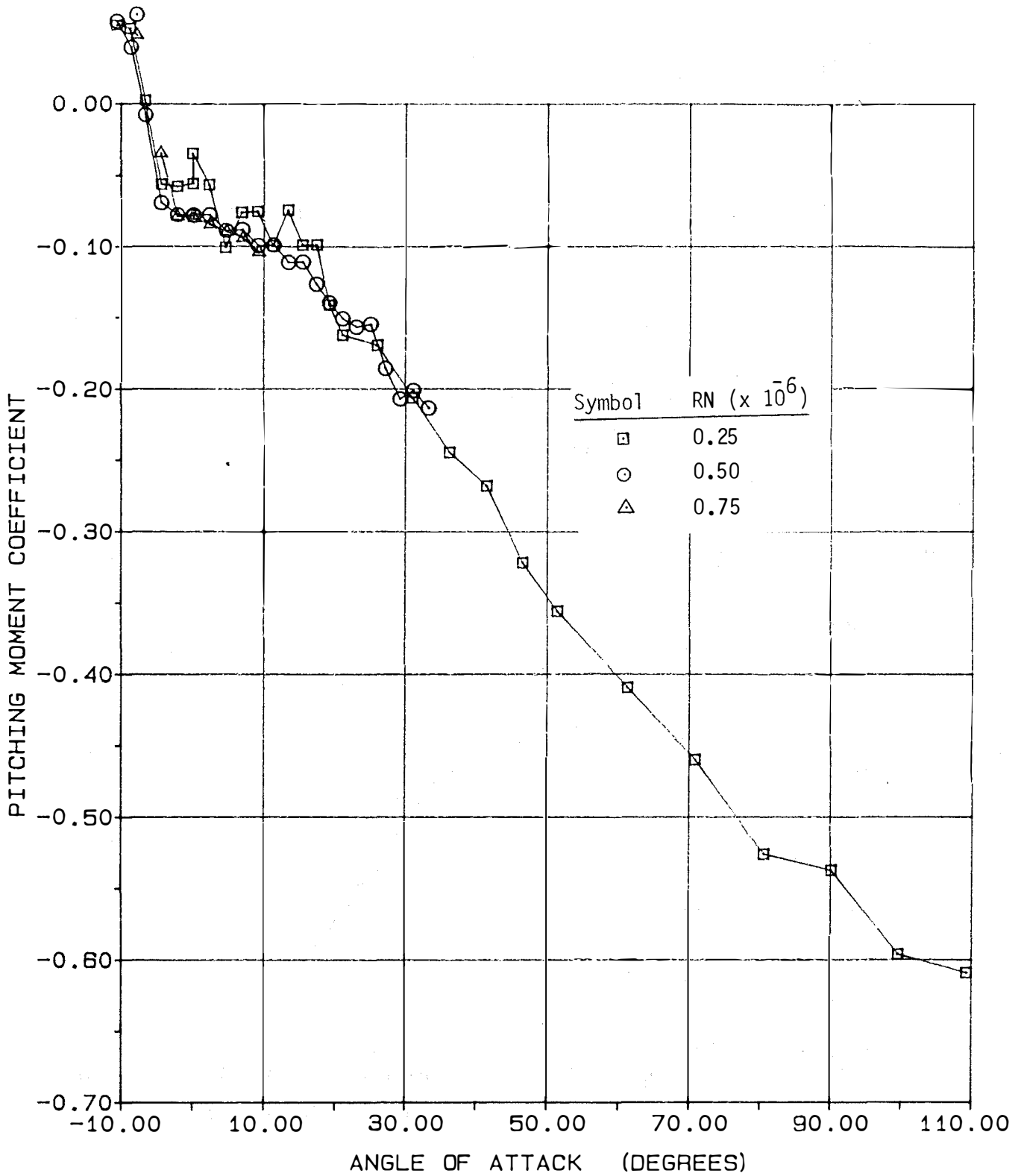
(a) Lift

Figure A.13- Aerodynamic Coefficients of the NACA 4409 Airfoil, $AR = \infty$.



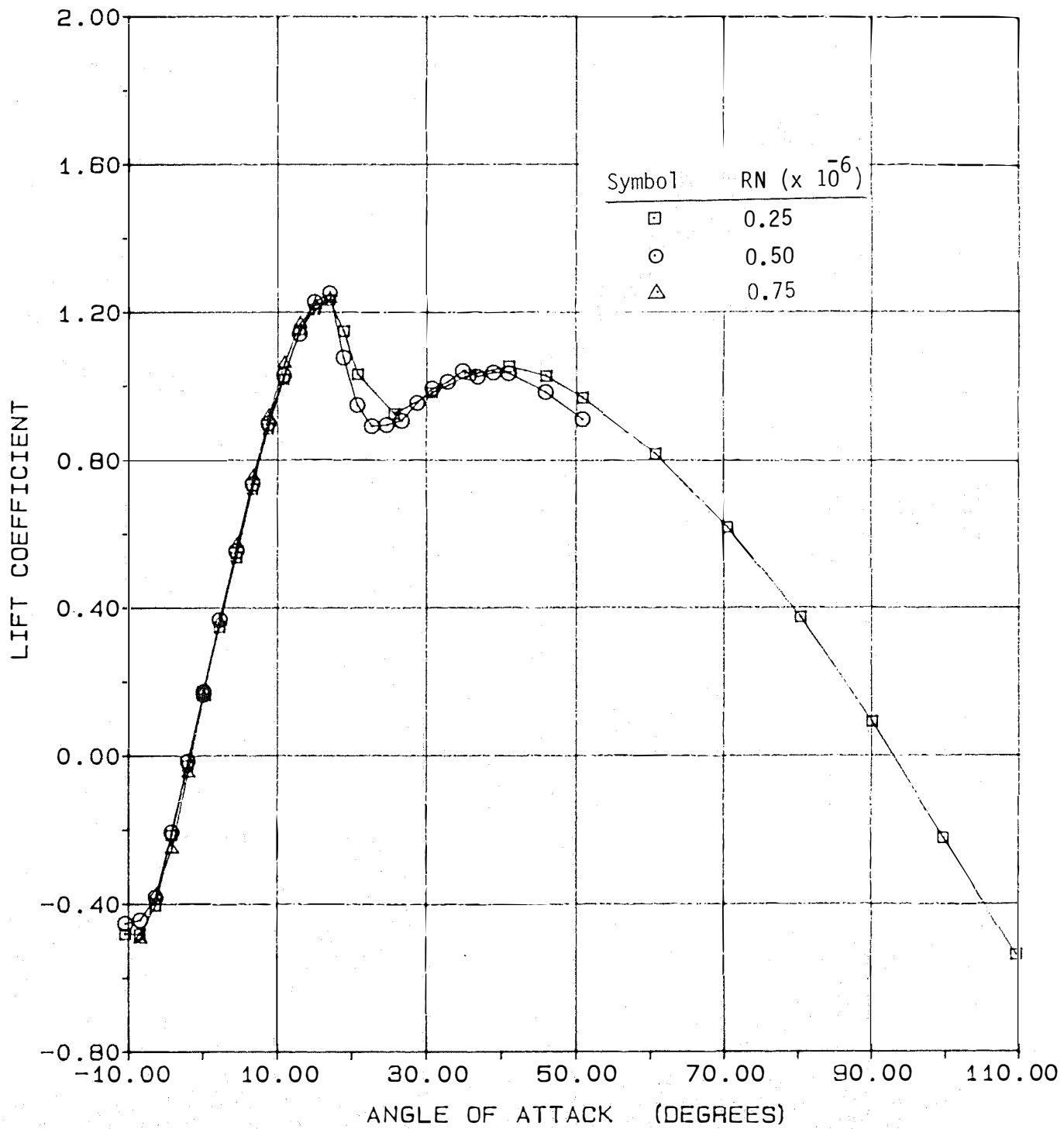
(b) Drag

Figure A.13- Continued.



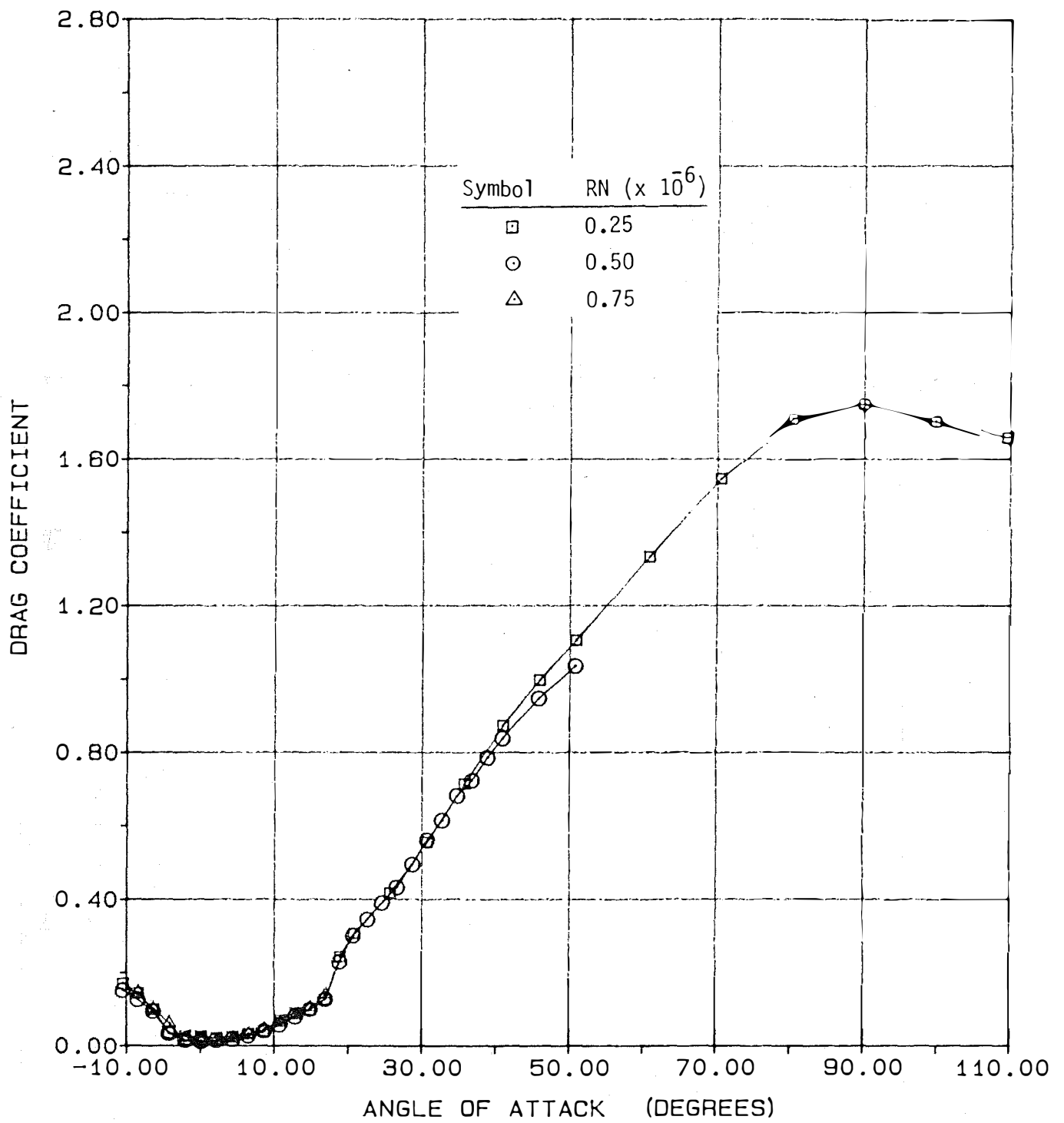
(c) Pitching Moment

Figure A.13- Concluded.



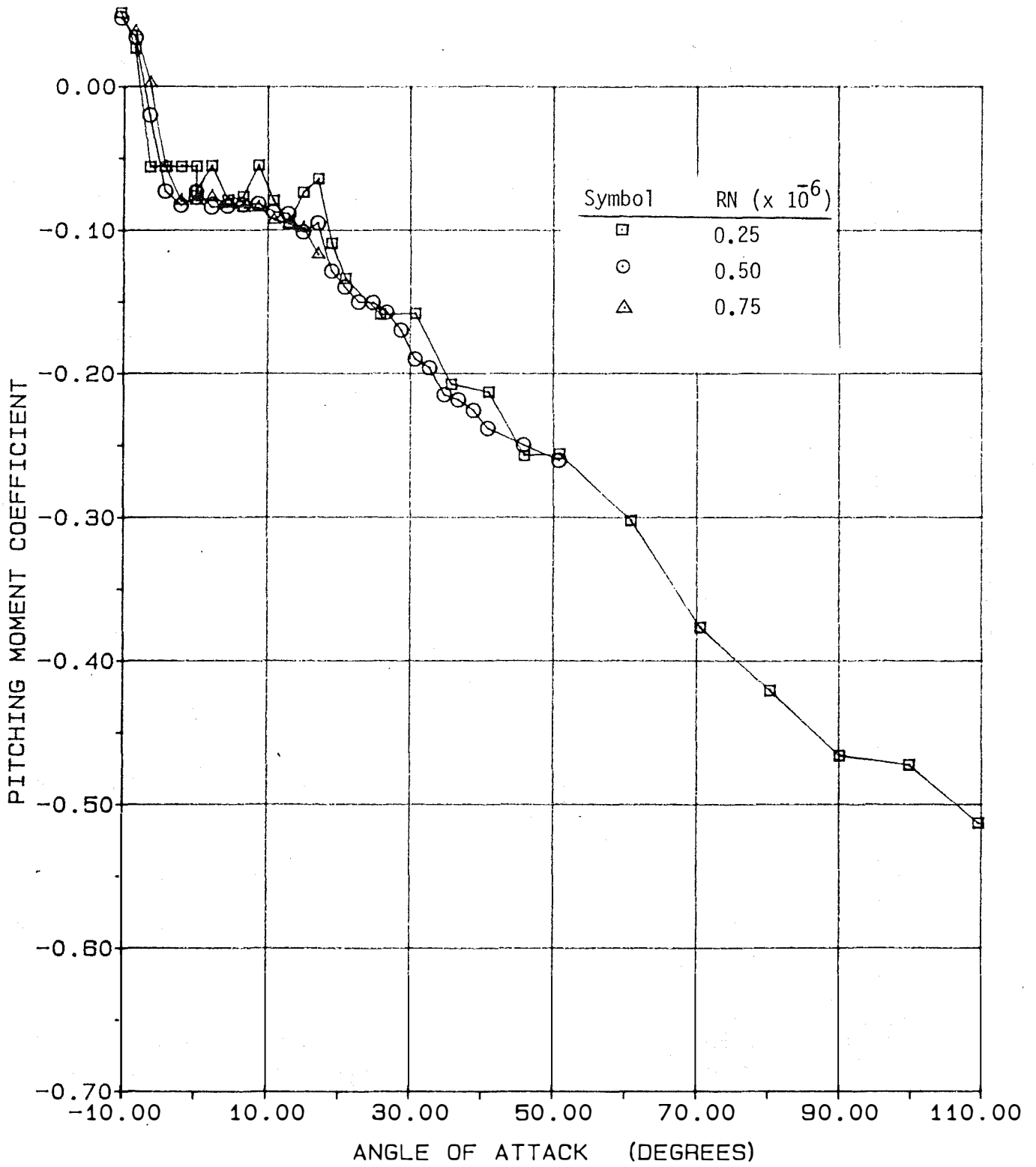
(a) Lift

Figure A.14- Aerodynamic Coefficients of the NACA 4409 Airfoil, AR = 12.



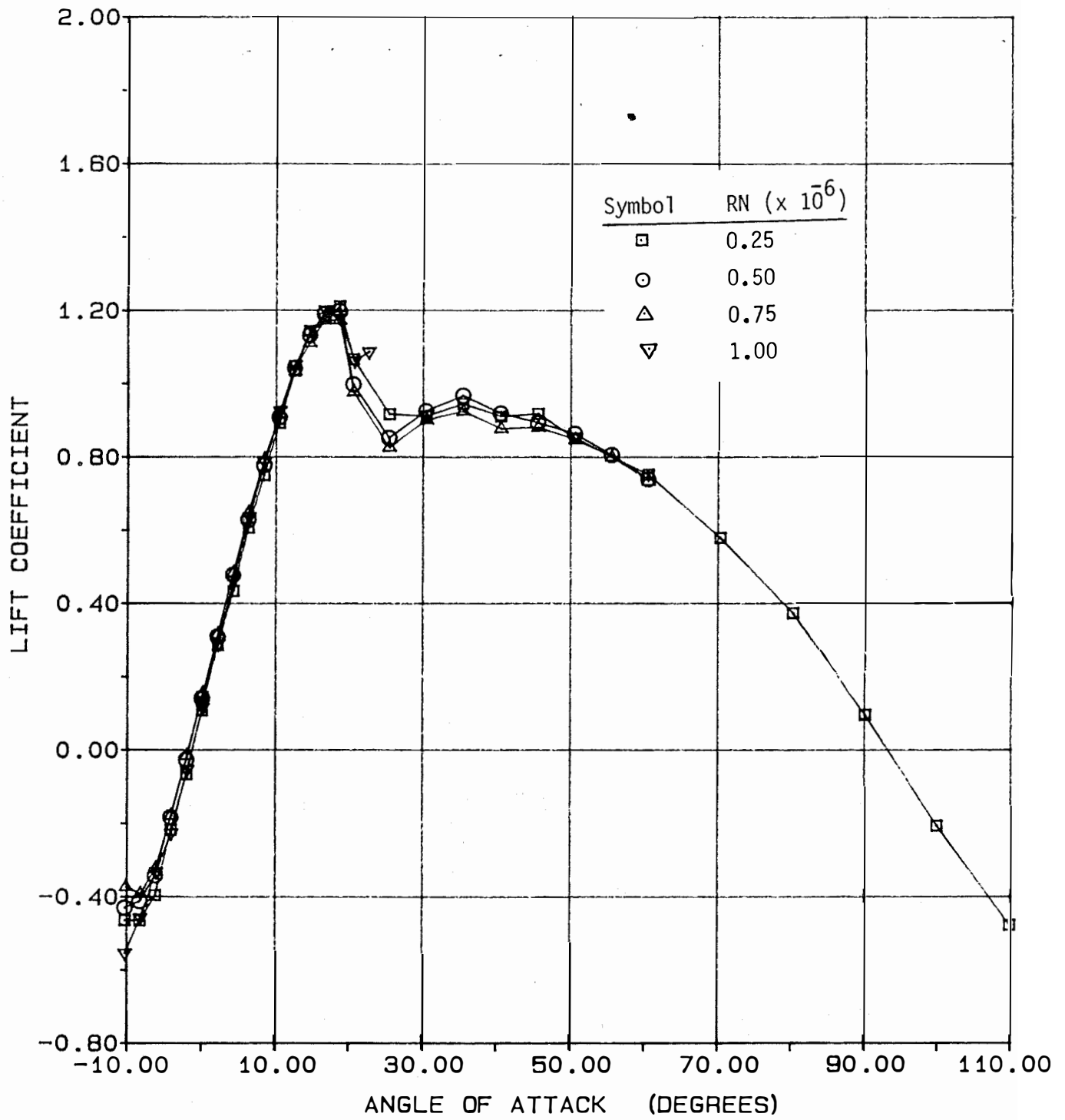
(b) Drag

Figure A.14- Continued.



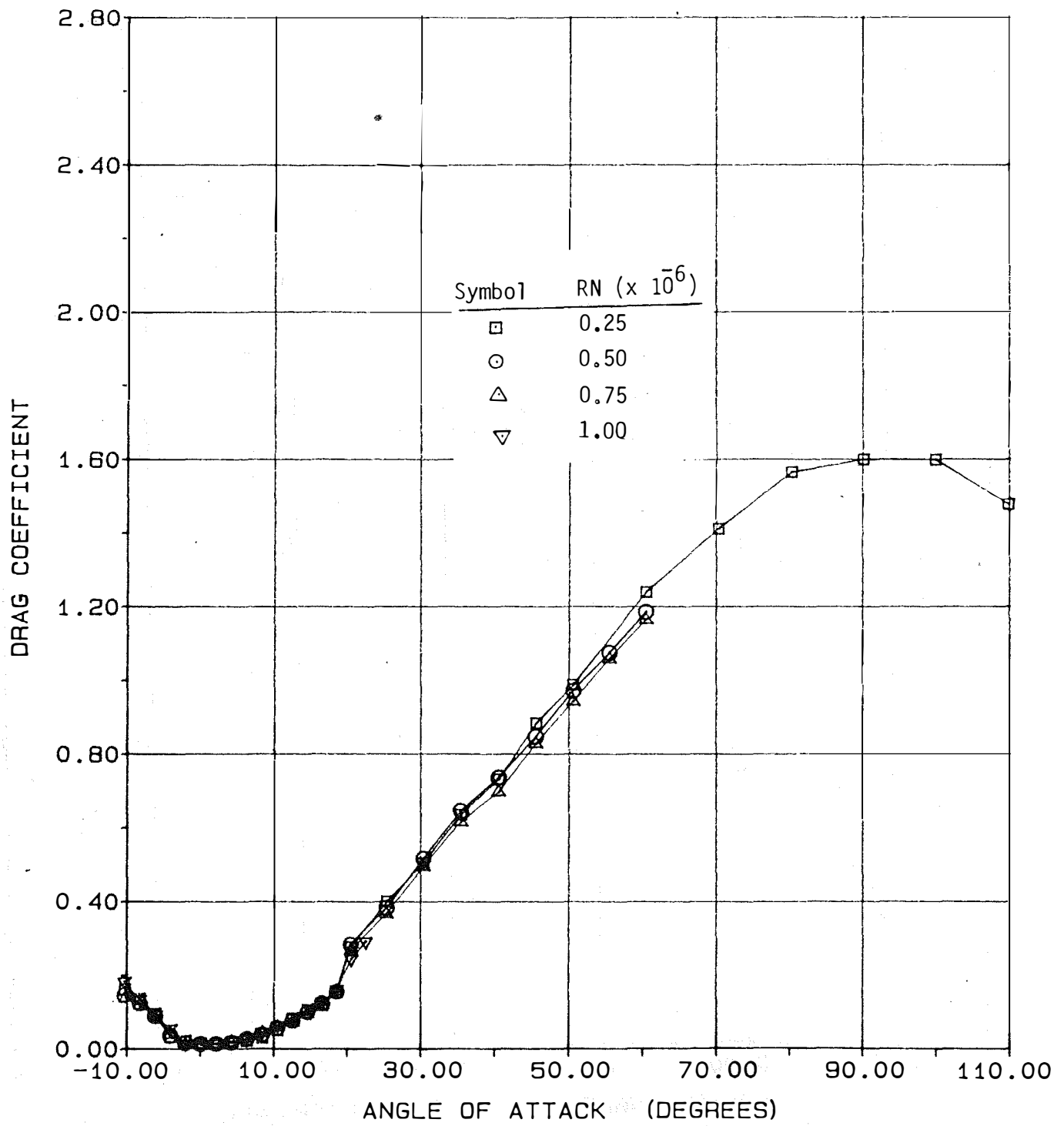
(c) Pitching Moment

Figure A.14- Concluded.



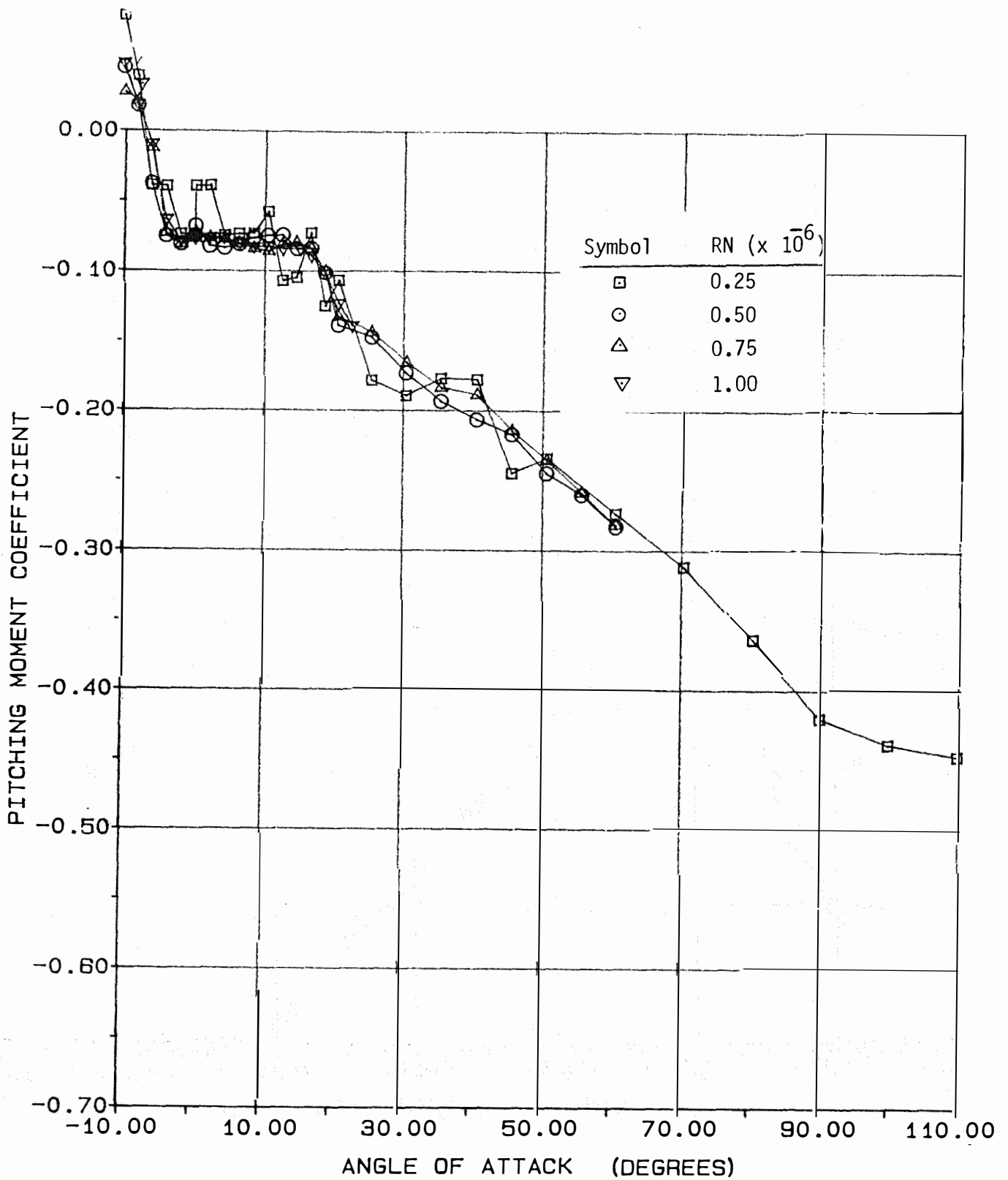
(a) Lift

Figure A.15- Aerodynamic Coefficients of the NACA 4409 Airfoil, AR = 9.



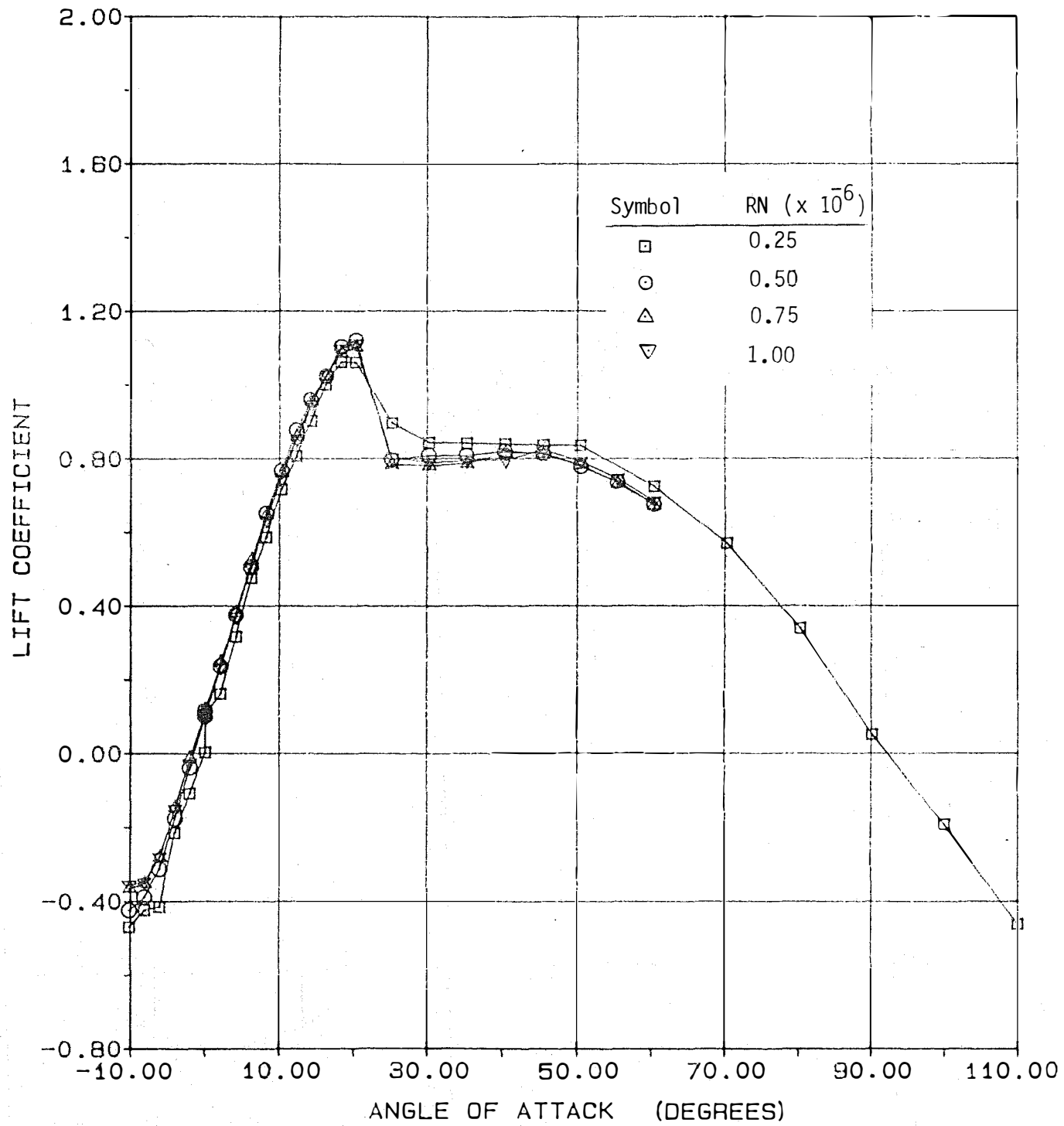
(b) Drag

Figure A.15- Continued.



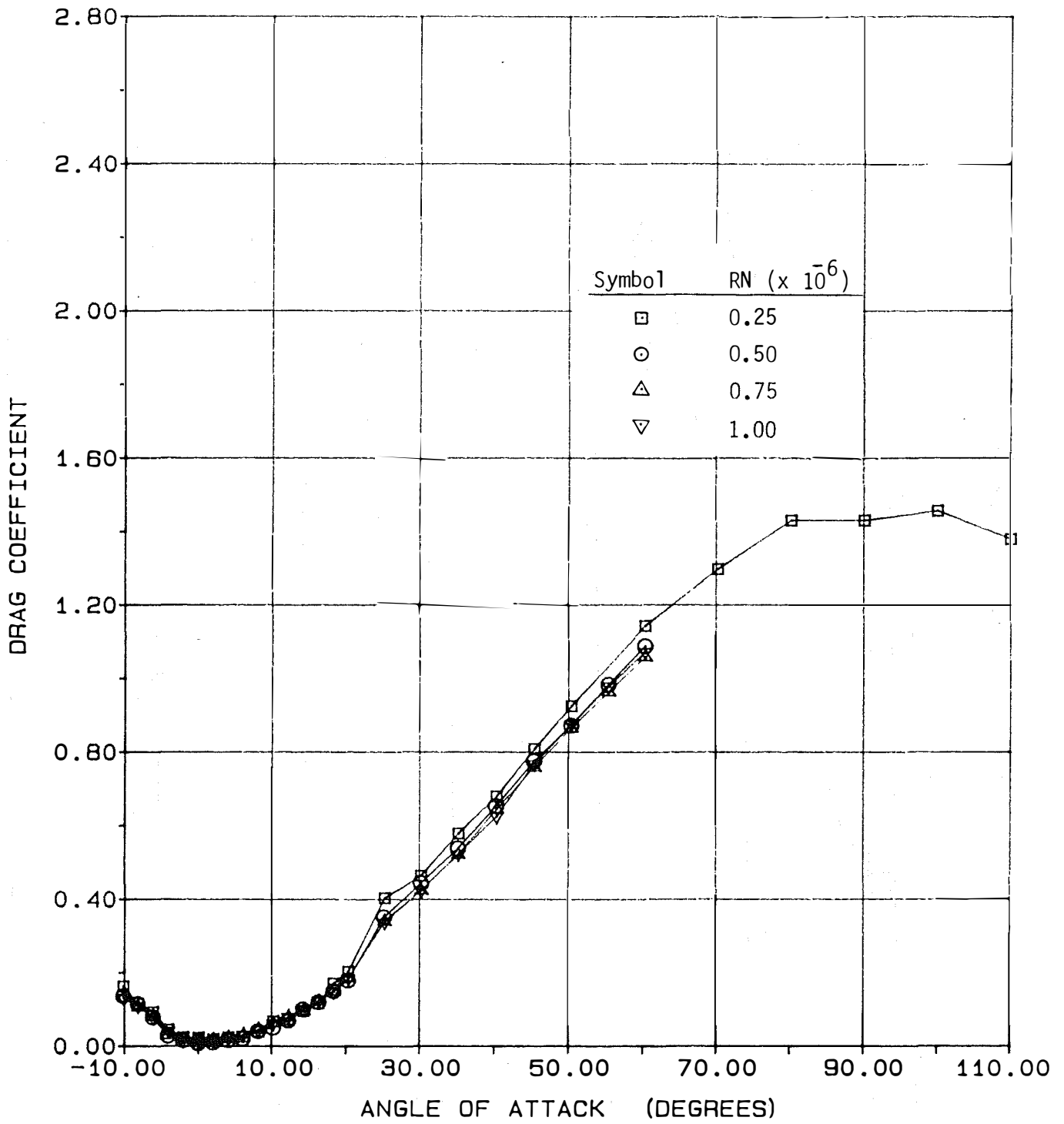
(c) Pitching Moment

Figure A.15- Concluded.



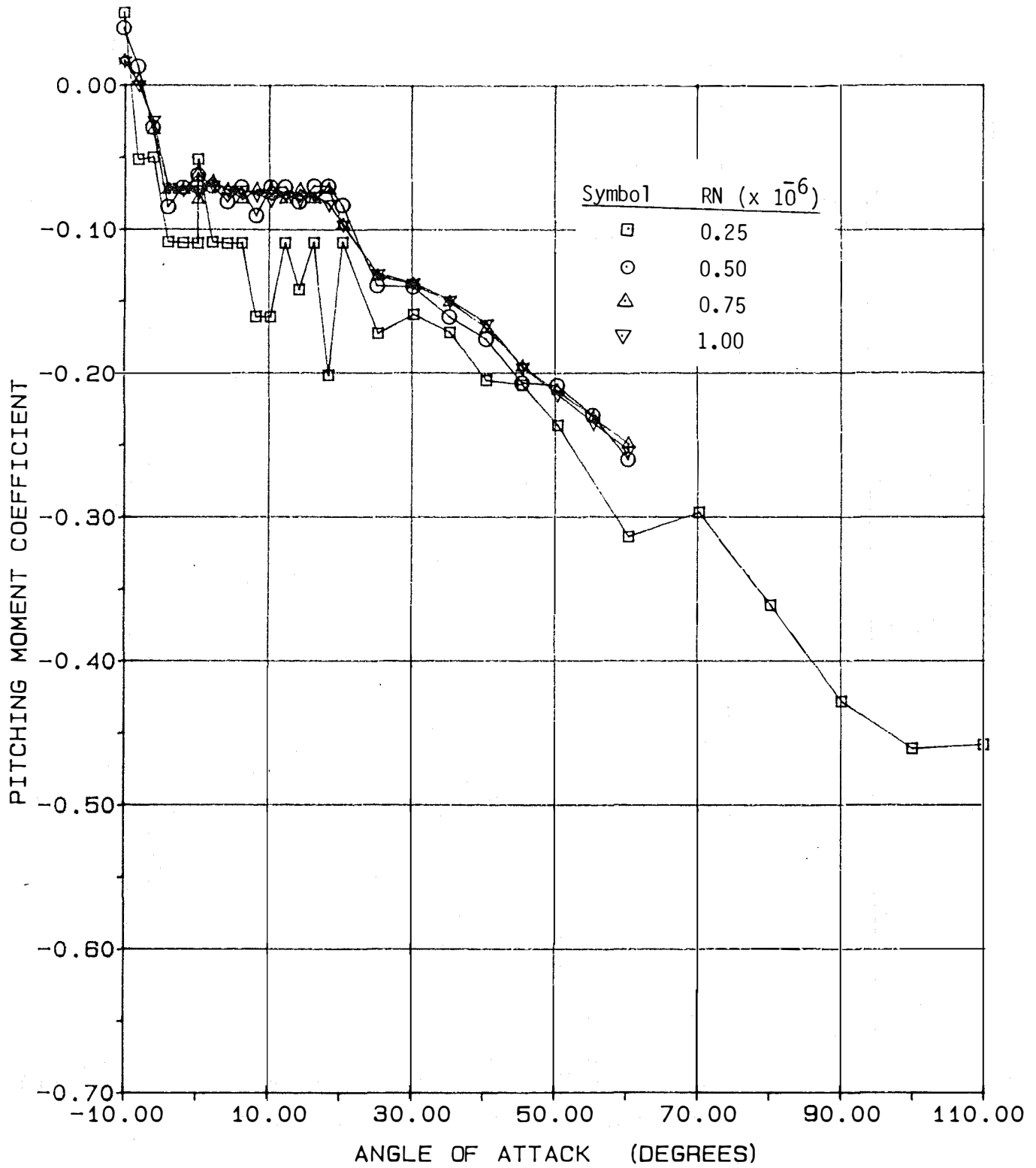
(a) Lift

Figure A.16- Aerodynamic Coefficients of the NACA 4409 Airfoil, AR = 6.



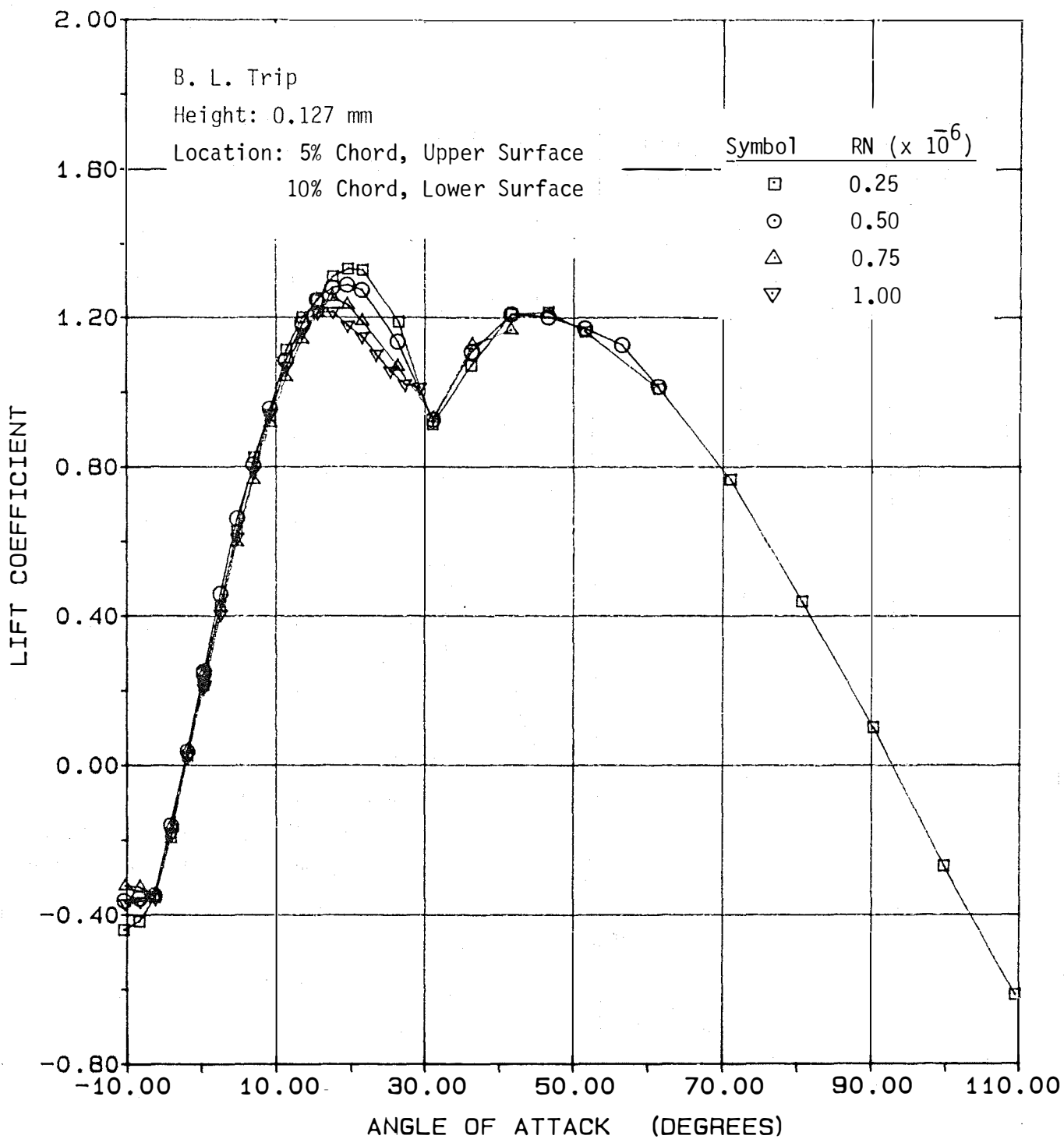
(b) Drag

Figure A.16- Continued.



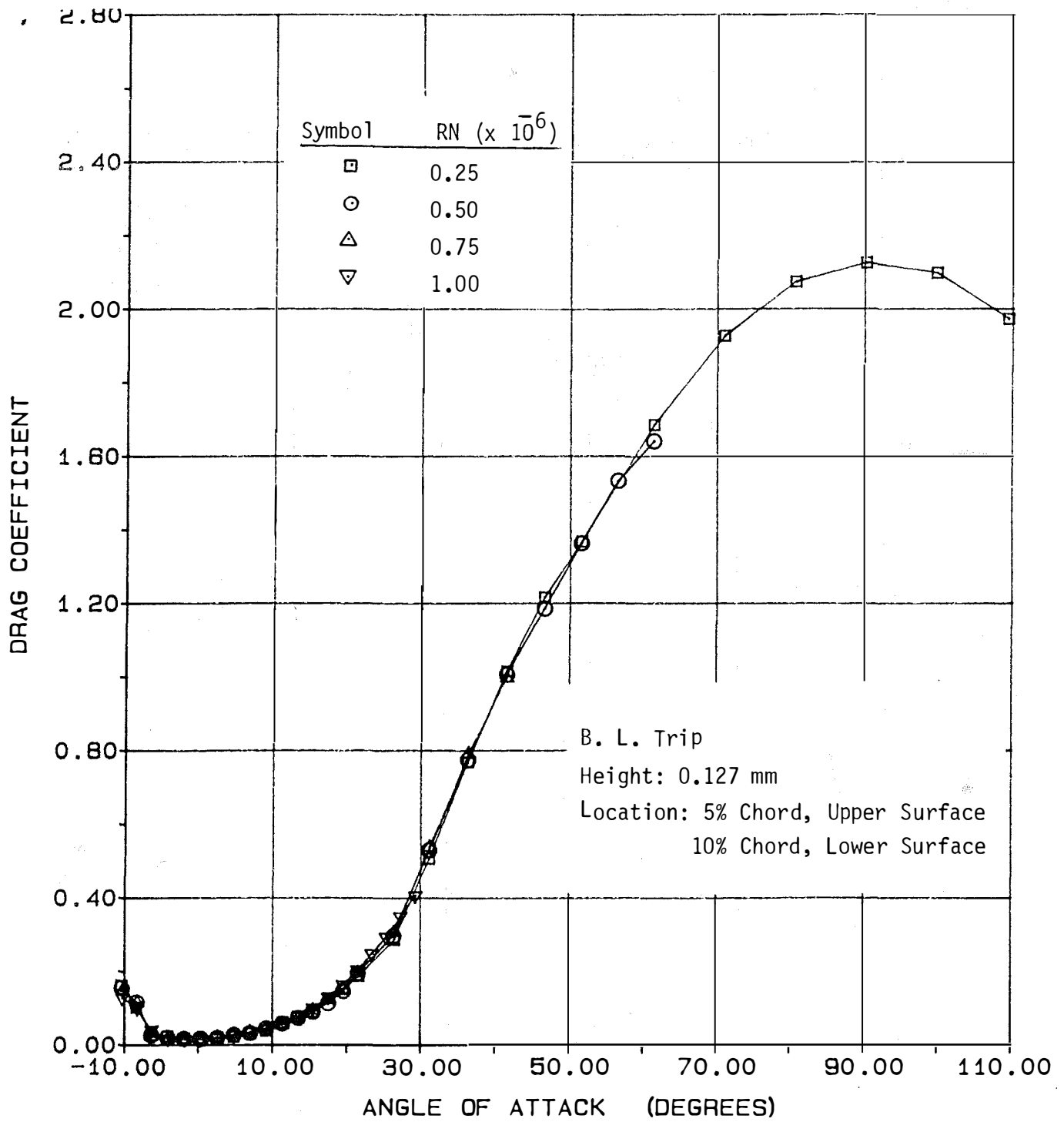
(c) Pitching Moment

Figure A.16- Concluded.



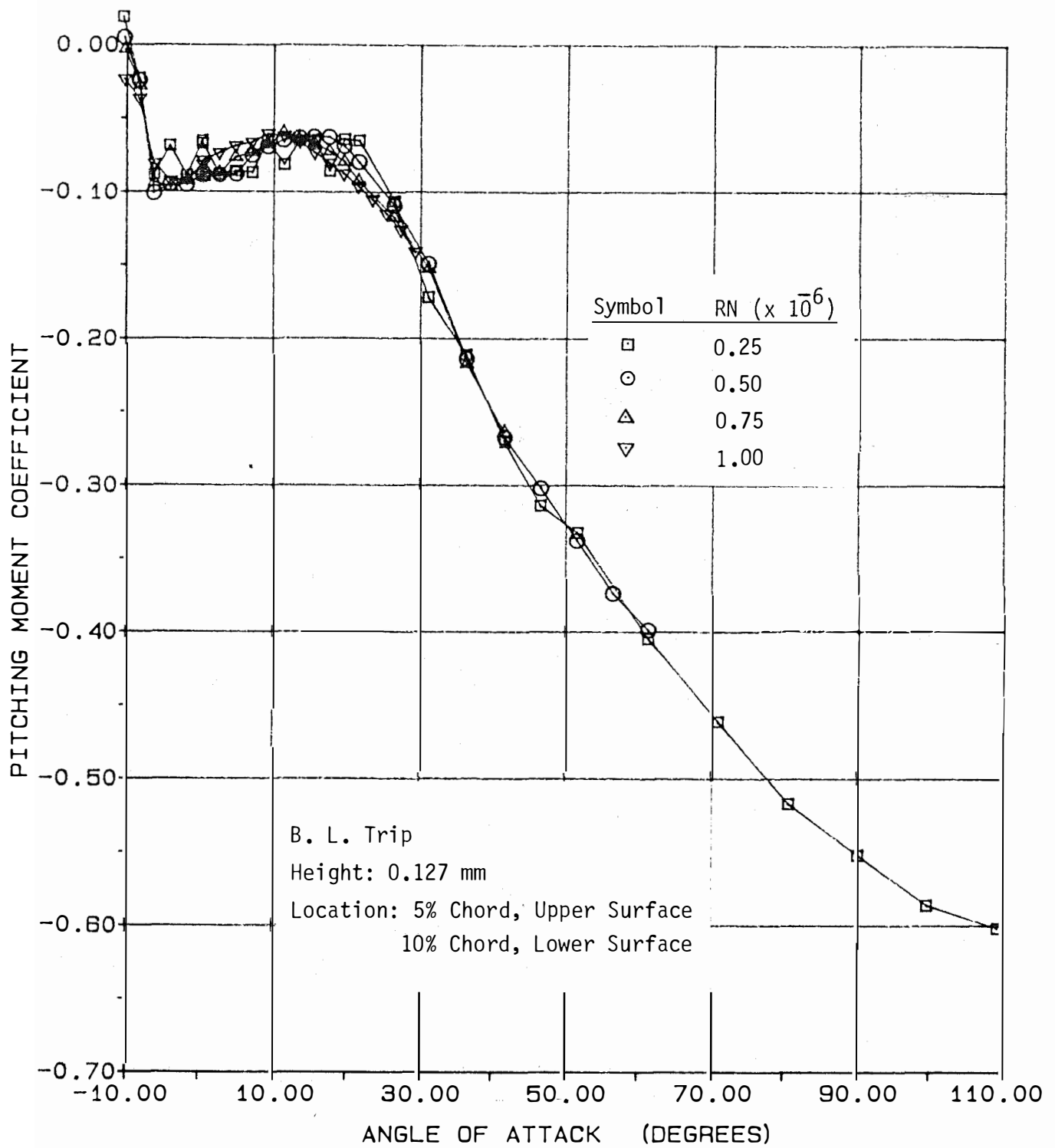
(a) Lift

Figure A.17- Aerodynamic Coefficients of the NACA 4415 Airfoil with Boundary Layer Trip, $AR = \infty$.



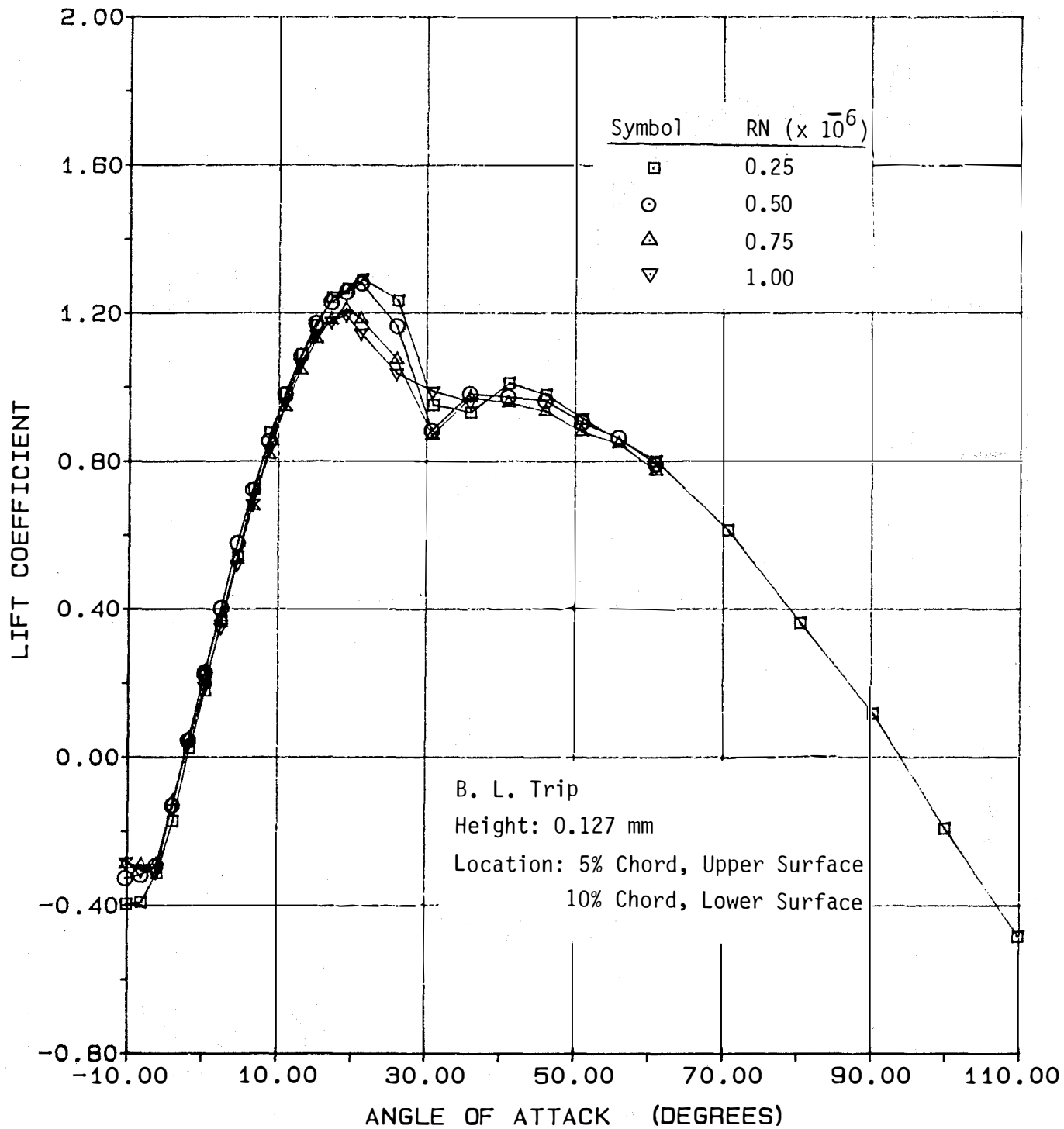
(b) Drag

Figure A.17- Continued.



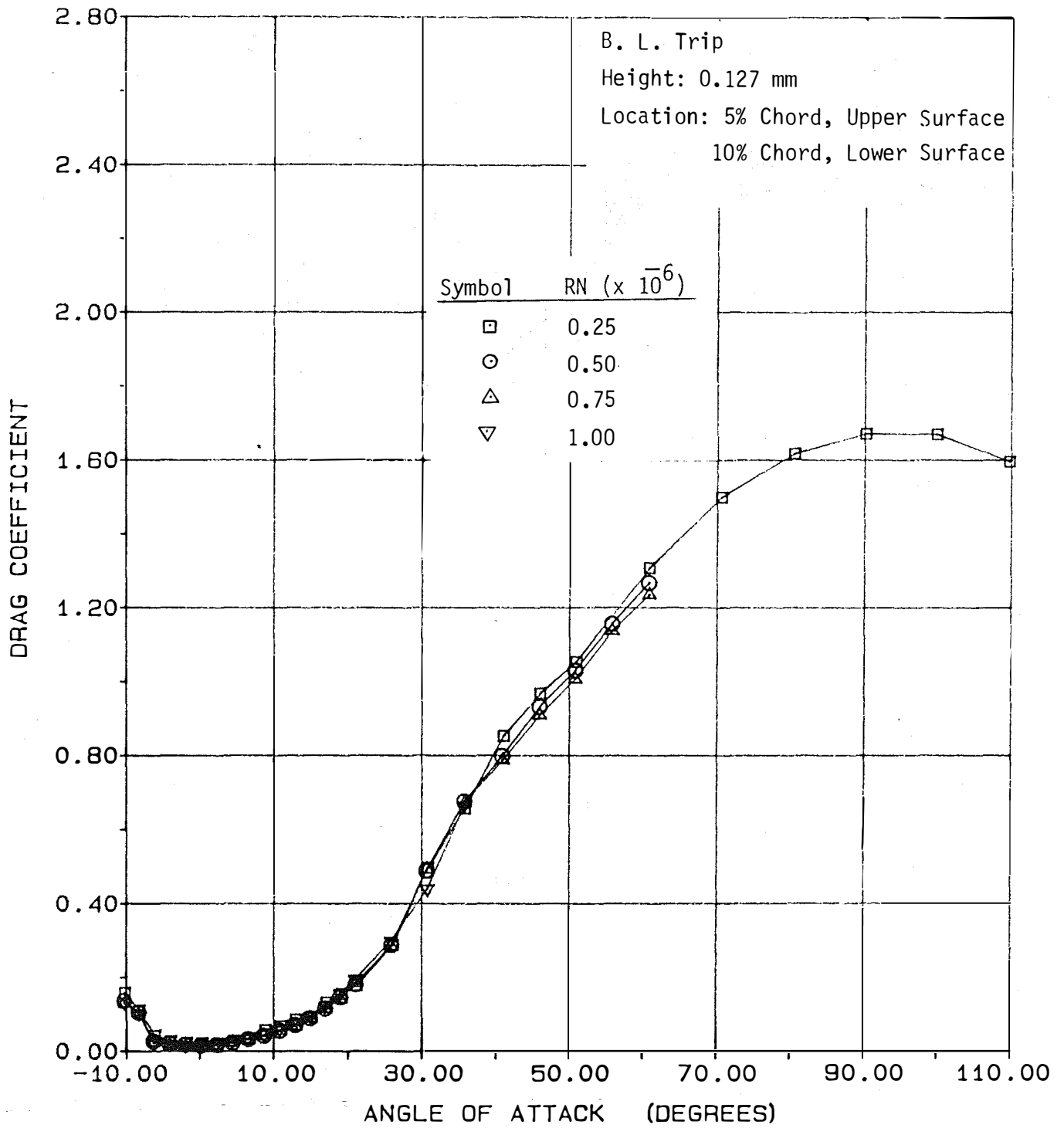
(c) Pitching Moment

Figure A.17- Concluded.



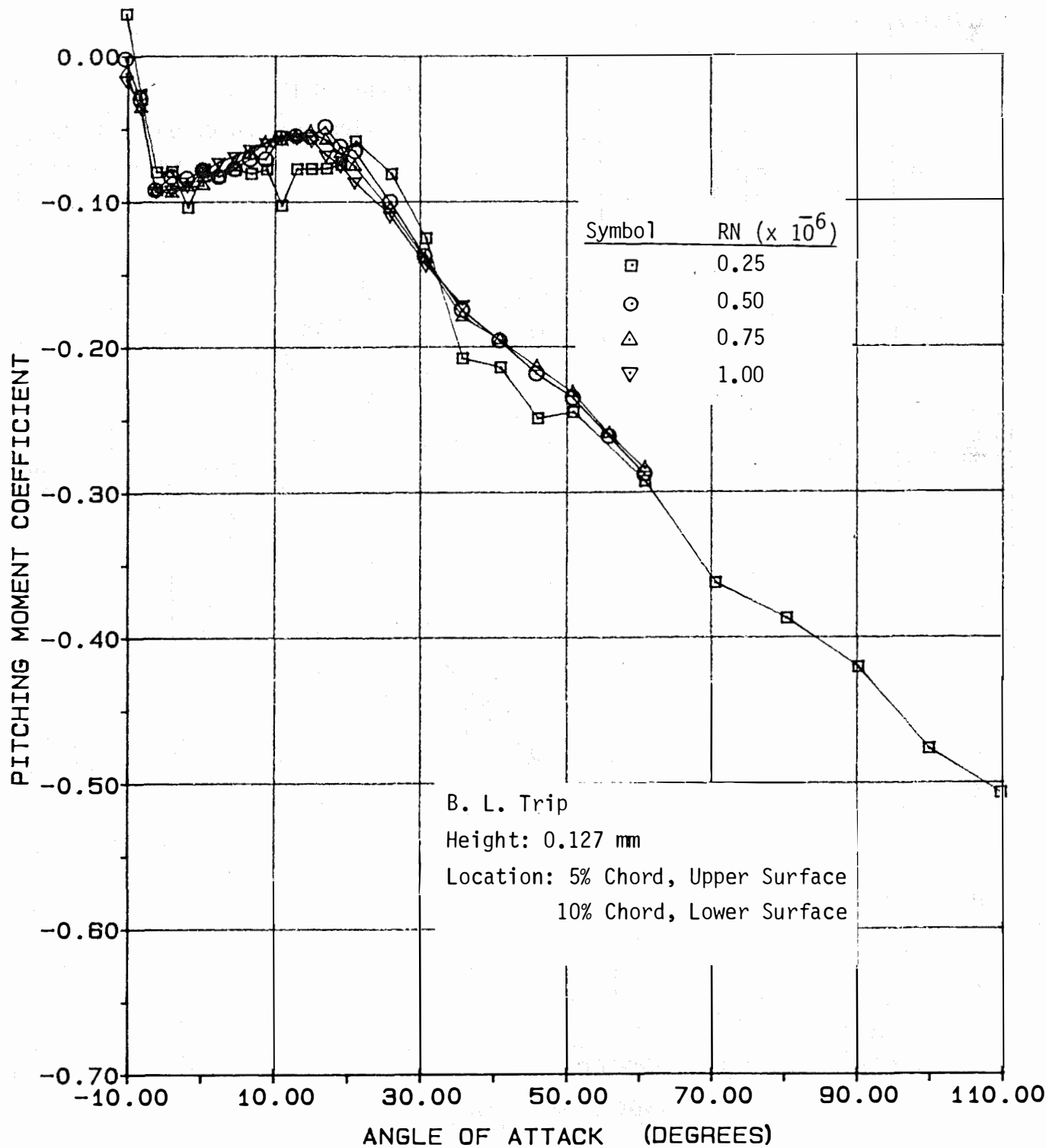
(a) Lift

Figure A.18- Aerodynamic Coefficients of the NACA 4415 Airfoil with Boundary Layer Trip, AR = 12.



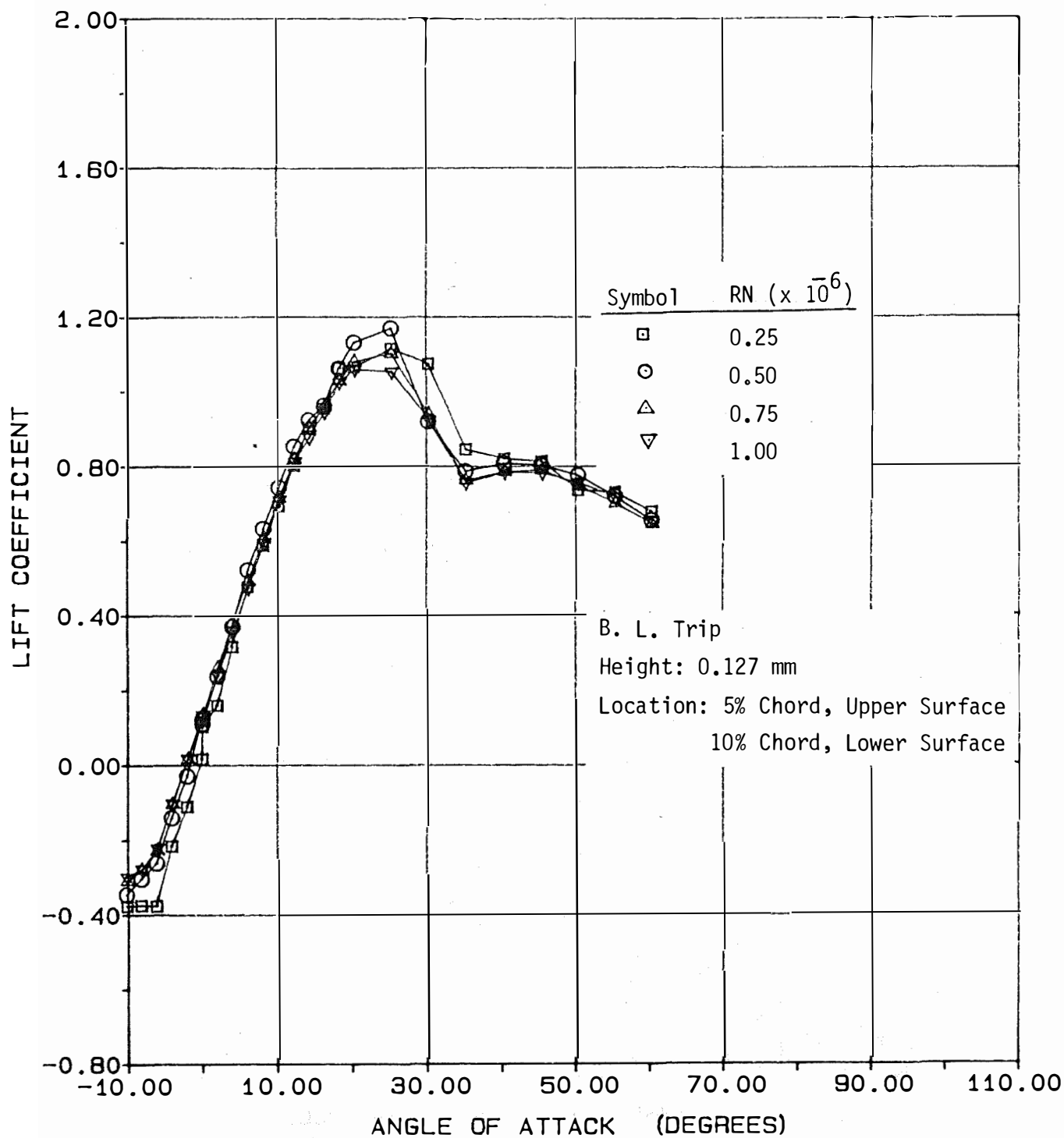
(b) Drag

Figure A.18- Continued.



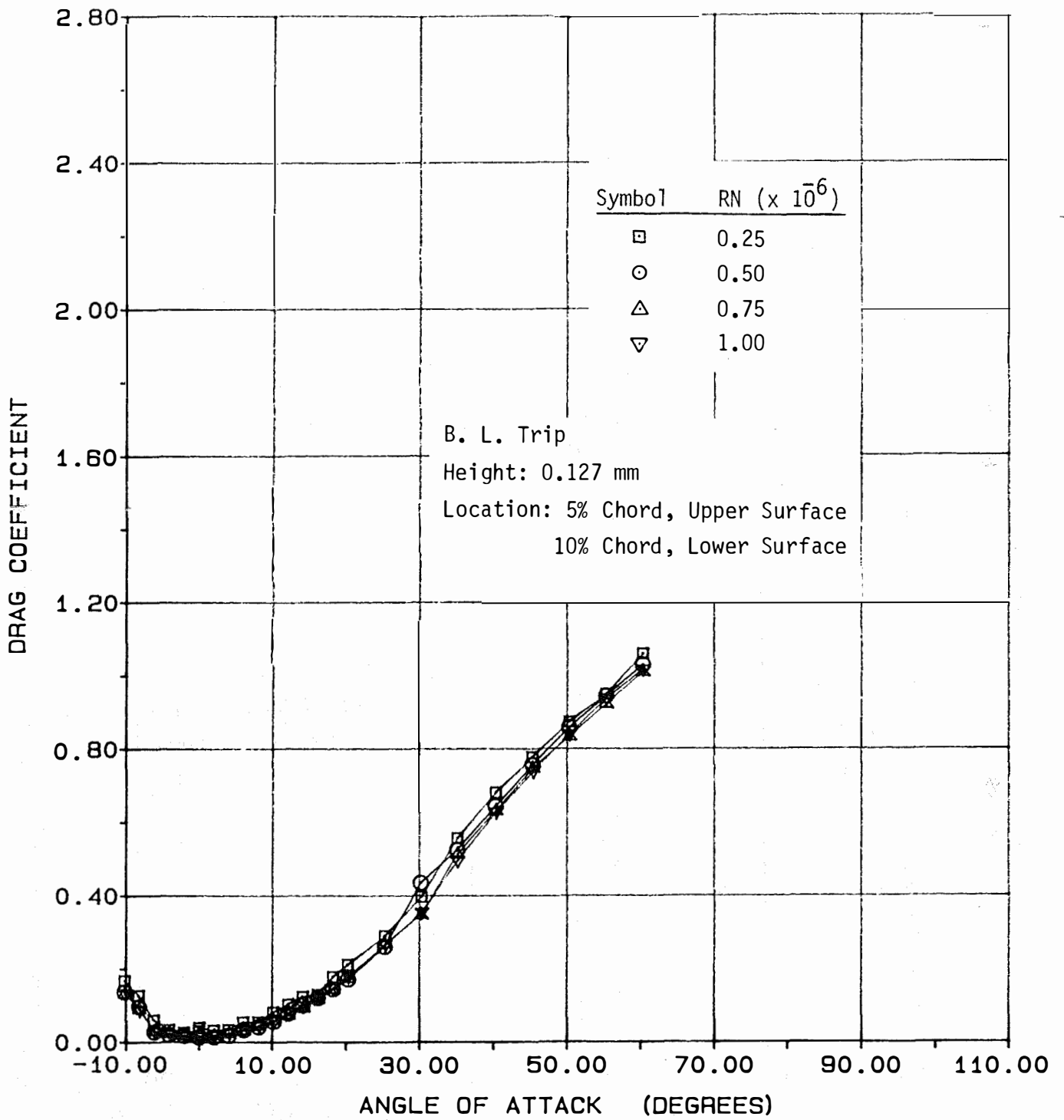
(c) Pitching Moment

Figure A.18- Concluded.



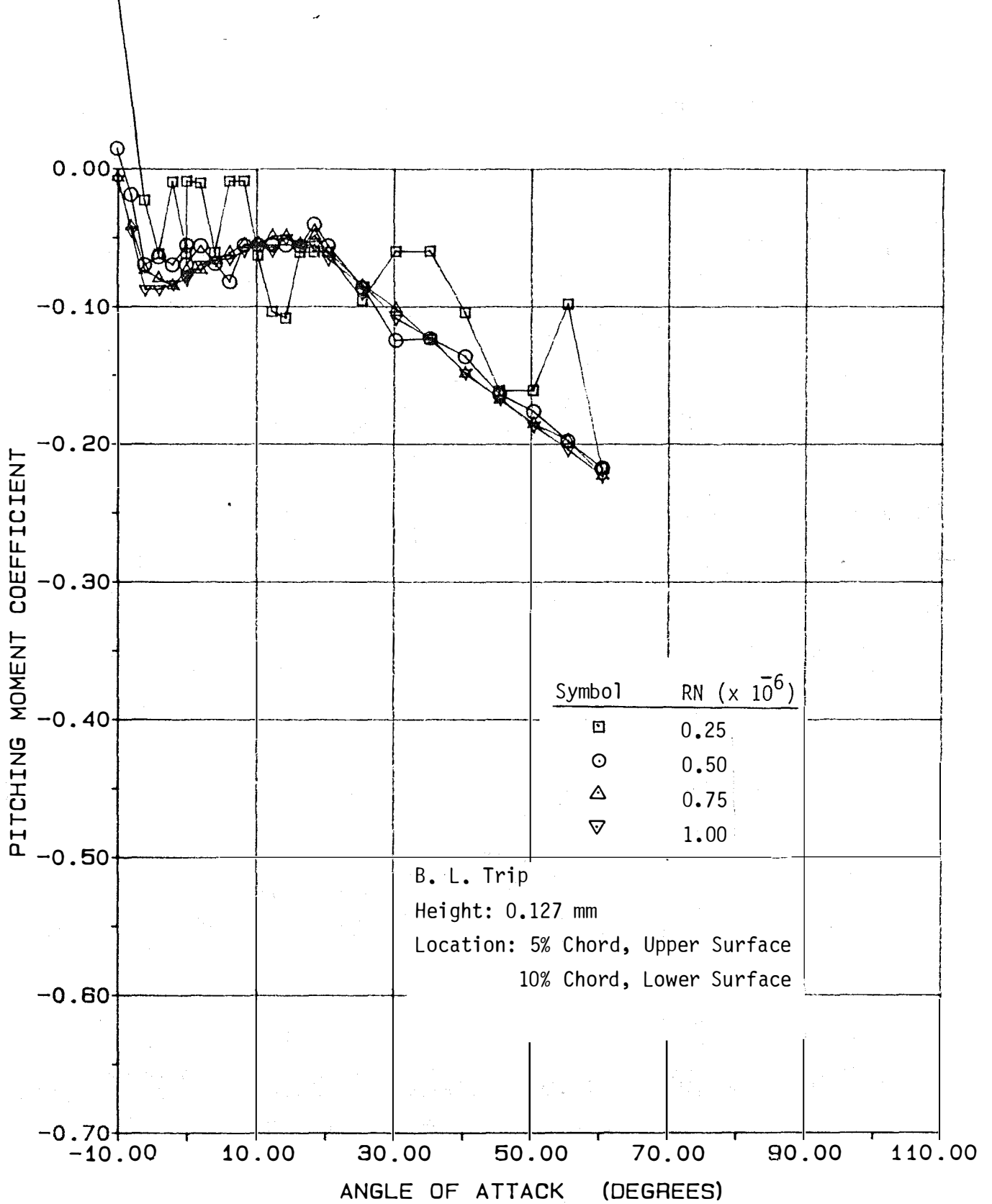
(a) Lift

Figure A.19- Aerodynamic Coefficients of the NACA 4415 Airfoil with Boundary Layer Trip, AR = 6.



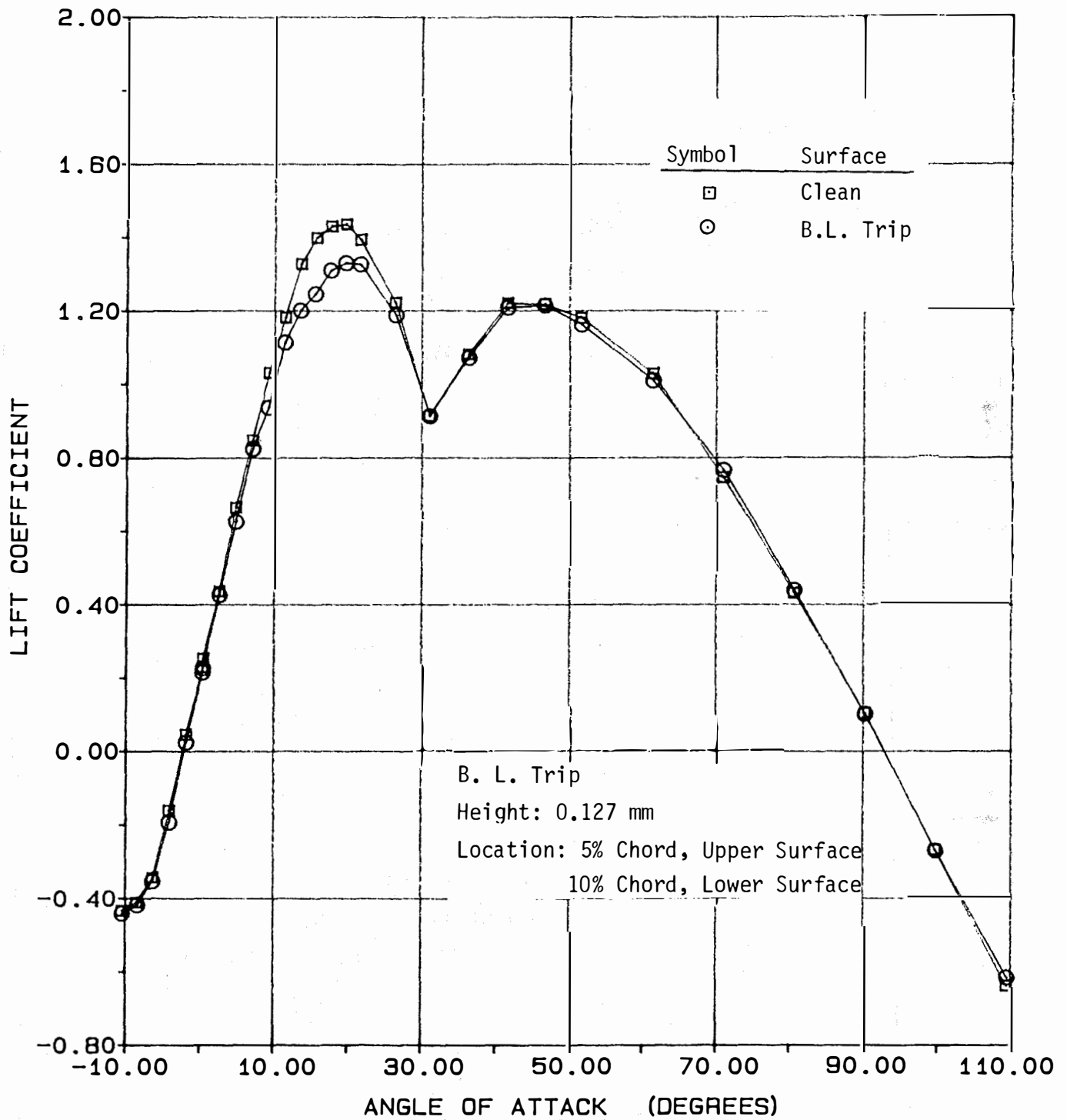
(b) Drag

Figure A.19- Continued.



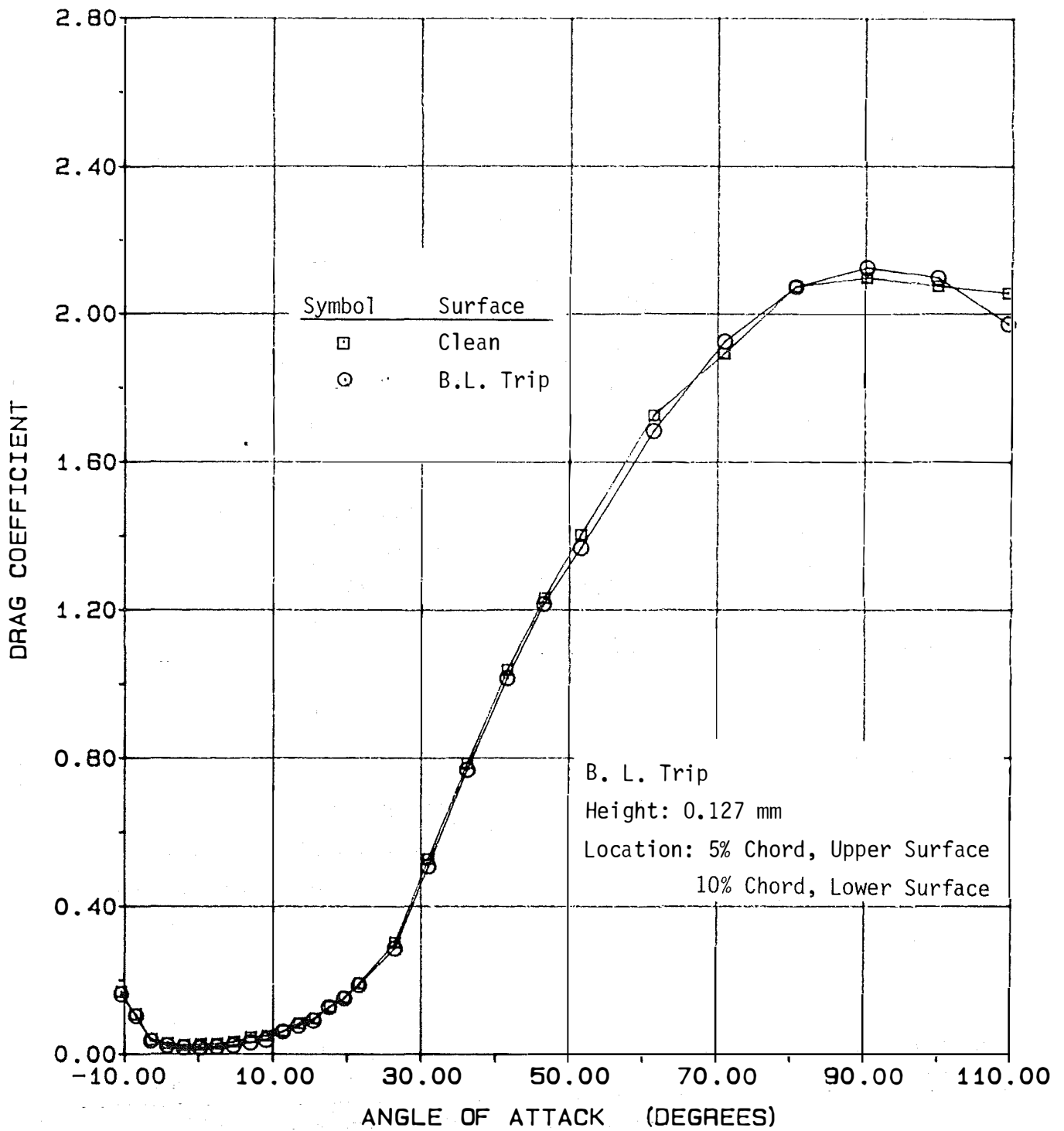
(c) Pitching Moment

Figure A.19- Concluded.



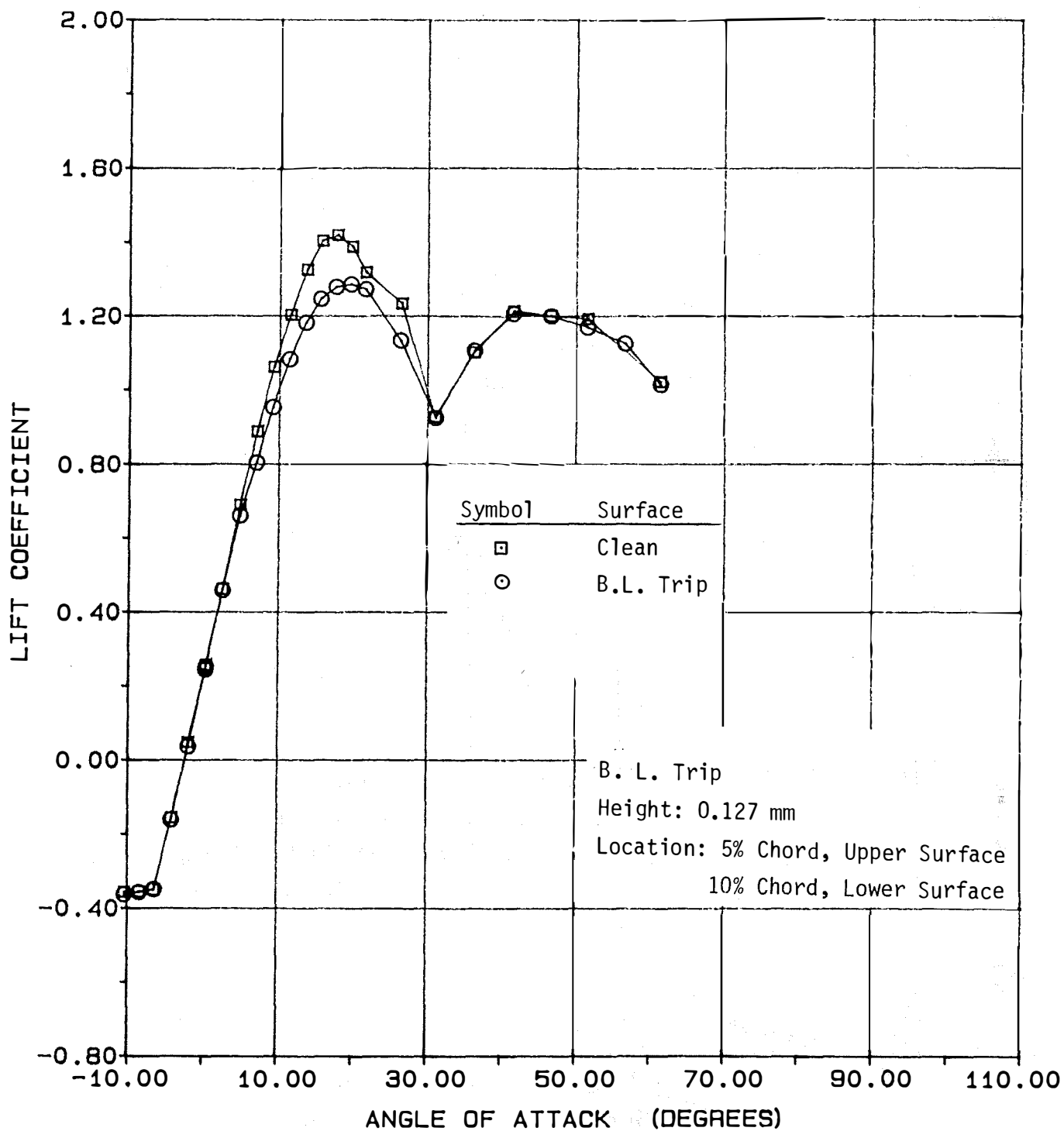
(a) Lift

Figure A.20- Effect of Boundary Layer Trip on Aerodynamic Coefficients of the NACA 4415 Airfoil, $AR = \infty$, $Re = 0.25 \times 10^6$.



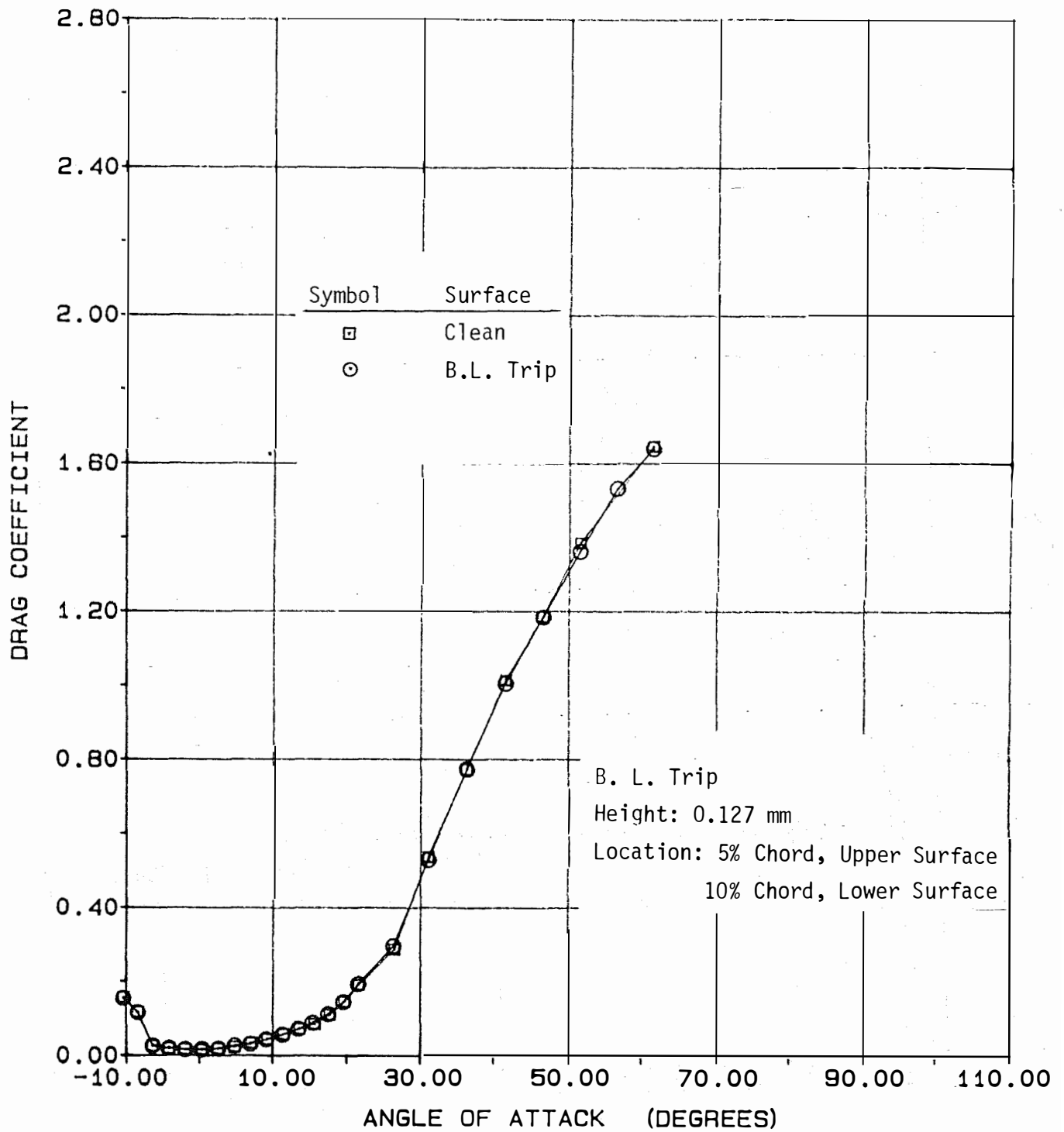
(b) Drag

Figure A.20- Concluded.



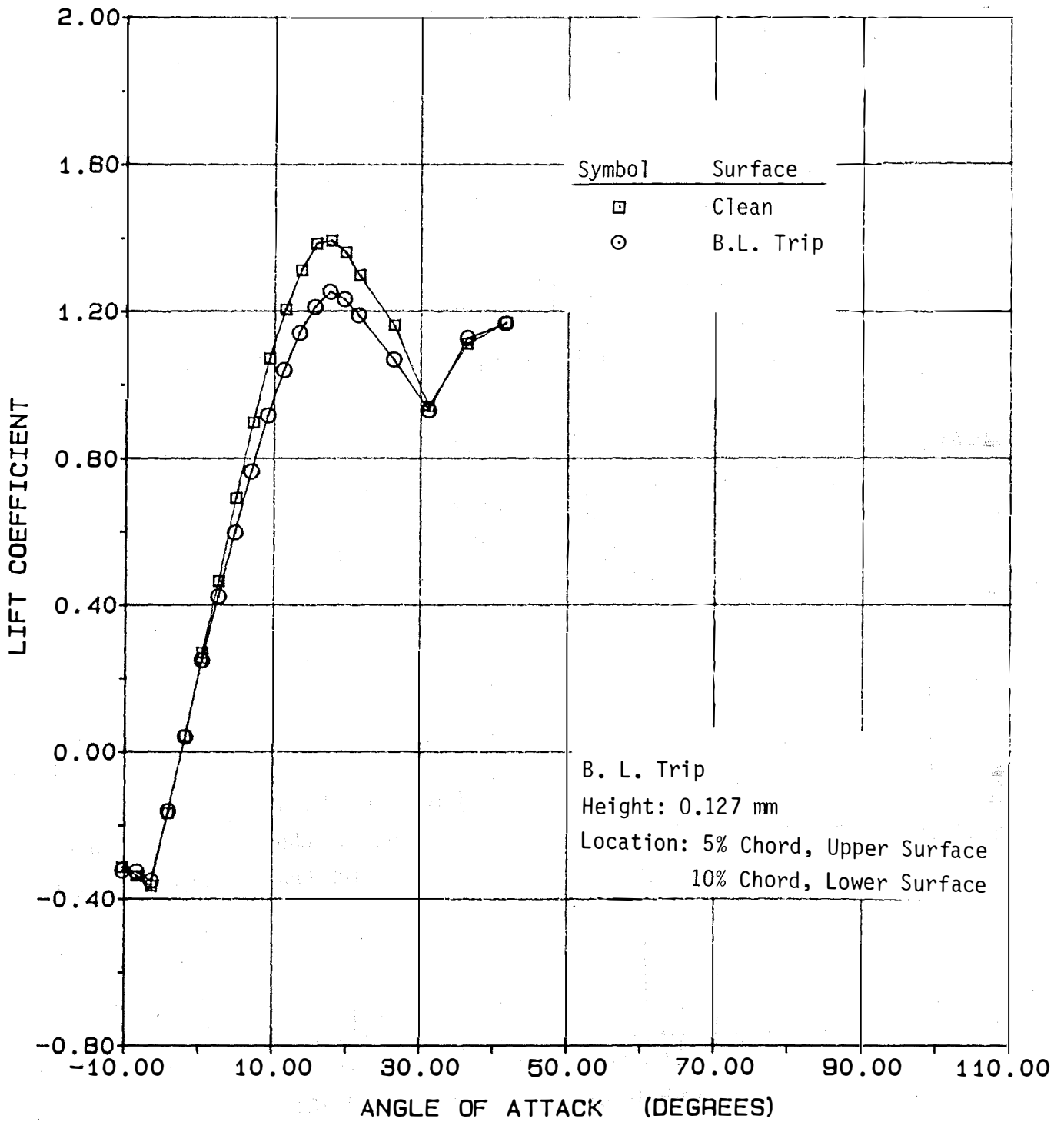
(a) Lift

Figure A.21- Effect of Boundary Layer Trip on Aerodynamic Coefficients of the NACA 4415 Airfoil, $AR = \infty$, $RN = 0.50 \times 10^6$.



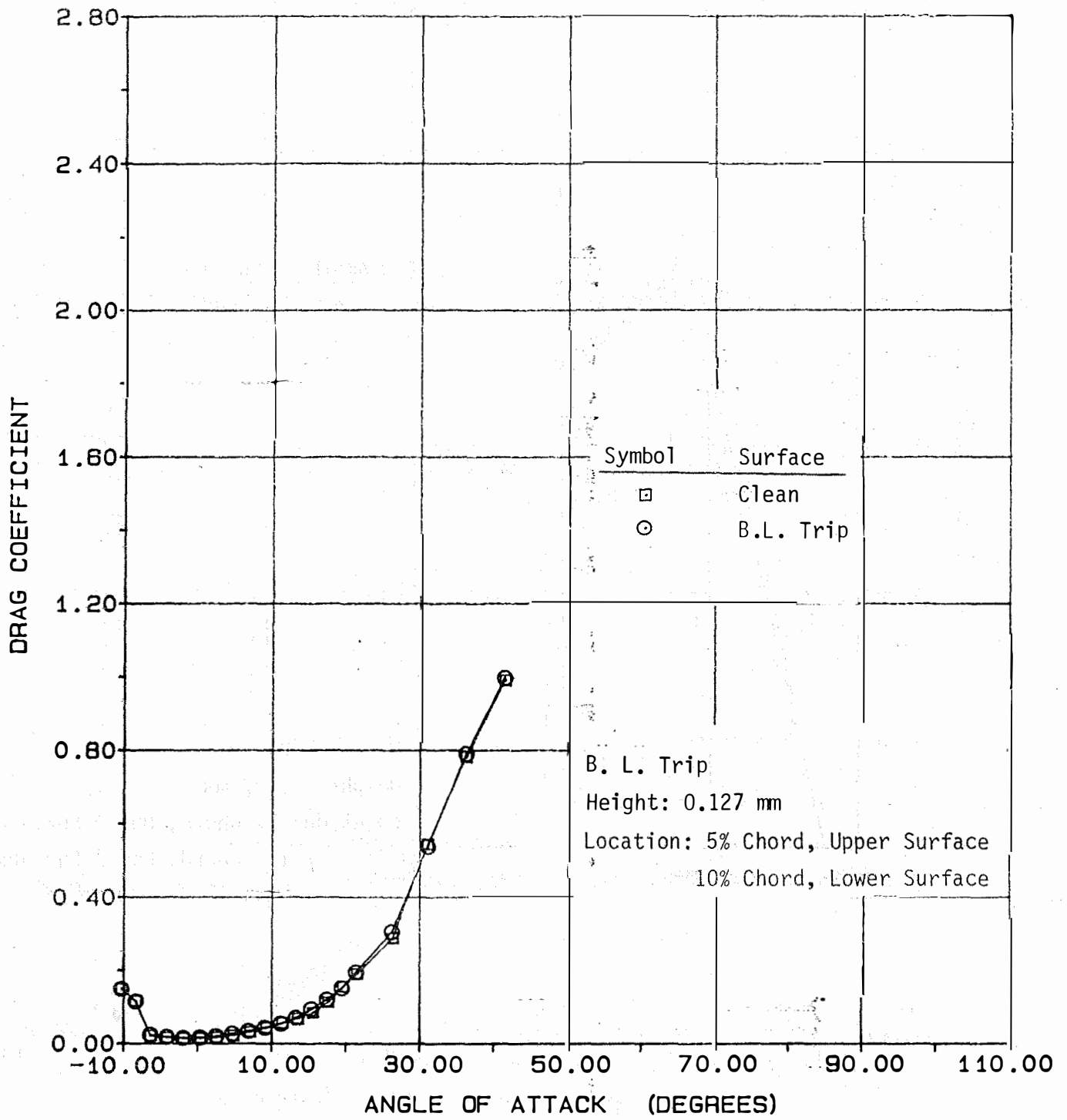
(b) Drag

Figure A.21- Concluded.



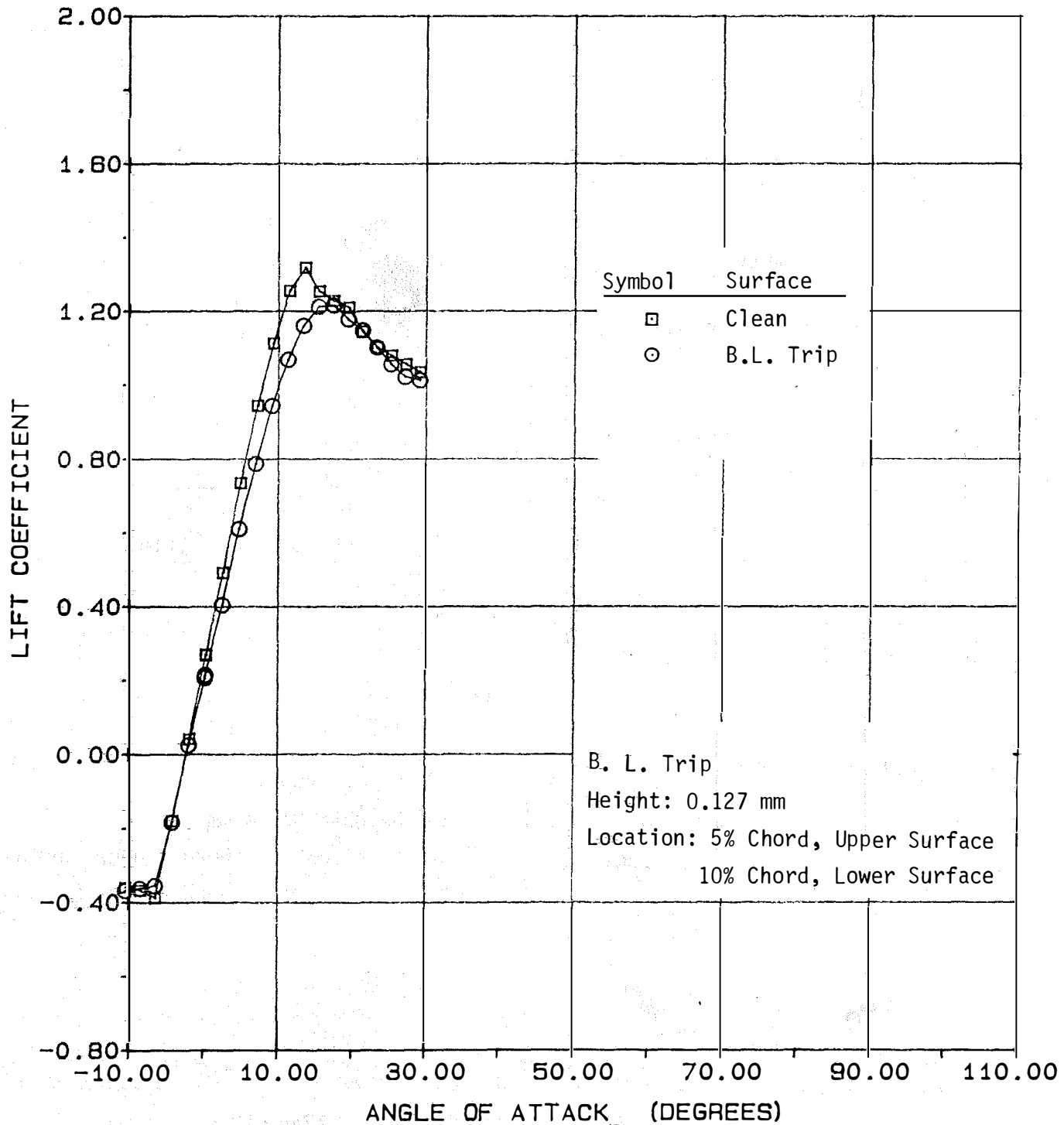
(a) Lift

Figure A.22- Effect of Boundary Layer Trip on Aerodynamic Coefficients of the NACA 4415 Airfoil, $AR = \infty$, $RN = 0.75 \times 10^6$.



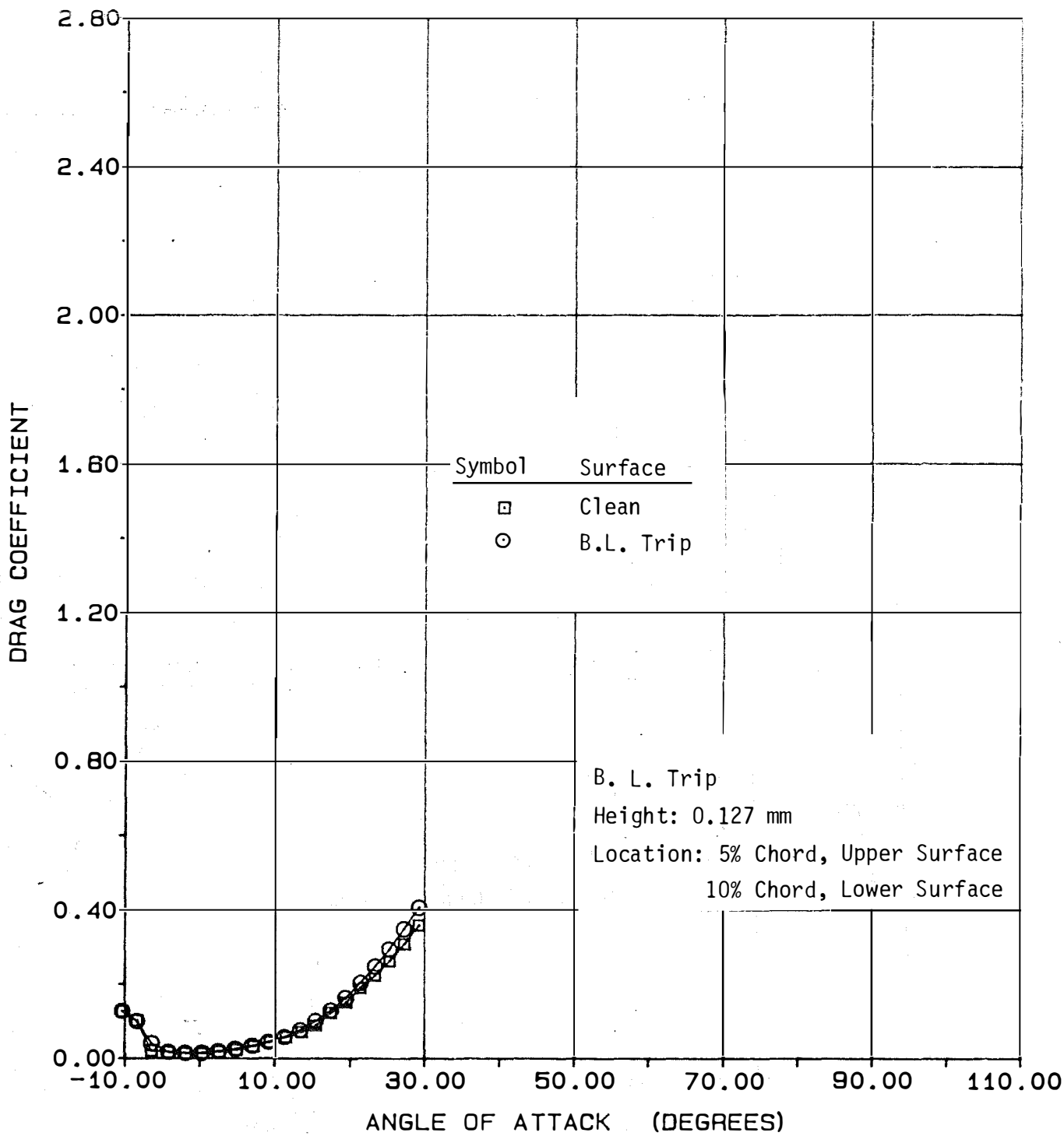
(b) Drag

Figure A.22- Concluded.



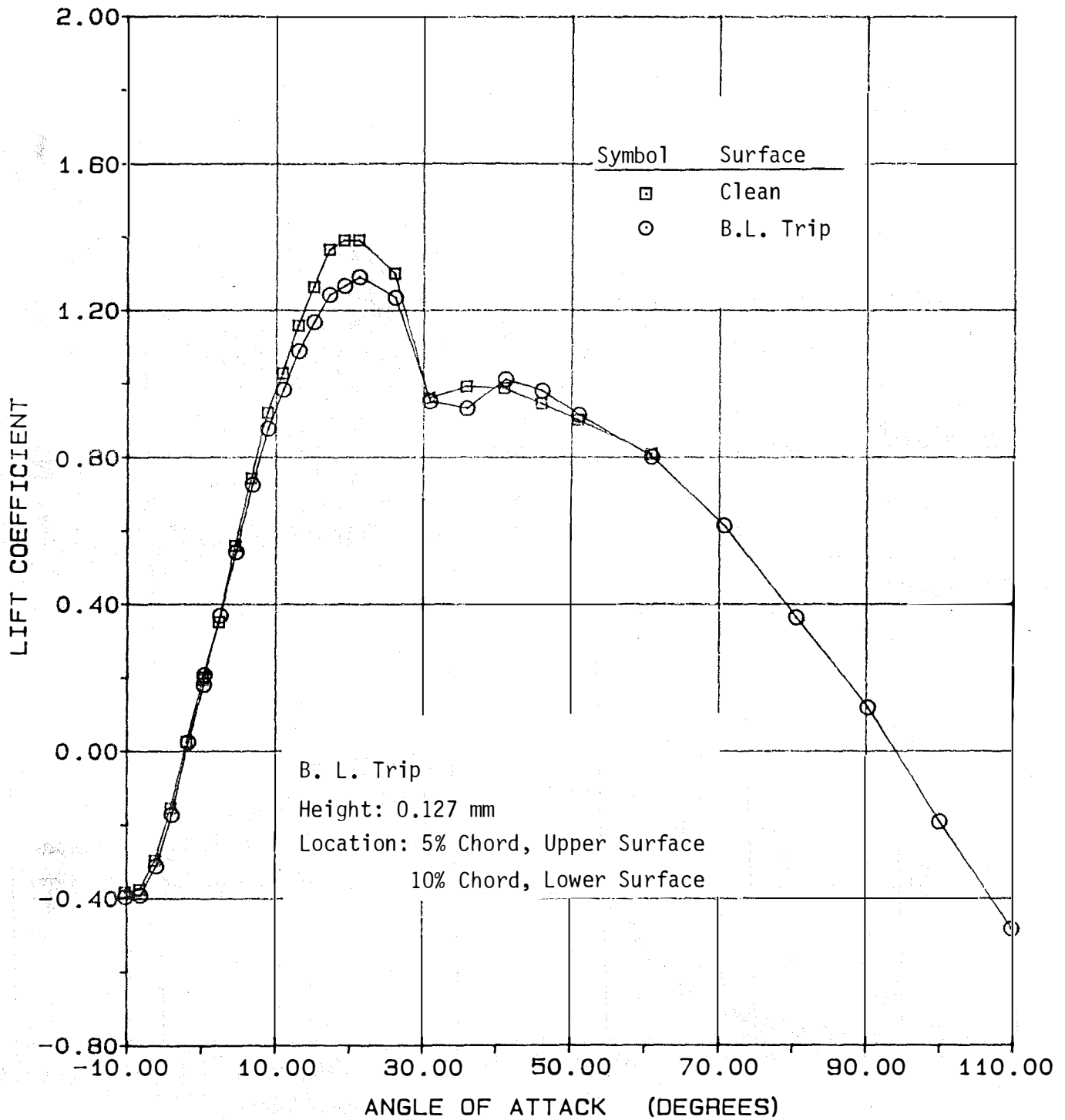
(a) Lift

Figure A.23- Effect of Boundary Layer Trip on Aerodynamic Coefficients of the NACA 4415 Airfoil, $AR = \infty$, $RN = 1.00 \times 10^6$.



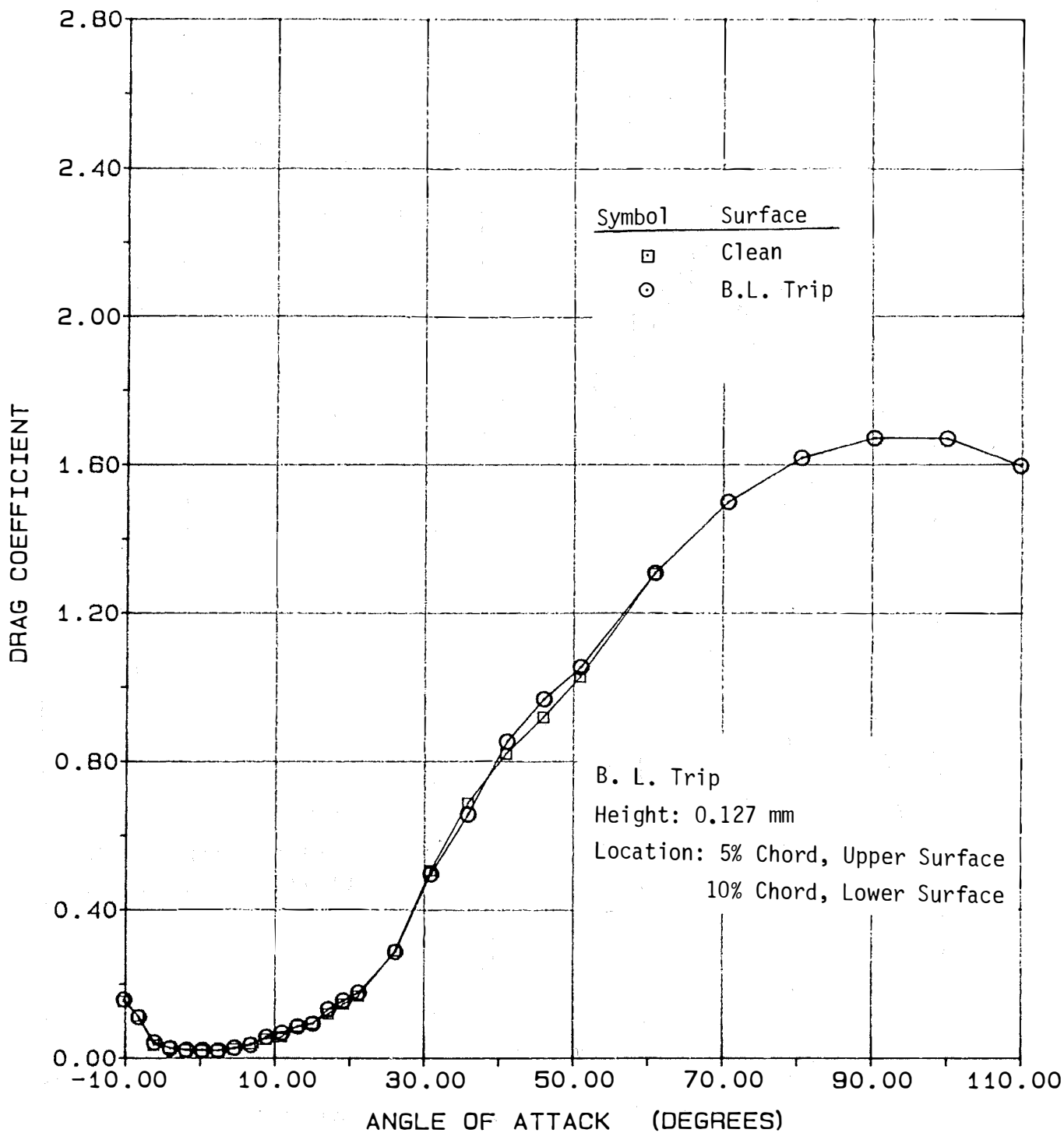
(b) Drag

Figure A.23- Concluded.



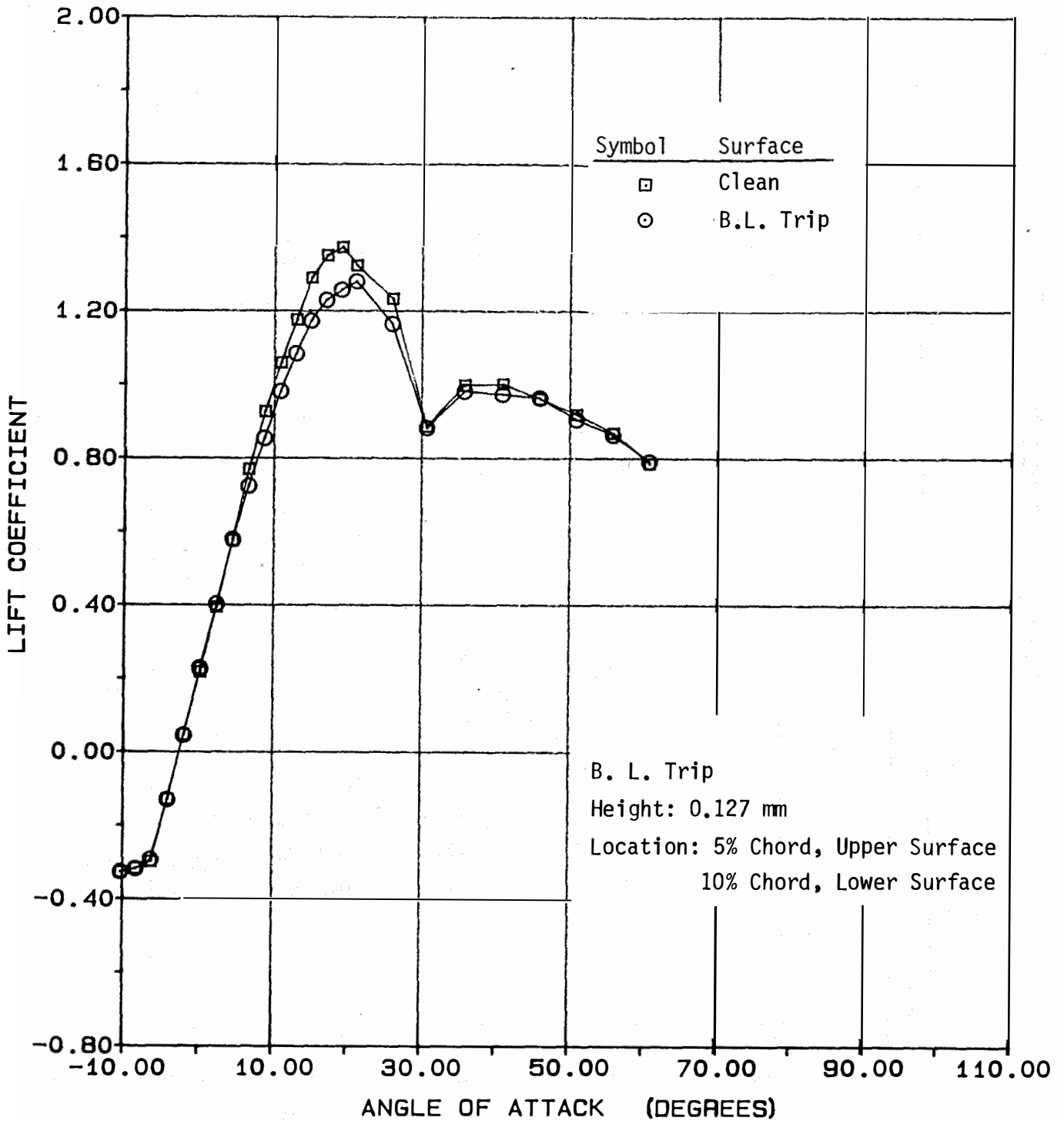
(a) Lift

Figure A.24- Effect of Boundary Layer Trip on Aerodynamic Coefficients of the NACA 4415 Airfoil, AR = 12, RN = 0.25 x 10⁶.



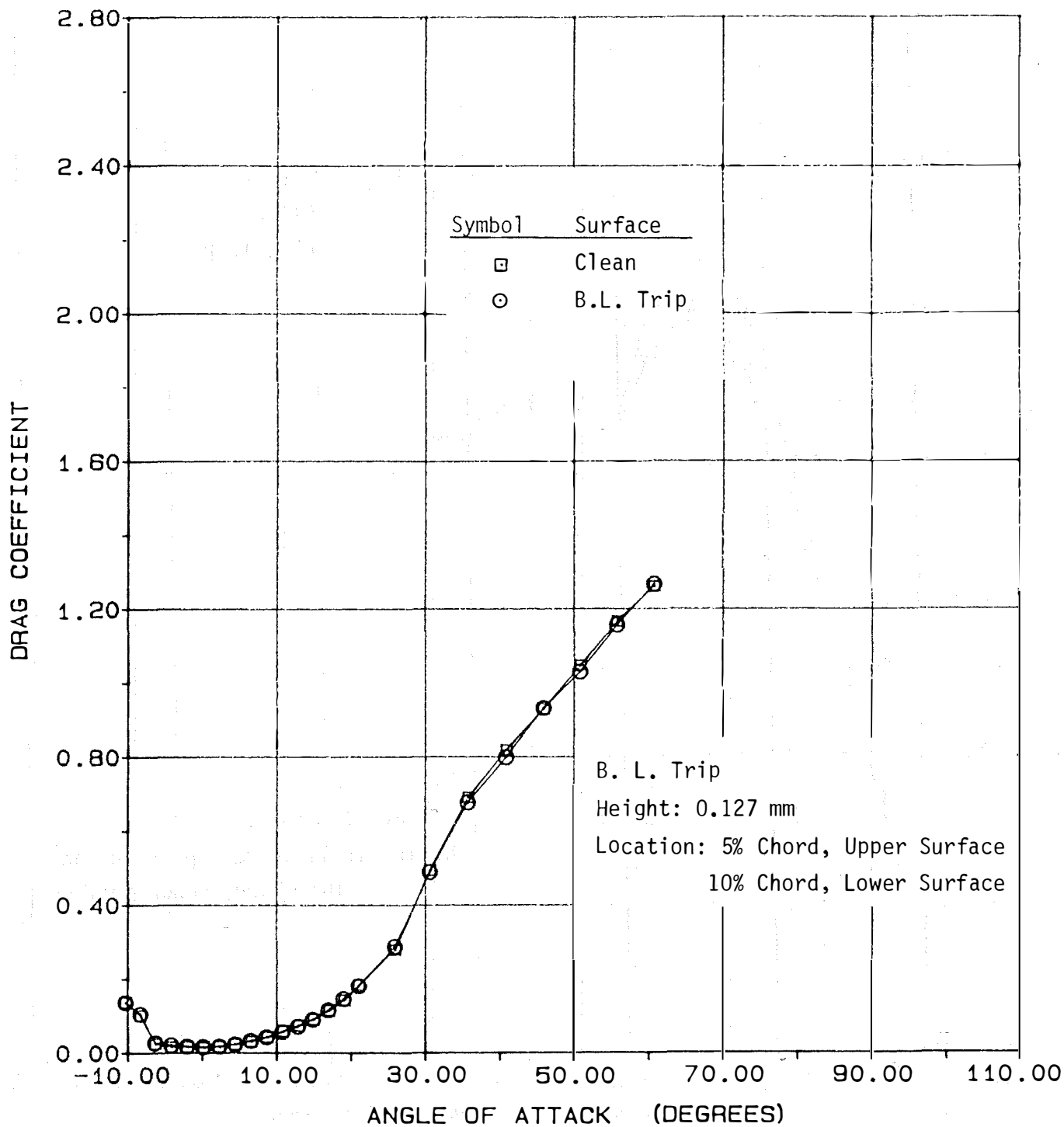
(b) Drag

Figure A.24- Concluded.



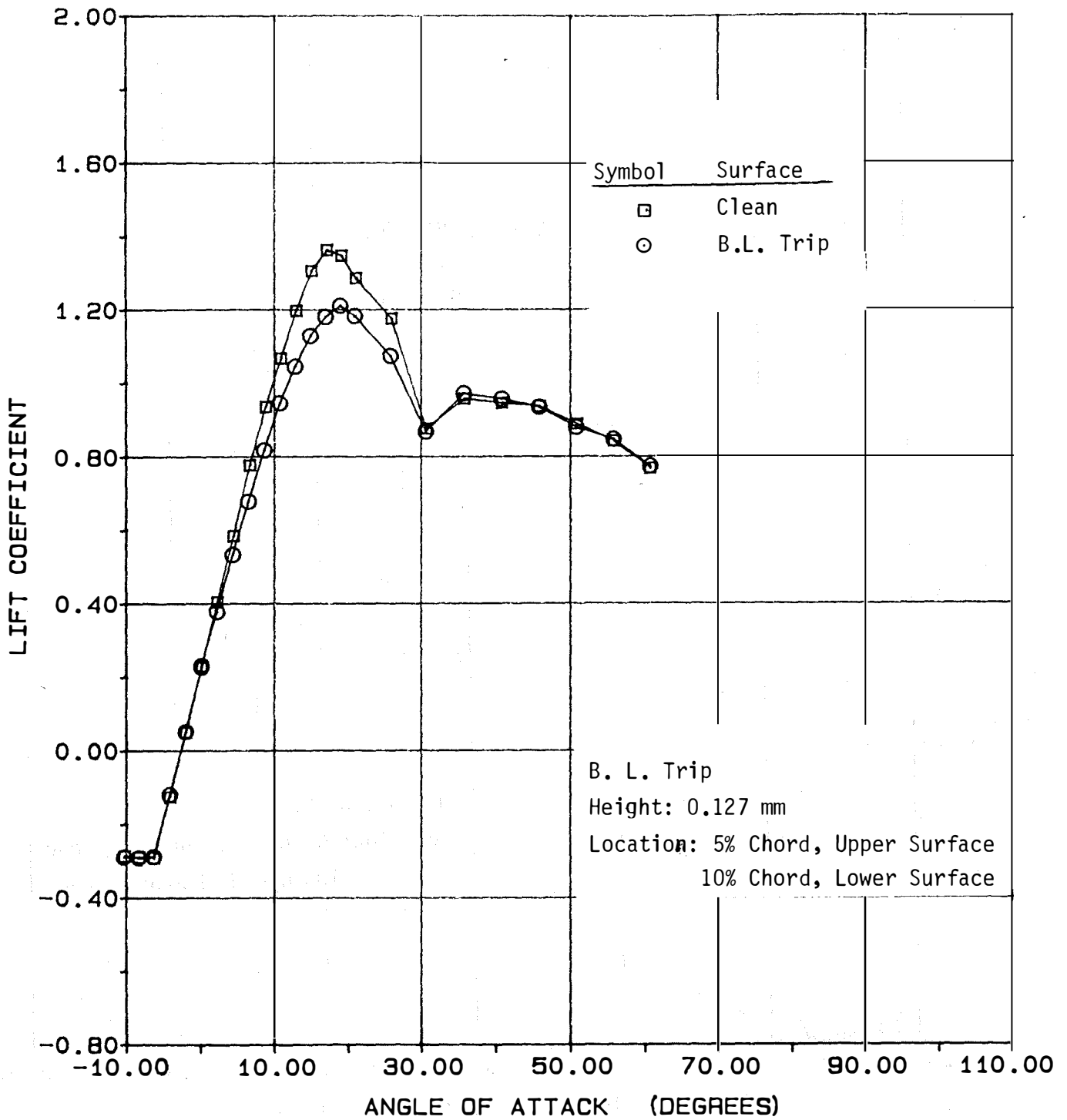
(a) Lift

Figure A.25- Effect of Boundary Layer Trip on Aerodynamic Coefficients of the NACA 4415 Airfoil, AR = 12, RN = 0.50×10^6 .



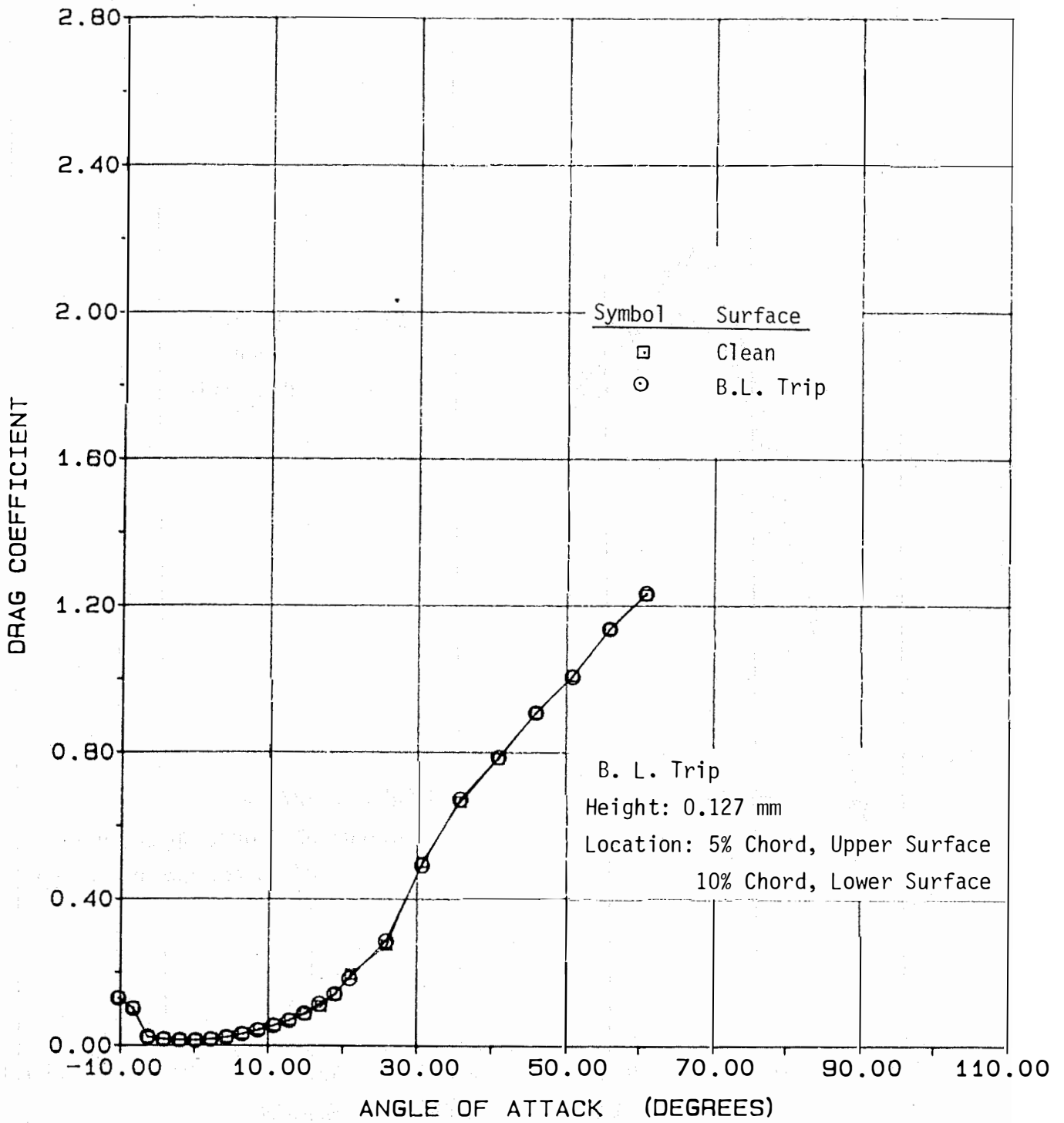
(b) Drag

Figure A.25- Concluded.



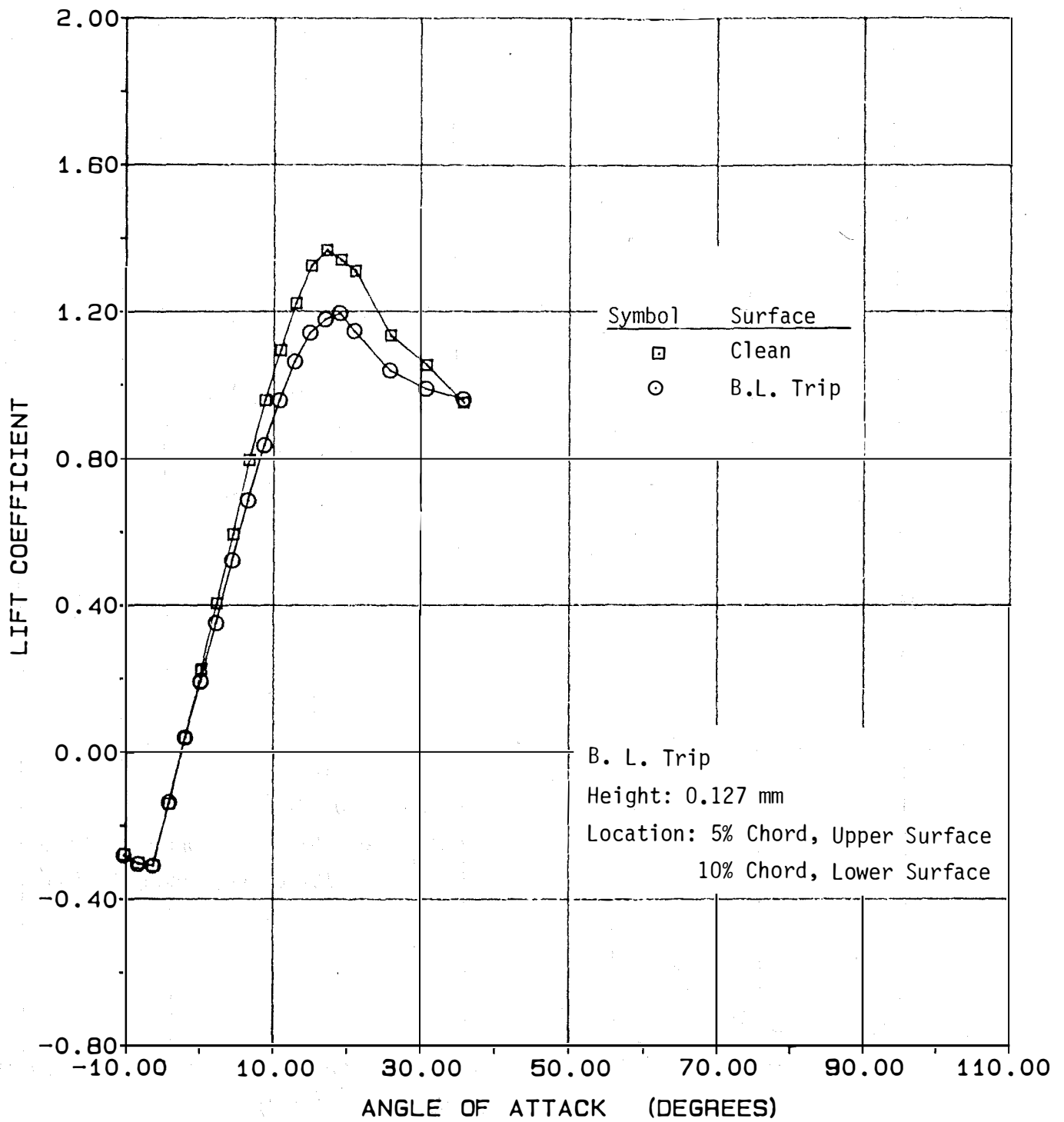
(a) Lift

Figure A.26- Effect of Boundary Layer Trip on Aerodynamic Coefficients of the NACA 4415 Airfoil, AR = 12, RN = 0.75×10^6 .



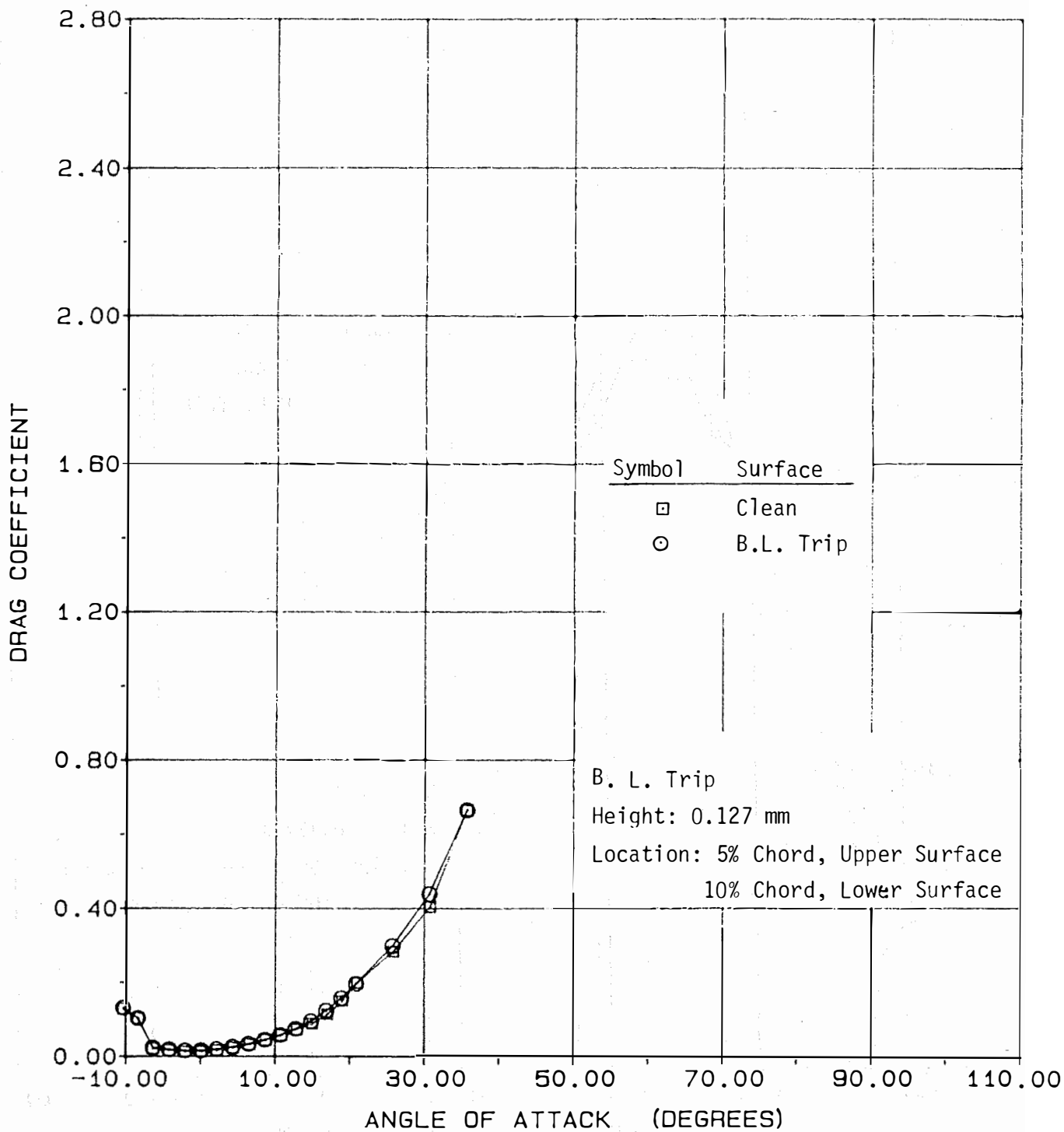
(b) Drag

Figure A.26- Concluded.



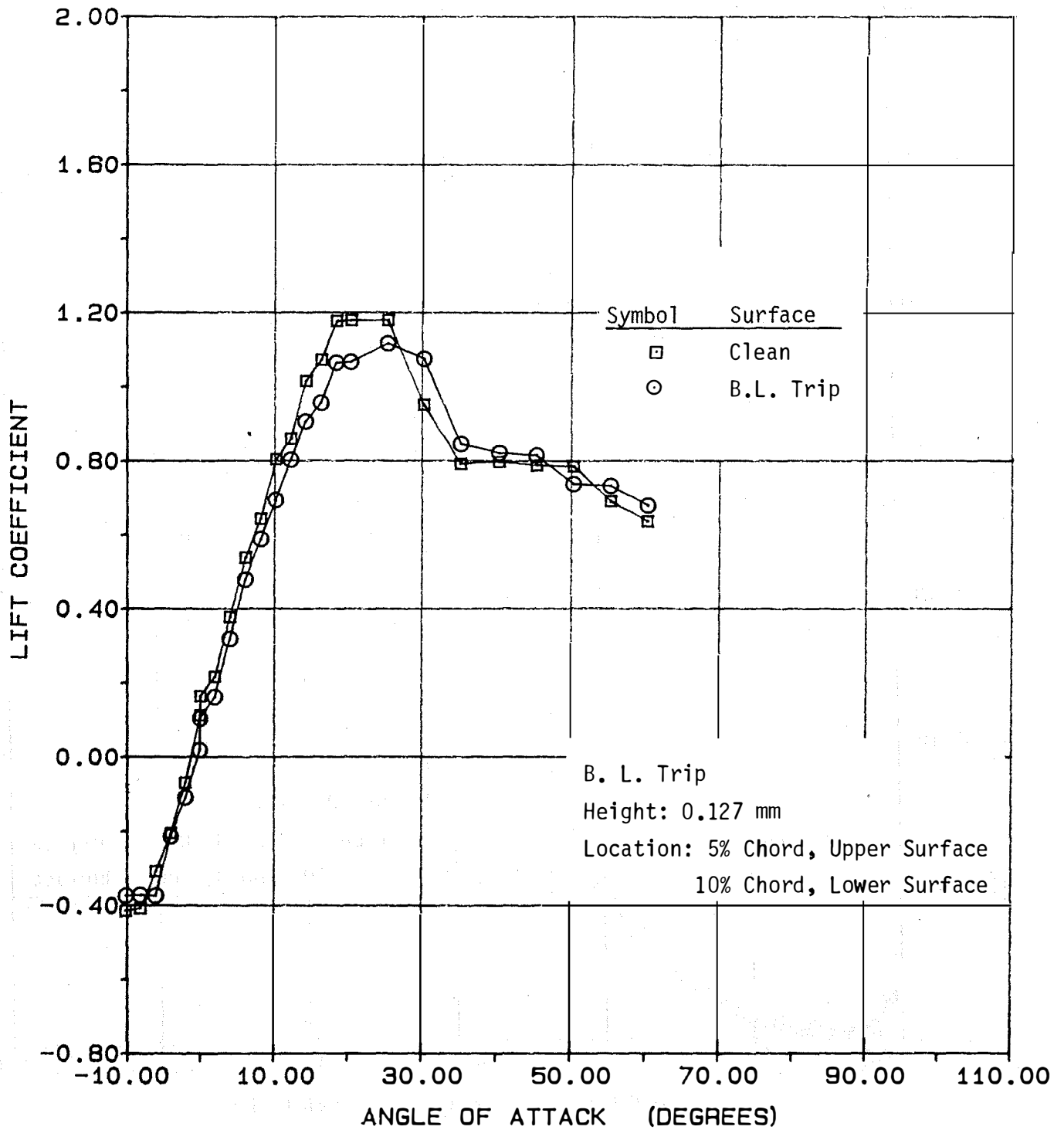
(a) Lift

Figure A.27- Effect of Boundary Layer Trip on Aerodynamic Coefficients of the NACA 4415 Airfoil, AR = 12, RN = 1.00×10^6 .



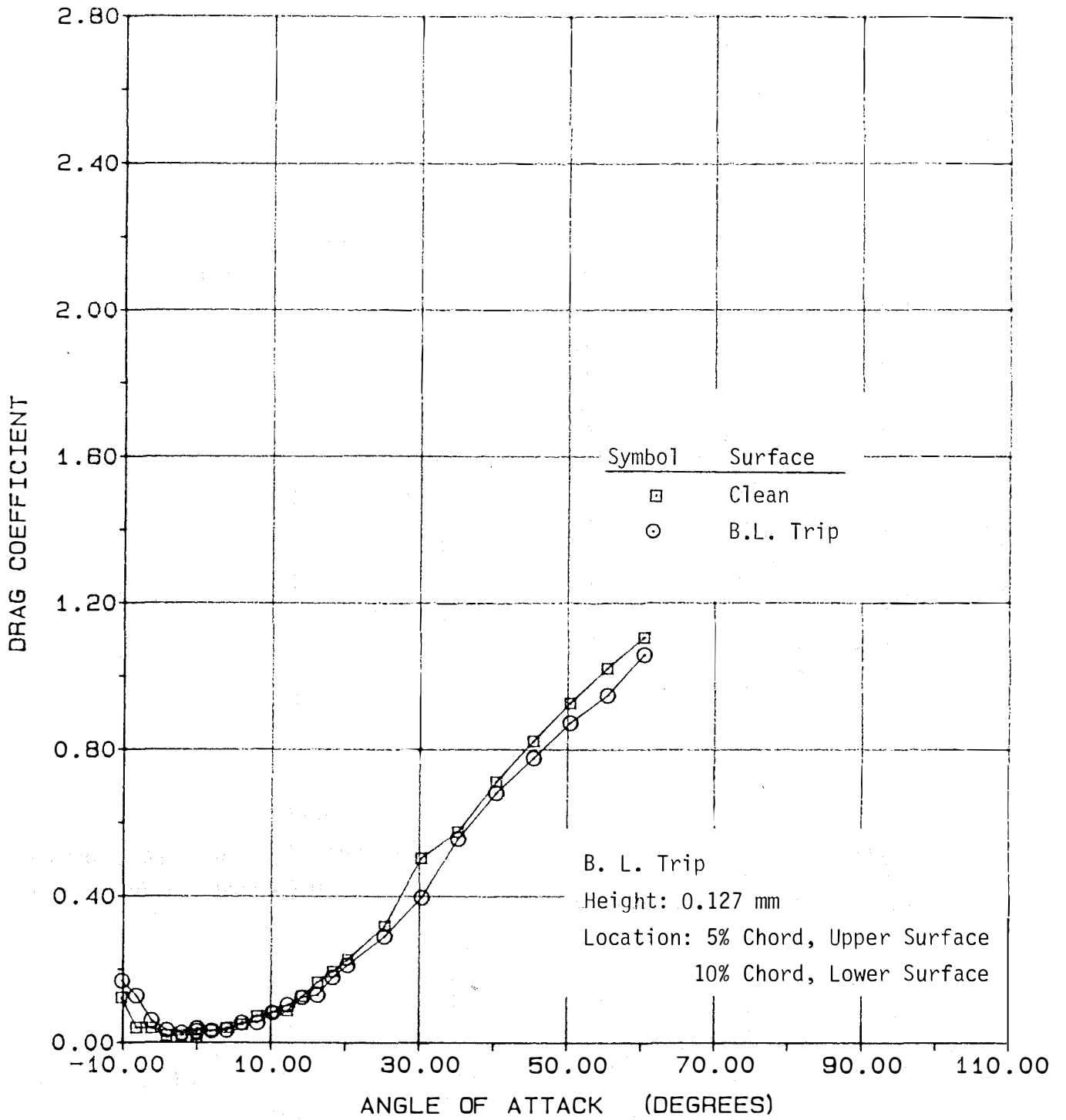
(b) Drag

Figure A.27- Concluded.



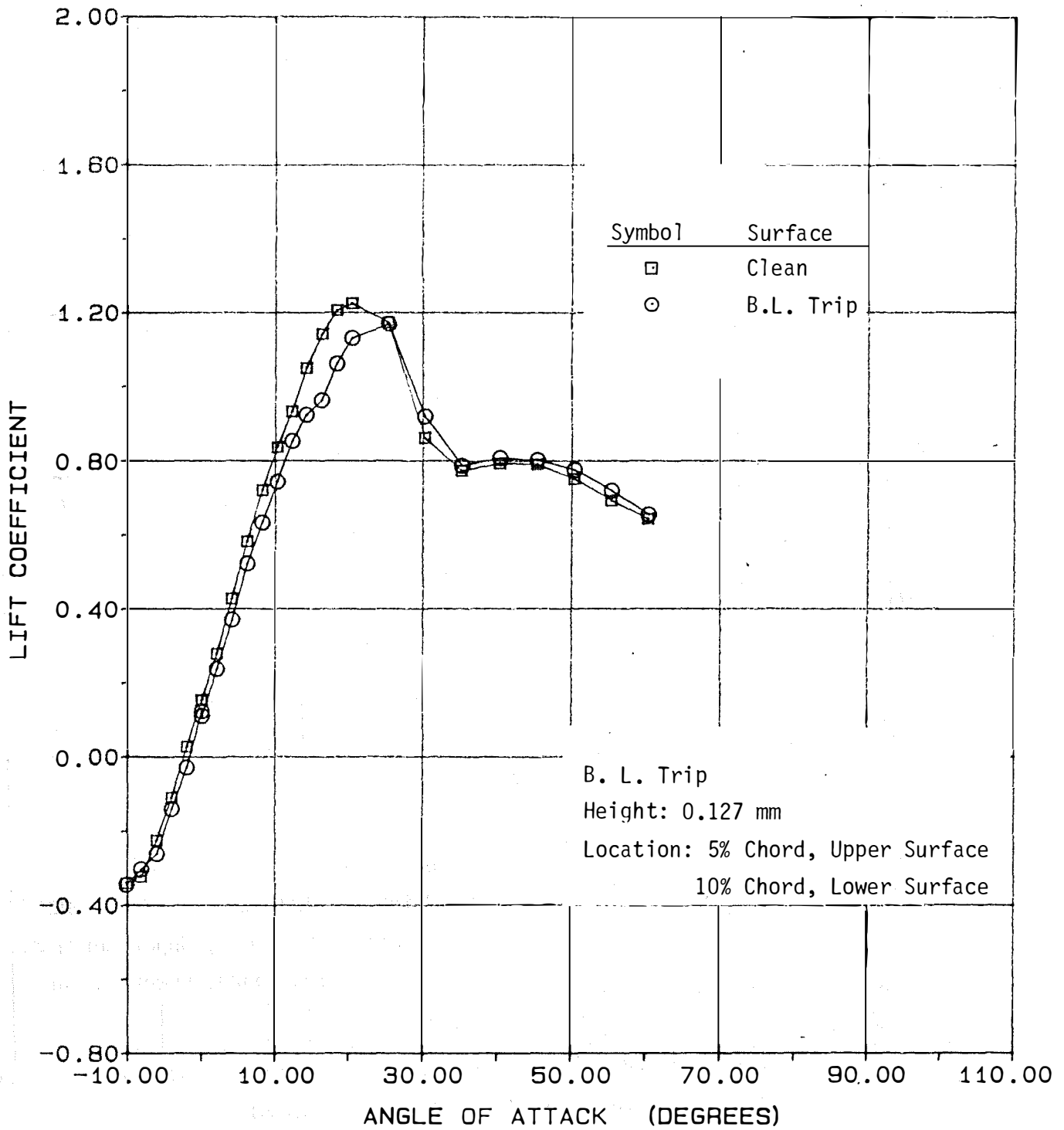
(a) Lift

Figure A.28- Effect of Boundary Layer Trip on Aerodynamic Coefficients of the NACA 4415 Airfoil, AR = 6, RN = 0.25×10^6 .



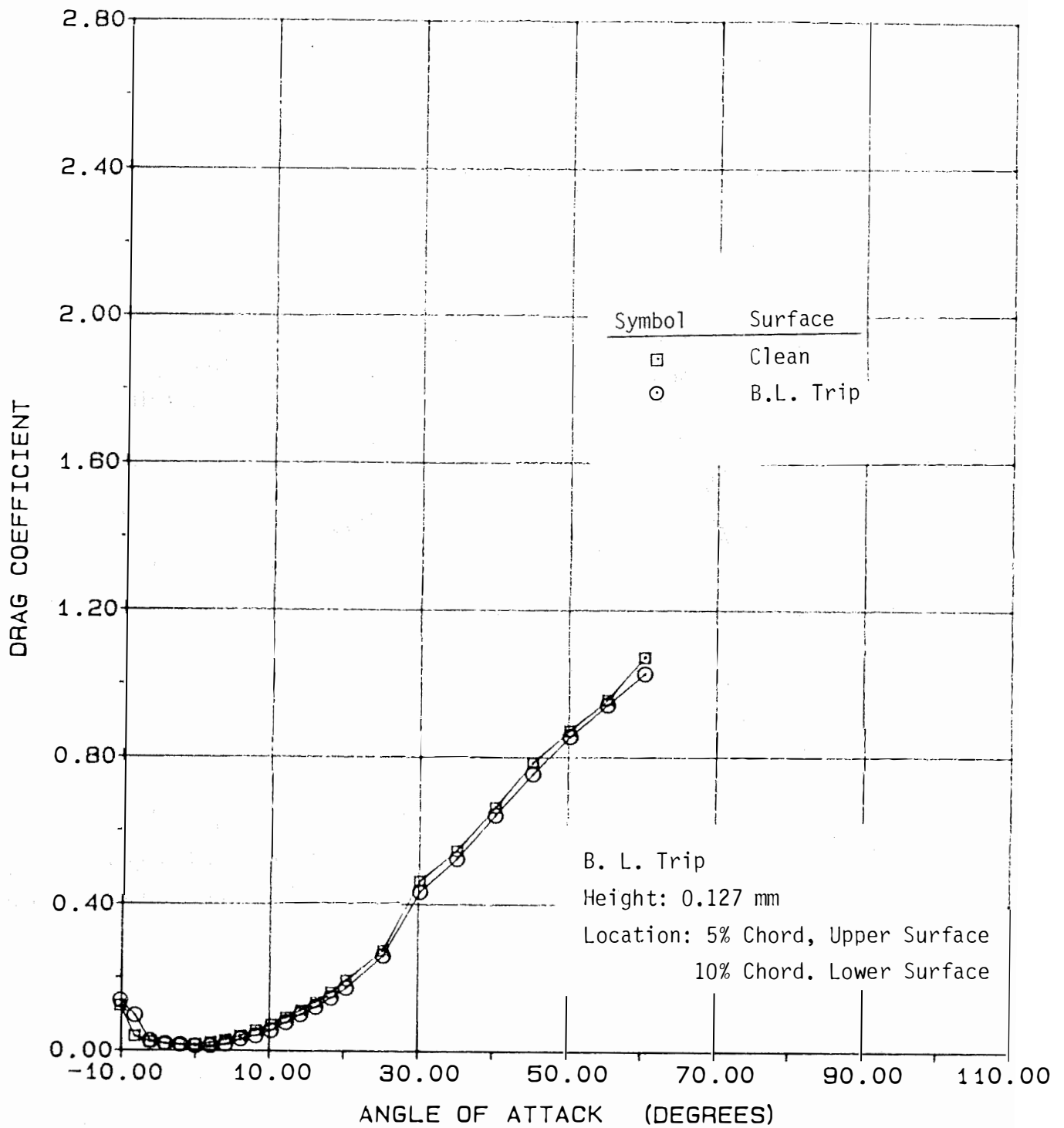
(b) Drag

Figure A.28- Concluded.



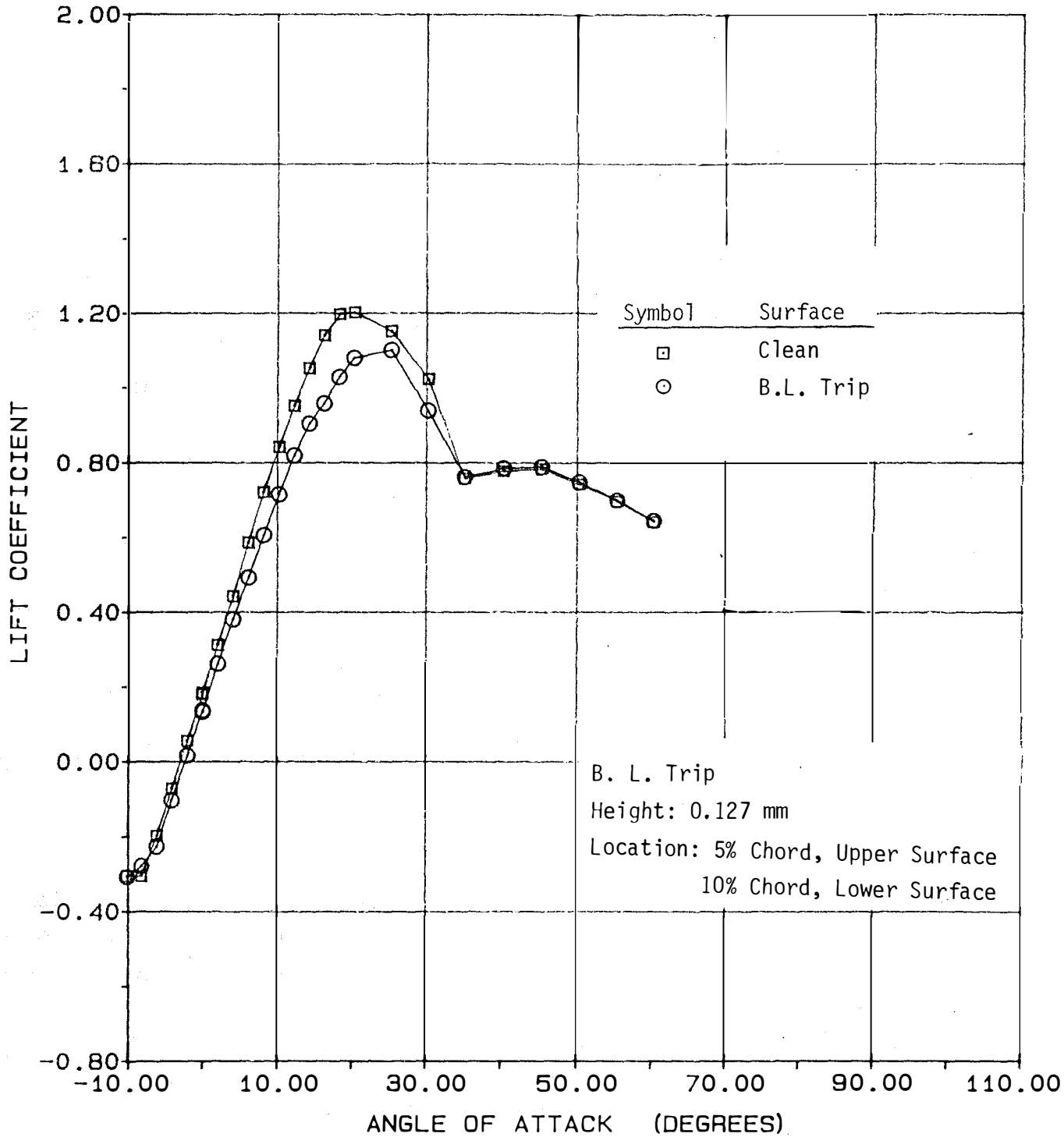
(a) Lift

Figure A.29- Effect of Boundary Layer Trip on Aerodynamic Coefficients of the NACA 4415 Airfoil, AR = 6, RN = 0.50×10^6 .



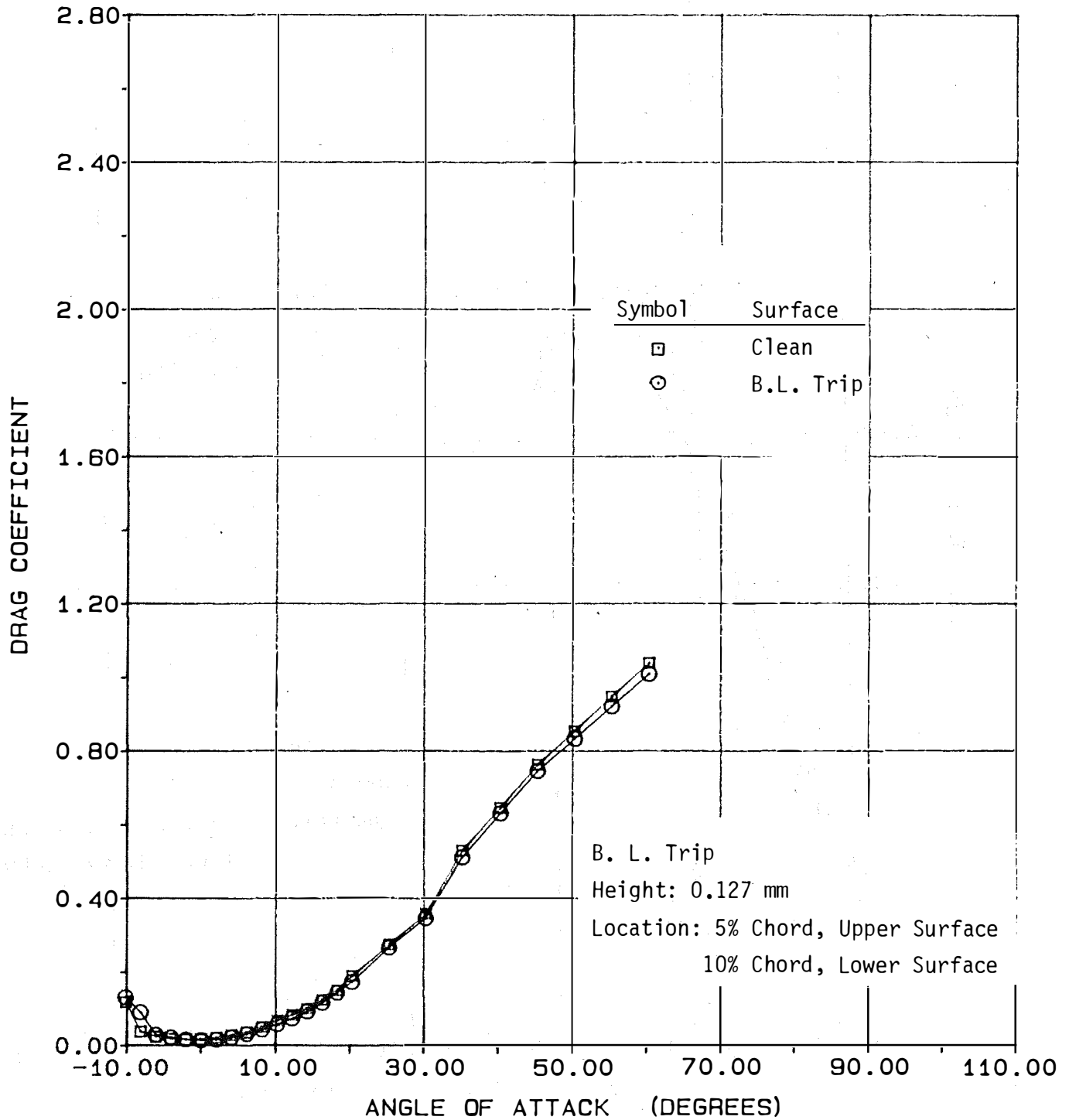
(b) Drag

Figure A.29- Concluded.

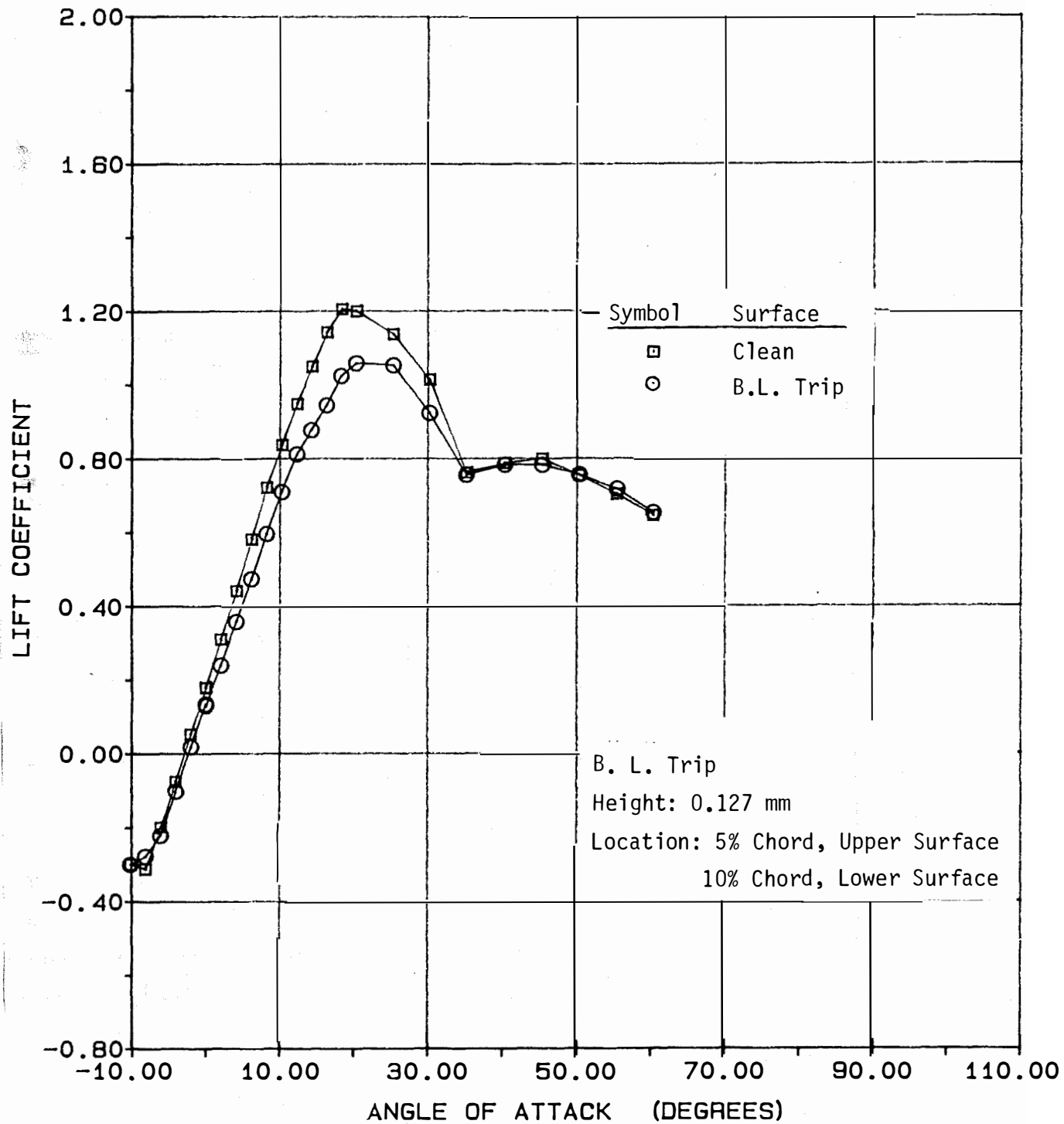


(a) Lift

Figure A.30- Effect of Boundary Layer Trip on Aerodynamic Coefficients of the NACA 4415 Airfoil, AR = 6, RN = 0.75×10^6 .

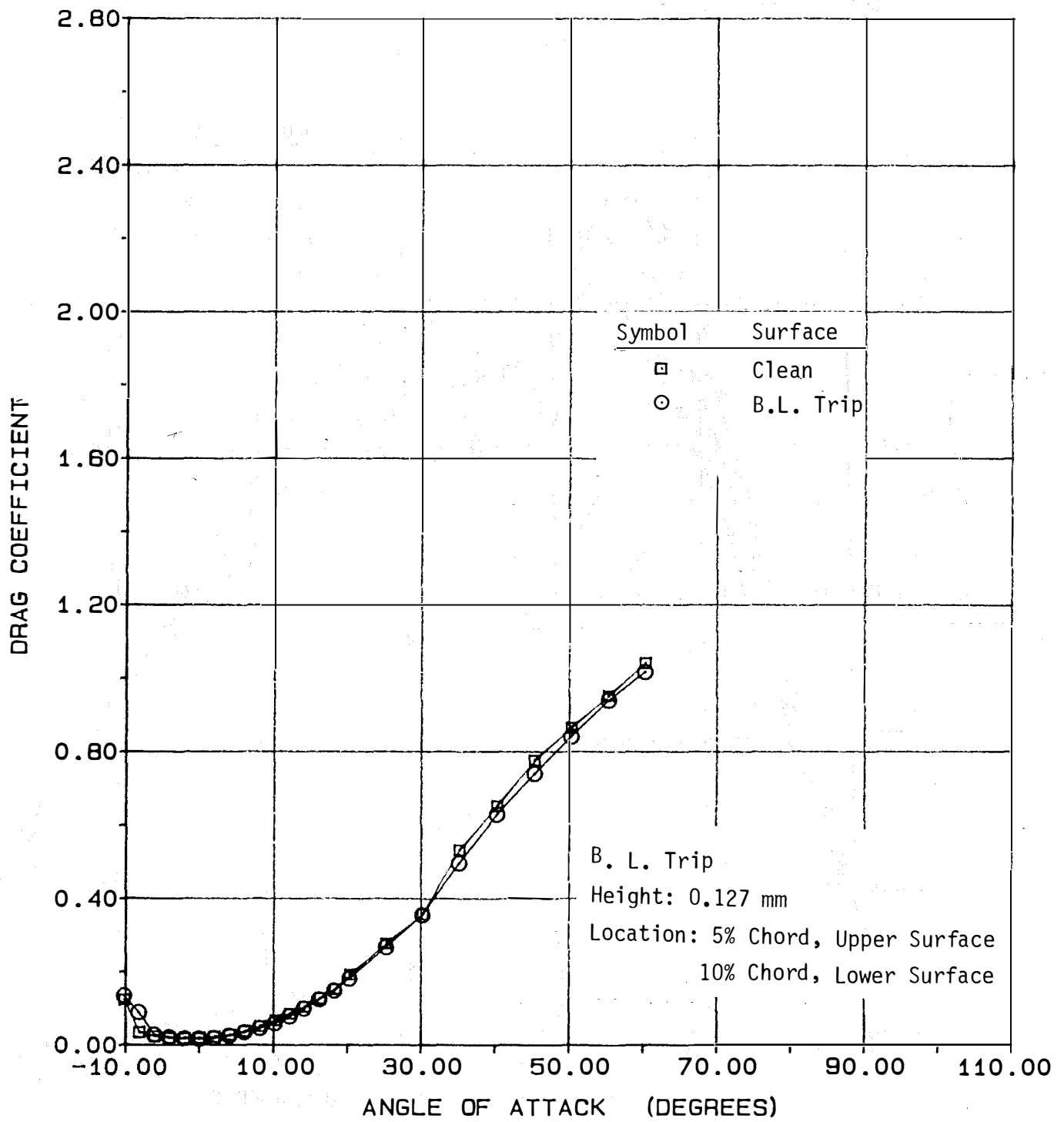


(b) Drag



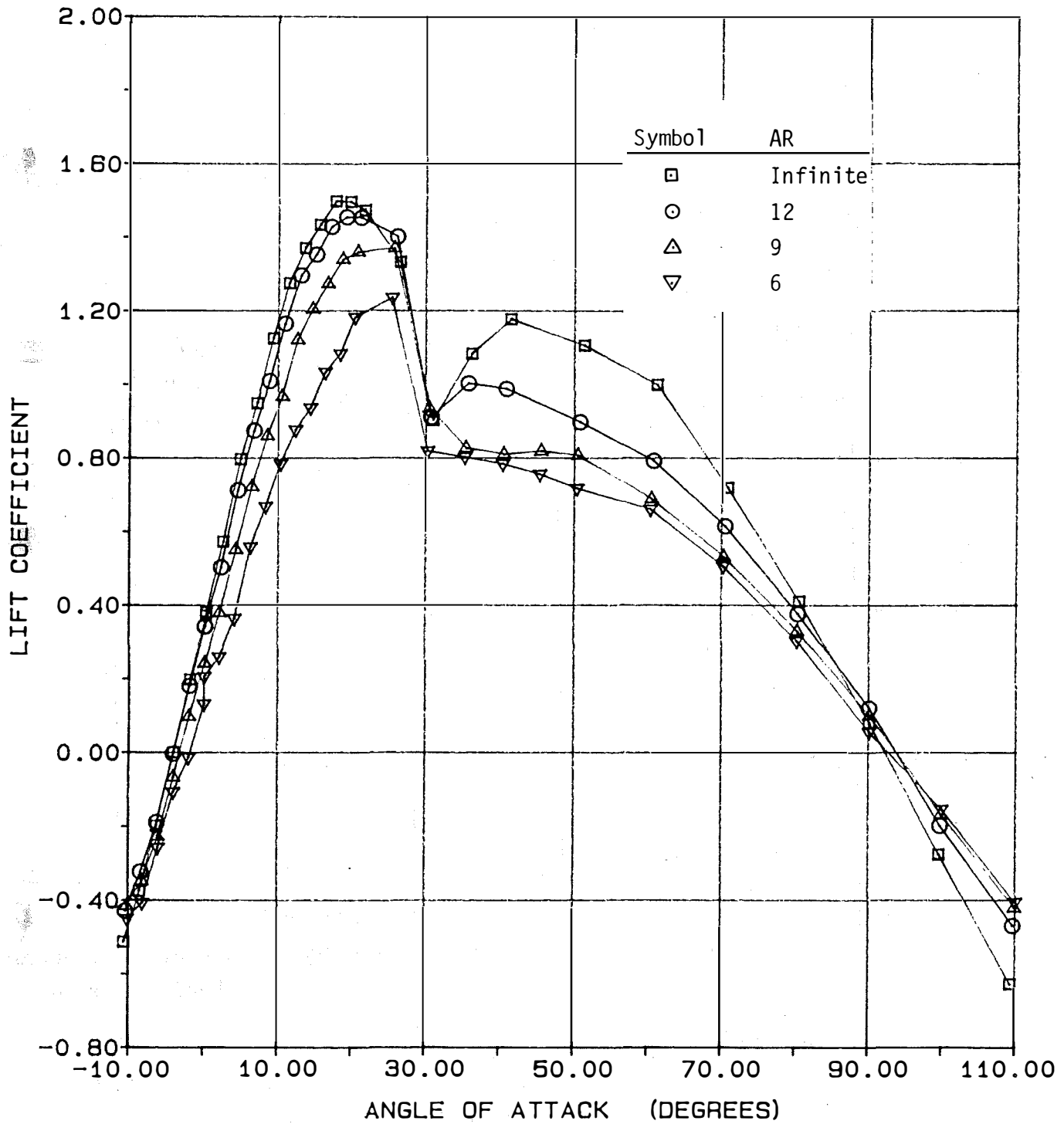
(a) Lift

Figure A.31- Effect of Boundary Layer Trip on Aerodynamic Coefficients of the NACA 4415 Airfoil, AR = 6, RN = 1.00 x 10⁶.



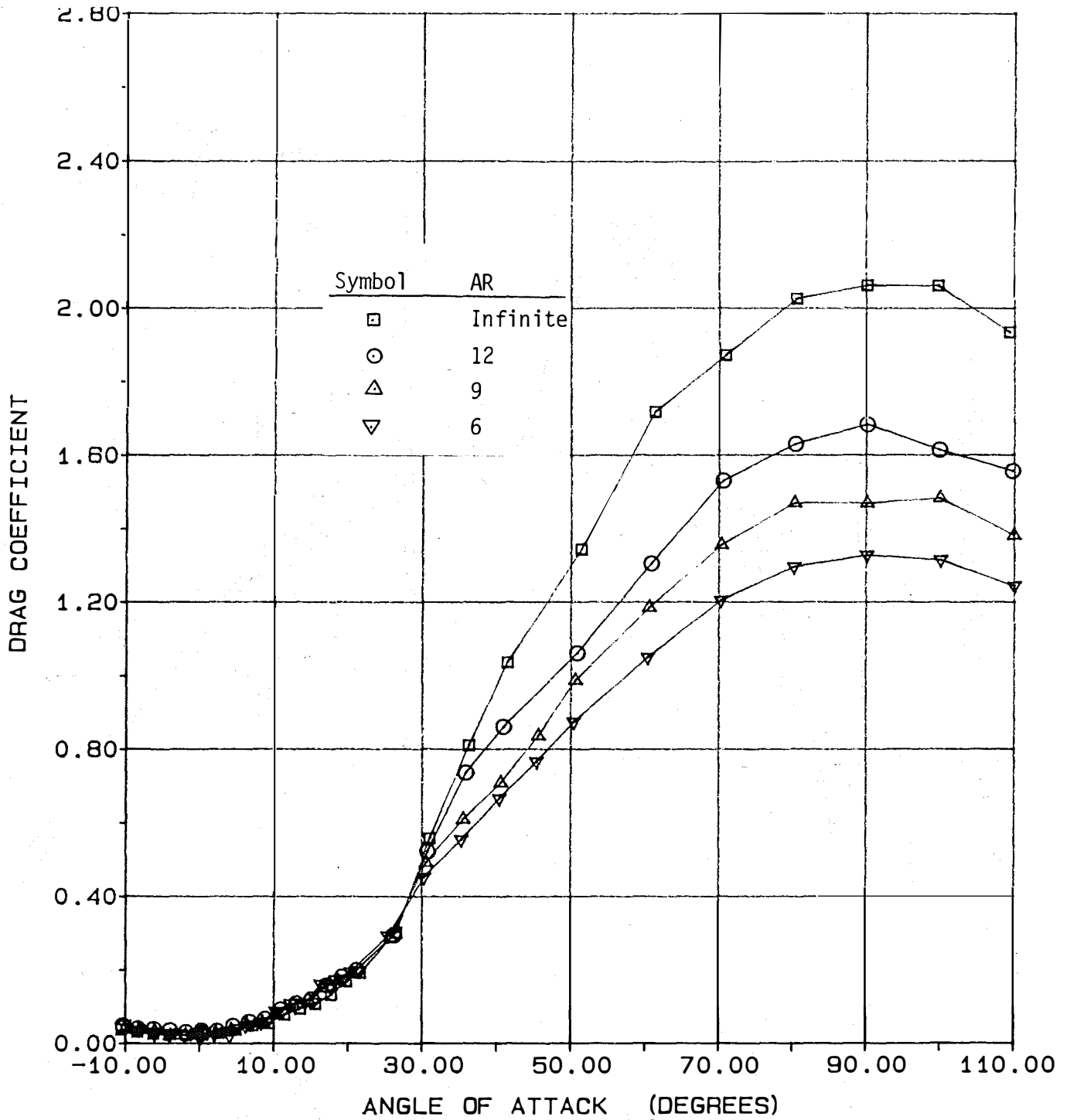
(b) Drag

Figure A.31- Concluded.



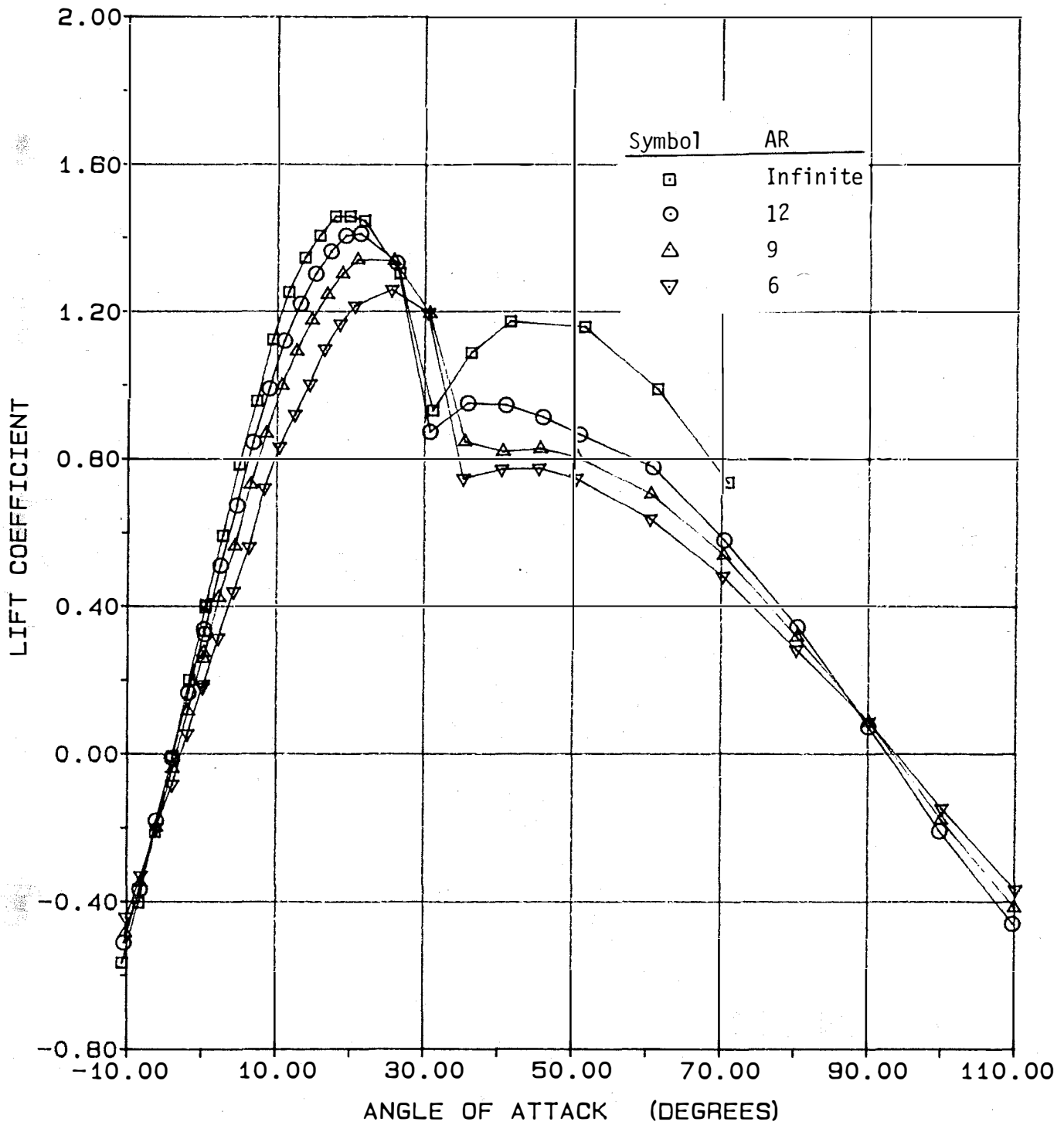
(a) Lift

Figure A.32- Effect of Aspect Ratio on Aerodynamic Coefficients of the NACA 4418 Airfoil at $RN = 0.25 \times 10^6$.



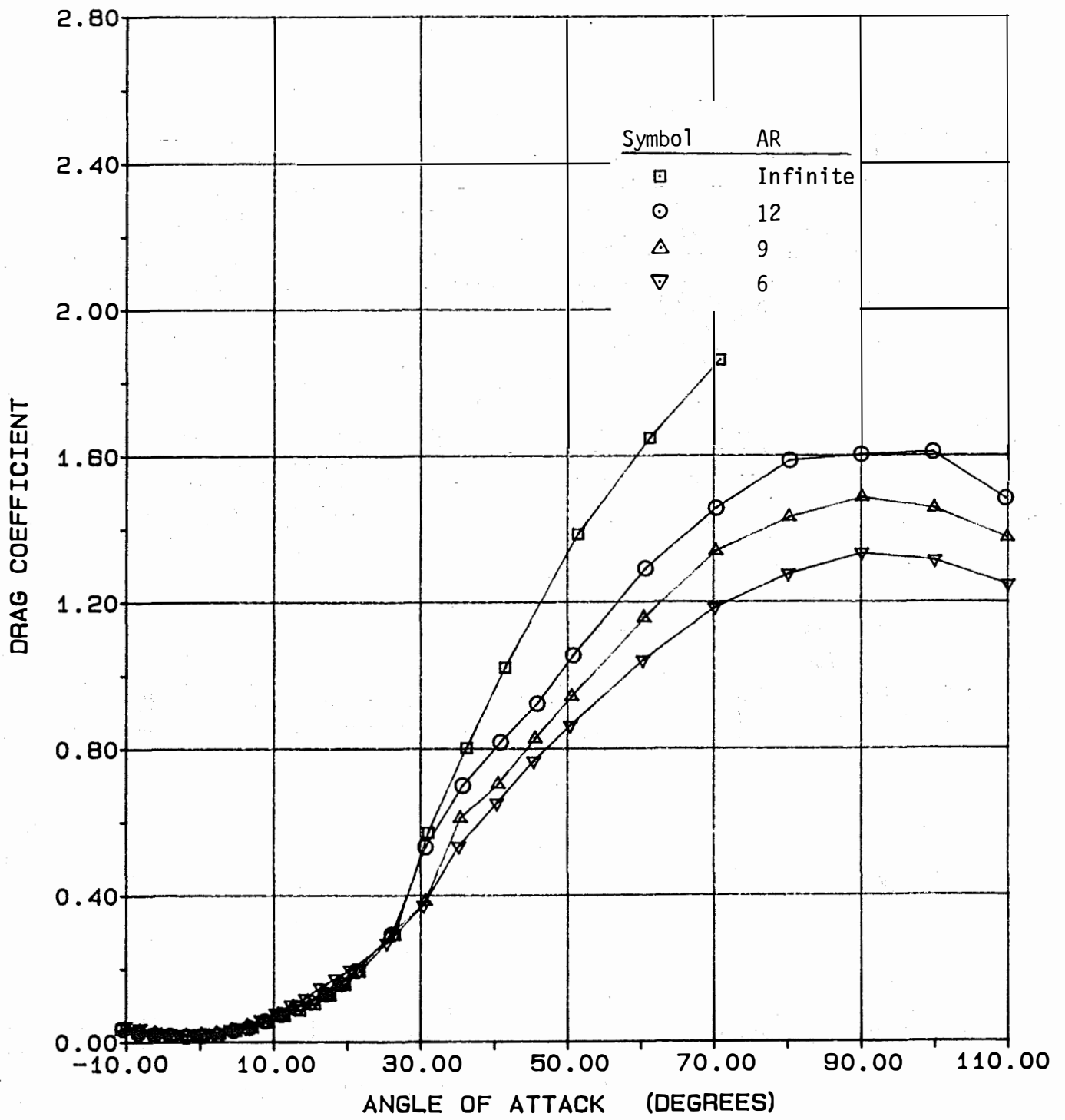
(b) Drag

Figure A.32- Concluded.



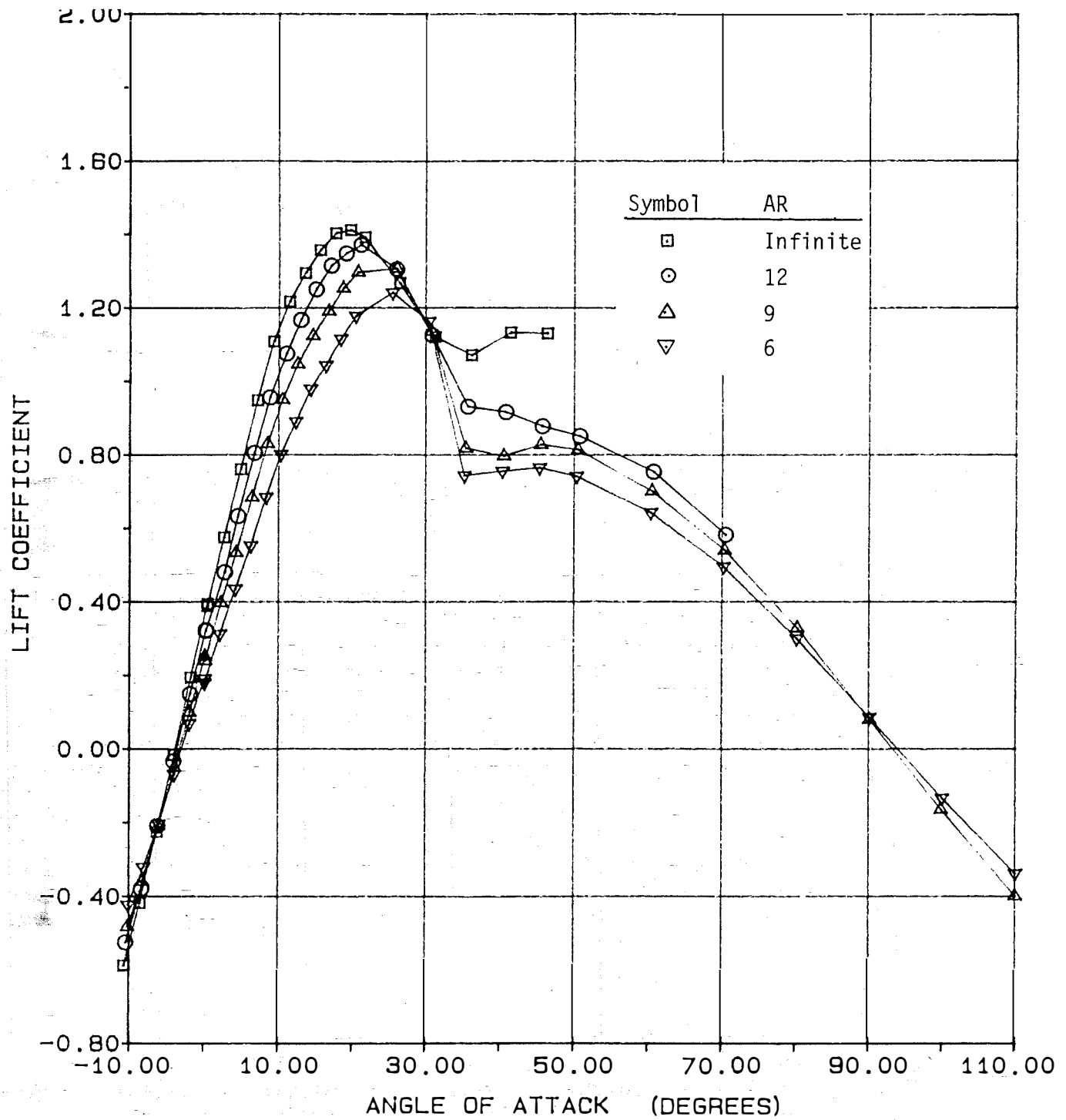
(a) Lift

Figure A.33- Effect of Aspect Ratio on Aerodynamic Coefficients of the NACA 4418 Airfoil at $RN = 0.50 \times 10^6$.



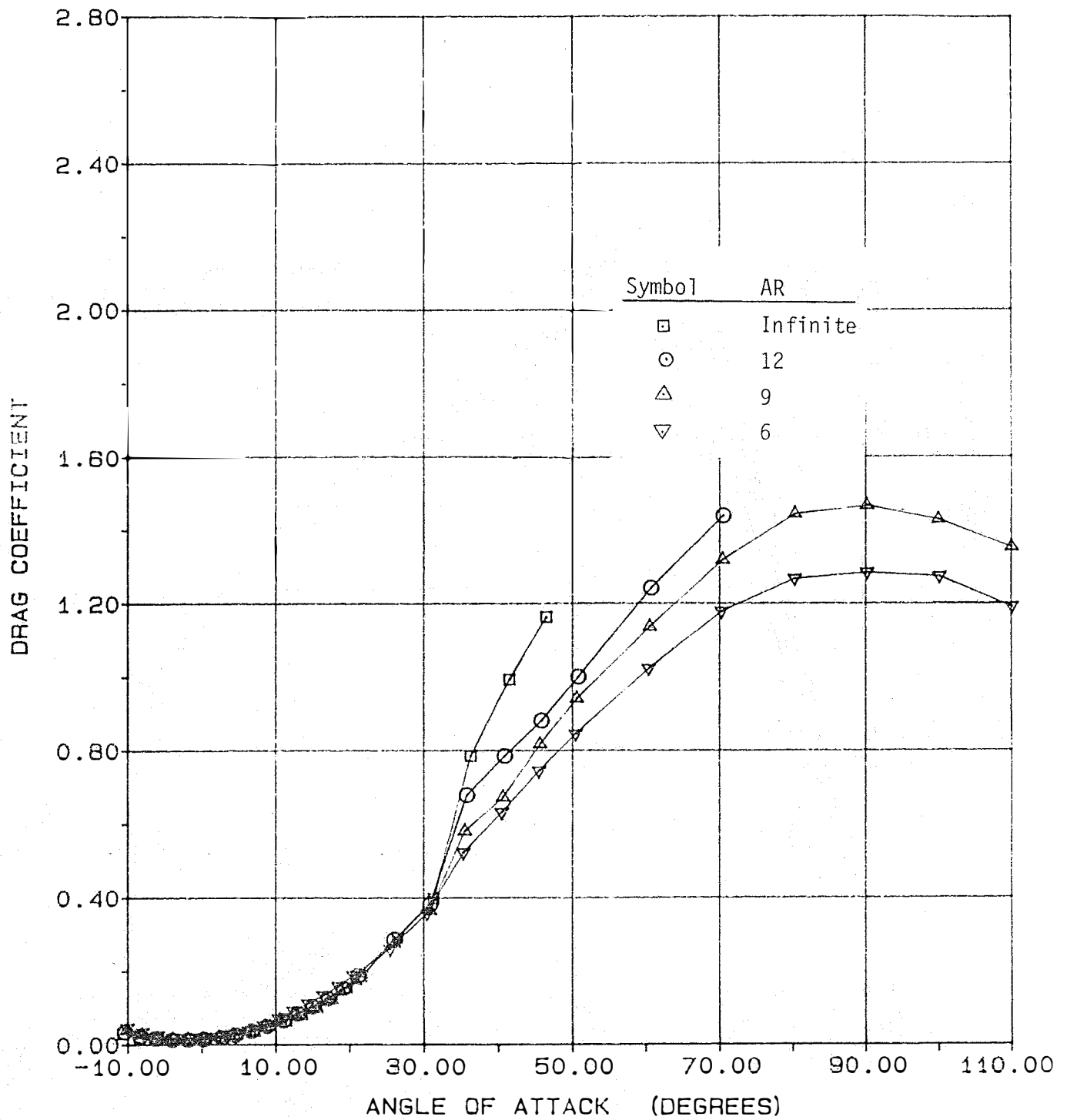
(b) Drag

Figure A.33- Concluded.



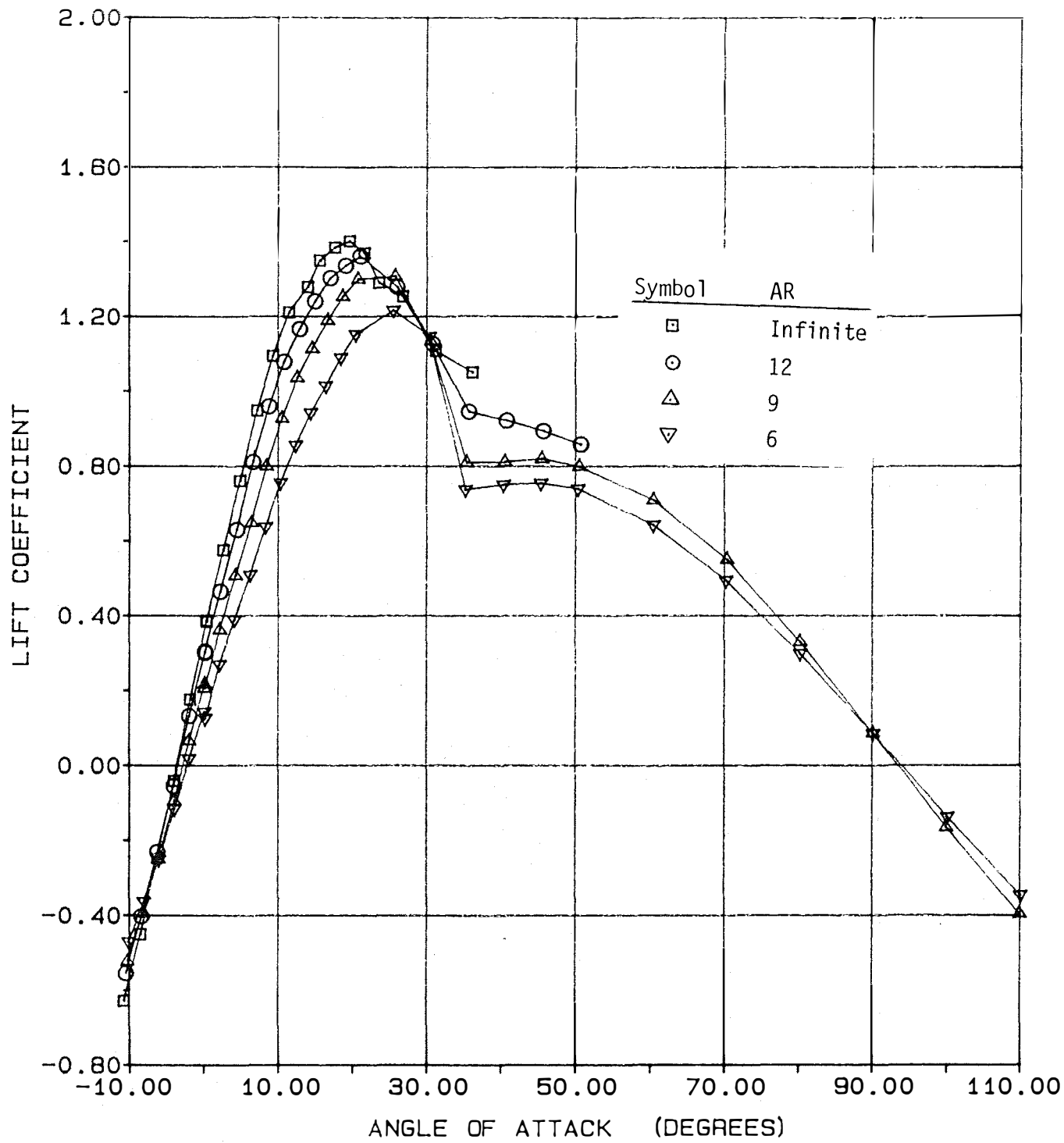
(a) Lift

Figure A.34- Effect of Aspect Ratio on Aerodynamic Coefficients of the NACA 4418 Airfoil at $RN = 0.75 \times 10^6$.



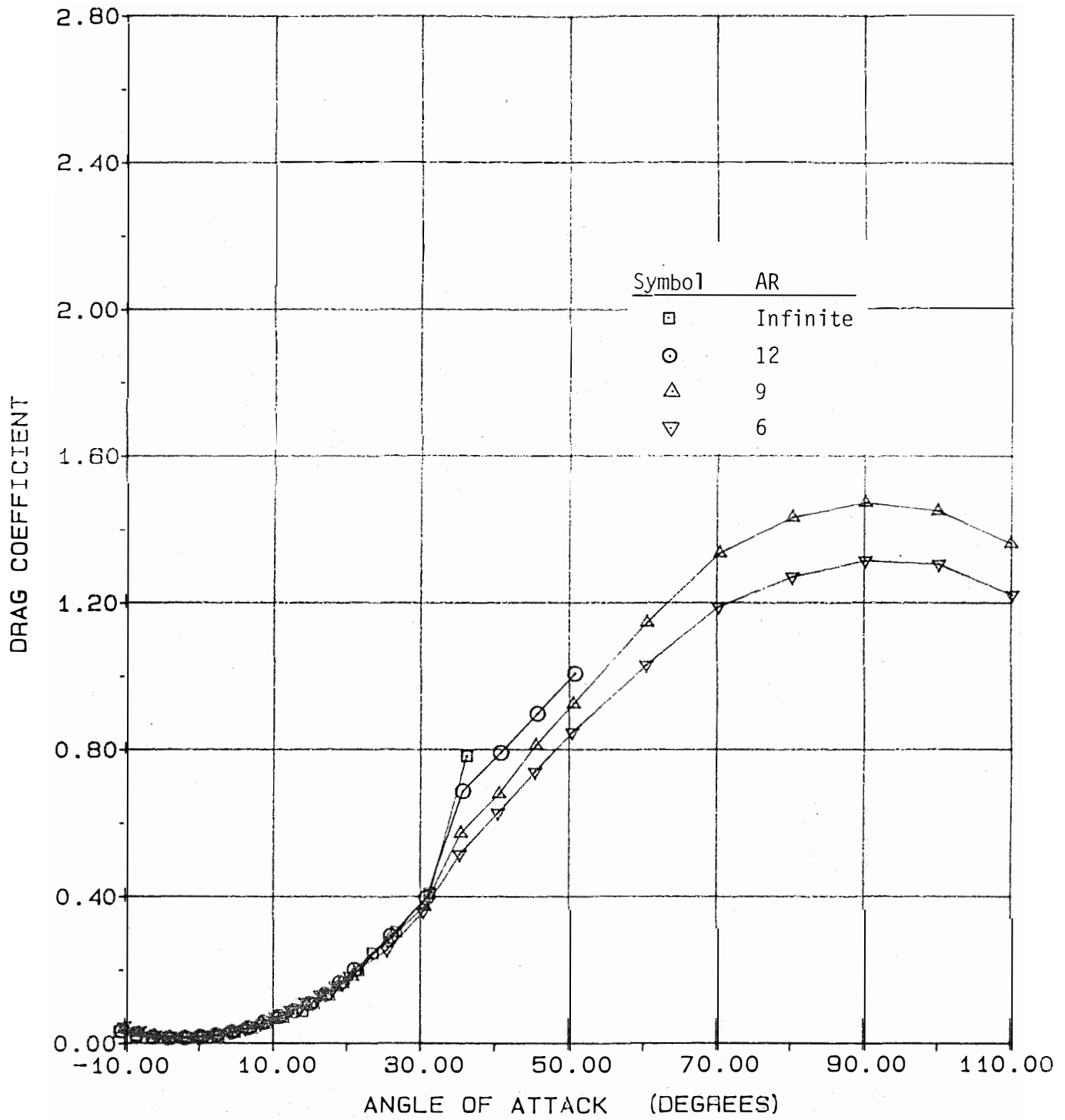
(b) Drag

Figure A.34 - Concluded.



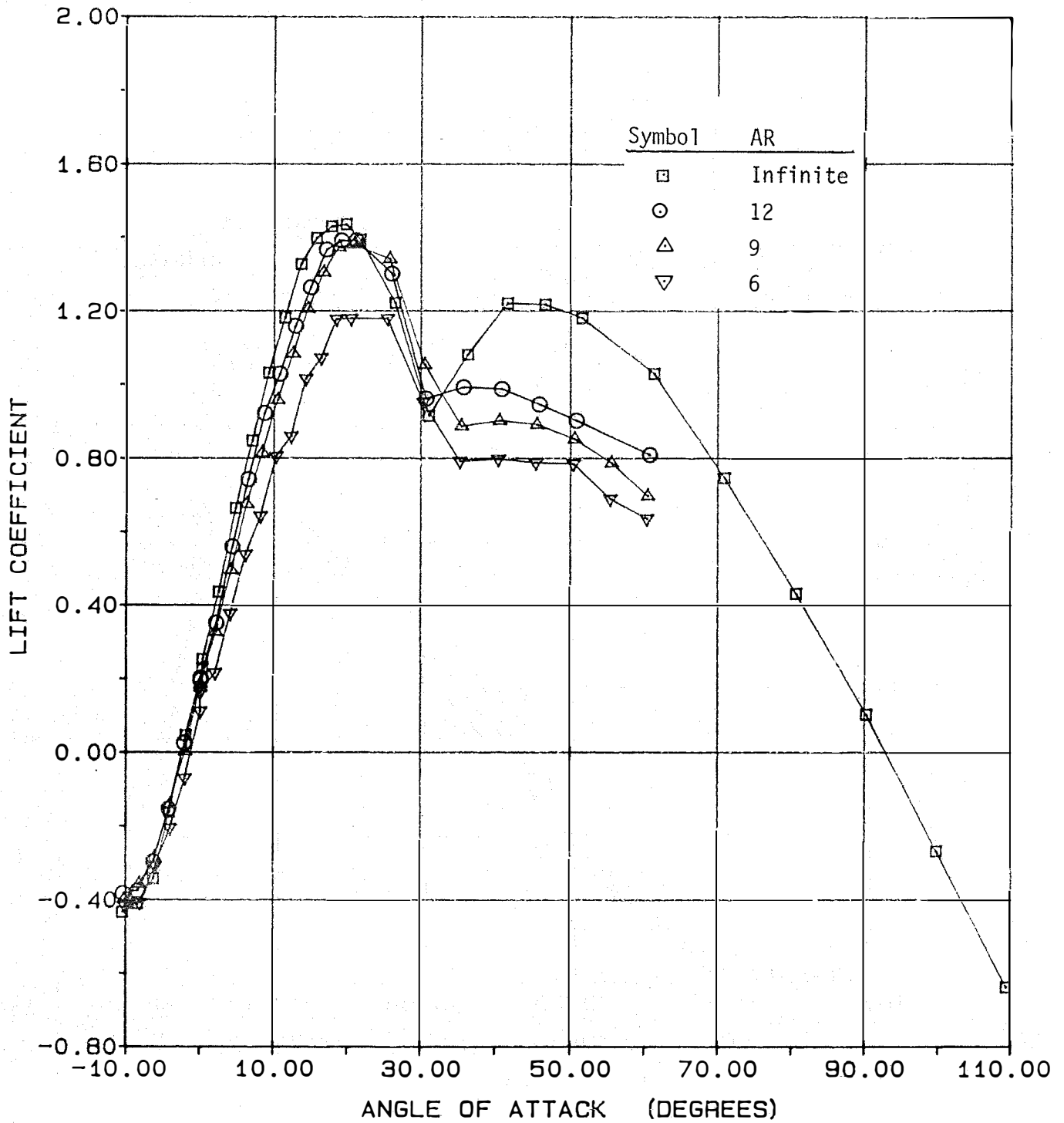
(a) Lift

Figure A.35- Effect of Aspect Ratio on Aerodynamic Coefficients of the NACA 4418 Airfoil at $RN = 1.00 \times 10^6$.



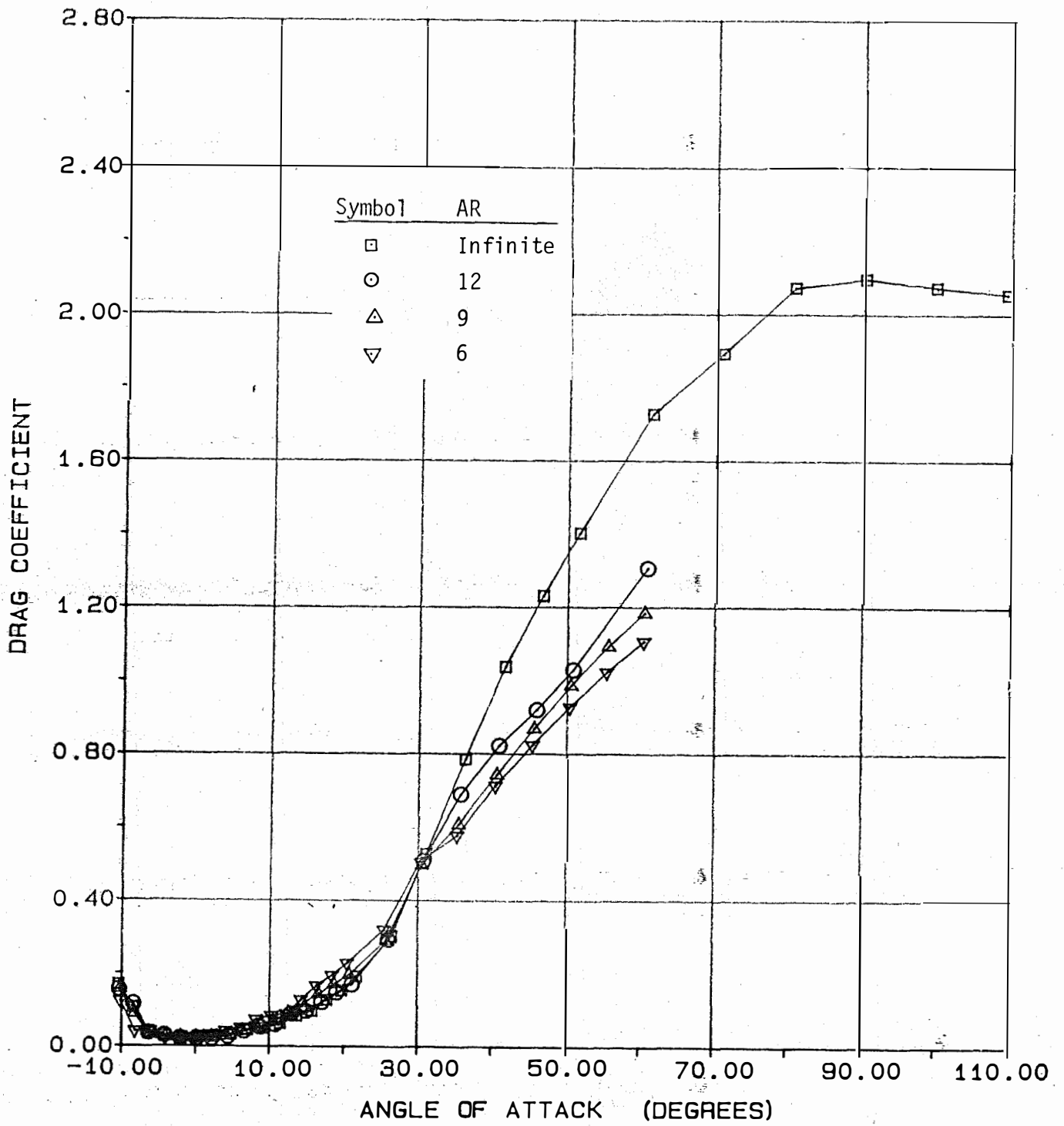
(b) Drag

Figure A.35- Concluded.



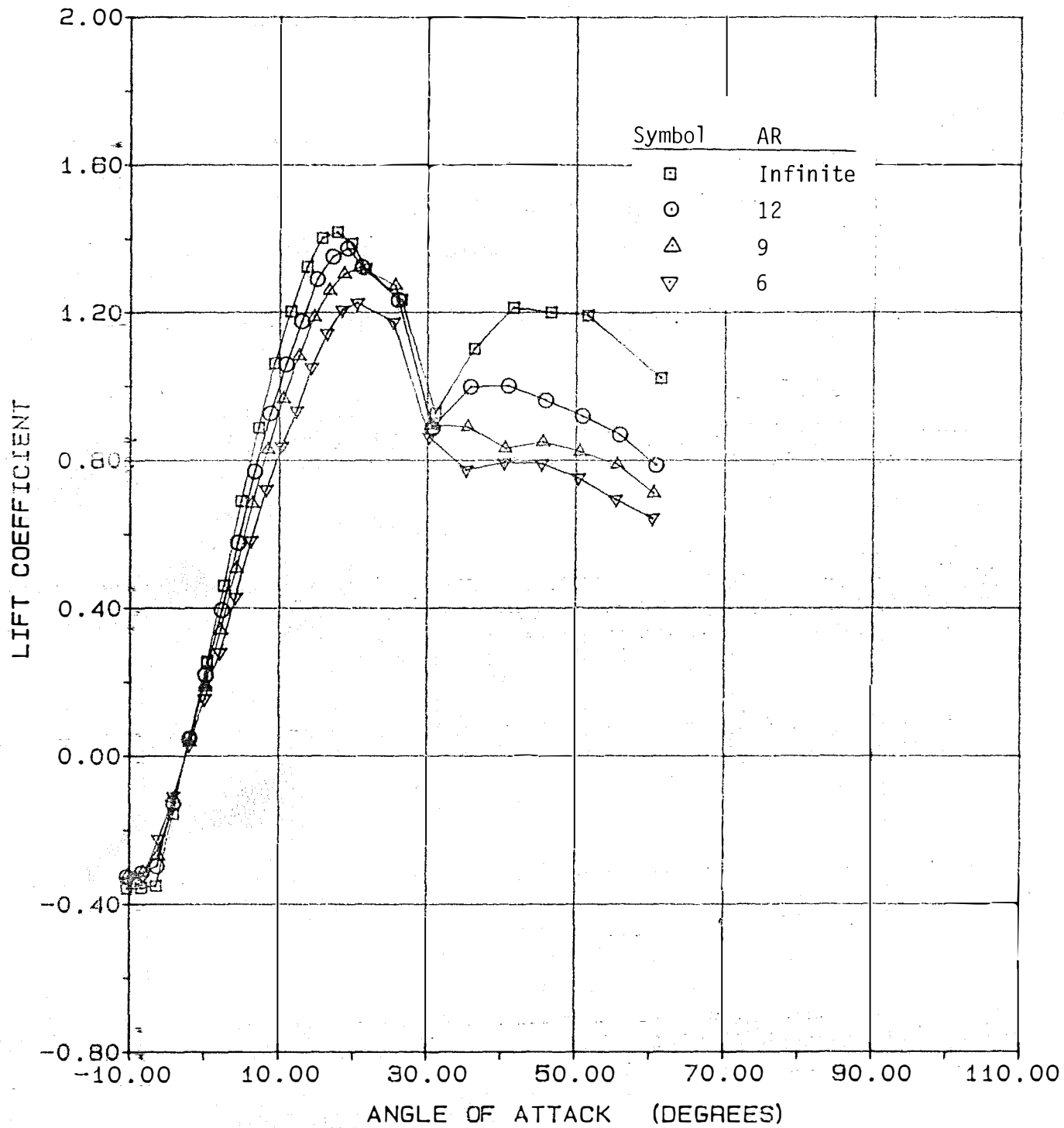
(a) Lift

Figure A.36- Effect of Aspect Ratio on Aerodynamic Coefficients of the NACA 4415 Airfoil at $RN = 0.25 \times 10^6$.



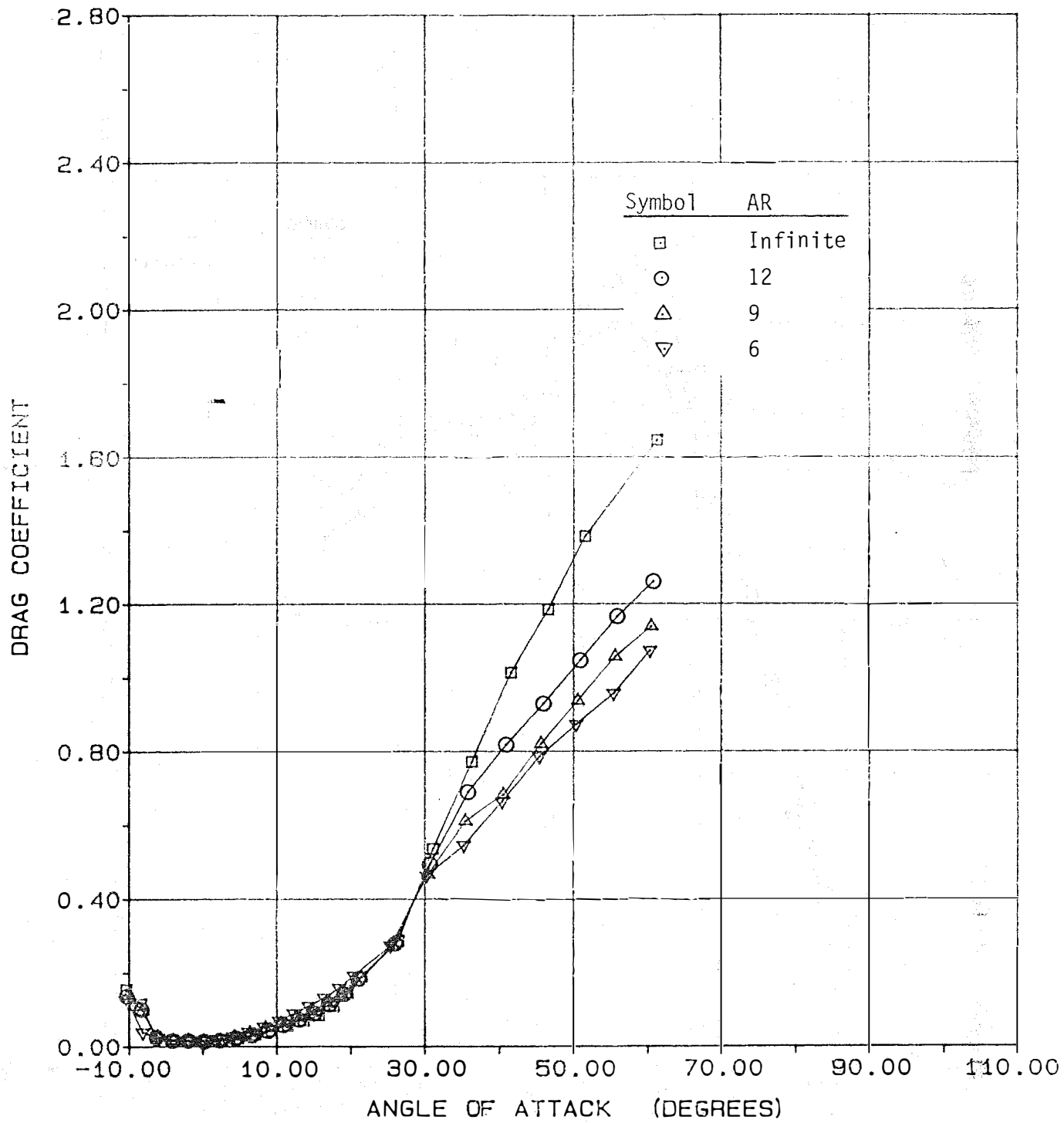
(b) Drag

Figure A.36- Concluded.



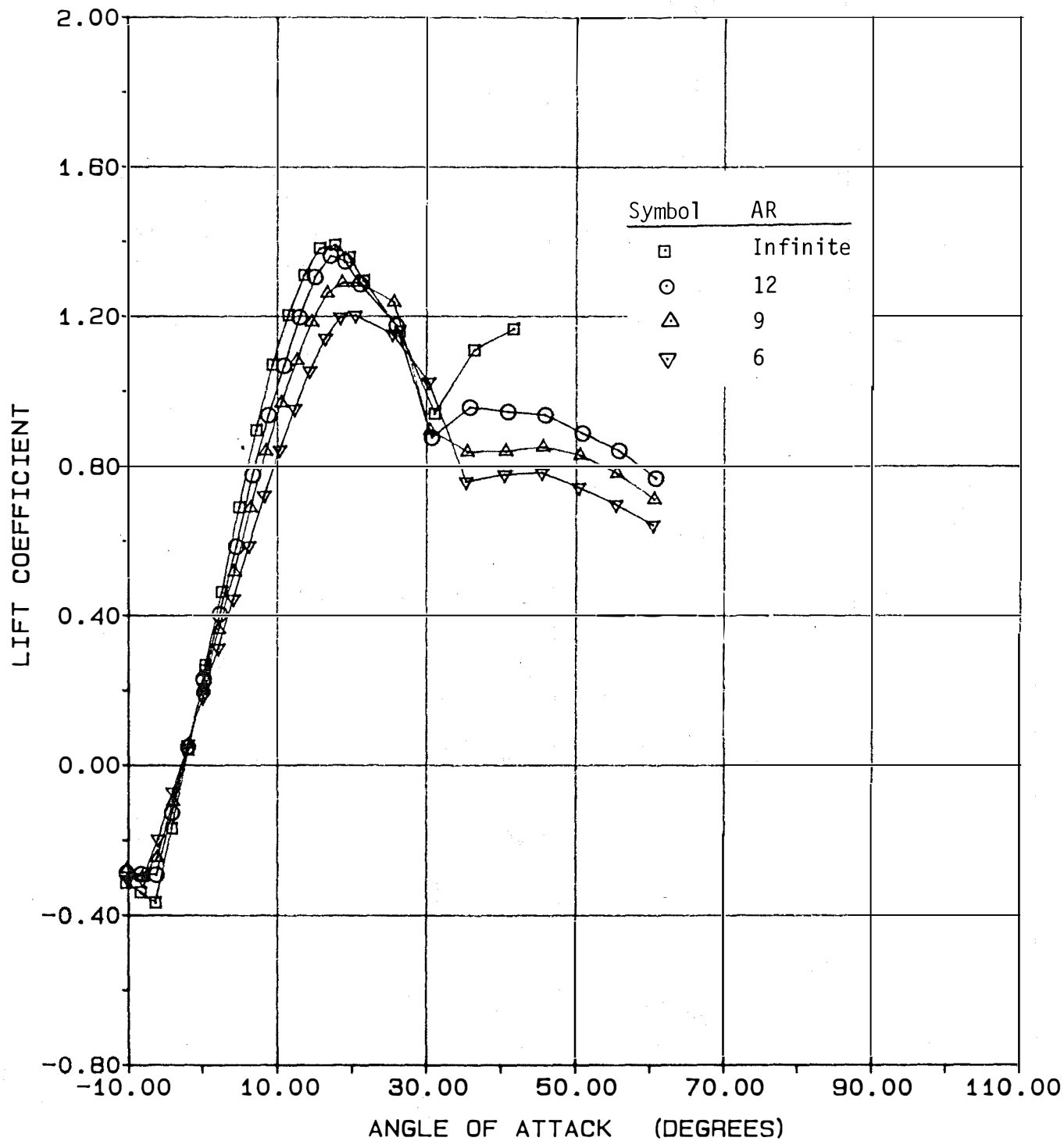
(a) Lift

Figure A.37- Effect of Aspect Ratio on Aerodynamic Coefficients of the NACA 4415 Airfoil at $RN = 0.50 \times 10^6$.



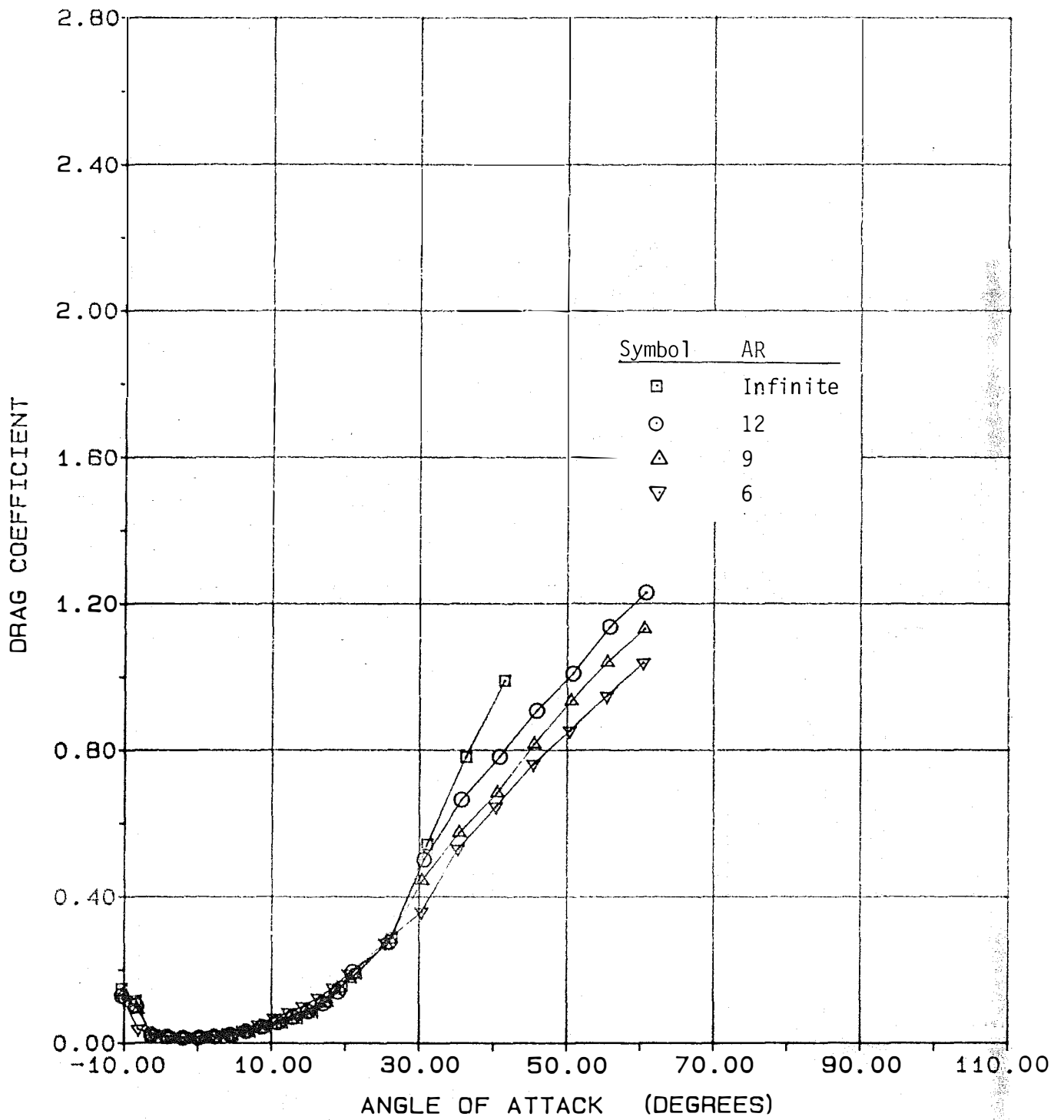
(b) Drag

Figure A.37- Concluded.



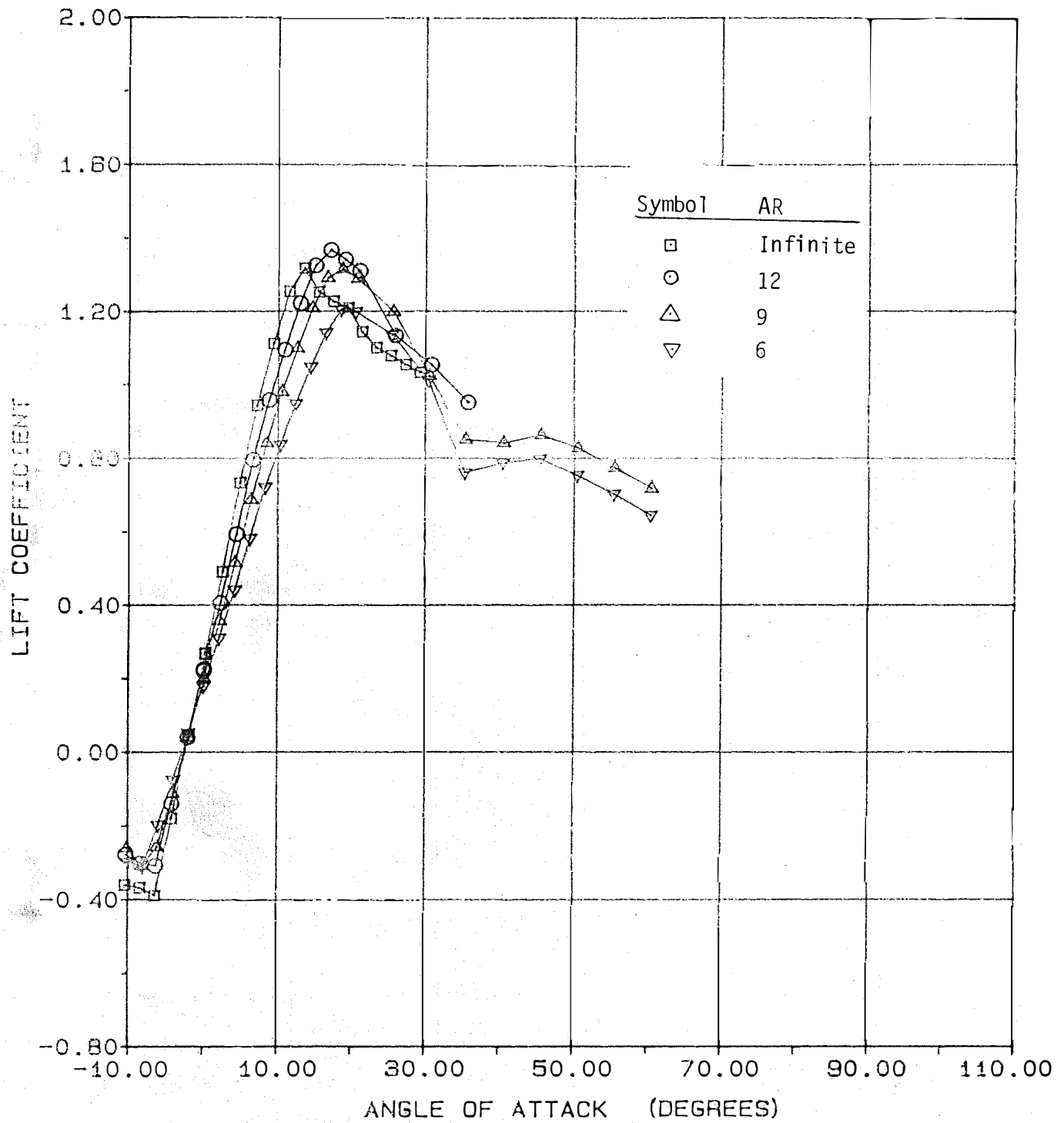
(a) Lift

Figure A.38- Effect of Aspect Ratio on Aerodynamic Coefficients of the NACA 4415 Airfoil at $RN = 0.75 \times 10^6$.



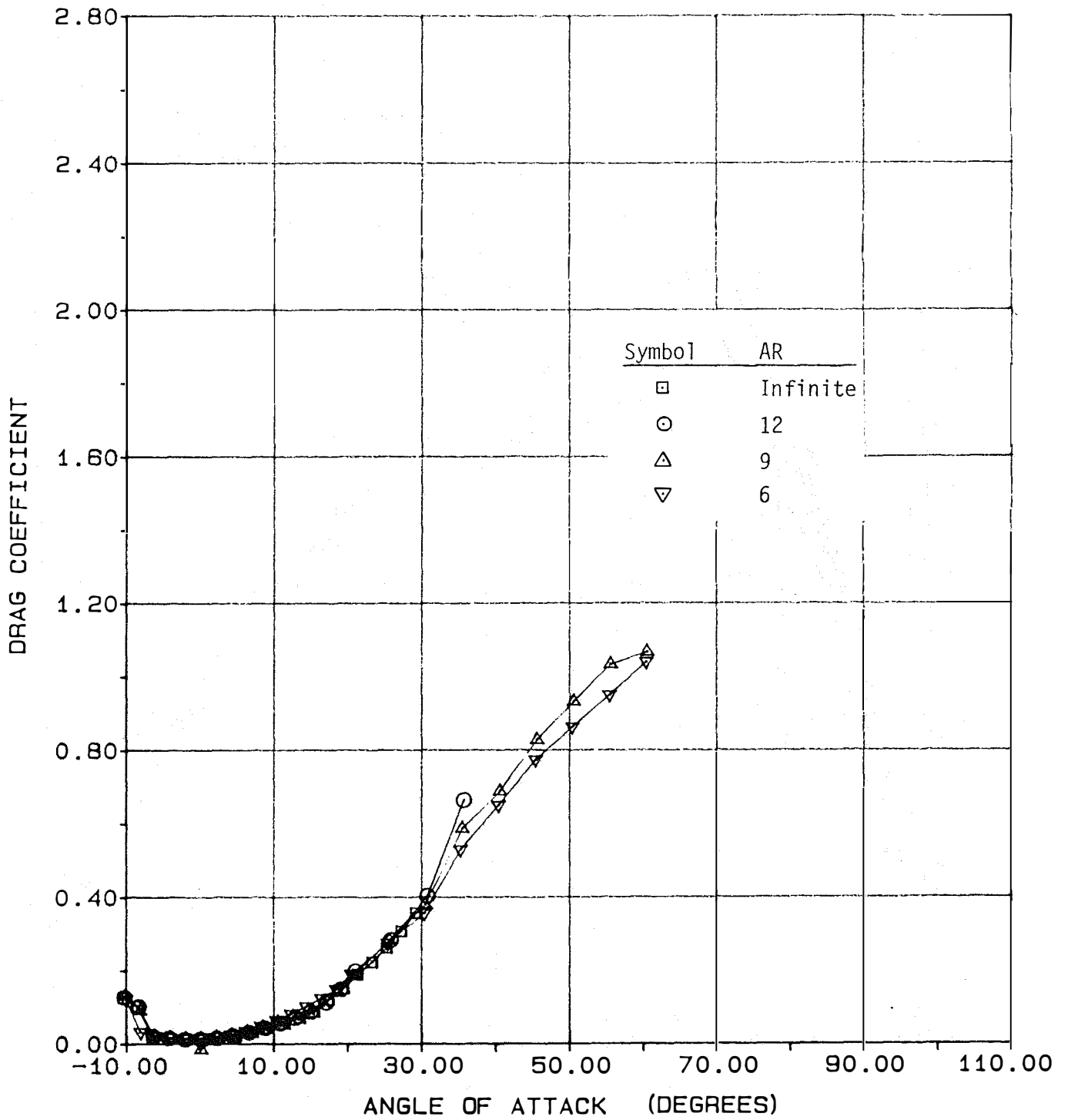
(b) Drag

Figure A.38- Concluded.



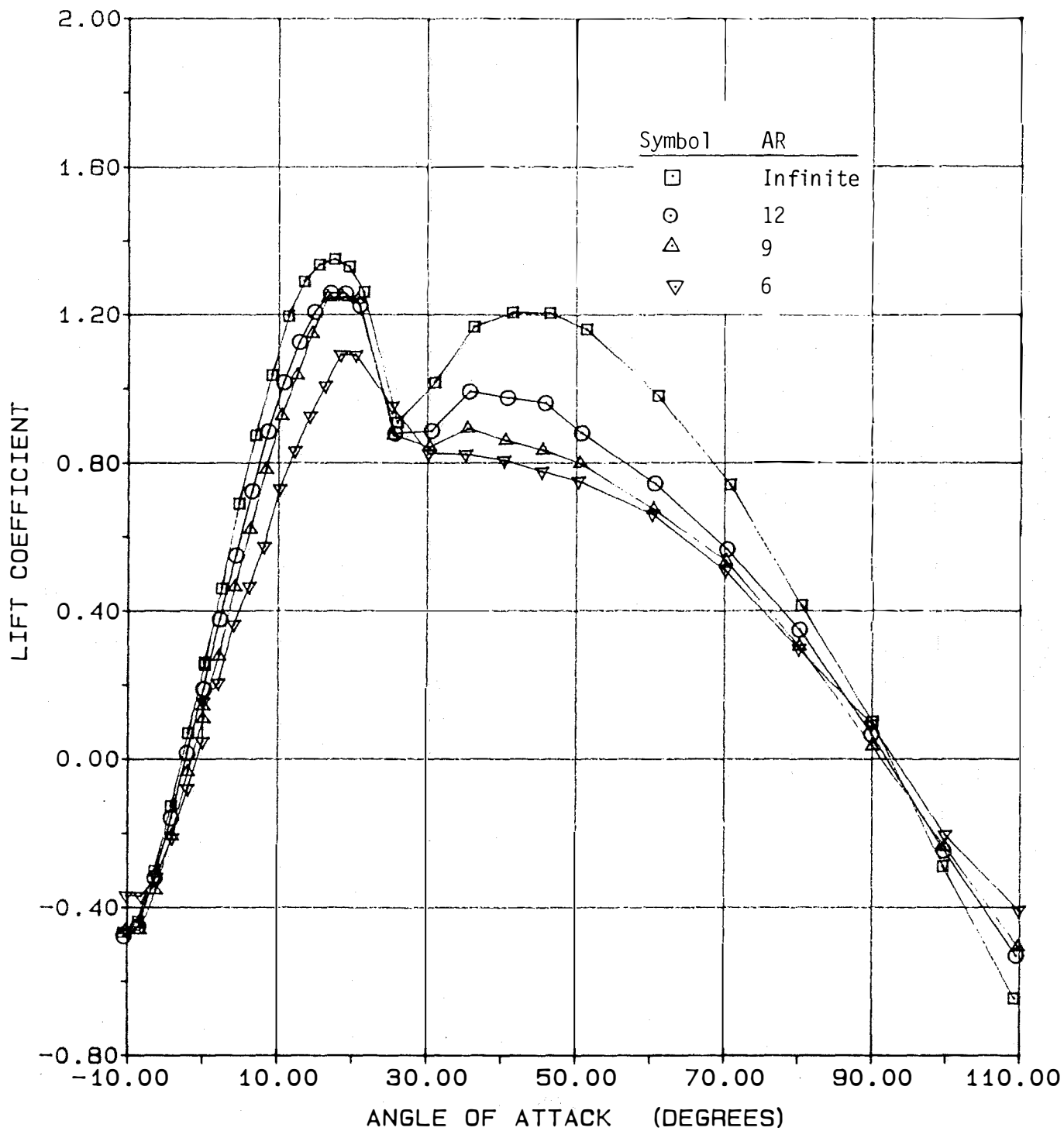
(a) Lift

Figure A.39- Effect of Aspect Ratio on Aerodynamic Coefficients of the NACA 4415 Airfoil at $RN = 1.00 \times 10^6$.



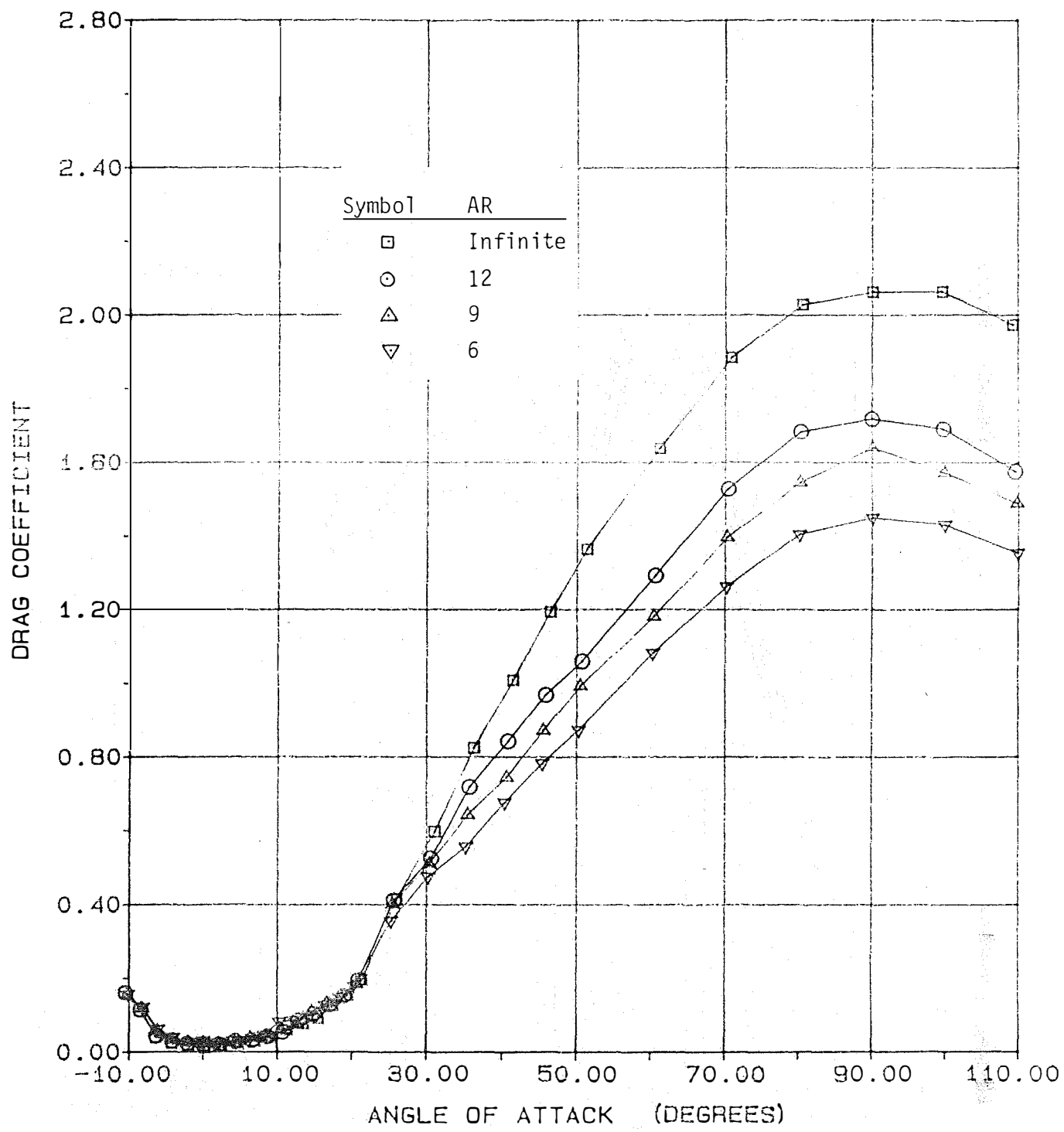
(b) Drag

Figure A.39- Concluded.



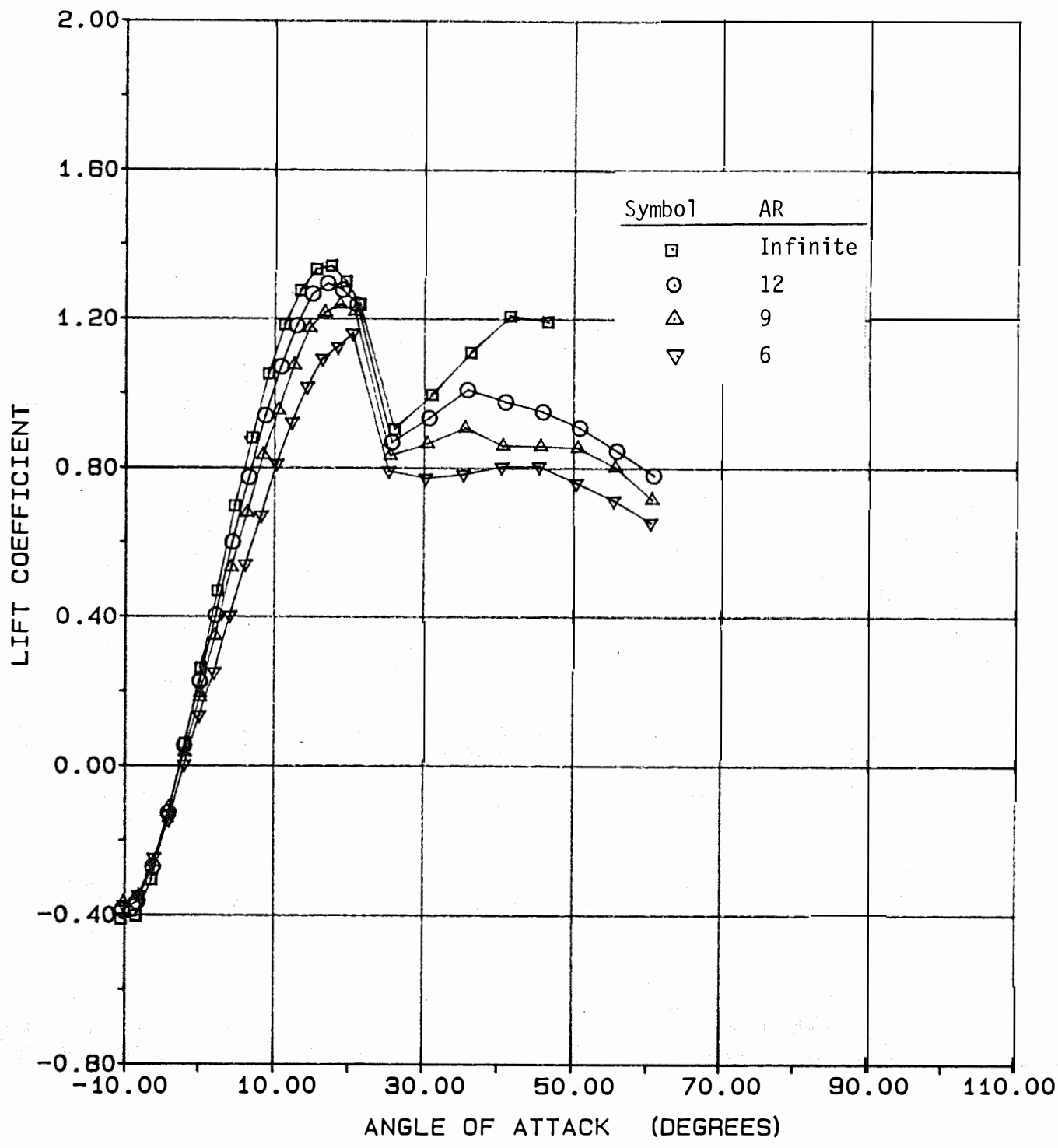
(a) Lift

Figure A.40- Effect of Aspect Ratio on Aerodynamic Coefficients of the NACA 4412 Airfoil at $RN = 0.25 \times 10^6$.



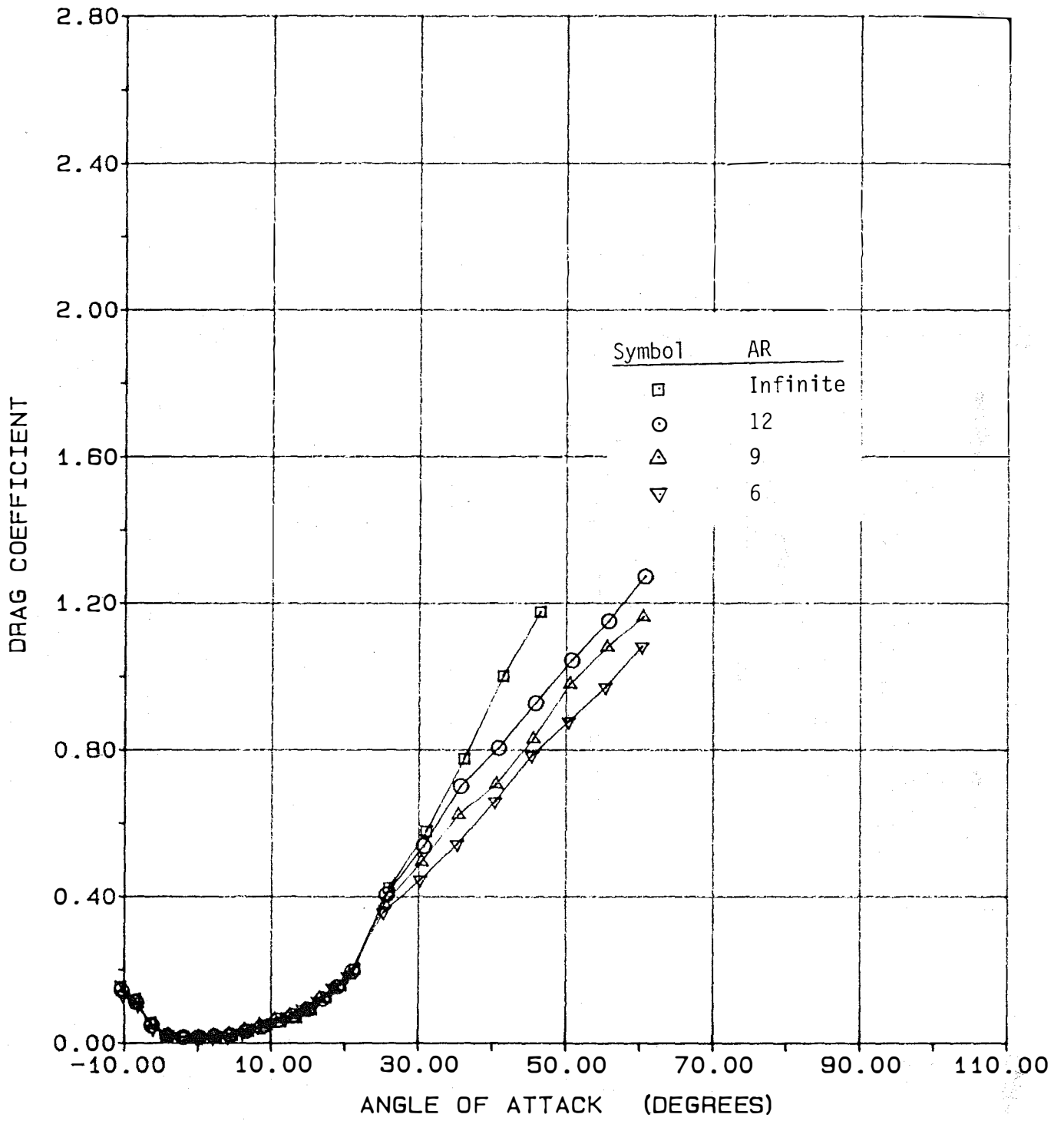
(b) Drag

Figure A.40- Concluded.



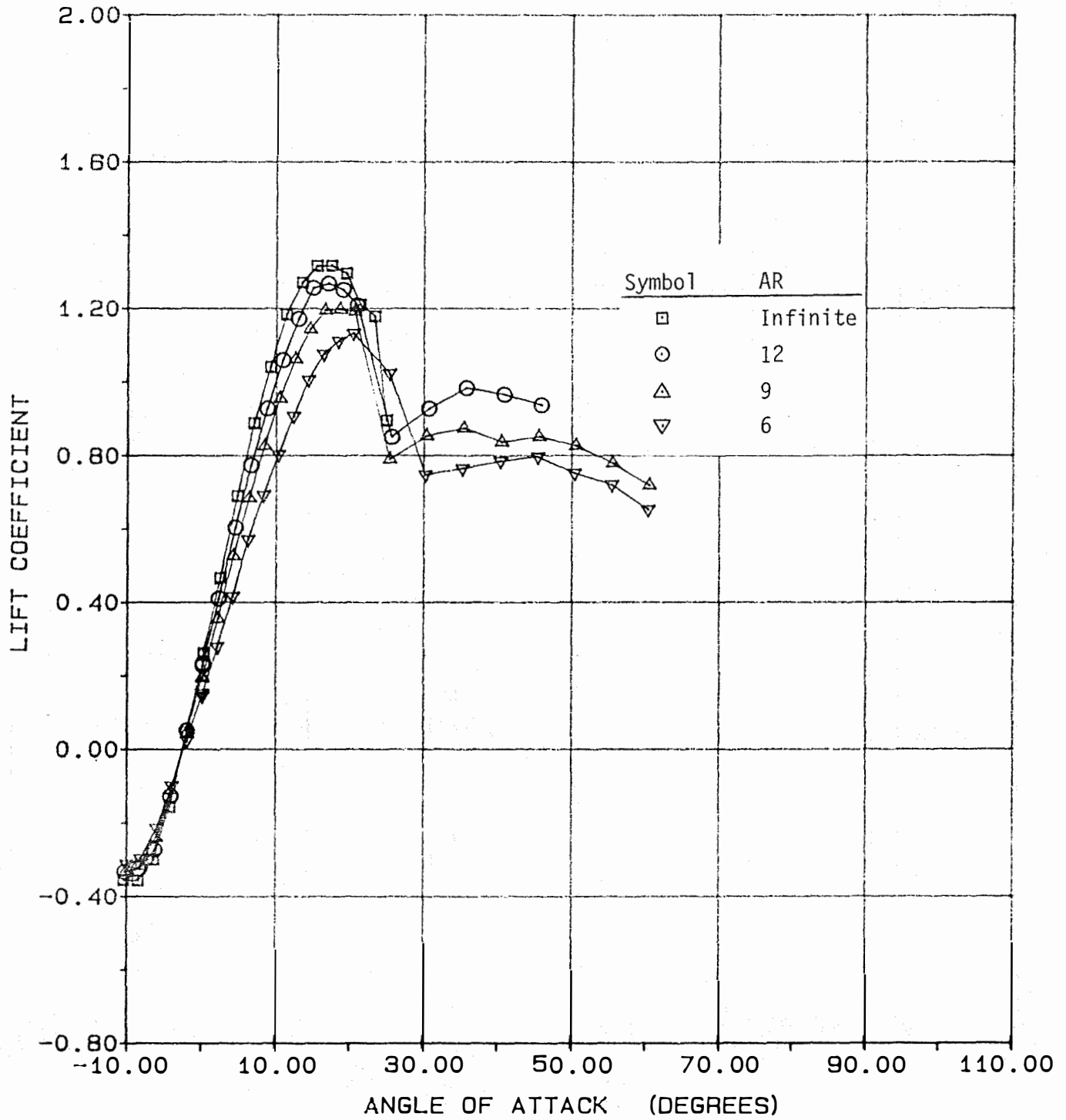
(a) Lift

Figure A.41- Effect of Aspect Ratio on Aerodynamic Coefficients of the NACA 4412 Airfoil at $RN = 0.50 \times 10^6$.



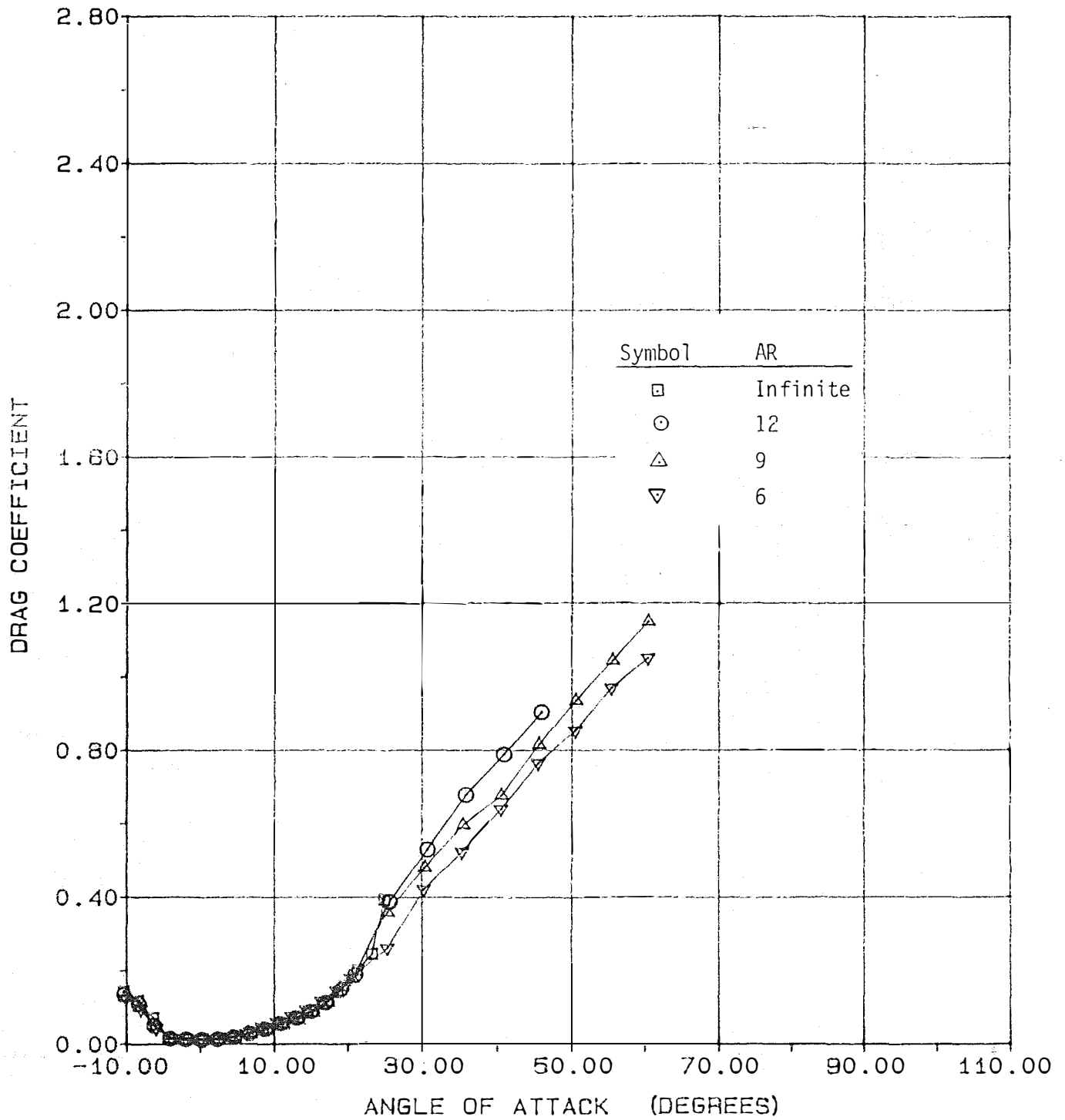
(b) Drag

Figure A.41- Concluded.



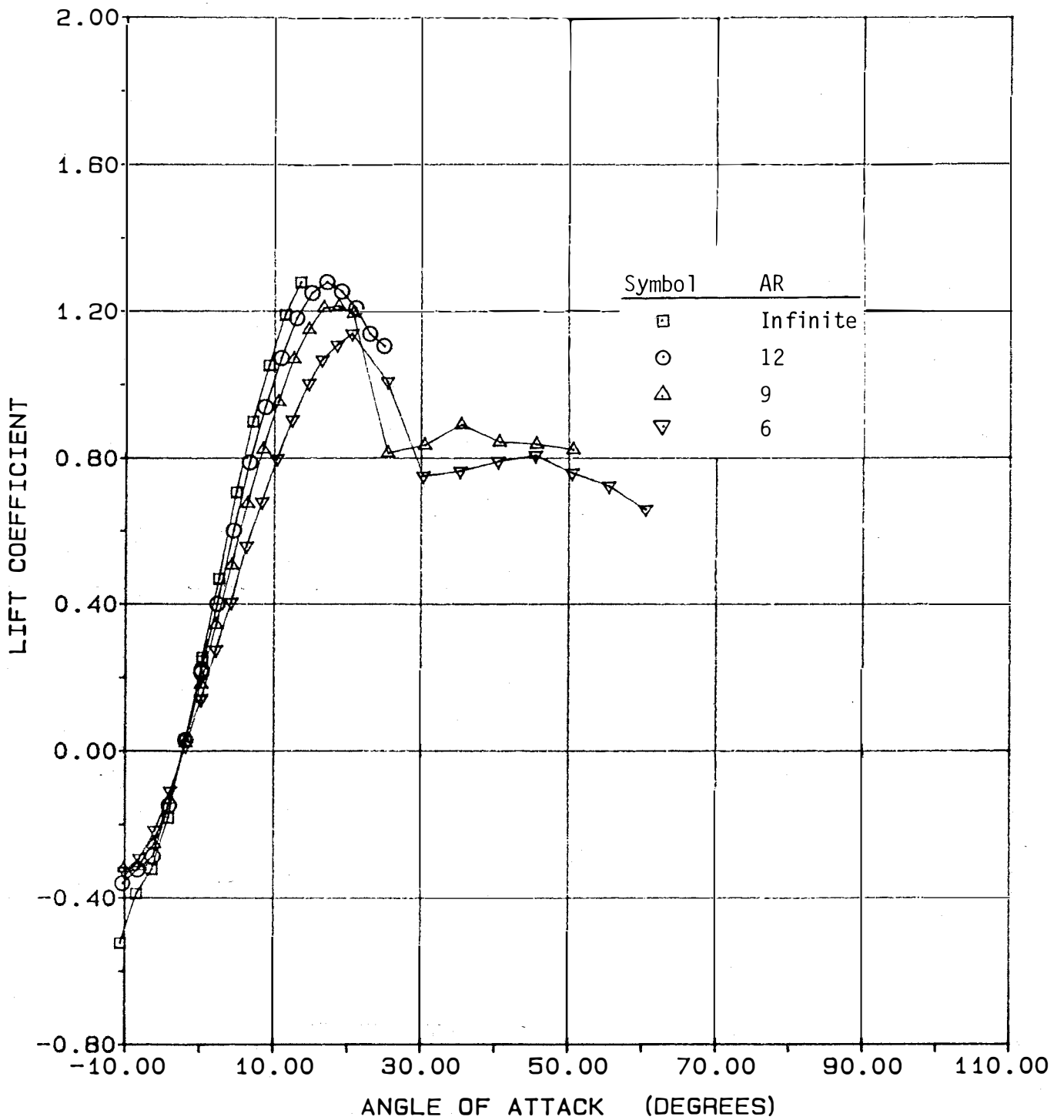
(a) Lift

Figure A.42- Effect of Aspect Ratio on Aerodynamic Coefficients of the NACA 4412 Airfoil at $RN = 0.75 \times 10^6$.



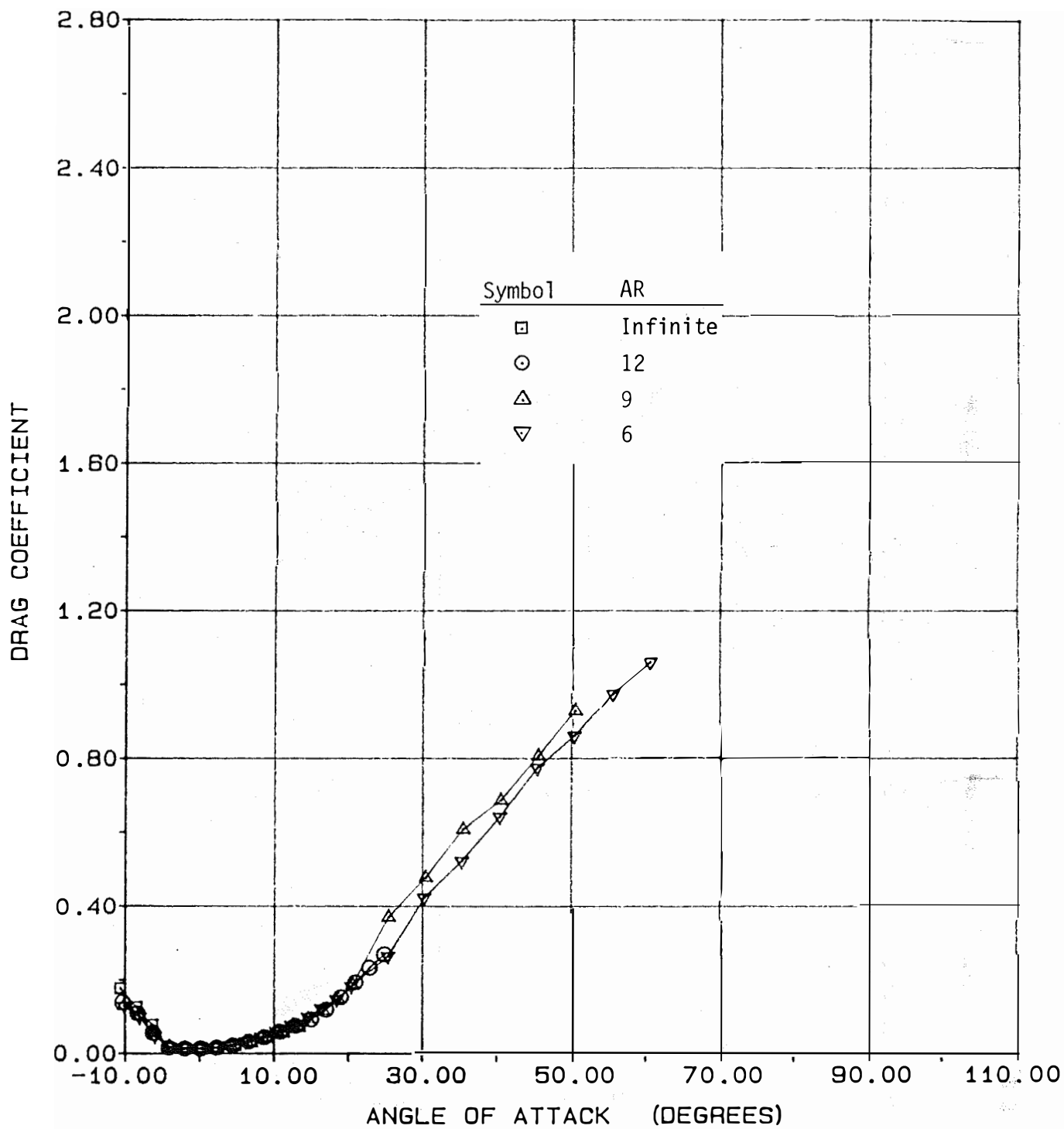
(b) Drag

Figure A.42- Concluded.



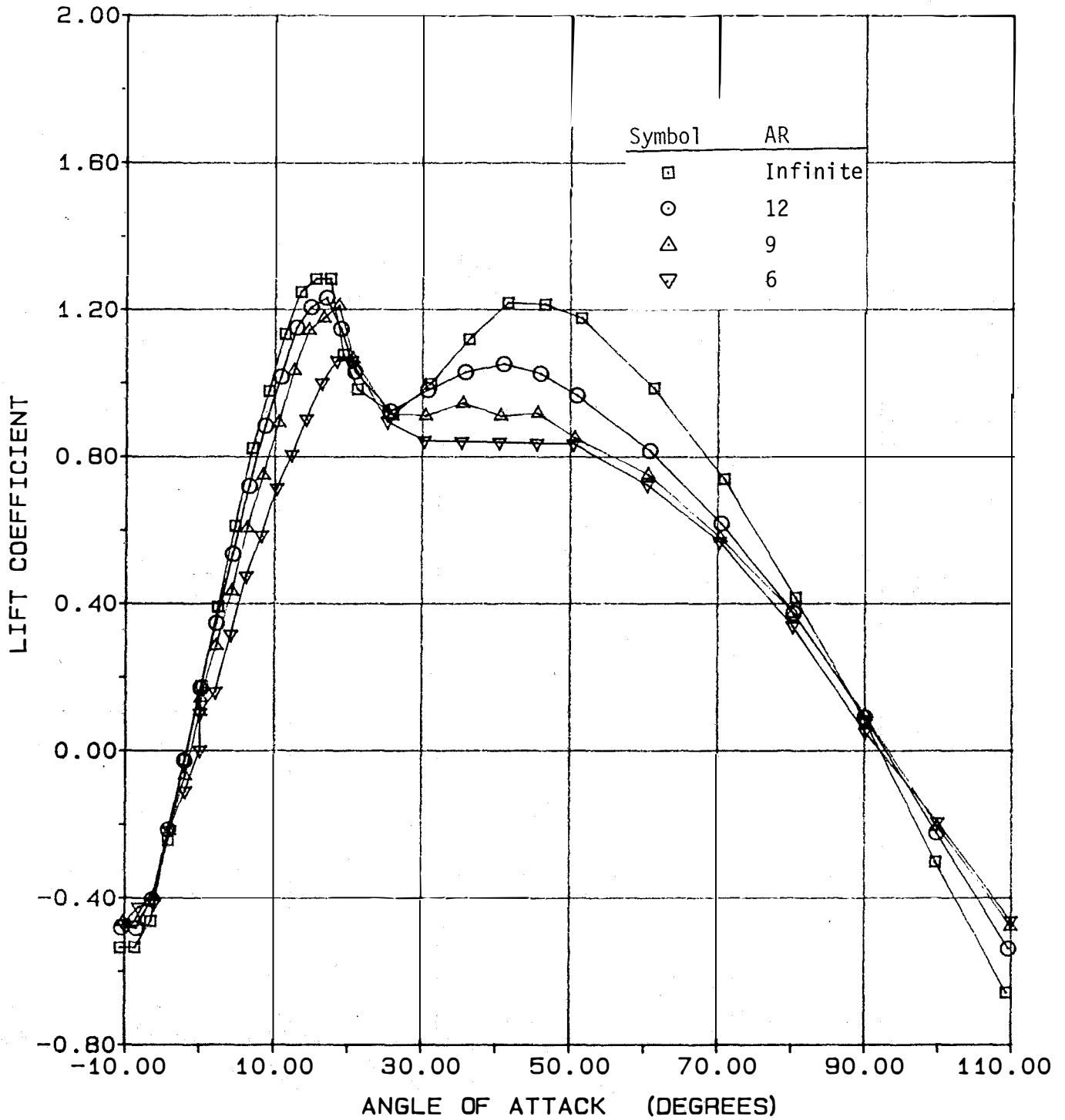
(a) Lift

Figure A.43- Effect of Aspect Ratio on Aerodynamic Coefficients of the NACA 4412 Airfoil at $RN = 1.00 \times 10^6$.



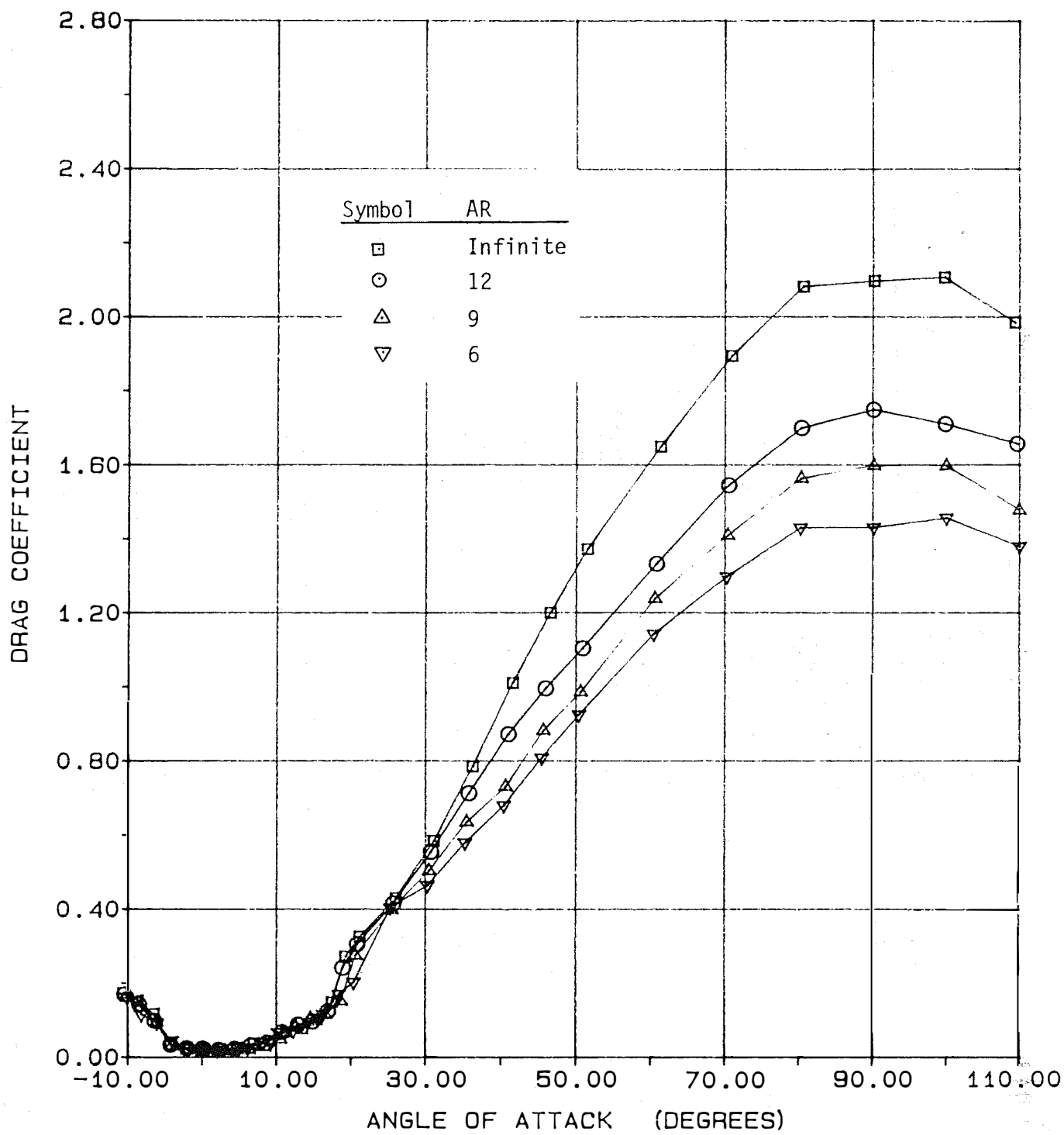
(b) Drag

Figure A.43- Concluded.



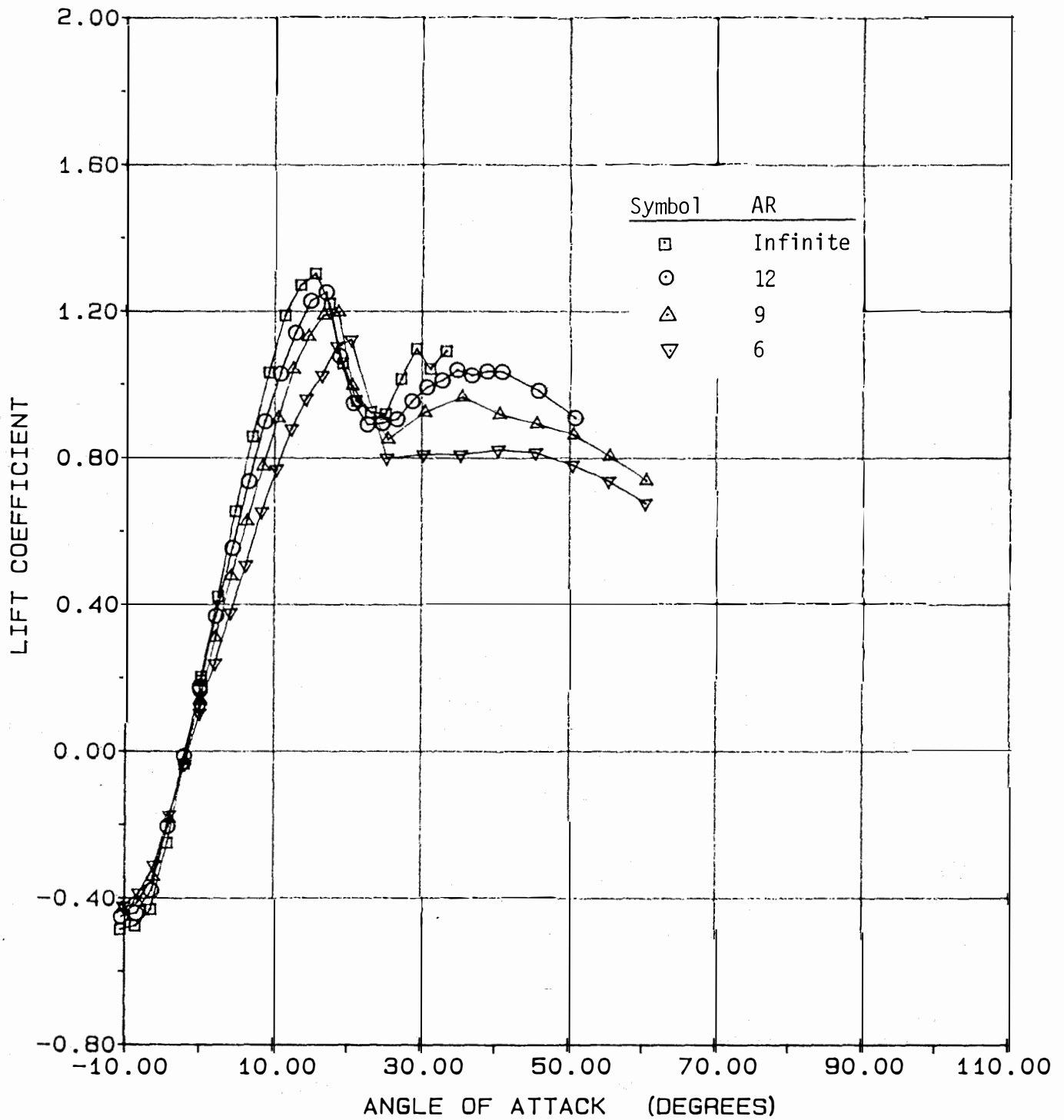
(a) Lift

Figure A.44- Effect of Aspect Ratio on Aerodynamic Coefficients of the NACA 4409 Airfoil at $RN = 0.25 \times 10^6$.



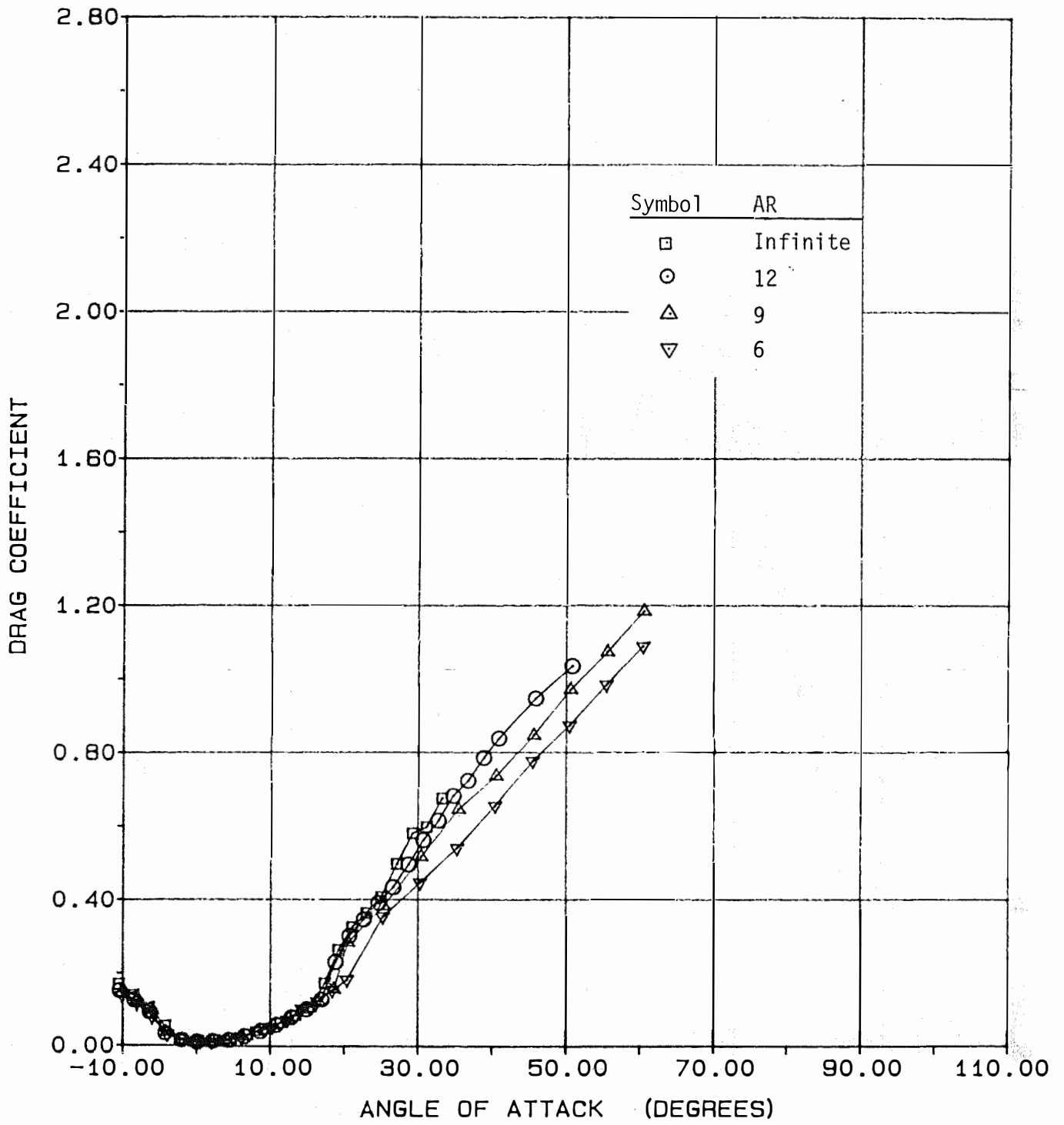
(b) Drag

Figure A.44- Concluded.



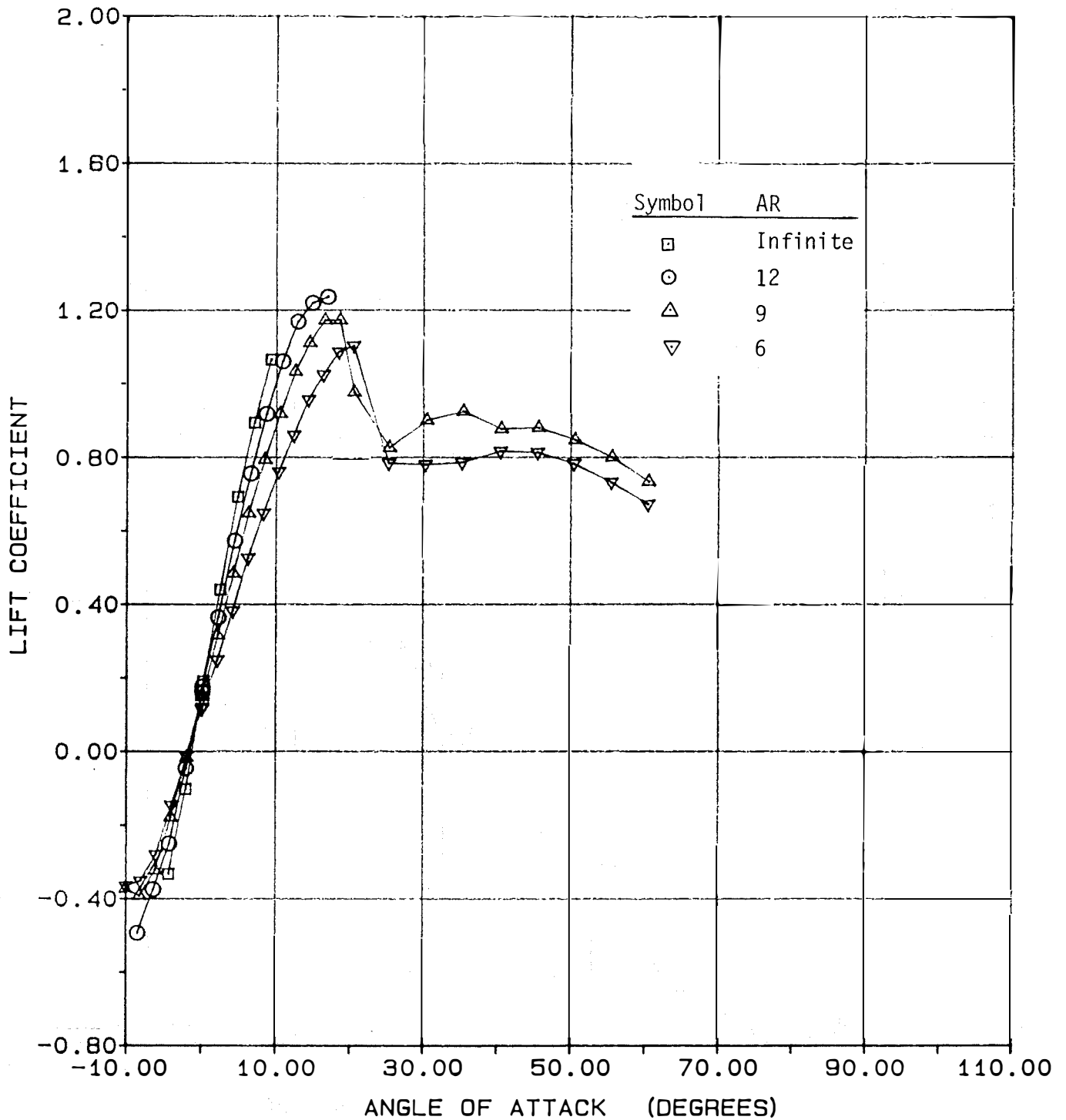
(a) Lift

Figure A.45- Effect of Aspect Ratio on Aerodynamic Coefficients of the NACA 4409 Airfoil at $RN = 0.50 \times 10^9$.



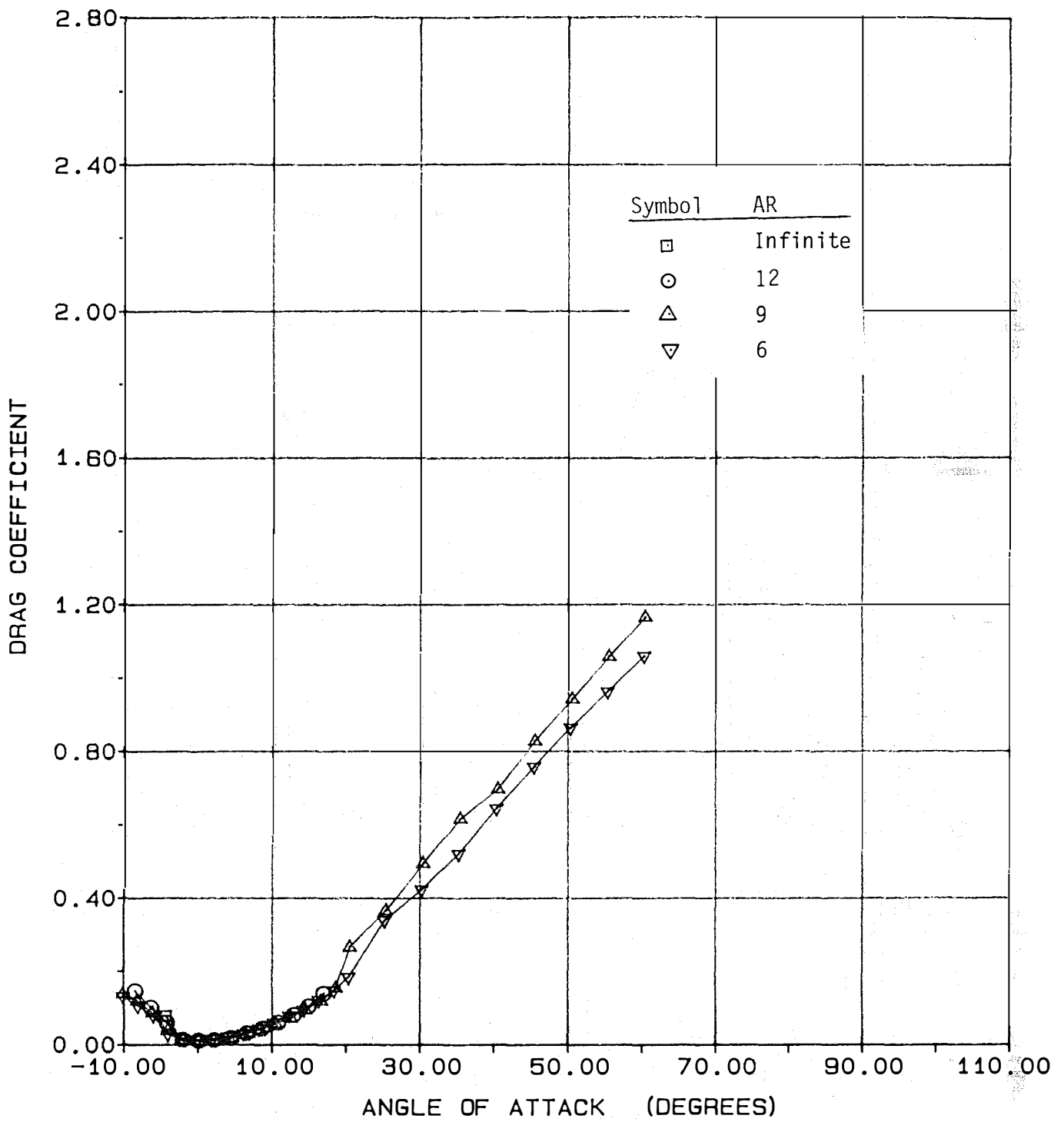
(b) Drag

Figure A.45- Concluded.



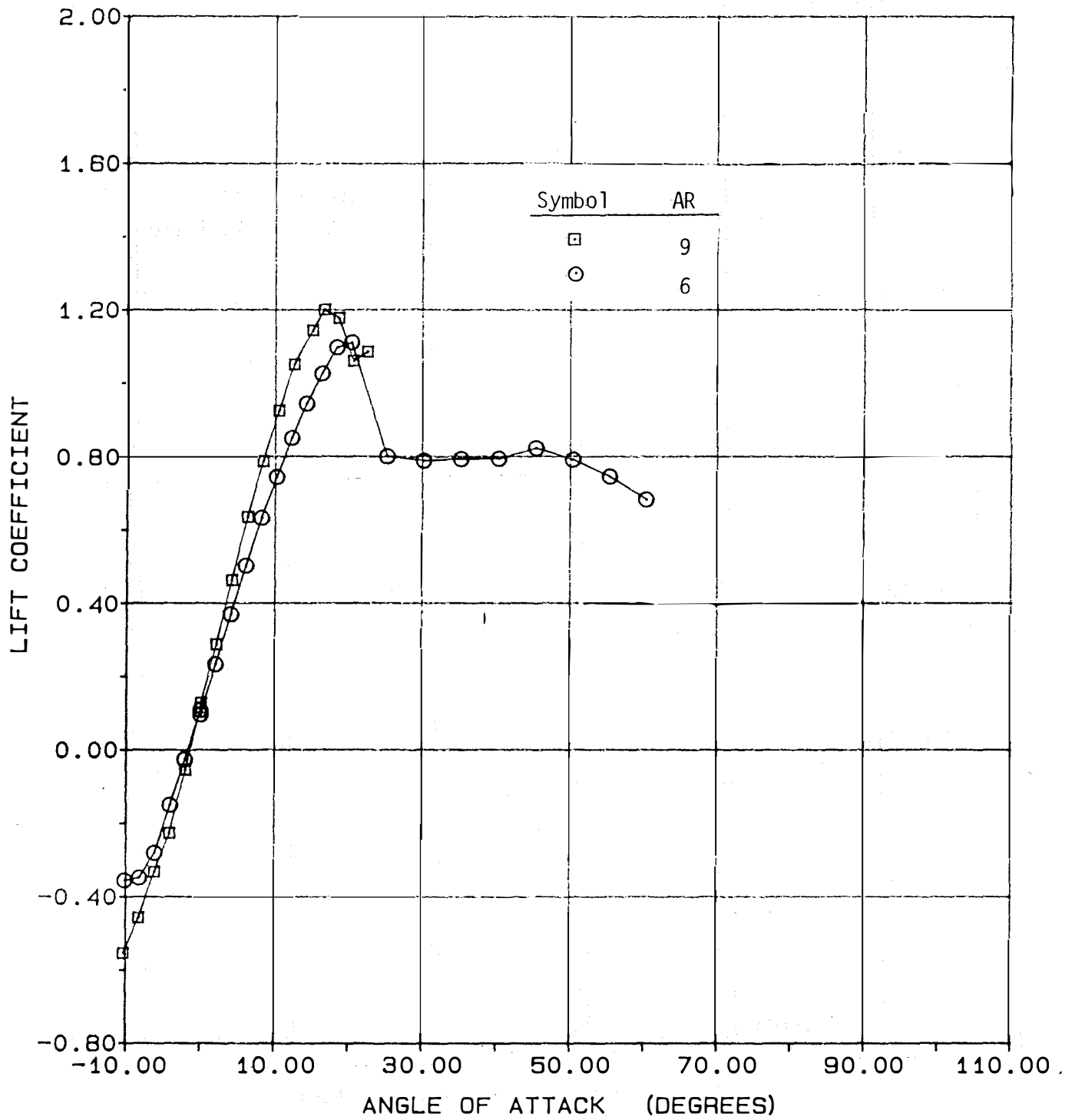
(a) Lift

Figure A.46- Effect of Aspect Ratio on Aerodynamic Coefficients of the NACA 4409 Airfoil at $RN = 0.75 \times 10^6$.



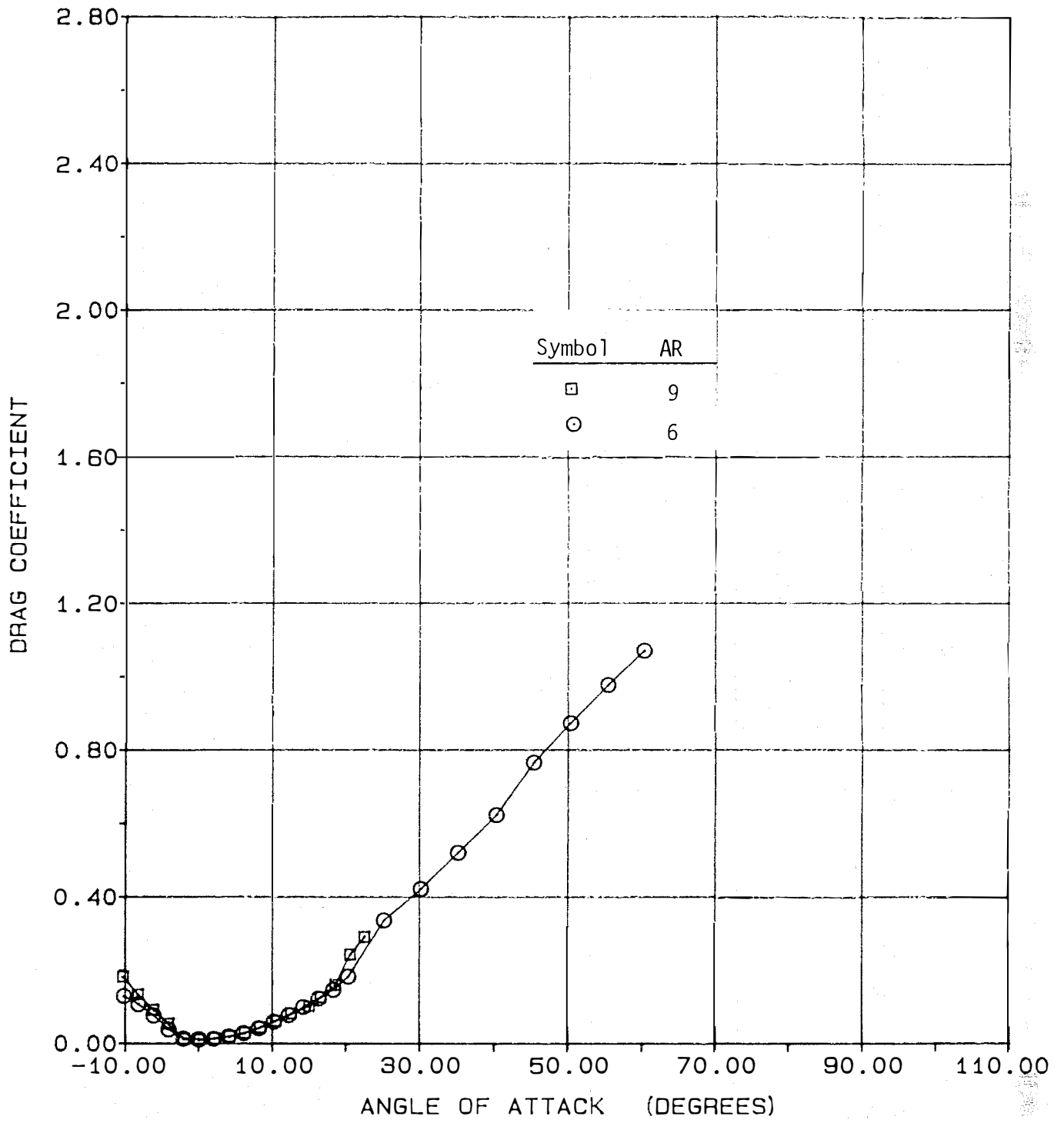
(b) Drag

Figure A.46- Concluded.



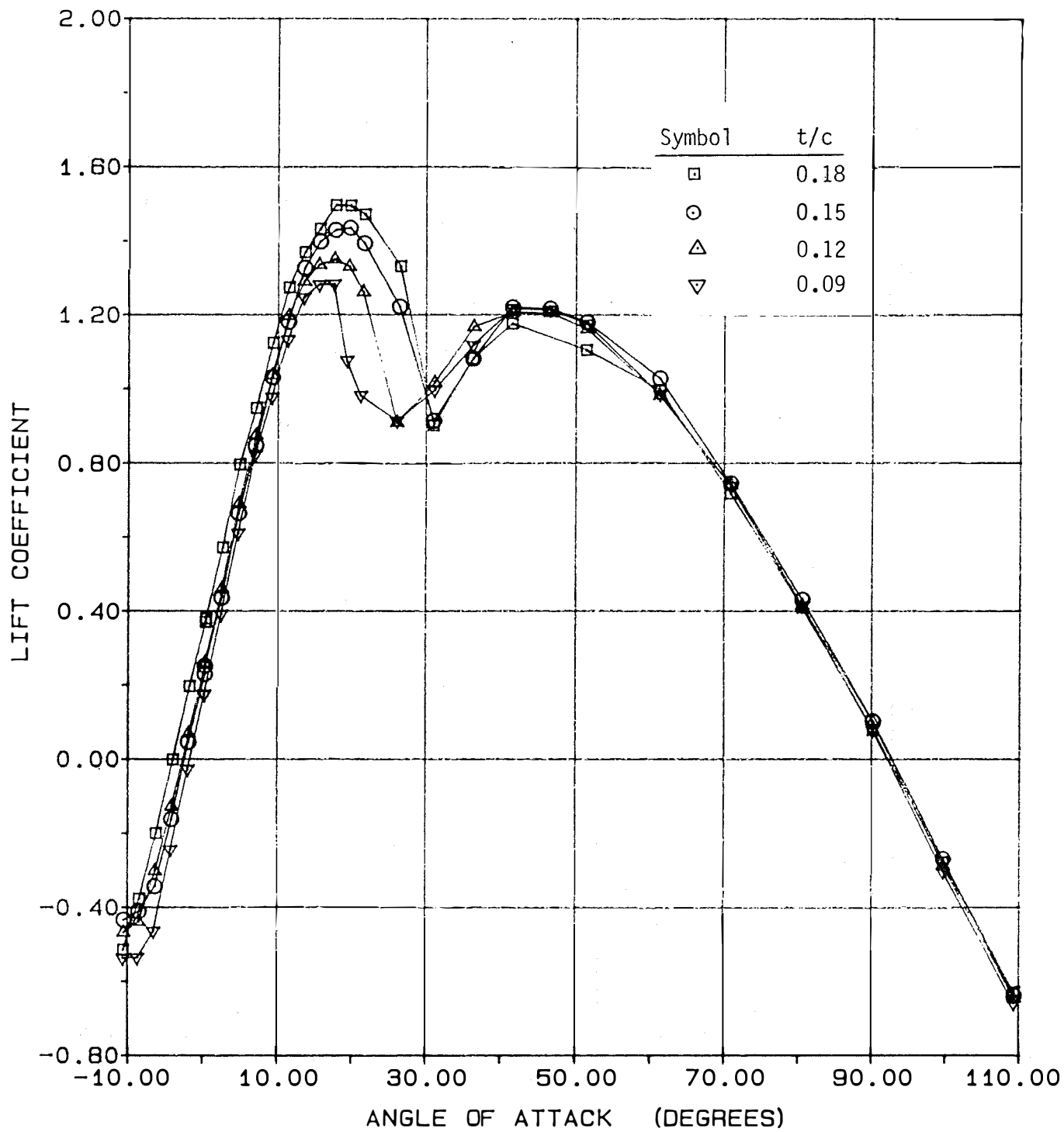
(a) Lift

Figure A.47- Effect of Aspect Ratio on Aerodynamic Coefficients of the NACA 4409 Airfoil at $RN = 1.00 \times 10^6$.



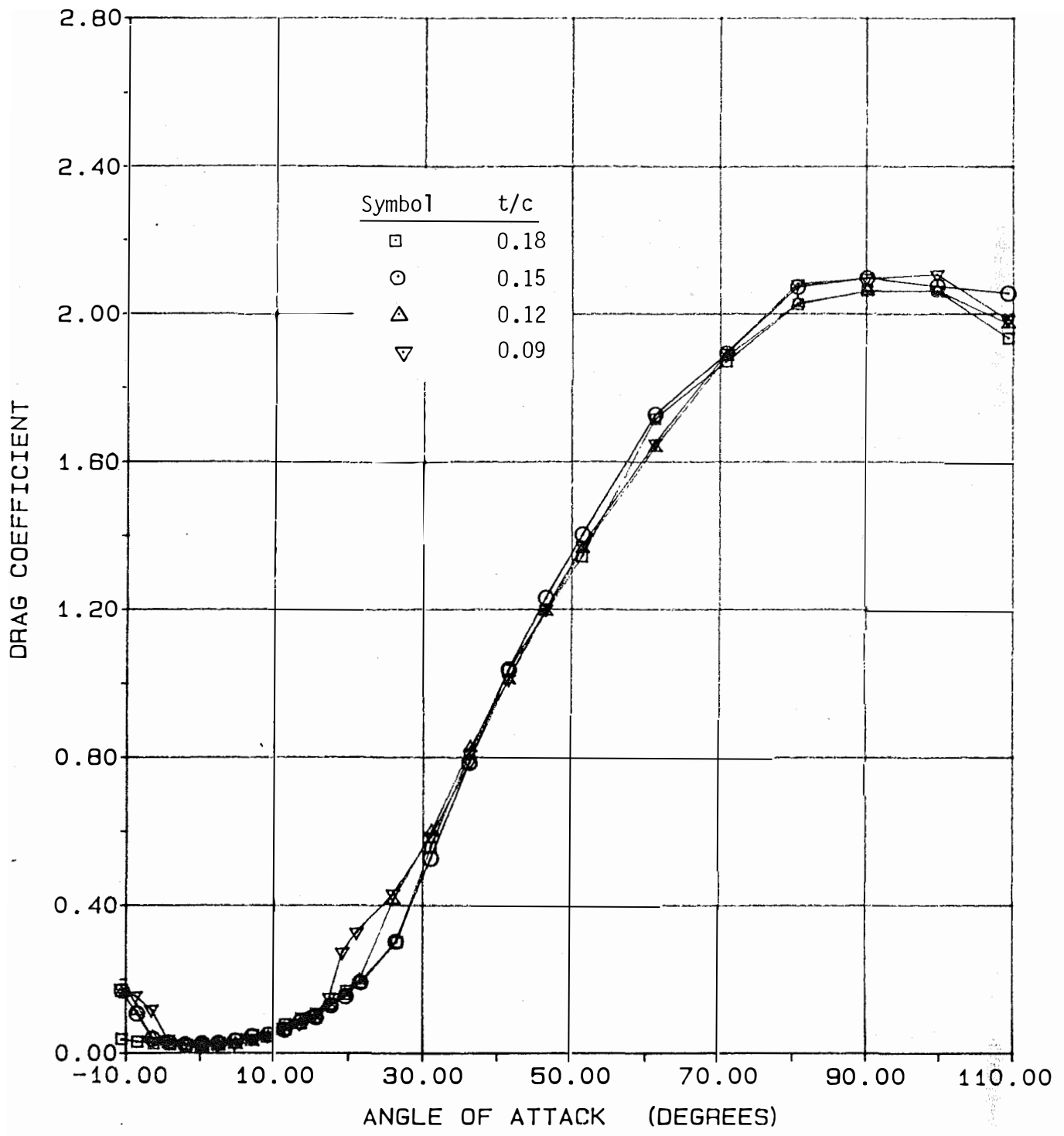
(b) Drag

Figure A.47- Concluded.



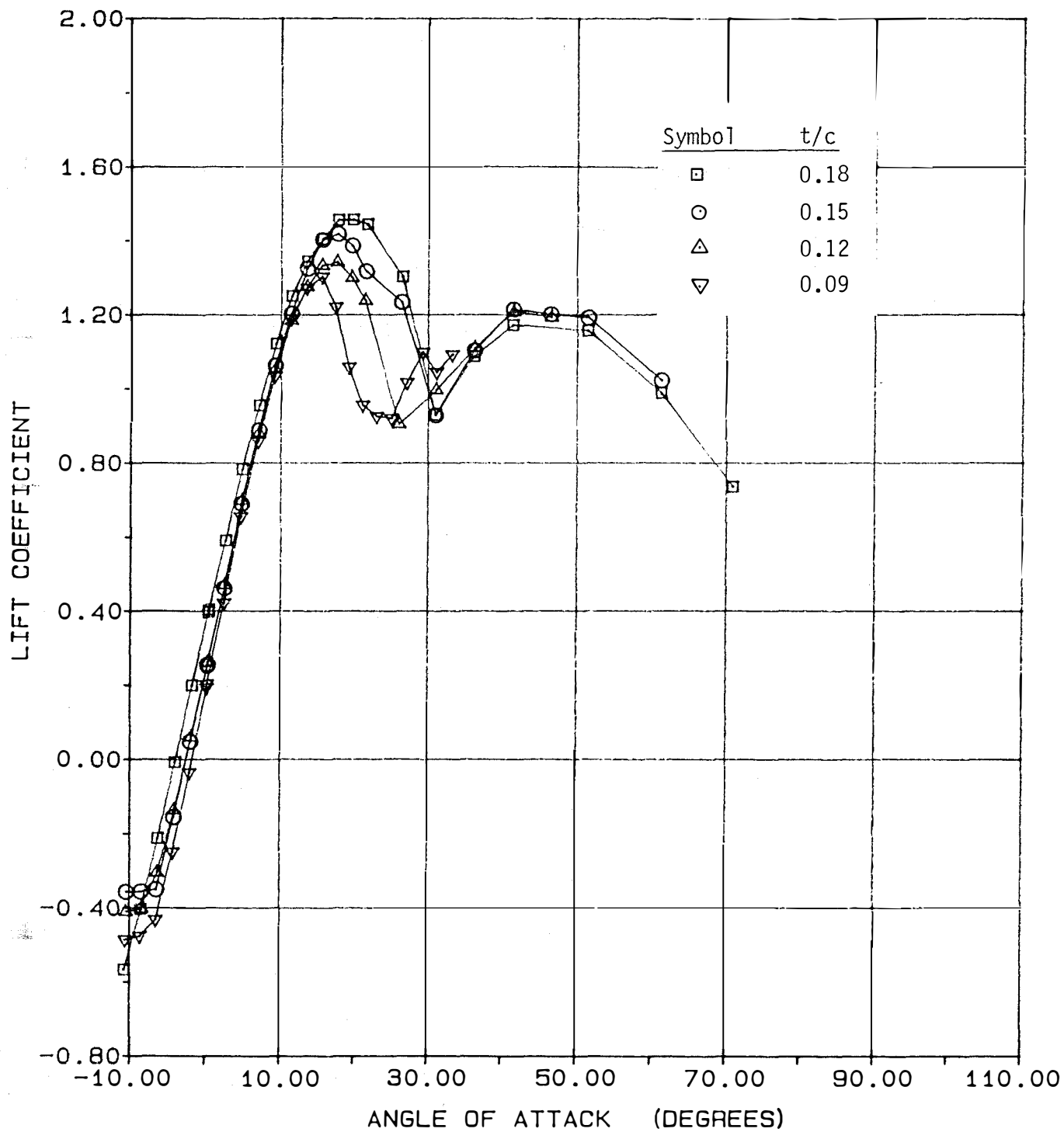
(a) Lift

Figure A.48- Effect of Airfoil Thickness on Aerodynamic Coefficients; Aspect Ratio = ∞ , $RN = 0.25 \times 10^6$.



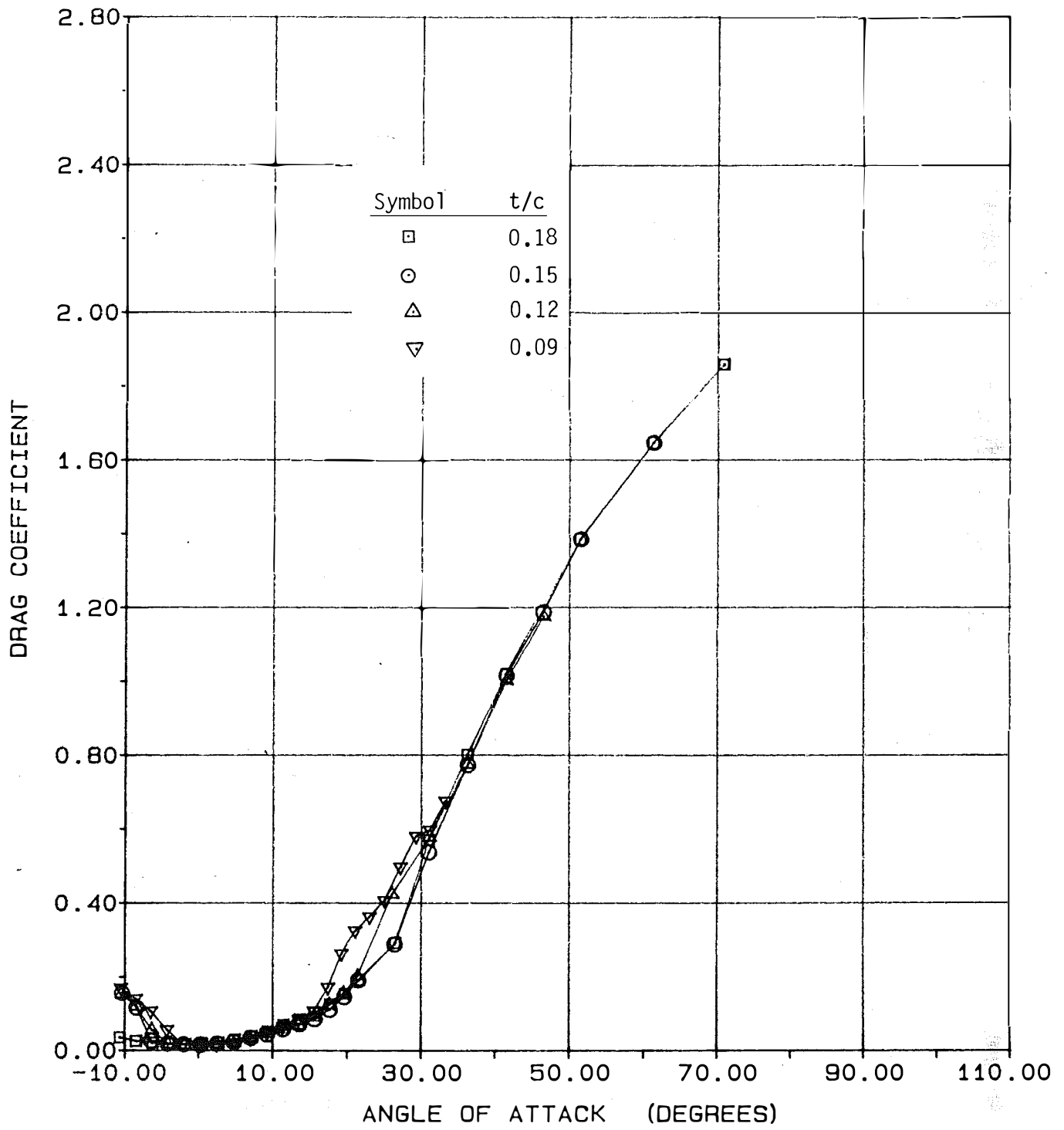
(b) Drag

Figure A.48- Concluded.



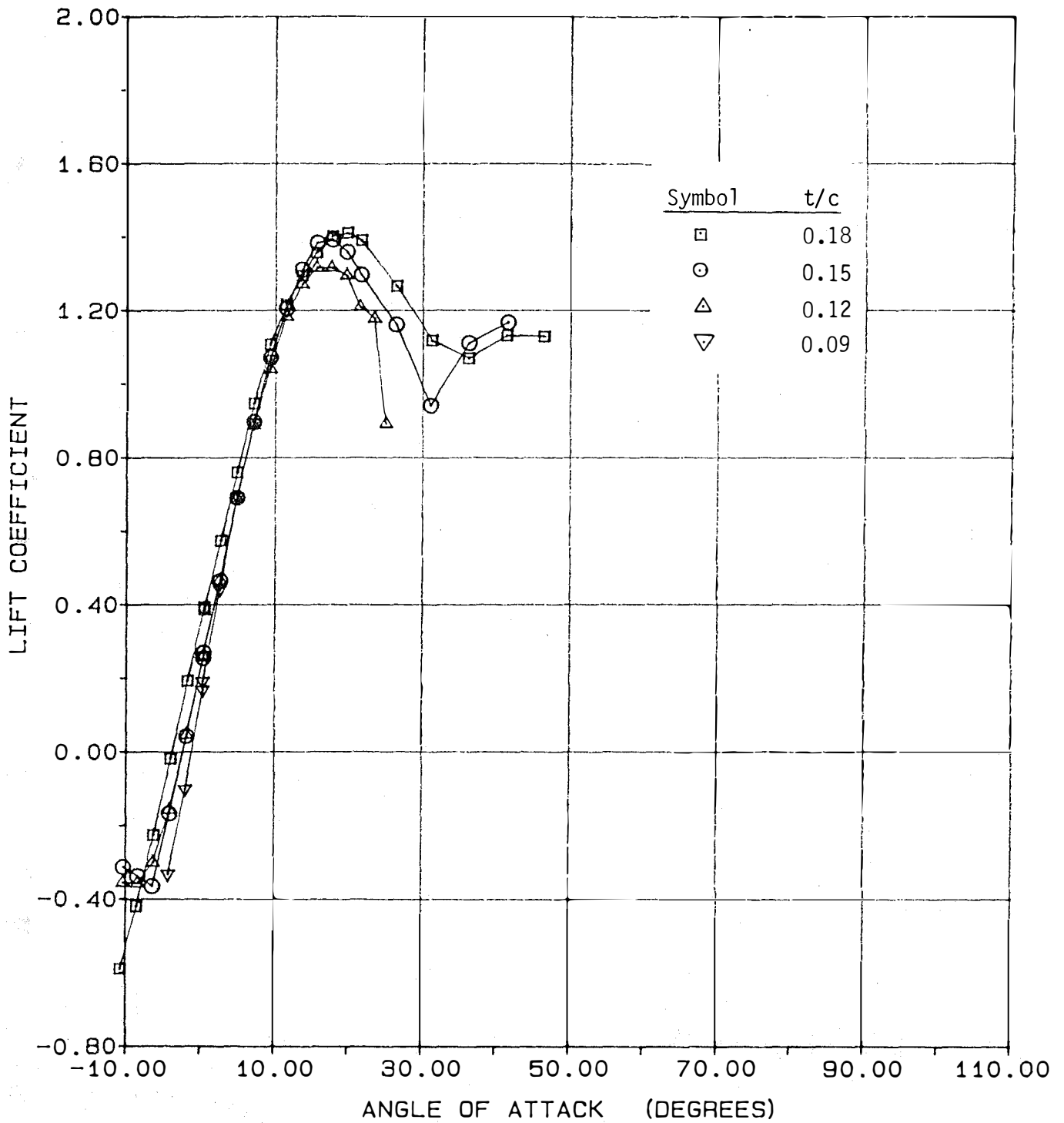
(a) Lift

Figure A.49- Effect of Airfoil Thickness on Aerodynamic Coefficients; Aspect Ratio = ∞ , $RN = 0.50 \times 10^6$.



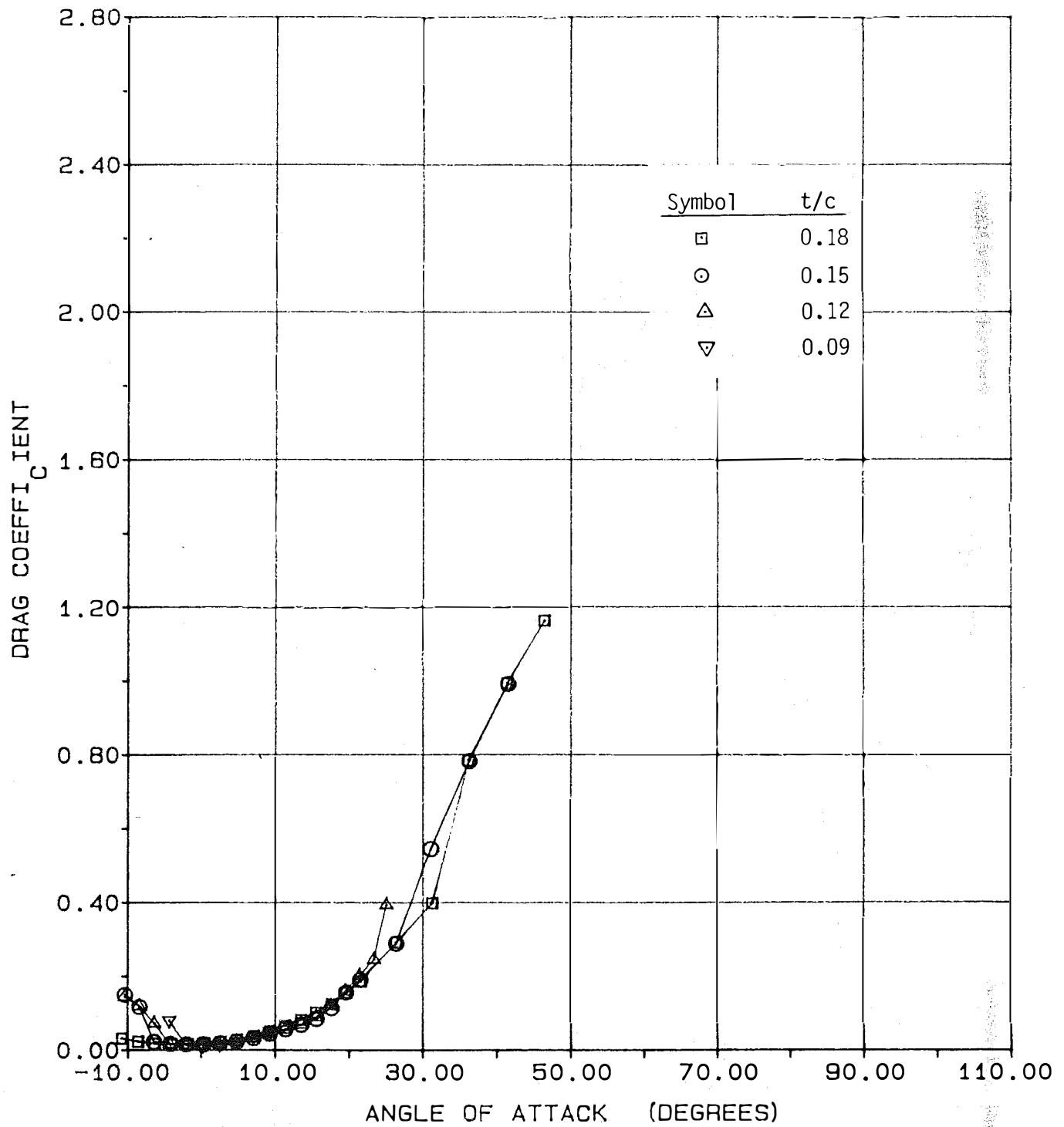
(b) Drag

Figure A.49- Concluded.



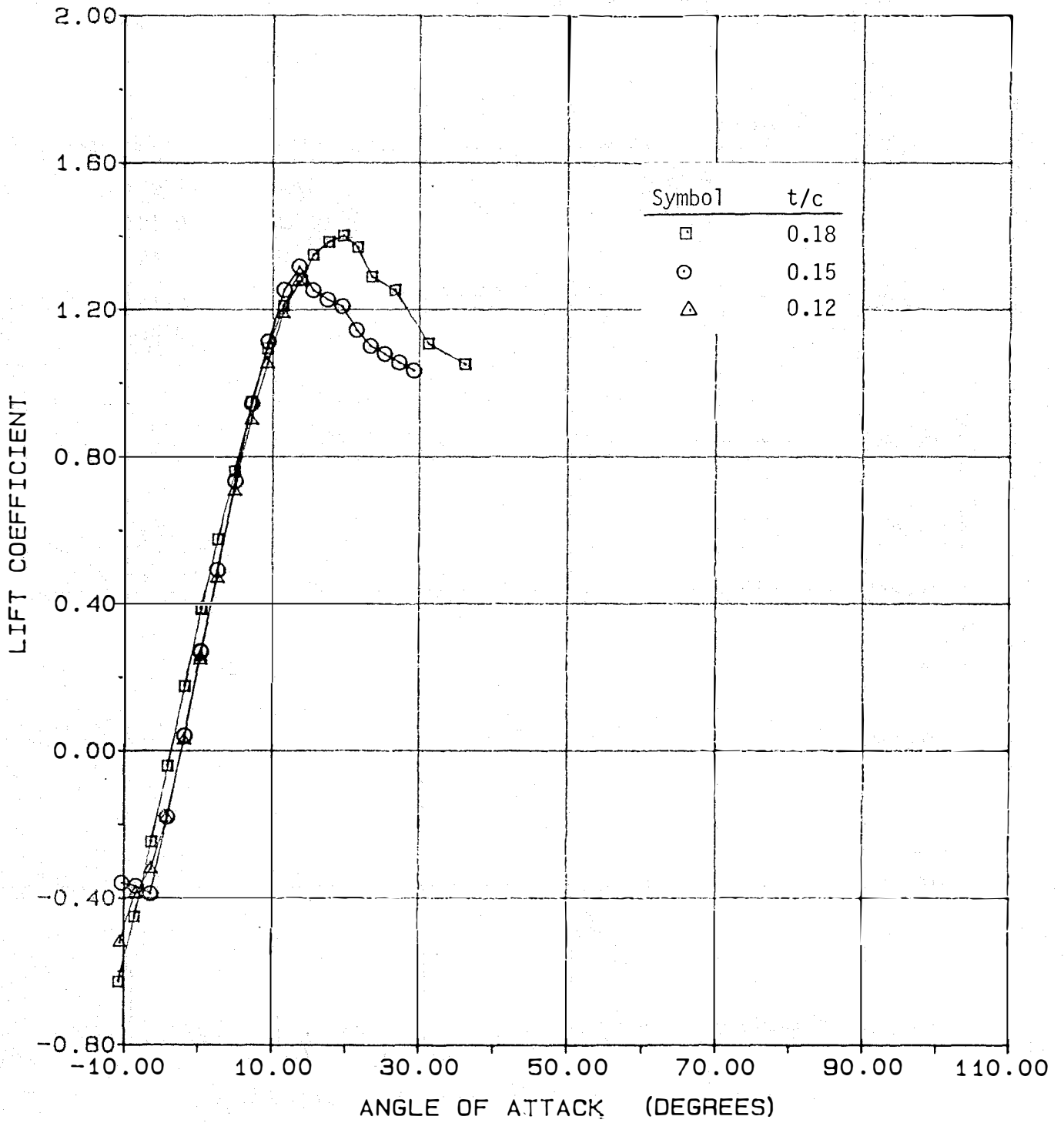
(a) Lift

Figure A.50- Effect of Airfoil Thickness on Aerodynamic Coefficients; Aspect Ratio = ∞ , $RN = 0.75 \times 10^6$.



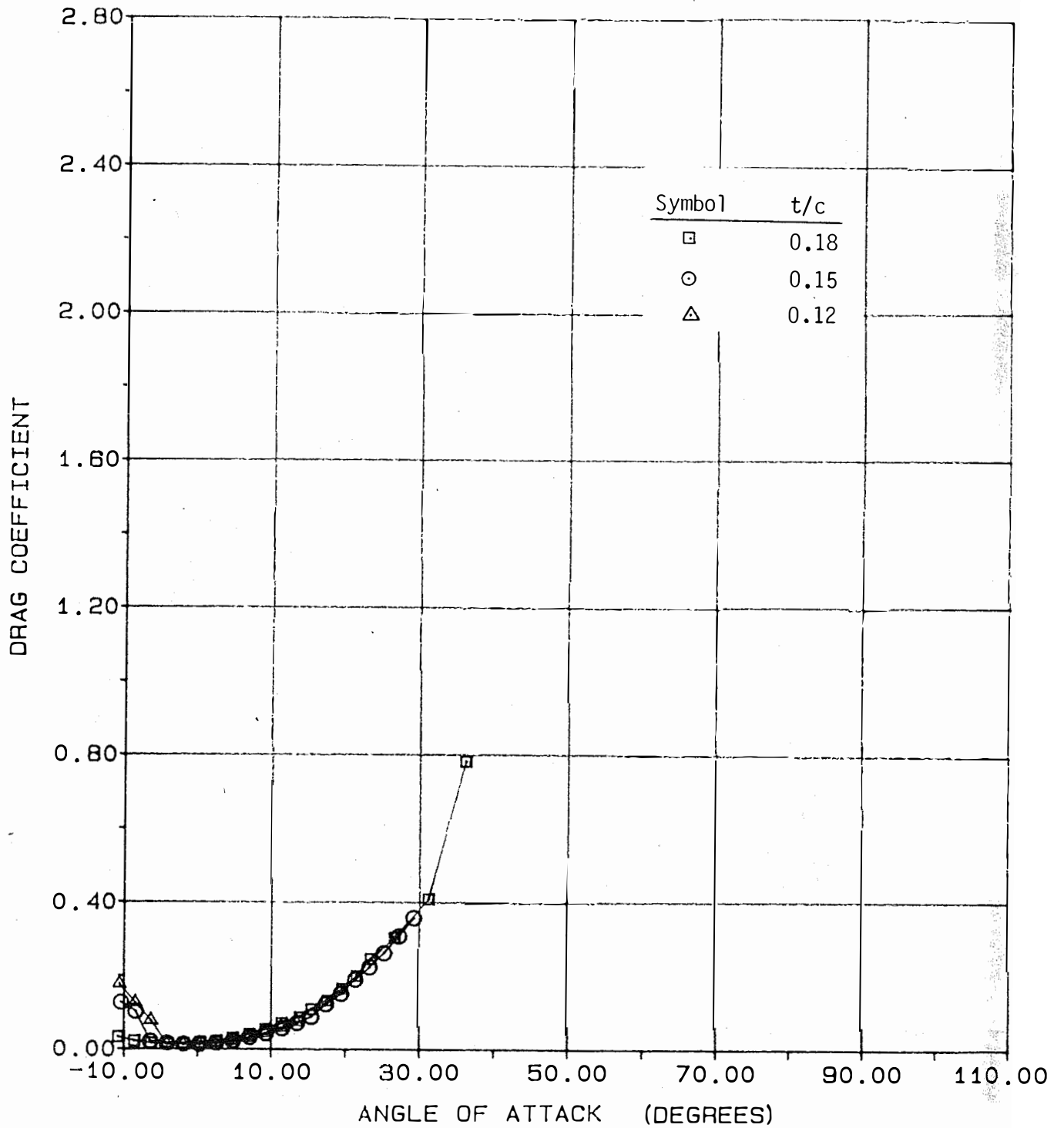
(b) Drag

Figure A.50- Concluded.



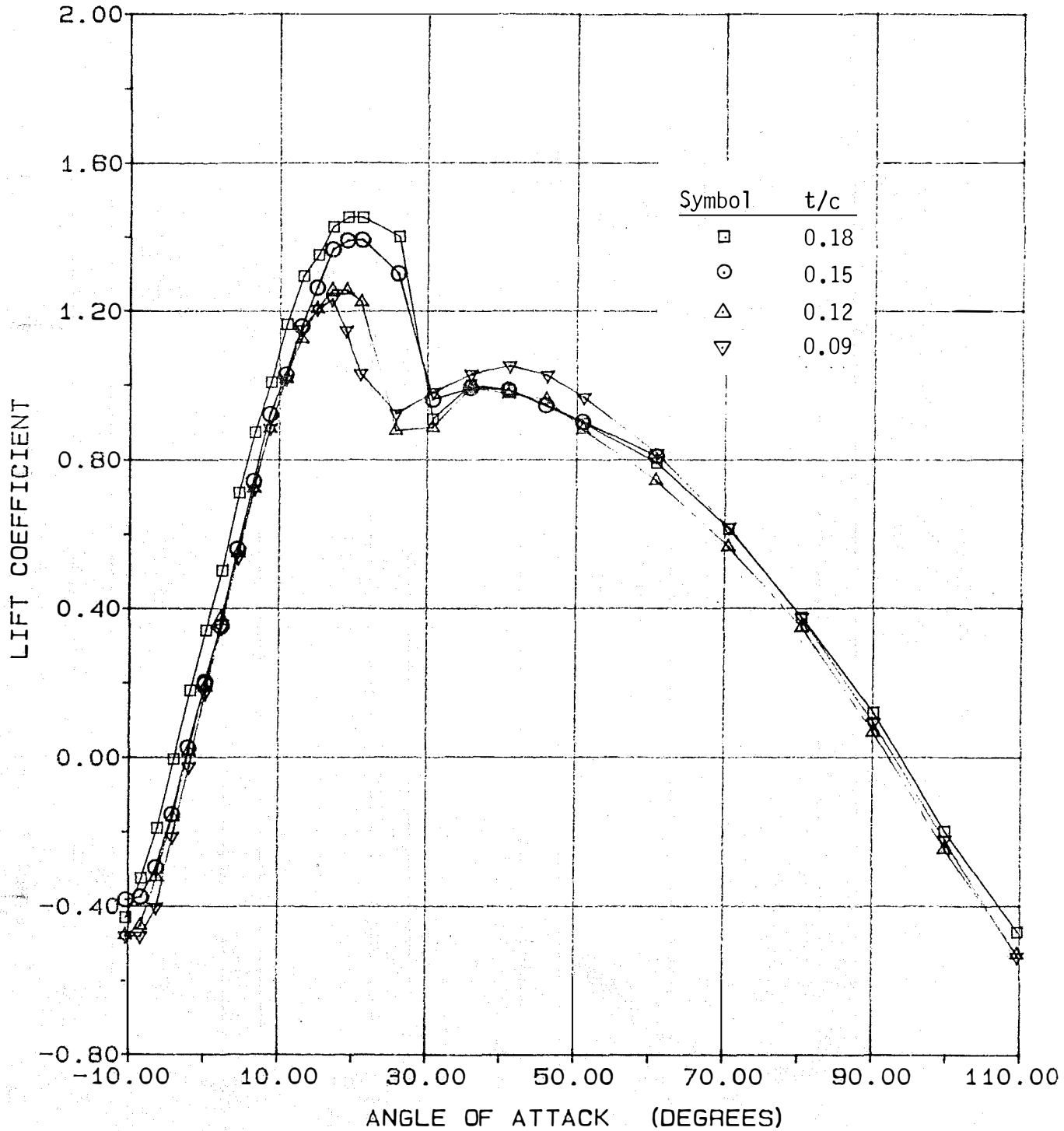
(a) Lift

Figure A.51- Effect of Airfoil Thickness on Aerodynamic Coefficients; Aspect Ratio = ∞ , $Re = 1.00 \times 10^6$.



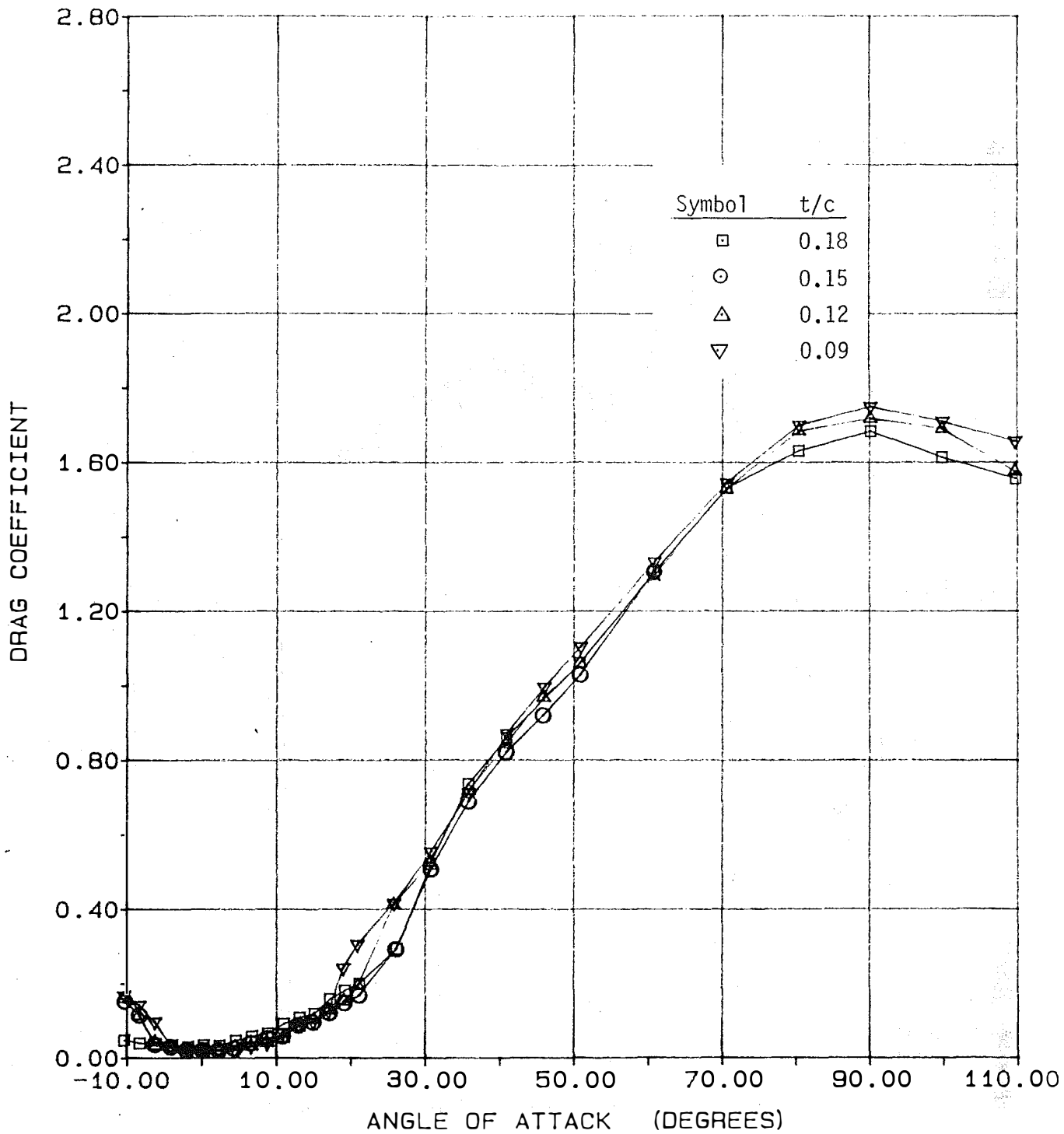
(b) Drag

Figure A.51- Concluded.



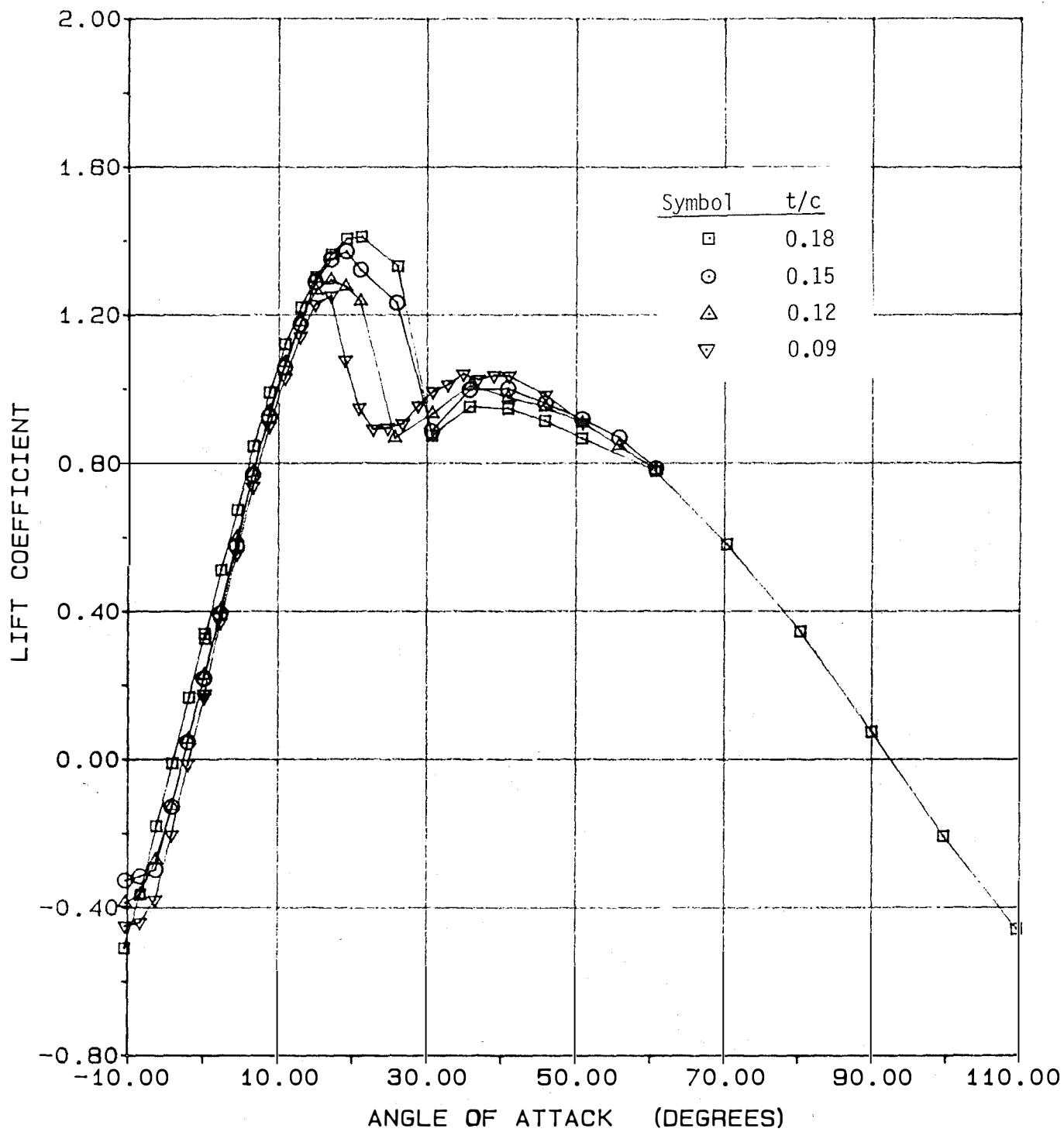
(a) Lift

Figure A.52- Effect of Airfoil Thickness on Aerodynamic Coefficients; Aspect Ratio = 12, $RN = 0.25 \times 10^6$.



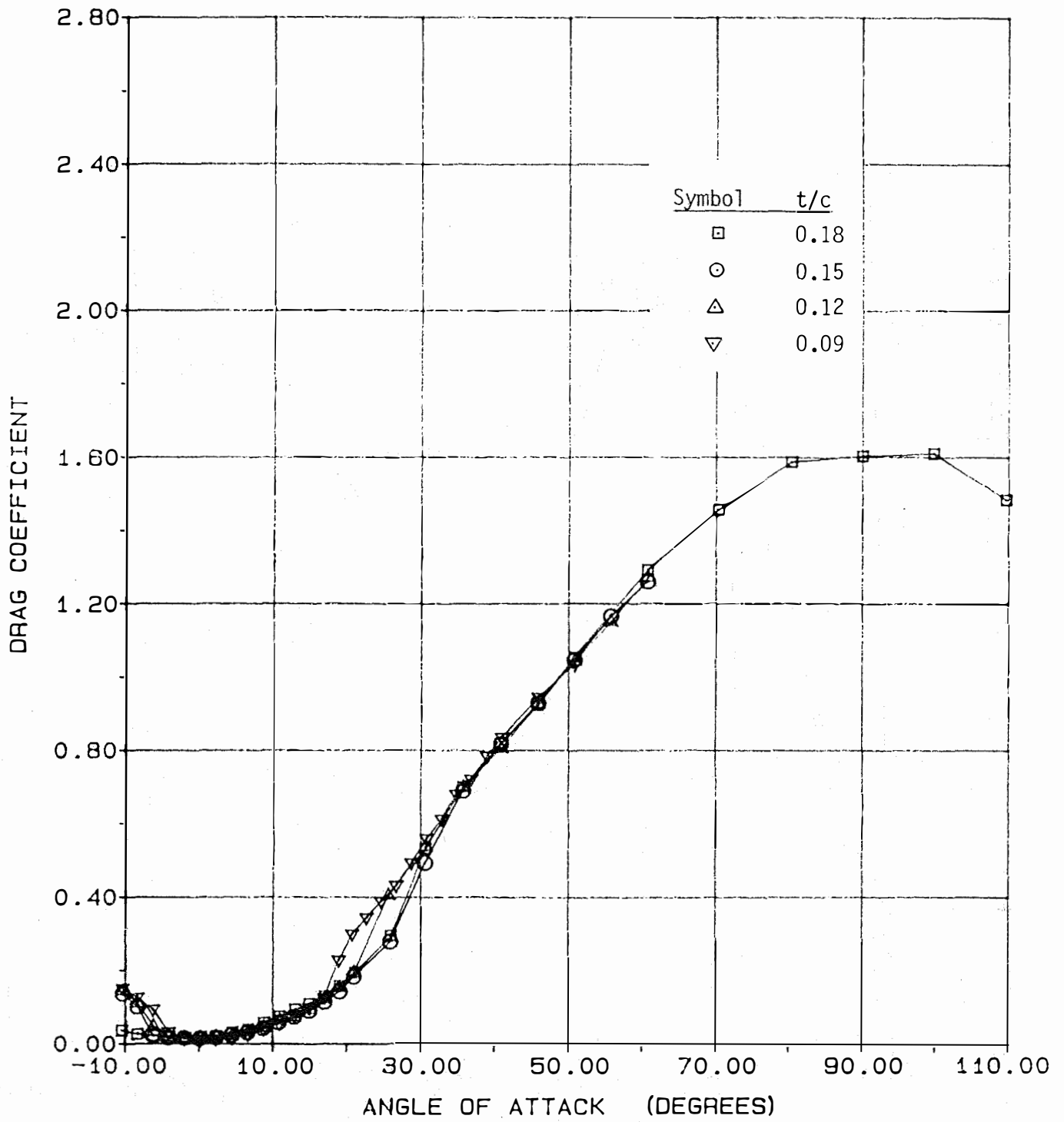
(b) Drag

Figure A.52- Concluded.



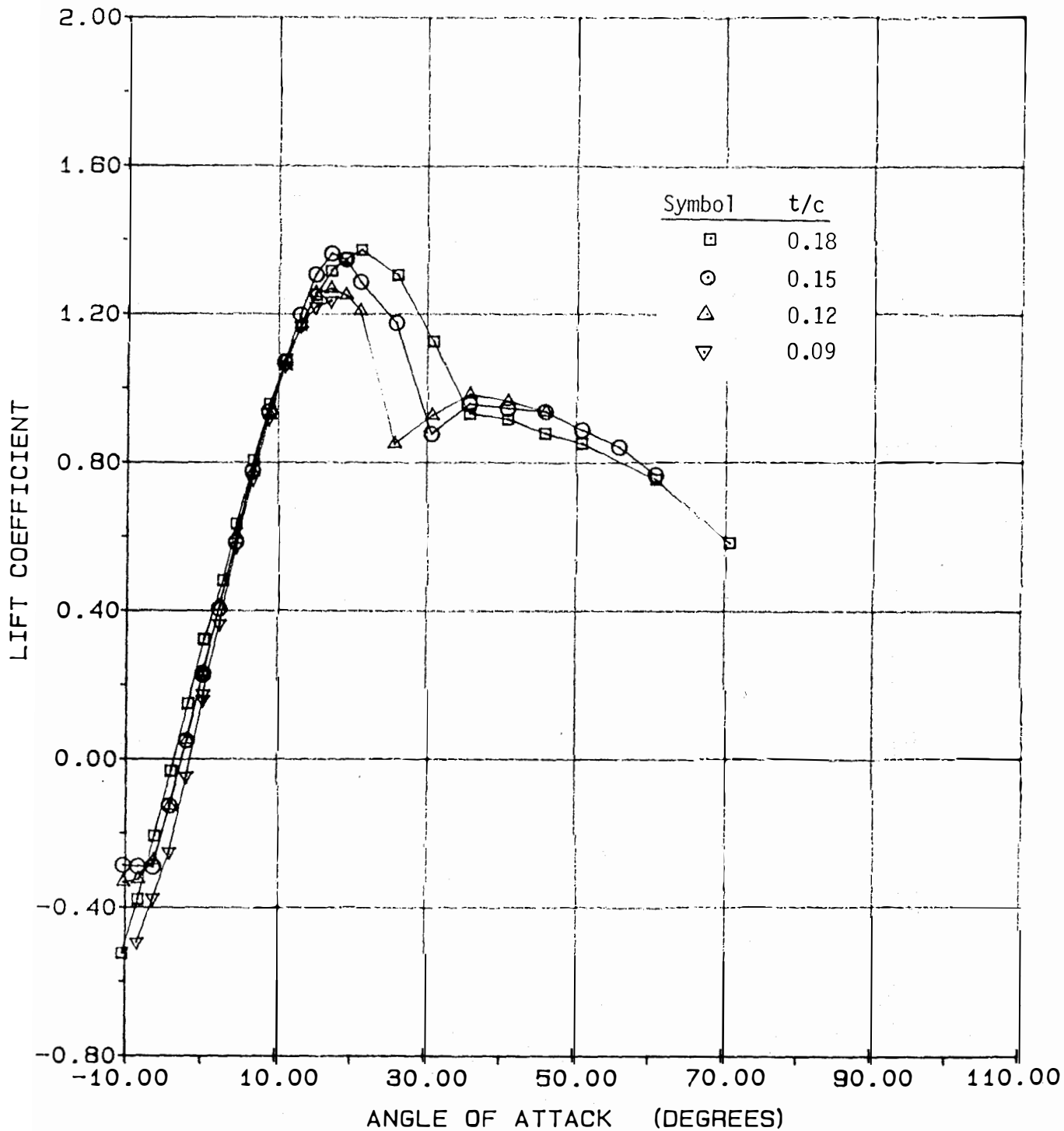
(a) Lift

Figure A.53- Effect of Airfoil Thickness on Aerodynamic Coefficients; Aspect Ratio = 12, $RN = 0.50 \times 10^6$.



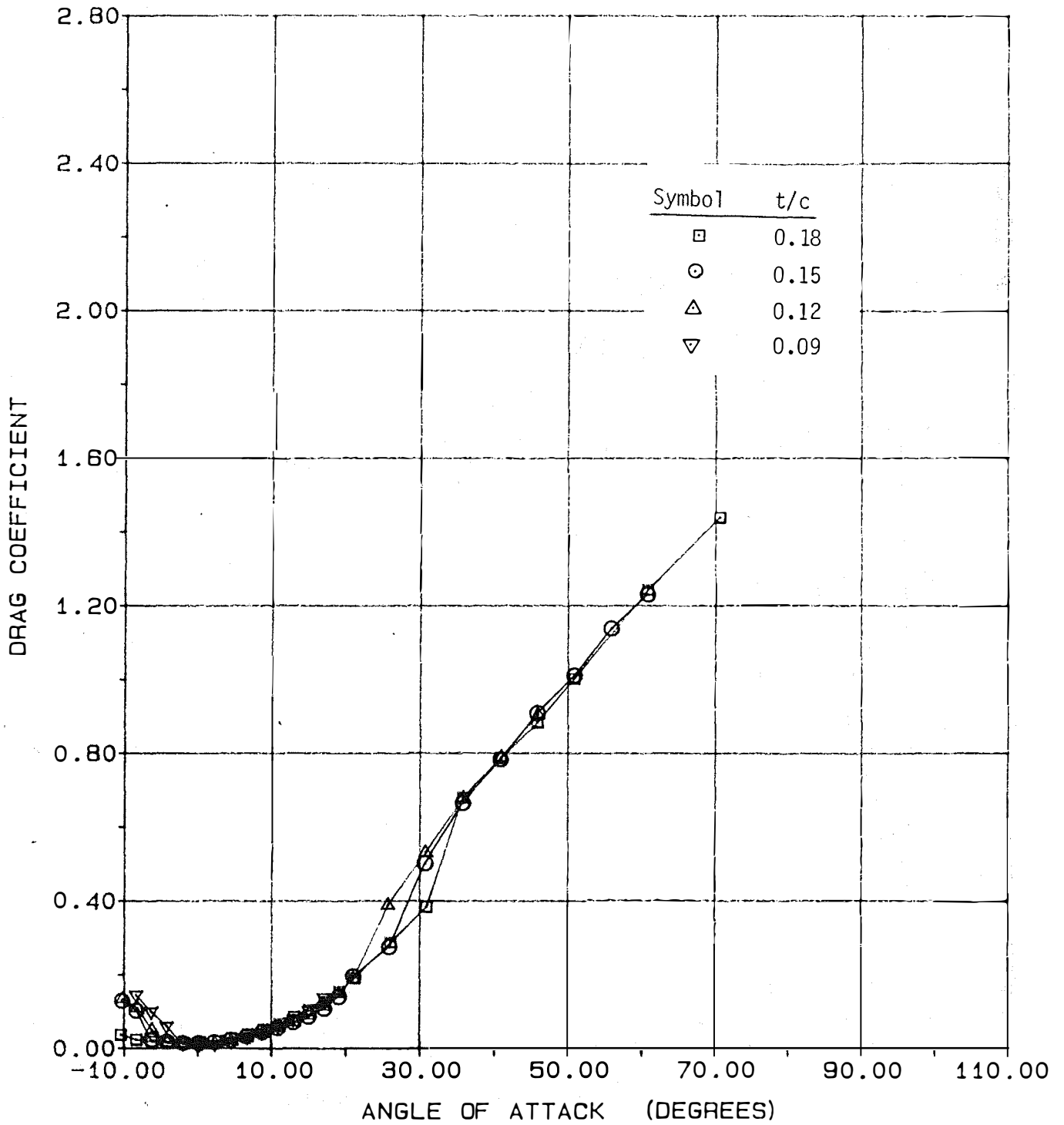
(b) Drag

Figure A.53- Concluded.



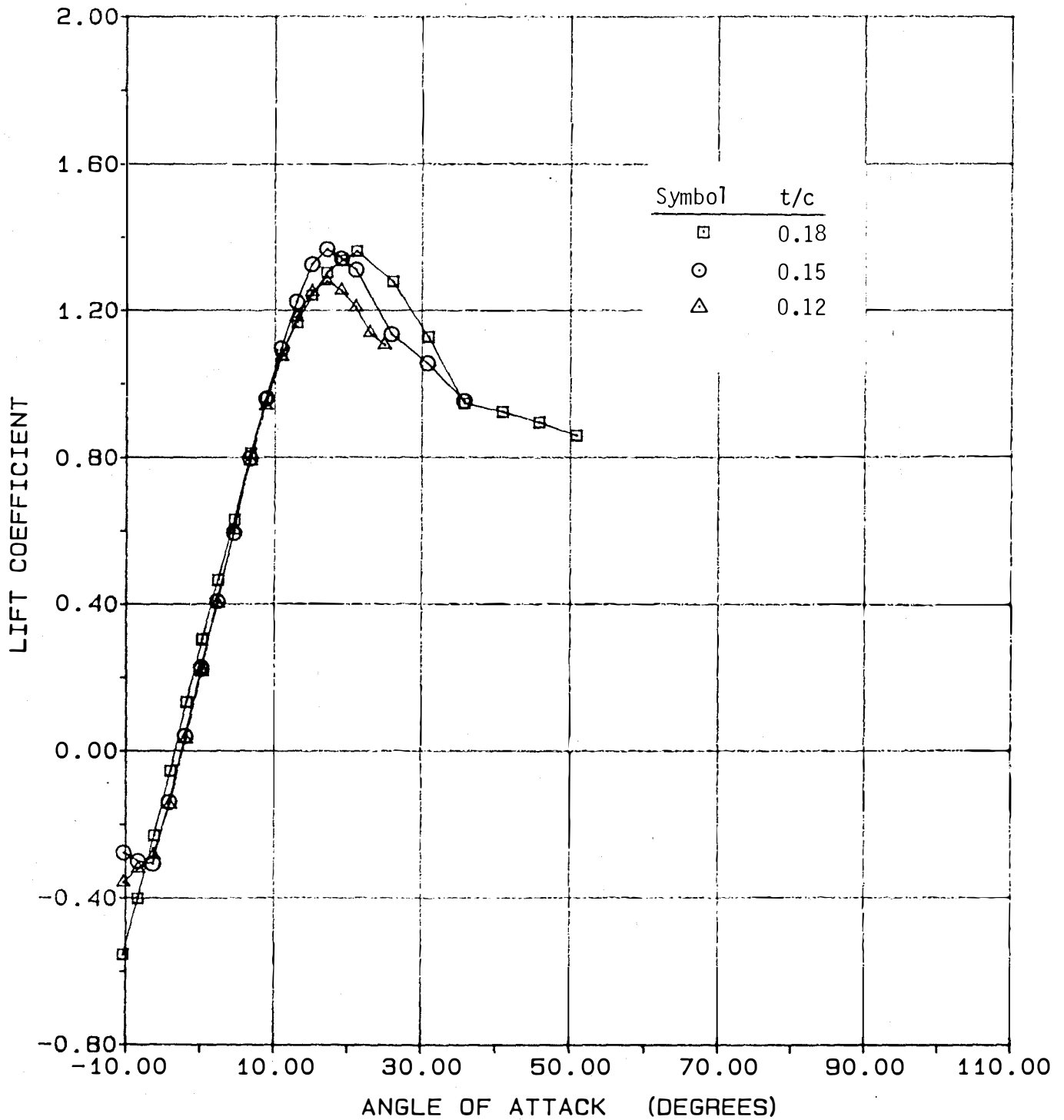
(a) Lift

Figure A.54- Effect of Airfoil Thickness on Aerodynamic Coefficients; Aspect Ratio = 12, $RN = 0.75 \times 10^6$.



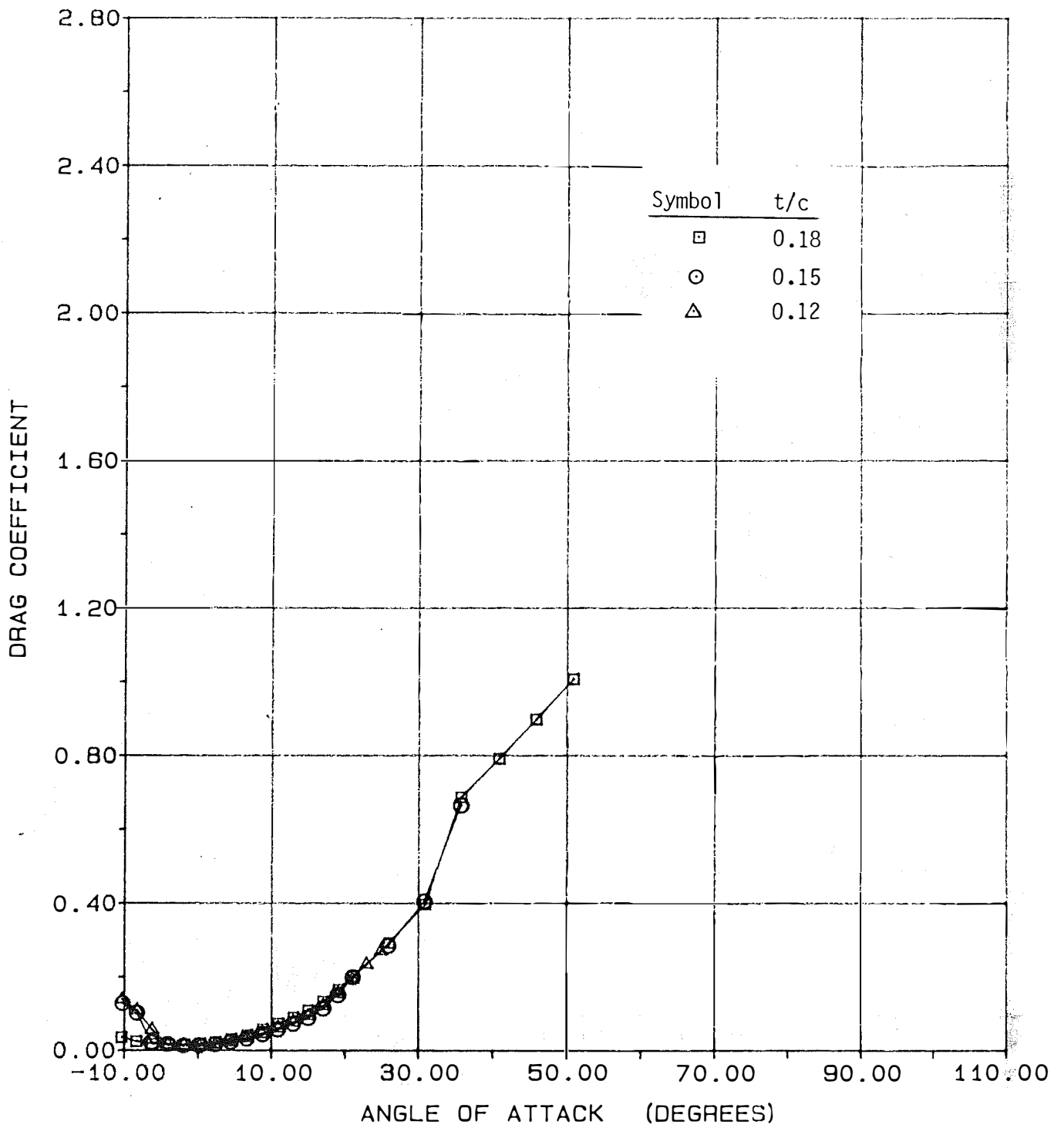
(b) Drag

Figure A.54- Concluded.



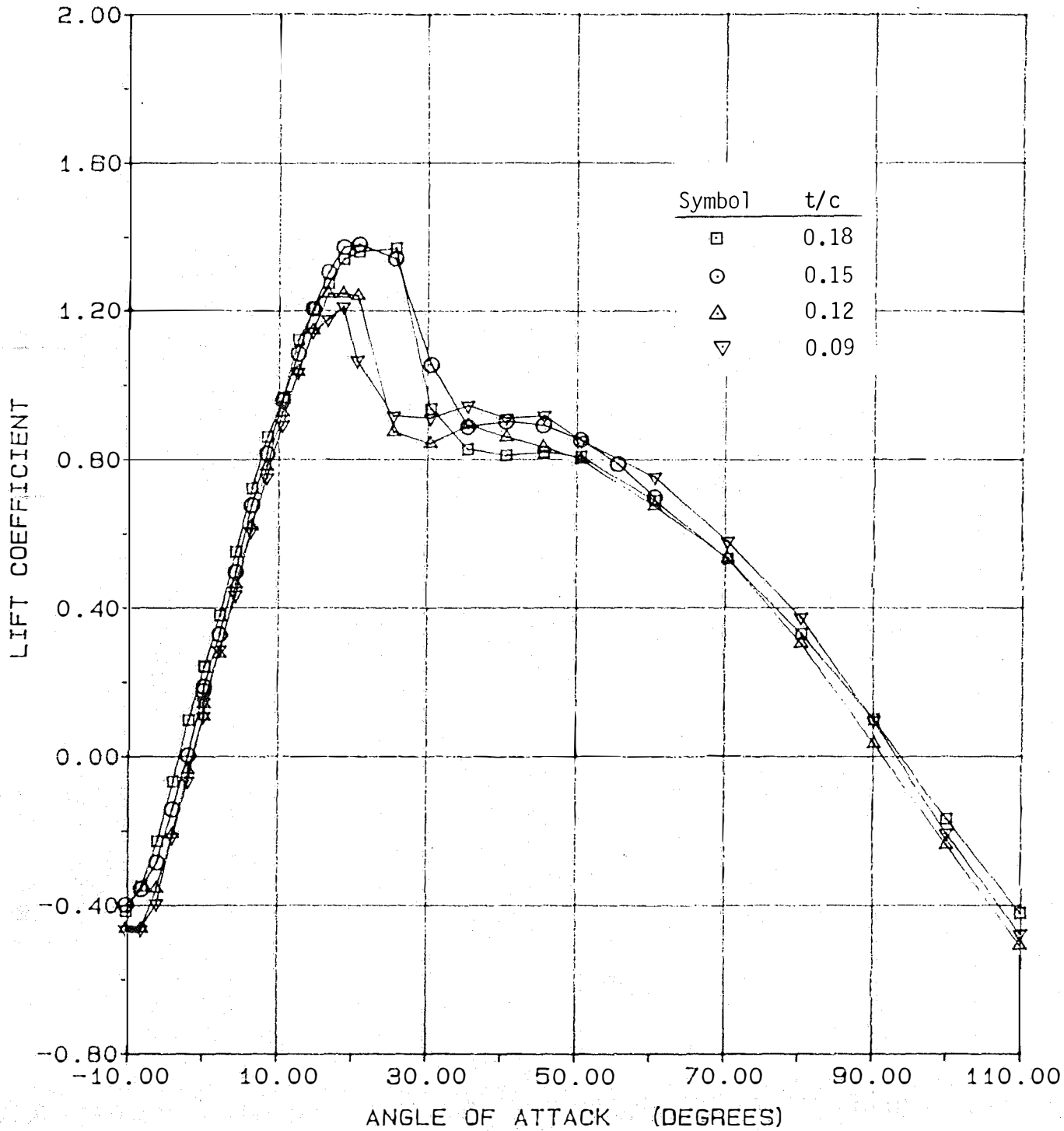
(a) Lift

Figure A.55- Effect of Airfoil Thickness on Aerodynamic Coefficients; Aspect Ratio = 12 , $RN = 1.00 \times 10^6$.



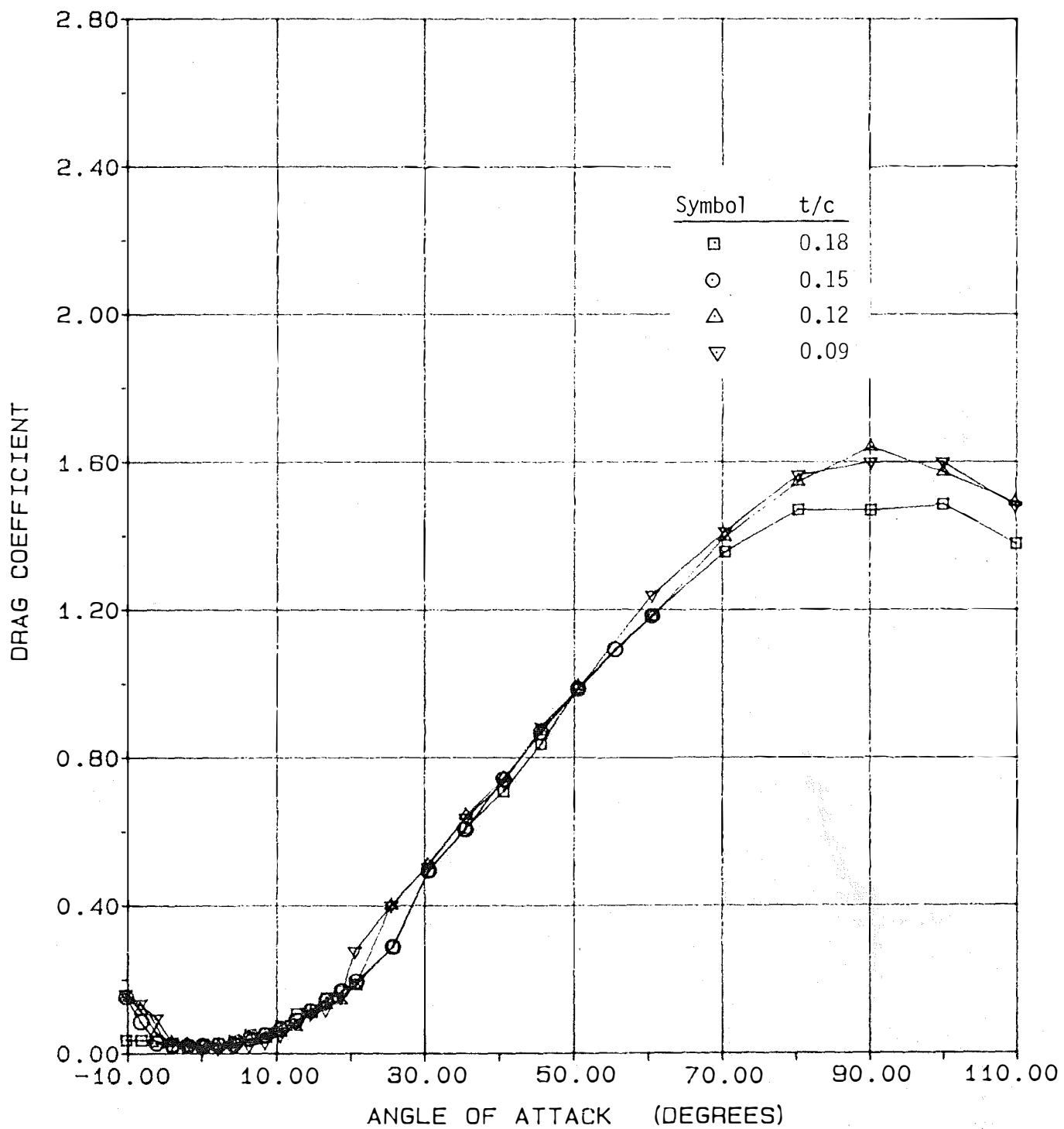
(b) Drag

Figure A.55- Concluded.



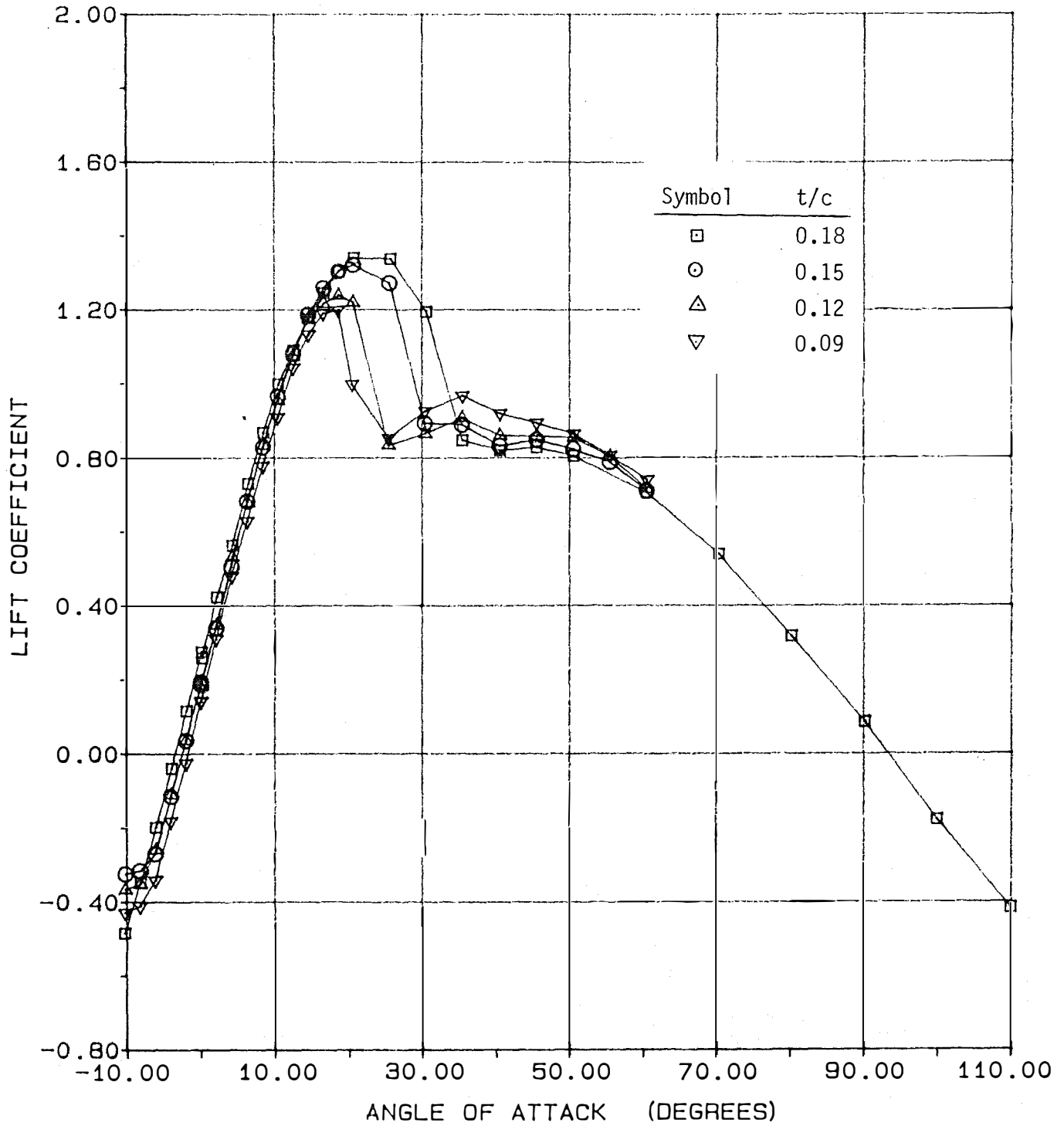
(a) Lift

Figure A.56- Effect of Airfoil Thickness on Aerodynamic Coefficients; Aspect Ratio = 9, $Re = 0.25 \times 10^6$.



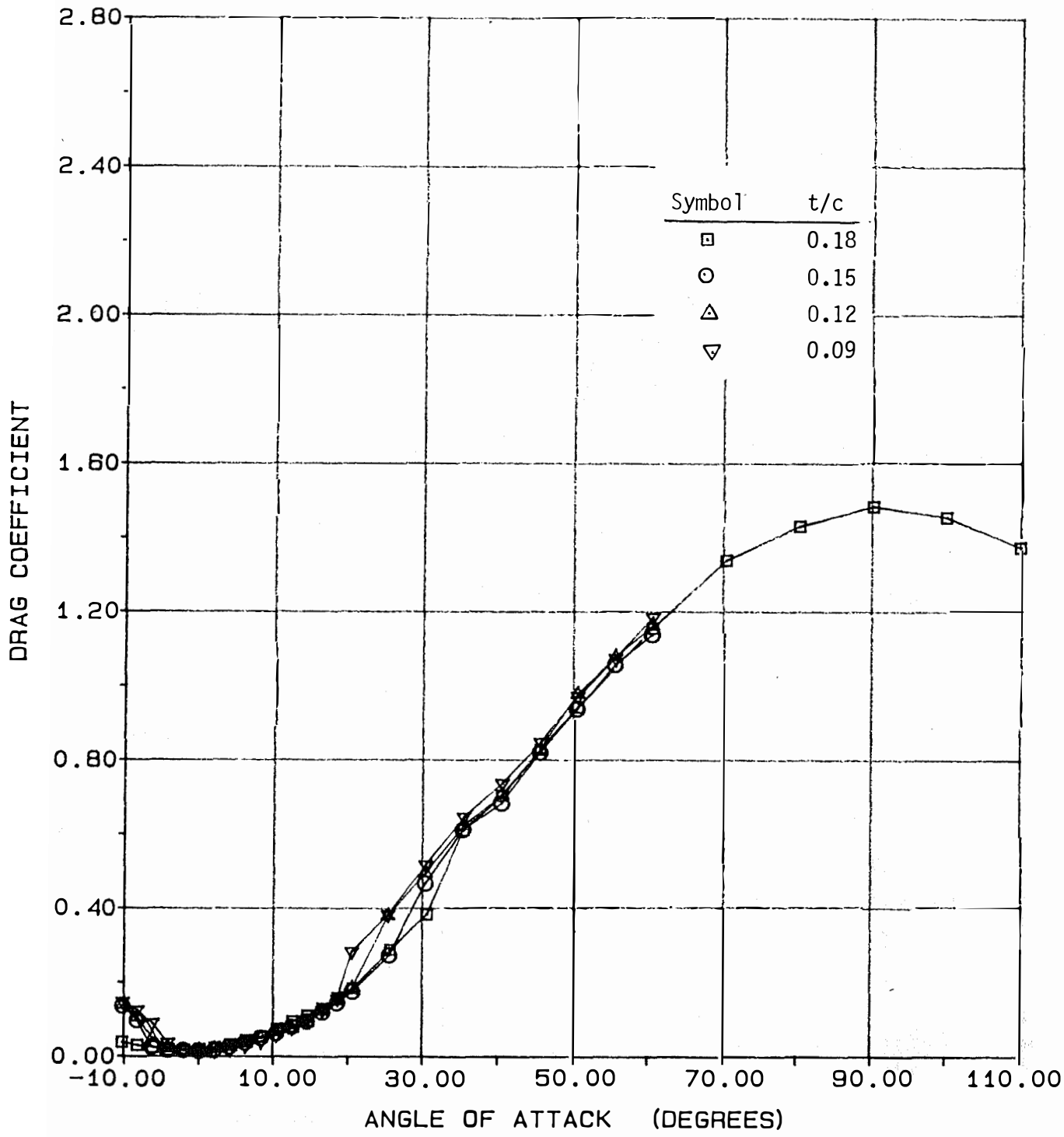
(b) Drag

Figure A.56- Concluded.



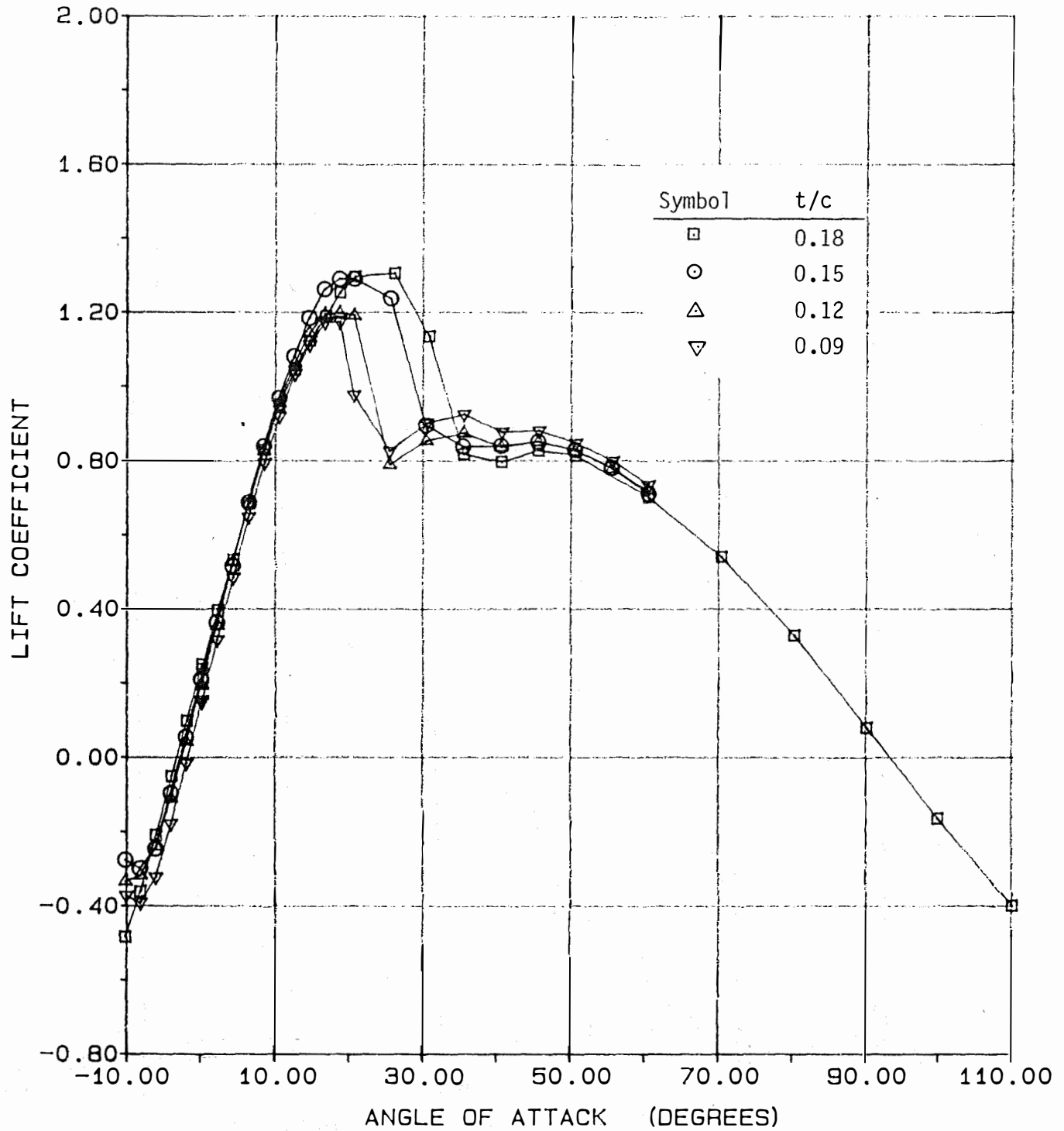
(a) Lift

Figure A.57- Effect of Airfoil Thickness on Aerodynamic Coefficients; Aspect Ratio = 9, $Re = 0.50 \times 10^6$.



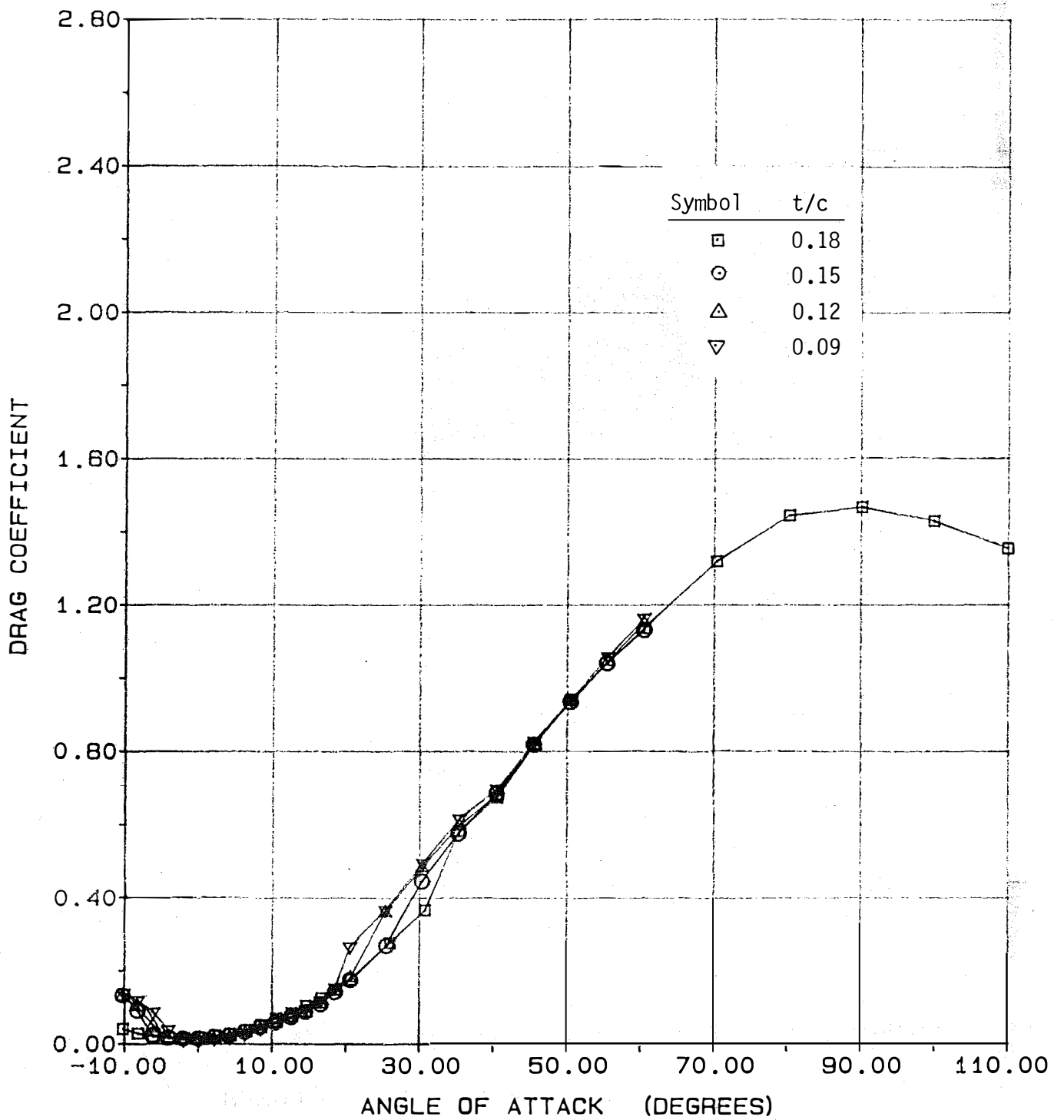
(b) Drag

Figure A.57- Concluded.



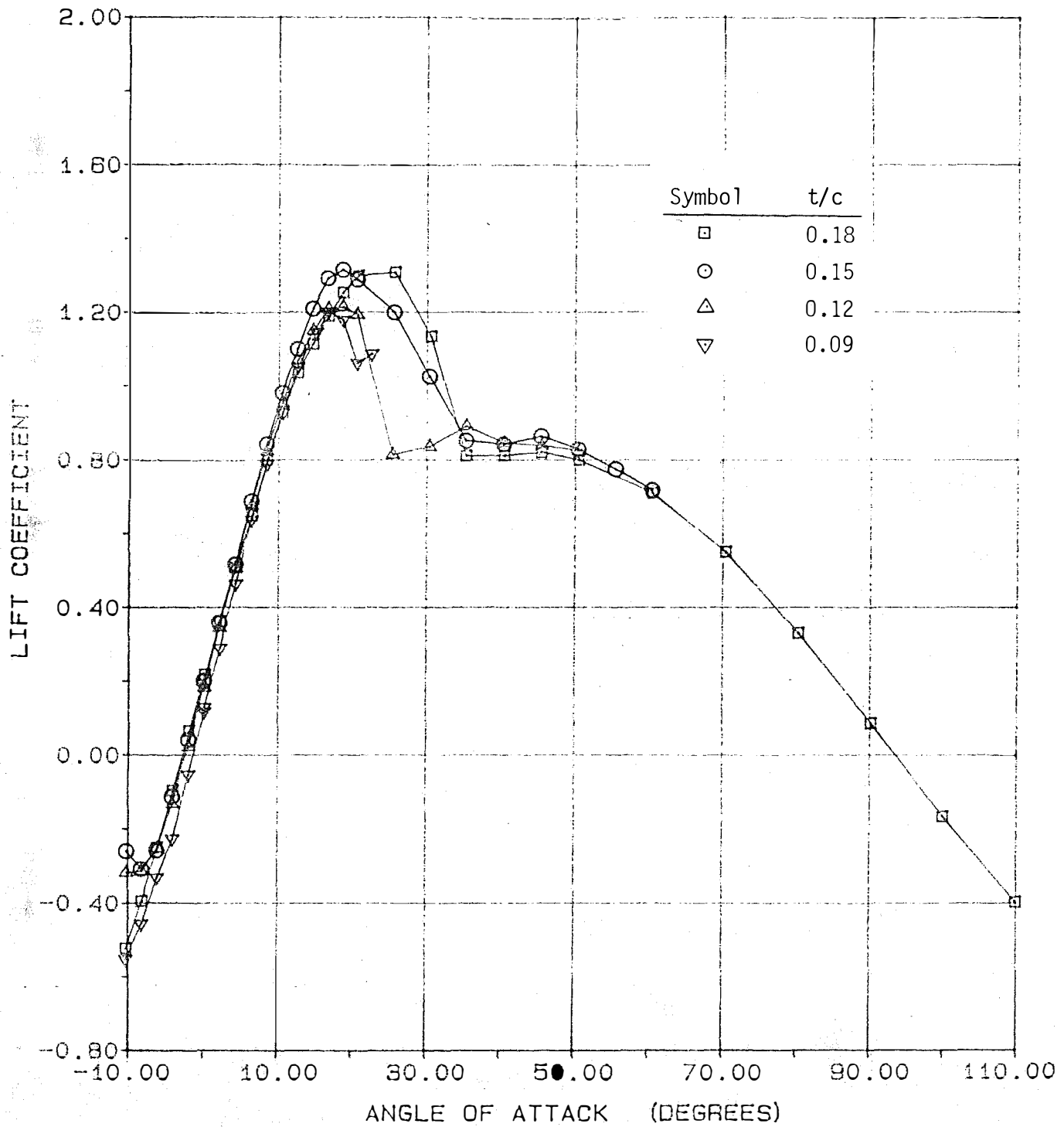
(a) Lift

Figure A.58- Effect of Airfoil Thickness on Aerodynamic Coefficients; Aspect Ratio = 9, $RN = 0.75 \times 10^6$.



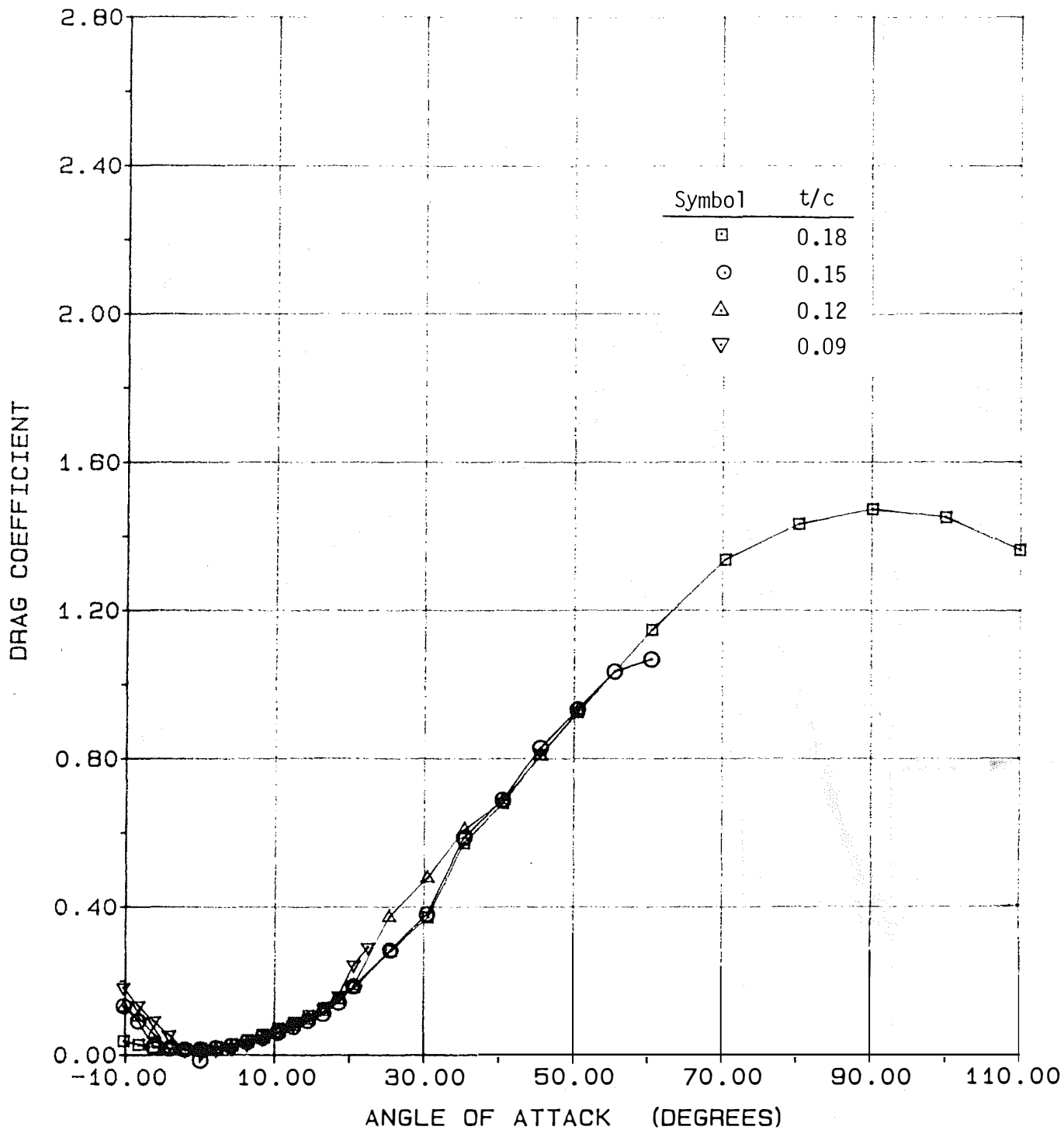
(b) Drag

Figure A.58- Concluded.



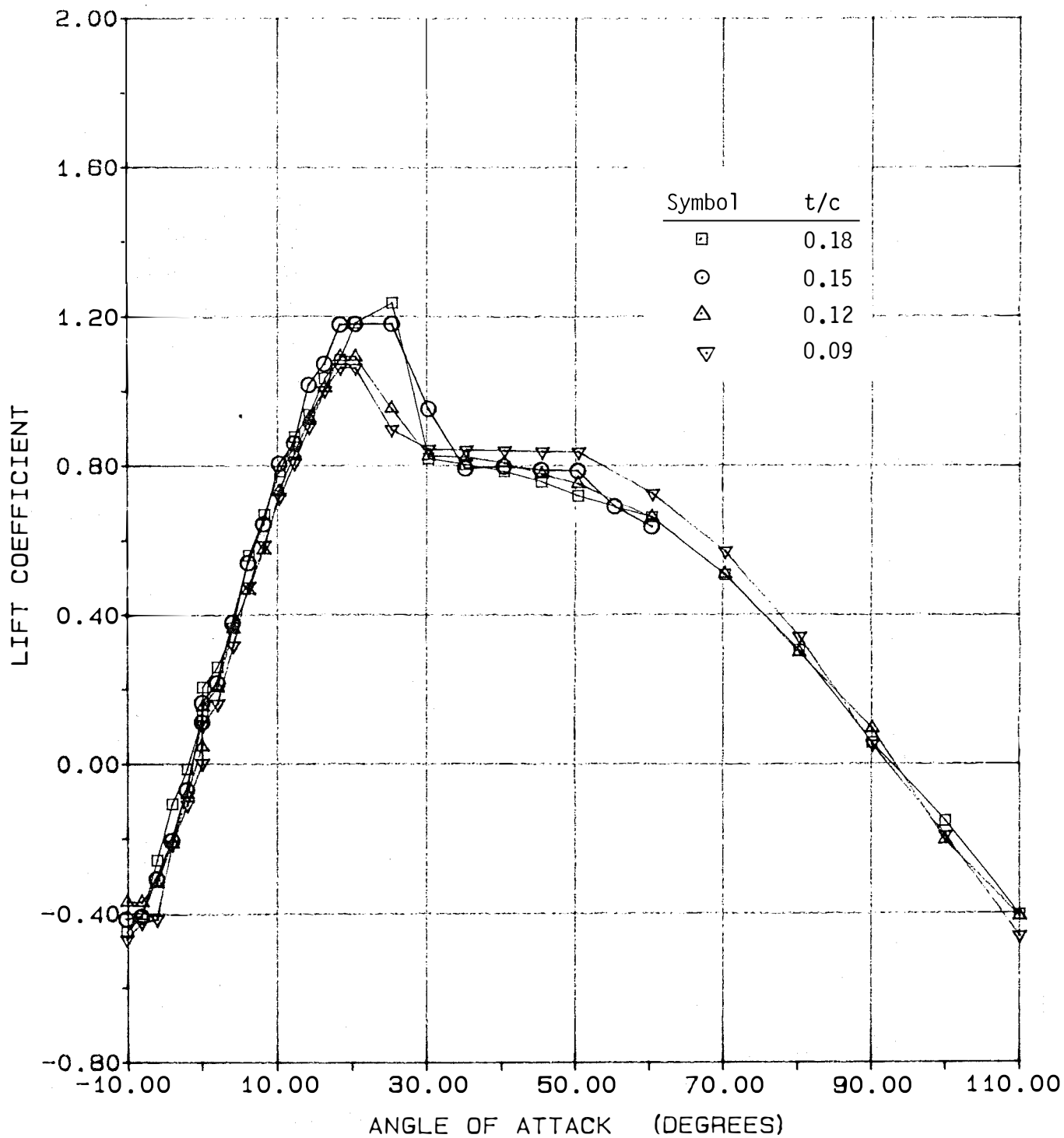
(a) Lift

Figure A.59- Effect of Airfoil Thickness on Aerodynamic Coefficients; Aspect Ratio = 9, $RN = 1.00 \times 10^6$.



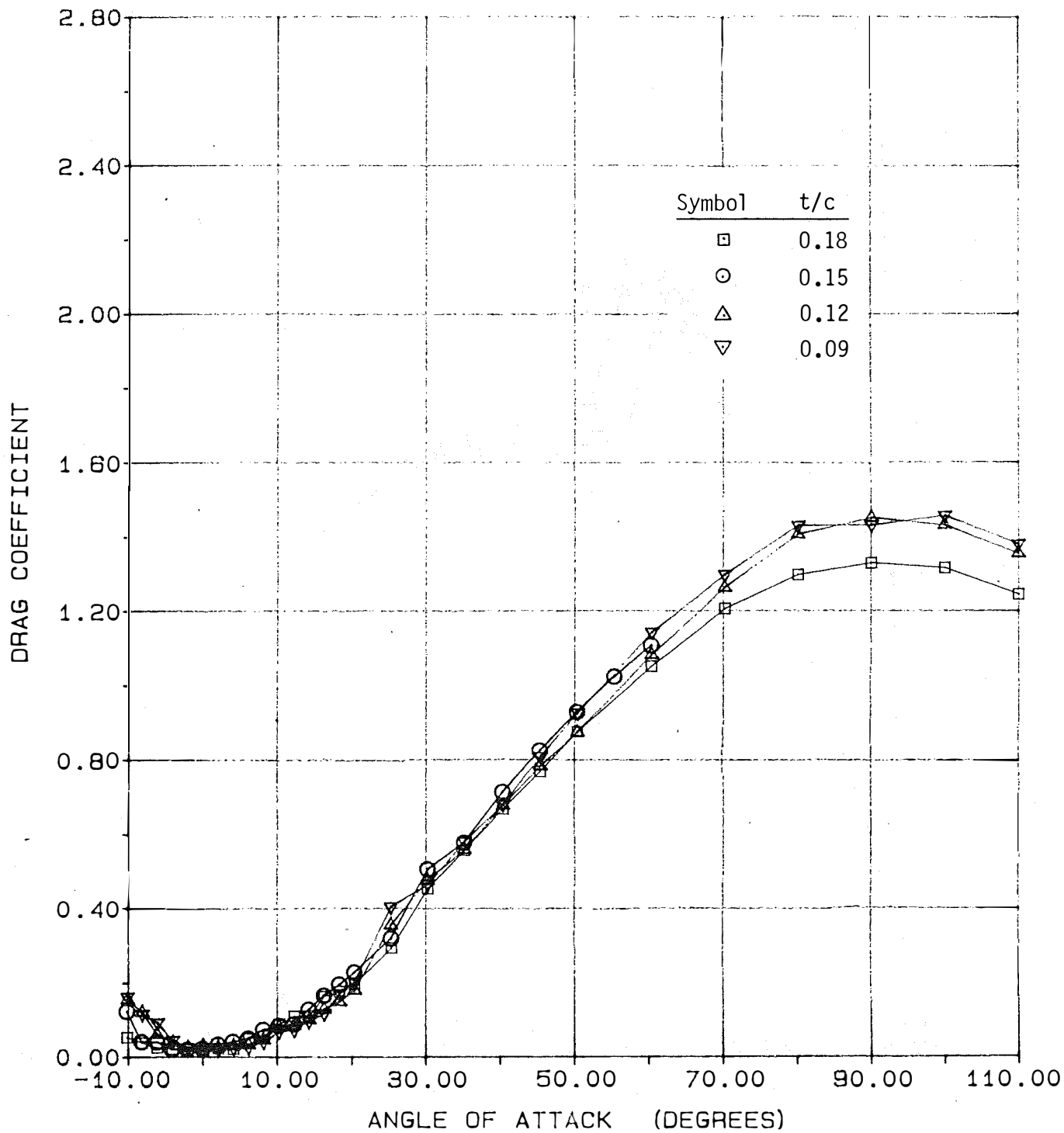
(b) Drag

Figure A.59- Concluded.



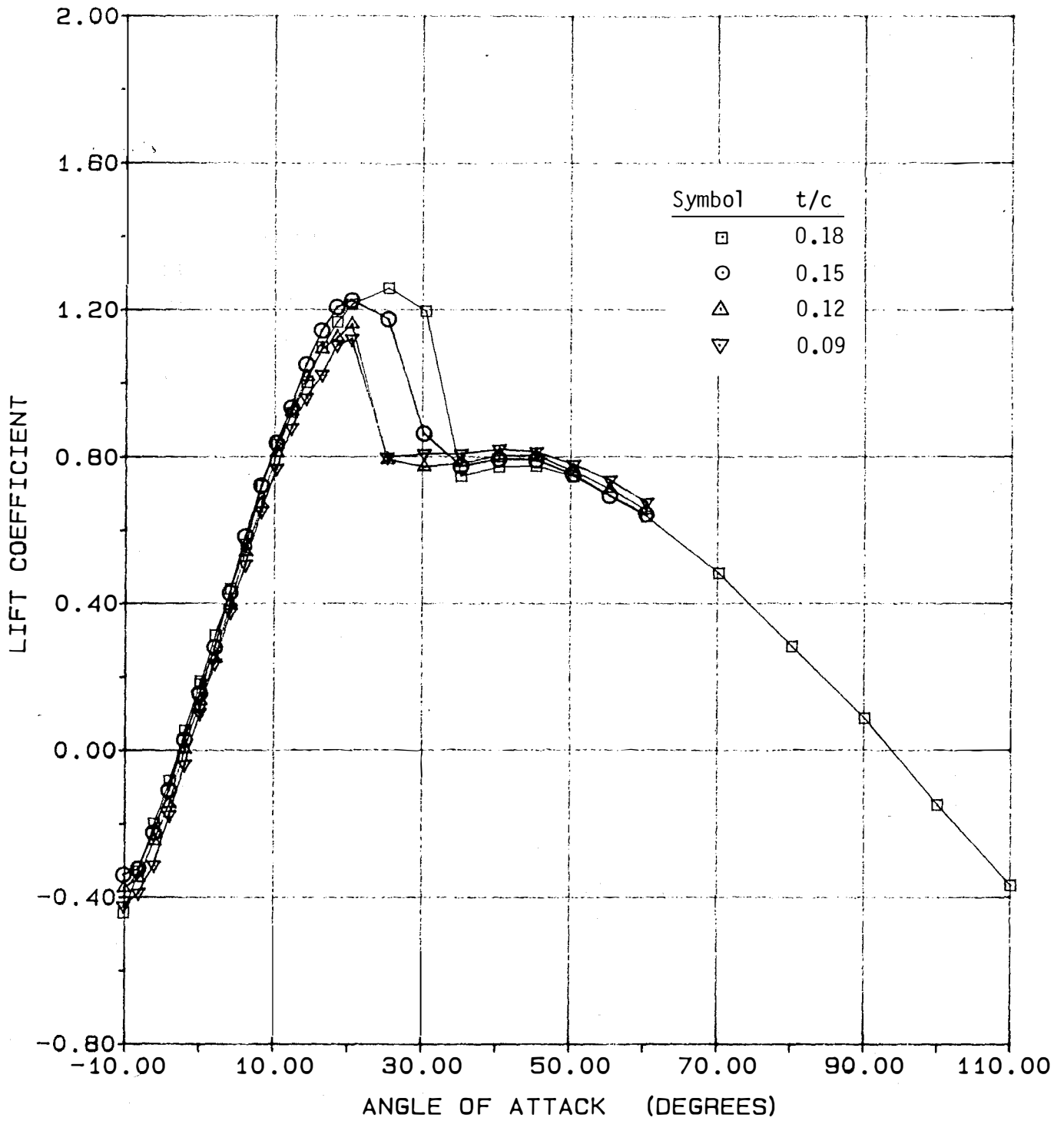
(a) Lift

Figure A.60- Effect of Airfoil Thickness on Aerodynamic Coefficients; Aspect Ratio = 6, $RN = 0.25 \times 10^6$.



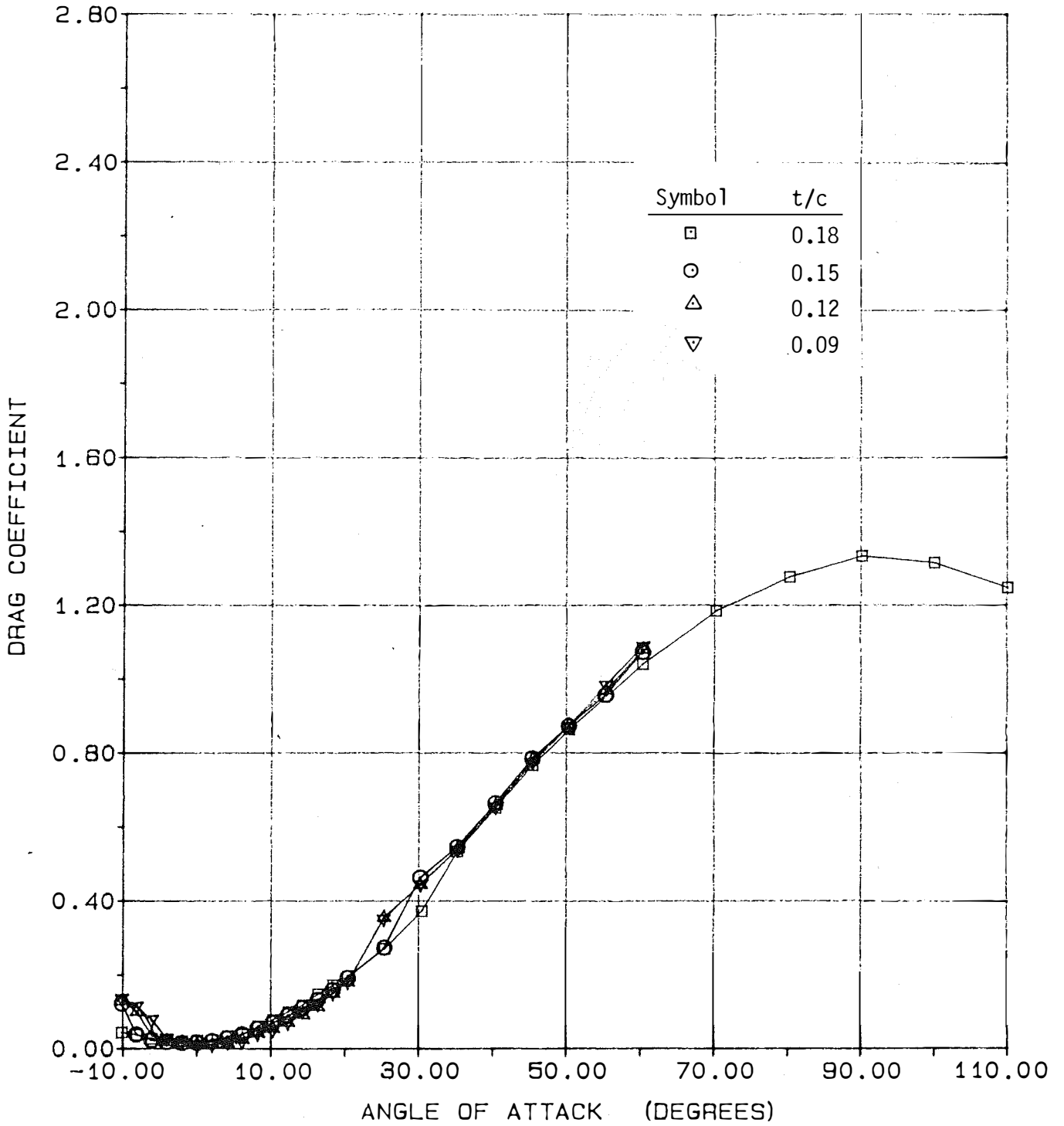
(b) Drag

Figure A.60- Concluded.



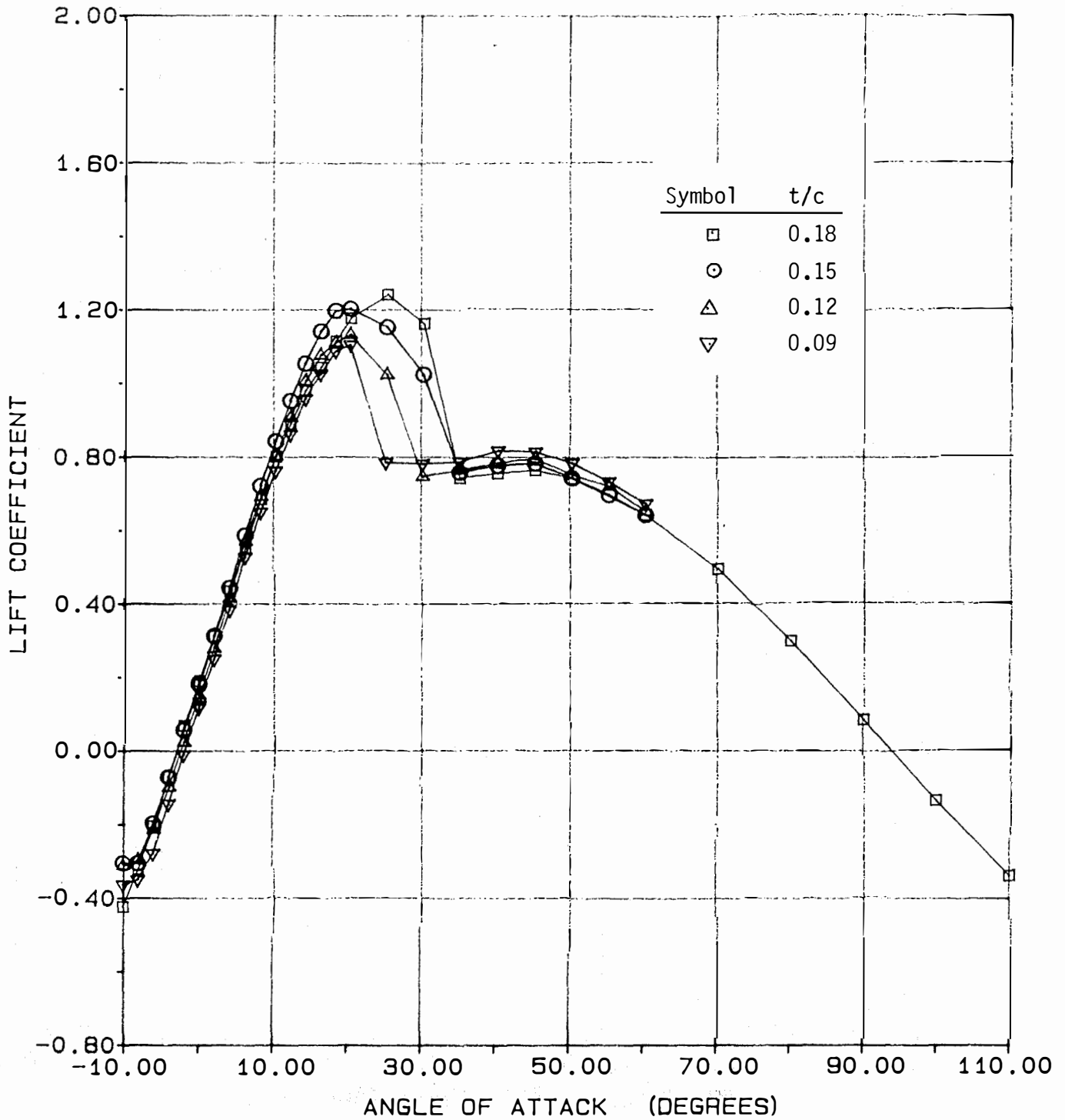
(a) Lift

Figure A.61- Effect of Airfoil Thickness on Aerodynamic Coefficients; Aspect Ratio = 6, $RN = 0.50 \times 10^6$.



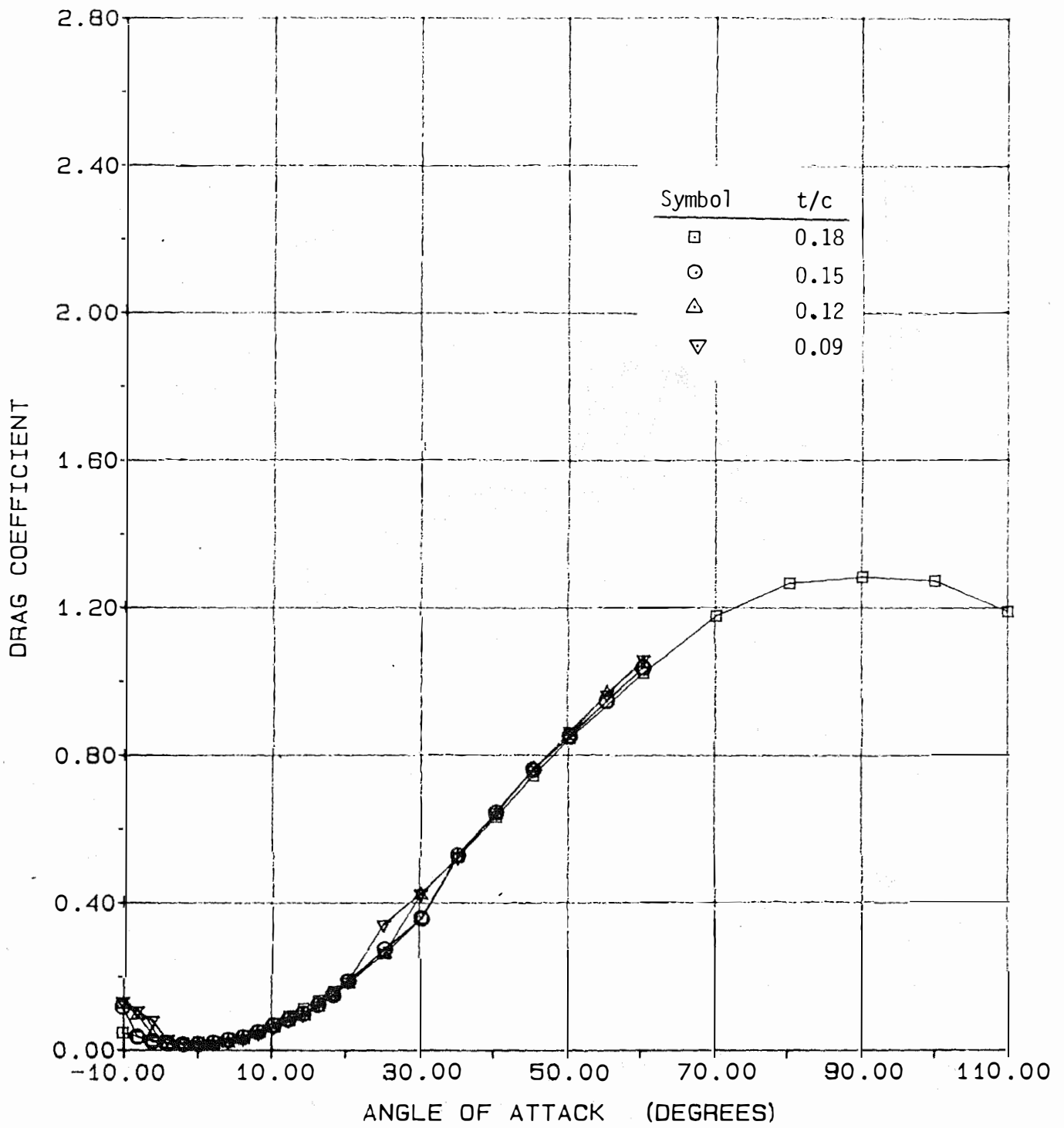
(b) Drag

Figure A.61- Concluded.



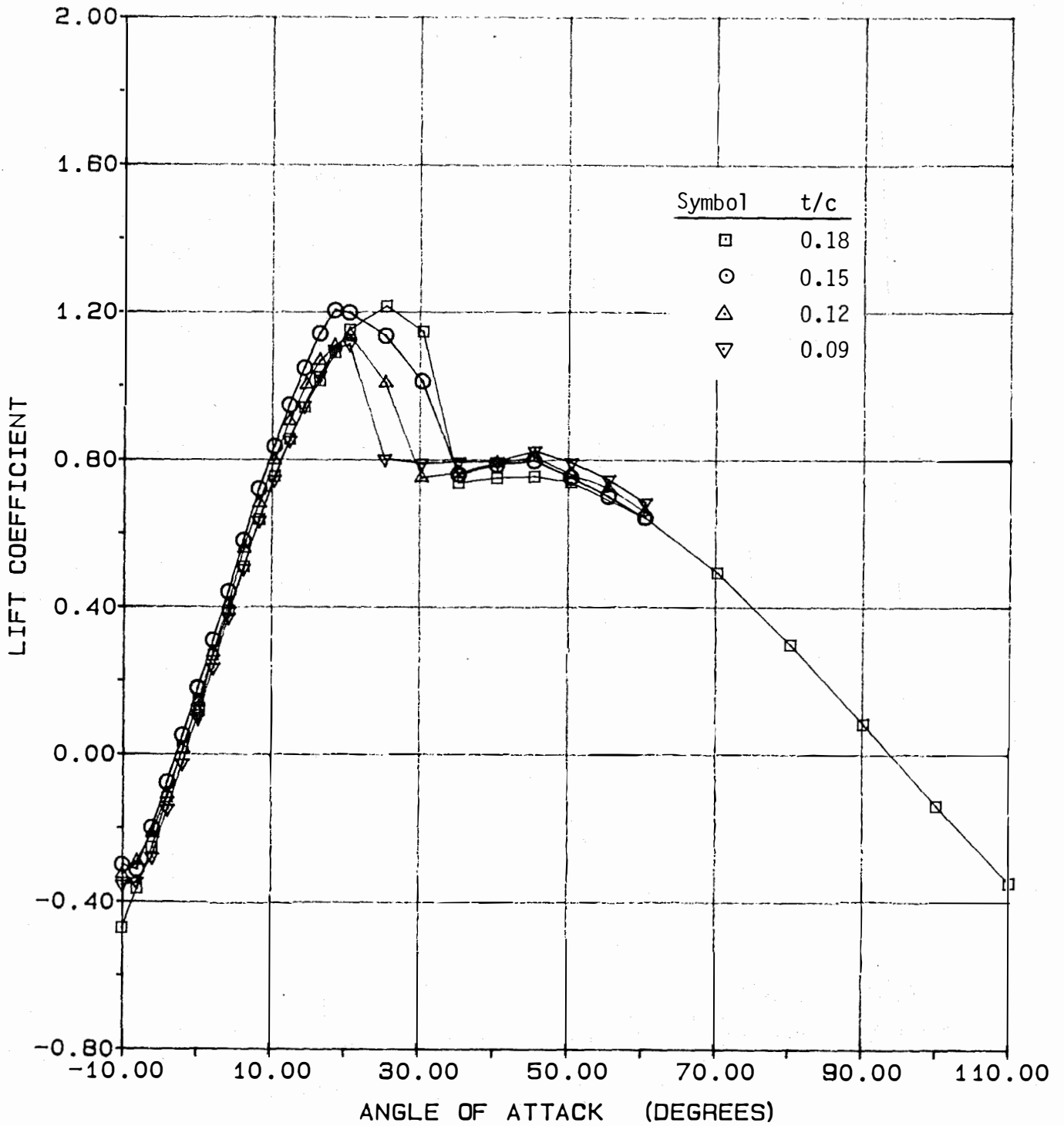
(a) Lift

Figure A.62- Effect of Airfoil Thickness on Aerodynamic Coefficients; Aspect Ratio = 6, $Re = 0.75 \times 10^6$.



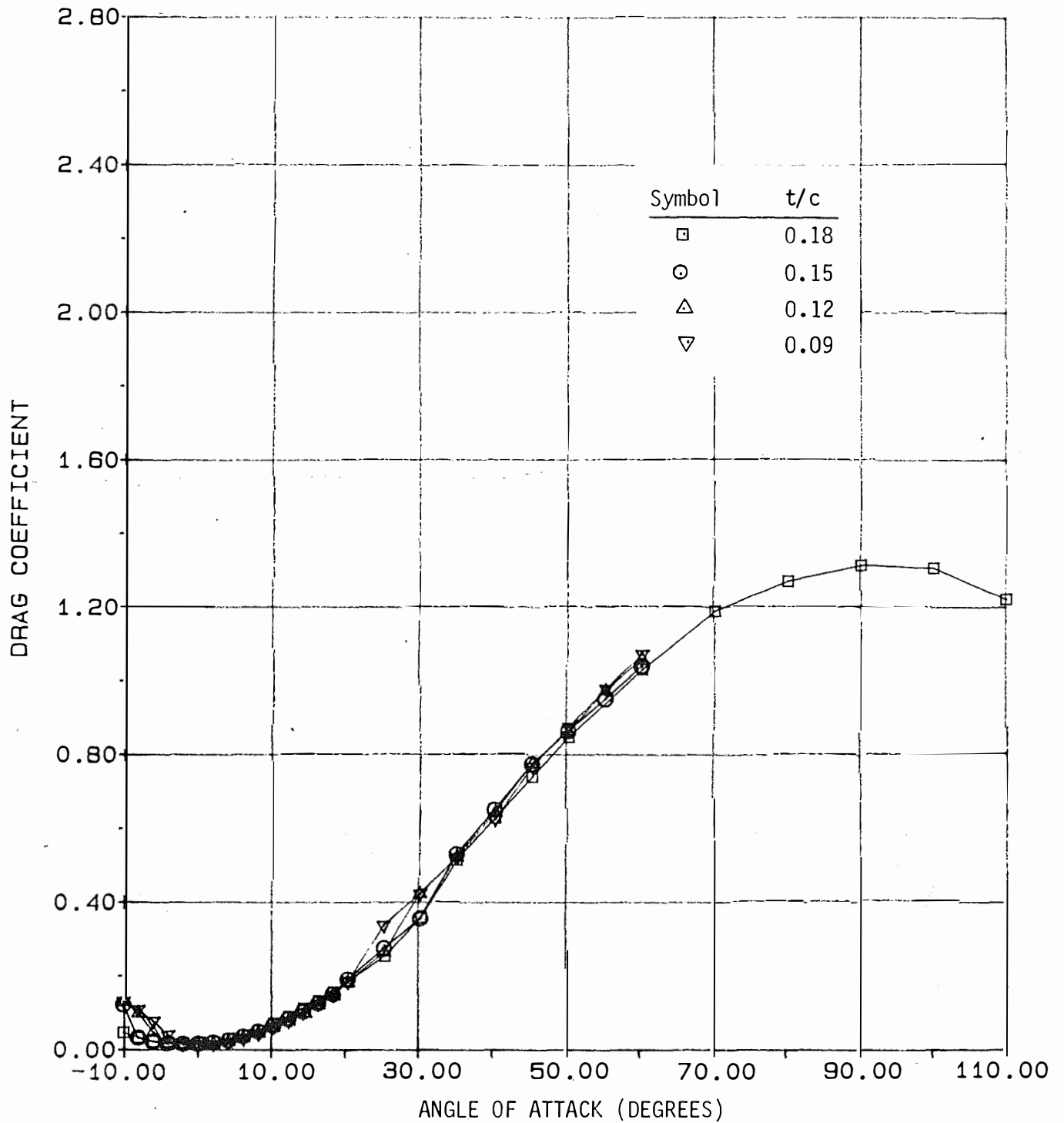
(b) Drag

Figure A.62- Concluded.



(a) Lift

Figure A.63- Effect of Airfoil Thickness on Aerodynamic Coefficients; Aspect Ratio = 6, $RN = 1.00 \times 10^6$.



(b) Drag

Figure A.63- Concluded.

APPENDIX B

WAKE RAKE DRAG ESTIMATION

Wake rake drag measurements are given for the four two-dimensional blades (Figures B.1 through B.4). The angle of attack range is restricted to -10° to 12° . This is done because the momentum defect method of estimating drag is not amenable to the highly separated flow regimes present beyond α_{stall} . These measurements are useful in estimating end plate drag using the procedure given below.

At pre-stall angles of attack, the end plate drag is the difference between force balance drag and the wake survey drag. The end plate drag consists of tare and interference drag. It depends upon the lift coefficient as well as airfoil section shape. In higher angle of attack regimes, the end plate drag is estimated by linearly extrapolating the (low lift coefficient) end plate drag curve. The extrapolation gives a reasonable estimate because at high angles of attack, the section drag is the dominant factor in the force balance measurement.

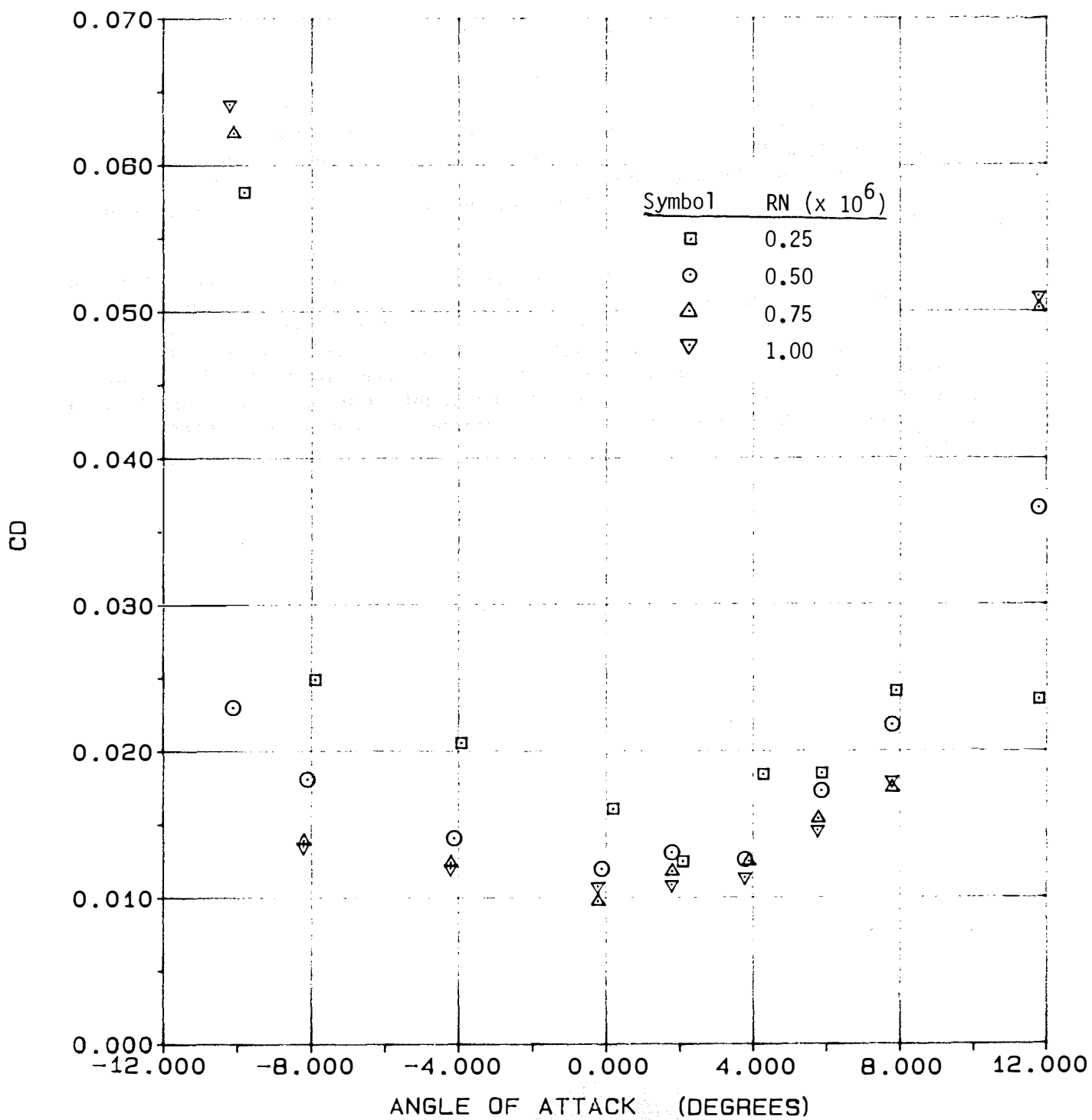


Figure B.1 - Wake Rake Drag Coefficient of the NACA 4418 Airfoil.
(Aspect Ratio = ∞).

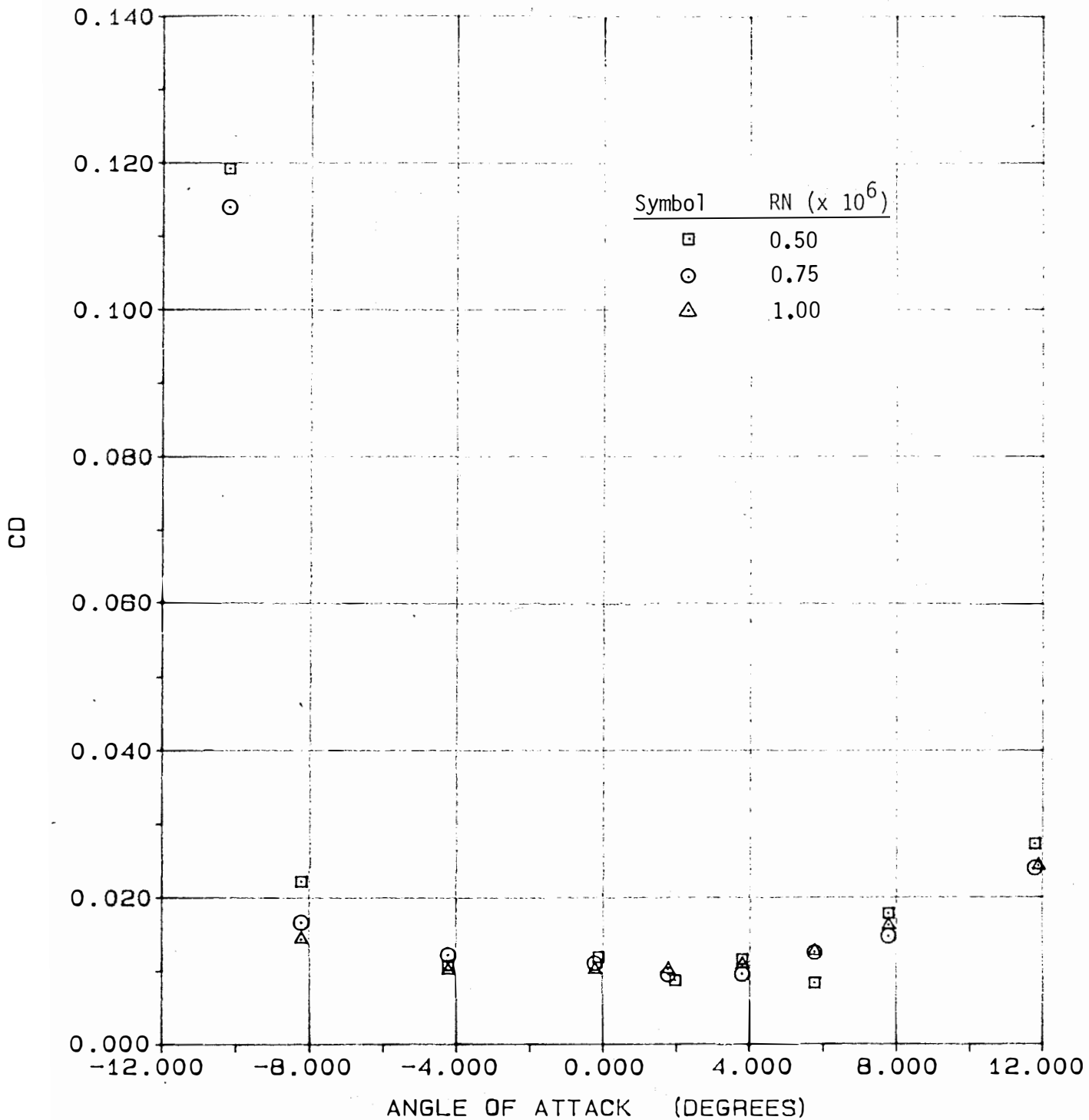


Figure B.2 - Wake Rake Drag Coefficient of the NACA 4415 Airfoil
(Aspect Ratio = ∞).

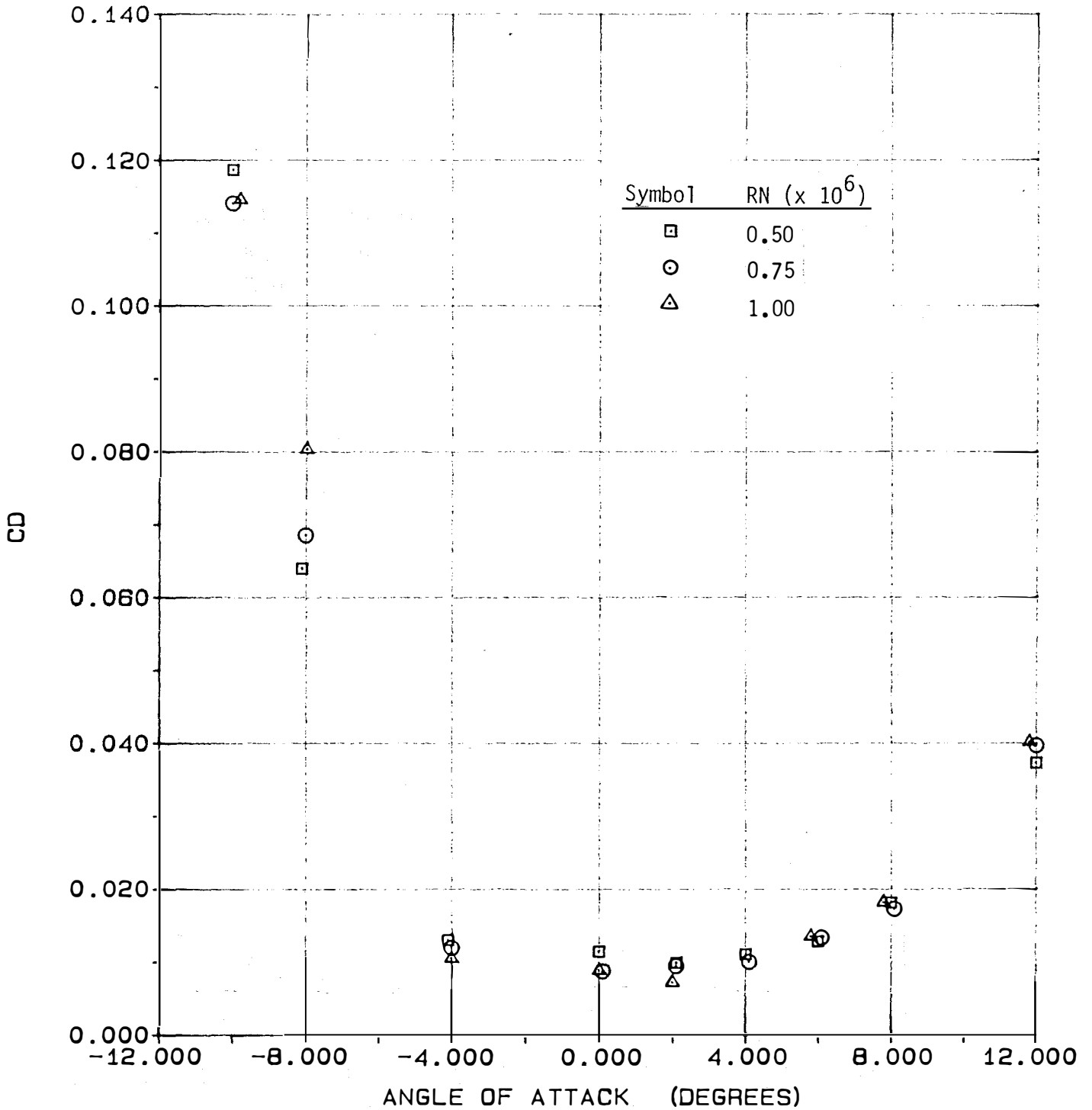


Figure B.3 - Wake Rake Drag Coefficient of the NACA 4412 Airfoil
(Aspect Ratio = ∞).

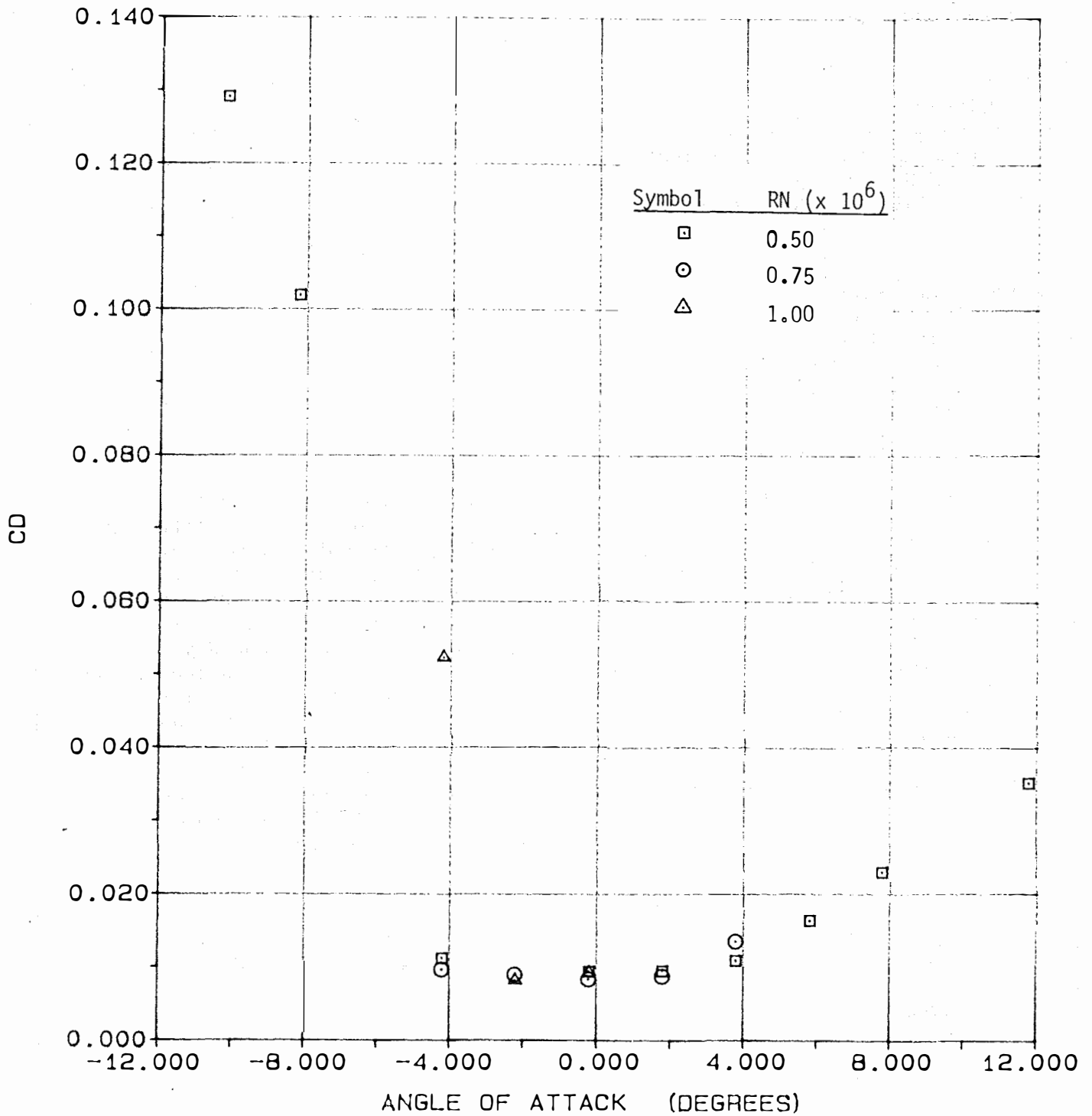


Figure B.4 - Wake Rake Drag Coefficient of the NACA 4409 Airfoil (Aspect Ratio = ∞).

Document Control Page	1. SERI Report No. SFRT/STR-217-2559	2. NTIS Accession No.	3. Recipient's Accession No.
	4. Title and Subtitle Post Stall Wind Tunnel Data for NACA 44XX Series Airfoil Sections		5. Publication Date January 1985
7. Author(s) C. Ostowari, D. Naik		6.	
9. Performing Organization Name and Address Aerospace Engineering Department Texas A&M University College Station, Texas 77843-3141		8. Performing Organization Rept. No.	10. Project/Task/Work Unit No. 4807.20
		11. Contract (C) or Grant (G) No. (C) DE-AC04-76DP03533 (G)	
12. Sponsoring Organization Name and Address Rockwell International Corporation Rocky Flats Plant Wind Energy Research Center Golden, Colorado 80402-0464		13. Type of Report & Period Covered Technical Report	
15. Supplementary Notes Technical Monitor: J. Tangler		14.	
16. Abstract (Limit: 200 words) Wind turbine blades operate over a wide angle of attach range. Unlike aircraft, a wind turbine's angle of attach range extends deep into stall where the three-dimensional performance characteristics of airfoils are not generally known. Peak power predictions upon which wind turbine components are sized depend on a good understanding of a blade's post-stall characteristics. The purpose of this wind tunnel study is to characterize the performance characteristics of a blade in stall as a function of its aspect ratio, airfoil thickness, and Reynolds number. This report documents results of the wind tunnel investigation of constant chord blades having four aspect ratios, with NACA 44XX series airfoil sections, at angles of attack ranging from -10° to 110° . Tests were conducted at Reynolds number ranging from 0.25×10^6 to 1.0×10^6 . The thickness ratios studied were 0.18, 0.15, 0.12, and 0.09. The aspect ratios were 6, 9, 12 and infinity. Results of force and pitching moment measurements over the angle of attack range for all combinations of Reynolds numbers, thickness, and aspect ratios, and the effects of boundary layer tripping are presented.			
17. Document Analysis a. Descriptors Aerodynamics ; Airfoils ; Boundary Layers ; Data ; Performance ; Reynolds Number ; Turbine Blades ; Wind Power ; Wind Tunnels ; Wind Turbines b. Identifiers/Open-Ended Terms c. UC Categories 60			
18. Availability Statement National Technical Information Service U.S. Department of Commerce 5285 Port Royal Road Springfield, Virginia 22161		19. No. of Pages 180	
		20. Price A09	